

Efficient multistate reweighting and configurational mapping algorithms for very large scale
thermodynamic property prediction from molecular simulations

A Dissertation

Presented to
the faculty of the School of Engineering and Applied Science
University of Virginia

in partial fulfillment
of the requirements for the degree

Doctor of Philosophy

by

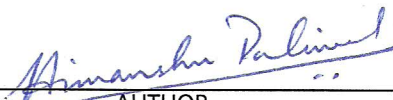
Himanshu Paliwal

May

2014

APPROVAL SHEET

The dissertation
is submitted in partial fulfillment of the requirements
for the degree of
Doctor of Philosophy


AUTHOR

The dissertation has been read and approved by the examining committee:

Prof. Michael R. Shirts

Advisor

Prof. John O'Connell

Prof. Gary Koenig, Jr.

Prof. Leonid V. Zhigilei

Prof. Cass Sackett

Accepted for the School of Engineering and Applied Science:



Dean, School of Engineering and Applied Science

May
2014

Acknowledgments

I would like to express my heartfelt gratitude to my advisor Prof. Michael R. Shirts. Without his help, support and vision, this work would not have been possible. I would like to thank my lab members Levi, Joe, Kai and Brittany. Their suggestions have contributed in bringing this effort to its final form.

I am extremely grateful to my teachers, Prof. O’Connell for teaching Thermodynamics, Prof. Zhigilei for teaching Atomistic Simulations, Prof. Cass Sackett for teaching Statistical Mechanics. These three subjects form the platform on which my research rests. I would like to thank Prof. Koenig for his very helpful suggestions and inputs.

I thank UVA ITC for their computing resources support.

Amit Acara prabhu and Mayapriya mataji, I would never be able to thank you enough for bringing meaning and direction in my life.

Last but not the least I thank my parents, my family, my friends at BYC and my wife Priya for all the emotional support they have provided me throughout the work.

Abstract

Thermodynamic property prediction using molecular simulation is a computationally expensive process and is the major bottleneck in large scale calculations where thermodynamic properties have to be evaluated multiple times. Examples of processes requiring multiple rounds of molecular simulation include molecular design, scanning of atomistic force field parameter space, simulation parameter space, and process design.

We present a reweighting technique which can accelerate property estimation by three orders of magnitude. We show the proof of this concept by doing a search in a combinatorially large simulation parameter space. The calculations in this exercise, if done without reweighting, would have taken 60 CPU years. However, with reweighting we were able to complete the search within one CPU month achieving an acceleration of 800 times. This search process makes error quantification of the simulation parameter space possible. The search also enabled us to choose a set of computationally inexpensive simulation parameters which gives statistically indistinguishable results compared to the most accurate but computationally most expensive set of parameters.

Estimating free energies between states having no overlap in the configurational space is very hard or sometimes impossible using standard free energy techniques. We have developed a multistate reweighting with configuration mapping algorithm which makes previously impossible problems trivially easy to solve. Free energy differences between rigid water models and free energy corresponding to change in the equilibrium bond length of a dipole is estimated using the newly developed algorithm. The calculations are not only easier to perform but are also three to five orders of magnitude faster compared to standard techniques.

Finally, we use a reweighting and configuration mapping algorithm to accelerate a multidimensional, multiobjective parameterization of rigid water model. The parameterization

also involved the design of an objective function which is able to simultaneously reduce error in all thermodynamic properties estimated using molecular simulations. The parameterization with standard techniques would have taken 1544 CPU years but with the application of the newly developed techniques the computational time was reduced to eight CPU weeks. The forcefield parameterization techniques based on pure fluid properties is extended to forcefield parameterization based on mixture properties and proposed as the next step in this research program.

Contents

1	Introduction	1
1.1	Why do we need efficient ways to estimate thermodynamic properties from molecular simulations?	1
1.1.1	Challenges in improving reliability and reproducibility in property estimation using molecular simulations	2
1.1.2	Design of molecular benchmark test set and statistical checks	2
1.1.3	Challenges in molecular design	3
1.1.4	Accelerating the force field space scans and simulation parameter space scans	5
1.1.5	Challenges in multiscale process design	14
1.1.6	Accelerating multiscale process design	17
2	Overview of important theoretical concepts	20
2.1	Model, method and parameters involved in the process of property prediction using molecular simulations	20
2.2	What is multistate reweighting?	24
2.2.1	Introduction	24
2.2.2	Reweighting Algorithms	27
2.2.2.1	Reweighting with one sampled state: Exponential Averaging	27
2.2.2.2	Reweighting with two states: Bennett Acceptance Ratio	28
2.2.2.3	Reweighting with multiple states: Multistate Bennett Acceptance Ratio	35

3	Using multistate reweighting to rapidly explore molecular simulation parameters space for nonbonded interactions	40
3.1	Introduction	40
3.2	Methods	47
3.2.1	Parameters in short and long range nonbonded interaction calculation	47
3.2.2	Phase one: Optimization of PME parameters	54
3.2.2.1	Difference in free energy estimates due to approximations introduced by simulation parameters	55
3.2.2.2	Difference in enthalpy of transformation	63
3.2.2.3	Difference in enthalpy of vaporization of water	66
3.2.3	Phase two: Optimization of the Coulomb switch	66
3.2.4	Phase three: Optimization of the Lennard-Jones parameters	67
3.3	Results	69
3.3.1	Optimized PME parameters	69
3.3.2	Optimized Coulomb switch	78
3.3.3	Optimized LJ cutoff and switch	83
3.3.4	Validation of the optimization procedure	90
3.4	Conclusions	101
4	Free energy calculation for alchemical transformations involving changes in molecular geometry using MBAR and extended warp bridge sampling.	106
4.1	Introduction	106
4.2	Methods	112
4.2.1	Derivation of multistate mapping formalism	113
4.2.2	Models	119

4.2.2.1	Truncated harmonic oscillators	119
4.2.2.2	Water models	123
4.2.2.3	Maps between water models	125
4.2.2.3.1	Mapping for TIP4P to TIP3P transformation . .	125
4.2.2.3.2	Mapping for SPC/E to TIP3P transformation . .	126
4.2.2.3.3	Mapping TIP4P to SPC/E transformation . . .	128
4.2.2.4	Dipole transformation	131
4.2.2.4.1	Mapping Dipole with different bond lengths . .	133
4.3	Results	134
4.3.1	Water models	134
4.3.1.1	Free energy differences	134
4.3.1.2	Enthalpy and entropy differences	141
4.3.2	Dipole transformation	146
4.4	Discussion and Conclusions	149
5	Using the multistate reweighting and mapping algorithm to identify and optimize models in water-like model parameter space	152
5.1	Introduction	152
5.2	Methods	157
5.2.1	Property estimation	157
5.2.1.1	Water properties from experimentally fitted equation of state	157
5.2.1.2	Water properties from SAFT based equation of state . . .	158
5.2.1.2.1	SAFT water model description	158
5.2.1.2.2	Property estimation from SAFT model	159

5.2.1.3	Water properties from an atomistic model	163
5.2.1.3.1	Atomistic model description	163
5.2.1.3.2	Property estimation from molecular simulations	164
5.2.1.4	Relationship between simulated and IAPWS95 residual Gibbs free energies	168
5.2.1.5	Estimating properties using free energies estimated using MBAR	176
5.2.1.6	Uncertainty in the property estimates	179
5.2.2	Defining the objective function	180
5.2.2.1	Objective function originally proposed	180
5.2.2.2	Revised objective function	181
5.2.2.3	Setting the water model parameter exploration space . . .	206
5.2.2.4	Work flow for the parameterization.	209
5.3	Results	210
5.4	Conclusions	229
6	Future work: Protocol to determine excess thermodynamic properties for methanol-water mixture using reweighting and mapping techniques and use it to parameterize water and methanol to reproduce both pure fluid properties as well as mixture properties at all compositions	231
6.1	Introduction	231
6.2	Methods	235
6.2.1	Calculation of excess Gibbs free energy, G^E	235
6.2.2	Calculation of excess enthalpy, H^E	240
6.2.3	Calculation of excess volume of mixing V^E	241

6.2.4	Calculation of excess entropy, S^E	241
6.2.5	Parameterization of water and methanol	242

References		244
-------------------	--	------------

List of Figures

- 1.1 The current procedure of estimating properties requires simulation or sampling at every thermodynamic state, which results in impractical computational costs. The total run time is sum over all the simulation time shown vertically above it. 6
- 1.2 We have developed a way in which we simulate at very few states and use only rerun potential energies along with sampled energies to substantially accelerate the property estimation process. The reweighting along with configurational mapping reduces the per state number of samples requirement, thus instead of 20 CPU hrs we need to collect samples for only 1 CPU hr. The rerun does not involve force calculation or integration of molecular dynamics and hence is significantly faster. Rerunning consists in only the last two steps in Figure 2.1. 7
- 1.3 Free energy and other thermophysical properties evaluated using the IAPWS95 free energy function for water are shown in this figure. If we can estimate the free energy as a function of temperature and pressure $G(T, P)$, we can estimate any thermophysical property which can be expressed as some function of the first or second derivative of free energy with respect to pressure and/or temperature. All thermophysical property surfaces viz. density $\rho(T, P)$, entropy $S(T, P)$, compressibility $\kappa(T, P)$, heat capacity $C_P(T, P)$ and the thermal expansion coefficient $\alpha(T, P)$ are embedded in the free energy surface $G(T, P)$ and can be easily extracted from it. 11

1.4	Design of a product at the atomistic scale affects the process design and design of process equipments. Design of reaction and separation networks, heat exchange networks, effluent treatment networks, to satisfy environmental constraints, all depend on the product's thermophysical and toxicity properties. Finally, the product and process design both affect the business/enterprise model by determining economic feasibility.	15
1.5	A fast method to generate dimensionless residual Gibbs free energy surface for TIP4P water model is shown in sub figures (a)-(c) along with the same property surface generated using IAPWS-95 equation of state shown in sub figure (d). (a) We generate samples at a few temperature and pressure combinations which takes less than an hour. (b) Next we predict properties at intermediate temperatures and pressures using reweighting. Reweighting calculations take less than a minute. (c) We could estimate the property at any temperature and pressure combination using bivariate spline or metamodel generated using the sampled and reweighted data. We used bivariate spline of order 5 in both temperature and pressure direction. On a closer inspection, we see that the interpolation is less accurate compared to reweighting. We could improve accuracy in interpolation by providing a much finer reweighted property mesh.	19
2.1	Properties estimated using molecular simulation, for example free energy change ΔG_{ij} , involves multiple steps. We have to make a choice of model methods and parameters at each step. All these choices effect the accuracy of the potential energies which eventually affect the accuracy of the estimated property. Frequently, little or no quantitative information is available to know how much each choice of parameter affects the results.	21

2.2	Free energy estimates are most accurate when information from multiple states is used with optimal reweighting. (a) Exponential averaging uses potential energy differences measured from only one state reweights using information from only one state. (b) BAR uses potential energy differences measured from two states and optimally reweights to estimate the free energy. (c) MBAR uses pairwise potential energy differences calculated from a state to every other state for multiple states and then optimally reweights to estimate the free energy.	39
3.1	$\Delta\Delta G_{Ei}$ for methane solvation between reference expensive PME parameters and a choice of the four PME parameters: Coulomb cutoff (x-axis of each graph), Fourier spacing (color), PME order (graphs arranged left to right), and Ewald tolerance (graphs arranged top to bottom). The difference in free energy differences goes to zero as the reference parameters are approached.	70
3.2	Change in enthalpy of methane solvation ($\langle H \rangle_{\lambda=1} - \langle H \rangle_{\lambda=0}$) between expensive reference PME parameters and a choice of the four PME parameters: Coulomb cutoff (x-axis of each graph), Fourier spacing (color), PME order (graphs arranged left to right), and Ewald tolerance (graphs arranged top to bottom). Although we can see the differences go to zero in the limit of the expensive reference parameters, because of the statistical noise in the enthalpy of solvation calculation, the level of bias for any given choice of parameters is difficult to identify.	71

3.3	Change in enthalpy of vaporization ΔH_{vap} for TIP3P water between expensive reference PME parameters and a choice of the four PME parameters: Coulomb cutoff (x-axis of each graph), Fourier spacing (color), PME order (graphs arranged left to right), and Ewald tolerance (graphs arranged top to bottom) for methane solvation, showing clear convergence to zero for more expensive parameters.	72
3.4	Simulation speed for methane solvation as a function of different PME parameters, Coulomb cutoff (x-axis of each graph), Fourier spacing (color), PME order (graphs arranged left to right), and Ewald tolerance (graphs arranged top to bottom) . Simulation speed is unaffected by the change in the order of interpolation and Ewald tolerance for high Fourier spacings but it increases with decreasing Fourier spacing and increasing Coulomb cut-off.	73
3.5	$\Delta\Delta G_{Ei}$ for dipole inversion between converged PME parameters and a choice of the four PME parameters Coulomb cutoff (x-axis of each graph), Fourier spacing (color), PME order (graphs arranged left to right), and Ewald tolerance (graphs arranged top to bottom).	75
3.6	Simulation speed for dipole inversion as a function of different PME parameters, Coulomb cutoff (x-axis of each graph), Fourier spacing (color), PME order (graphs arranged left to right), and Ewald tolerance (graphs arranged top to bottom).	76
3.7	$\Delta\Delta G_{Ei}$ for anthracene solvation between converged PME parameters and a choice of the four PME parameters Coulomb cutoff (x-axis of each graph), Fourier spacing (color), PME order (graphs arranged left to right), and Ewald tolerance (graphs arranged top to bottom).	77

3.8	Simulation speed for anthracene solvation as a function of different PME parameters, Coulomb cutoff (x-axis of each graph), Fourier spacing (color), PME order (graphs arranged left to right), and Ewald tolerance (graphs arranged top to bottom).	78
3.9	$\Delta\Delta G_{Ei}$ for methane solvation and ΔH_{vap} for TIP3P water between reference expensive PME parameters and the value of Coulomb switch width for a optimized Coulomb cutoff of 0.9 nm. Coulomb switch widths of less than 0.1 nm at this cutoff distance and optimized PME parameters are statistically indistinguishable from the reference PME potential. Error bars are one standard deviation.	79
3.10	Short range potential energies at Coulomb and LJ cutoff of 0.9 nm using different switching distances and an Ewald tolerance of 10^{-4}	81
3.11	Force spikes at Coulomb and LJ cutoff of 0.9nm using different switching distances and an Ewald Tolerance of 10^{-4}	82
3.12	$\Delta\Delta G_{solv}$ for dipole inversion (left) and anthracene solvation (right) as a function of different switching distances for a cutoff of 0.9 nm. Note the large y-axis energy scale for anthracene (approximately $6\times$ the dipole scale).	83

3.13	$\Delta\Delta G_{\text{solv}}$ for methane solvation (left), dipole inversion (center) and anthracene solvation (right) as a function of different Lennard-Jones switching distances for Lennard-Jones cutoffs in increments of 0.1 nm from 0.6 to the maximum allowed by the box. Each color represents a different cutoff distance, each and line within the color represents the value at a different switching distance, including statistical uncertainty. Note differences in y-axis energy scale, with the dipole inversion scale being approximately $10\times$ smaller than the other two. The inset for methane solvation demonstrates how $\Delta\Delta G$ converges to essentially zero at the largest Lennard-Jones cutoff of 1.3 nm, and below 0.007 kJ/mol for cutoffs of 0.9 nm or greater for any switch width.	84
3.14	ΔH_{vap} for TIP3P water as a function of different Lennard-Jones switching distances for Lennard-Jones cutoffs 0.6–1.3 nm. ΔH_{vap} at and beyond 0.9 nm Lennard-Jones cutoff is less than 0.005 kJ/mol for any switch distance .	85
4.1	The difference between analytically calculated free energy $\Delta G_{ij,g}$ and free energy calculated using MBAR with mapping $\Delta G_{ij,\ell}$ should be consistent with the difference in the solvation free energies calculated using MBAR without mapping for thermodynamic cycle (a) according to Eq. 4.22 for the three transformations. $\Delta G_{ij,\ell}$, $\Delta G_{jk,\ell}$ and $\Delta G_{ki,\ell}$ should add up to zero in thermodynamic cycle (b) according to Eq. 4.23.	123
4.2	(a) TIP4P to TIP3P transformation and (b) SPC/E to TIP3P transformation .	130
4.3	Transformation of equilibrium bond lengths in dipole	133
4.4	Free energy estimates converge with just five intermediate states for all the transformations.	138

4.5	Free energies differences along the transformation coordinate are plotted for the three water transformations. Three intermediate states are sufficient to accurately estimate the free energy difference, or a single intermediate state if less precision is required. Uncertainties are the same size as or smaller than the symbols.	138
4.6	$\Delta\Delta G_{hyd}$ for SPC/E–TIP4P estimated using MBAR with mapping with different number of states (2, 3, 5, 11, 21) and number of samples per state (10, 100, 1000, 10 000) has 2–3 orders lower uncertainty compared with $\Delta\Delta G_{hyd}$ for SPC/E–TIP4P estimated using MBAR without mapping with 21 states and 20 000 samples per state.	139
4.7	Ratio of samples required for MBAR without remapping vs. with remapping to achieve a target statistical uncertainty. Mapping and reweighting approaches requires 10^2 – 10^5 times fewer samples compared to MBAR without mapping to achieve the same precision in $\Delta\Delta G_{hyd}$	140
4.8	The free energy differences between dipoles of different equilibrium lengths are calculated using two approaches: (a) MBAR without mapping and (b) MBAR with mapping. Different number of states (2, 3, 5, 11) and number of samples in each state (10, 100, 1000, 10 000) are used to estimate the free energies. MBAR with mapping estimates converged free energies with low uncertainty using only 2 states and 100 to 1000 samples per state where as MBAR without mapping gives unconverged free energy estimate with high uncertainty unless many intermediates are used. In subplot (c) we see that the uncertainty in free energy using MBAR with mapping is an order lower compared to uncertainty in free energy estimated using MBAR without mapping using the same amount of sampling.	147

4.9	Log ratio of samples required for MBAR without remapping vs. with remapping to achieve a target statistical uncertainty for the free energy difference between dipoles of different lengths. Phase space remapping combined with MBAR requires 3–300 times fewer samples compared to MBAR without mapping to achieve the same precision in estimating free energies between dipoles of different length.	148
5.1	There are three nonbonded parameters, σ_O , ϵ_O , and q_O and three geometry or bonded parameters r_{OH} , $\angle HOH$, and r_{OM} in water model. σ and ϵ for hydrogen are zero and once q_O is fixed we also know the partial charge on the two hydrogens.	154
5.2	The isobaric specific heat capacity of rigid water model in ideal gas state (in black) is constant compared to a temperature dependent ideal gas heat capacity for real water (in red).	188
5.3	We start the minimization with TIP4P-2005 water model parameters. Even though we minimize error in residual free energy, the density versus temperature behavior gets totally distorted. We see that at $[T=274 \text{ K}, P=1\text{atm}]$, $[T=298 \text{ K}, P=1\text{atm}]$, $[T=372 \text{ K}, P=1\text{atm}]$ the constraints on density are followed however around the constraint points the curve rises and falls multiple times.	192
5.4	Subplots on the left show the values of the parameters at the start of the optimization; Subplots on the right show the values of the parameters at the end of optimization from 1000 SAFT model optimization runs using the objective function definition in Eq. 5.66. We see bands forming indicating possible location of a water like model however there is no prominent minima.	200

5.5	Subplots on the left show the values of the parameters at the start of the optimization; Subplots on the right show the values of the parameters at the end of optimization from 500 SAFT model optimization runs using the objective function definition in Eq. 5.68. We see a distinct value for ϵ and a single band of allowed values for σ	201
5.6	There exist low dimensional submanifolds which relate the SAFT model parameters. The association parameters K_{hb} , σ_{hb} , and ϵ_{hb} for which the mean square errors in molar volume, residual internal energy, residual entropy and residual Gibbs free energy is lower than 0.01 fall on a surface and the corresponding Lennard-Jones and coulomb parameters σ_{LJ} , ϵ_{LJ} and μ fall on a line.	203
5.7	This plot shows that in a two dimensional infinite space of σ_{LJ} , and ϵ_{LJ} parameters, there is a very small portion, a small and thin line, which corresponds to SAFT model parameters which reproduce experimental molar volume, residual internal energy, residual entropy and residual Gibbs free energy with a mean square error of 0.01.	204
5.8	There exists a single, distinct minima both with respect to bond length and bond angle in the potential energy surface of a water molecule in gas phase.	208
5.9	The workflow for the optimization. The thermodynamic observables are estimated using reweighting as opposed to running new molecular simulations. This should speed up the iterations in the workflow.	210
5.10	MSRE in V , U_{res} , S_{res} and f_{res} cannot simultaneously decrease indefinitely. MSRE in U_{res} , S_{res} and f_{res} has to be sacrificed to get reduction in MSRE in V	213

5.11	After we relax the tolerances in U_{res} , S_{res} and f_{res} at the sixth sampled set we see that all the parameters converge to a value for which MSRE in V is minimum.	215
5.12	MSRE in f_{res} reduces by 99% after optimization. (a) Experimental f_{res} surface, (b) TIP4P f_{res} surface, (c) GOPAL f_{res} surface (d) difference between TIP4P and experimental f_{res} surfaces, (e) difference between GOPAL and experimental f_{res} surface	219
5.13	MSRE in U_{res} reduces by 85% after optimization. (a) Experimental U_{res} surface, (b) TIP4P U_{res} surface, (c) GOPAL U_{res} surface (d) difference between TIP4P and experimental U_{res} surfaces, (e) difference between GOPAL and experimental U_{res} surfaces	220
5.14	MSRE in S_{res} reduces by 68% after optimization. (a) Experimental S_{res} surface, (b) TIP4P S_{res} surface, (c) GOPAL S_{res} surface (d) difference between TIP4P and experimental S_{res} surfaces, (e) difference between GOPAL and experimental S_{res} surfaces	221
5.15	MSRE in V reduces by 37% after optimization. Error in V gets redistributed evenly around $T = 310$ K after optimization. (a) Experimental V surface, (b) TIP4P V surface, (c) GOPAL V surface (d) difference between TIP4P and experimental V surfaces, (e) difference between GOPAL and experimental V surfaces	222
5.16	MSRE in density reduces by 35% after optimization. Error in density also gets redistributed evenly around $T = 310$ K after optimization. (a) Experimental density surface, (b) TIP4P density surface, (c) GOPAL density surface (d) difference between TIP4P and experimental density surfaces, (e) difference between GOPAL and experimental density surfaces	223

5.17	MSRE in H_{res} reduces by 85% after optimization. (a) Experimental H_{res} surface, (b) TIP4P H_{res} surface, (c) GOPAL H_{res} surface (d) difference between TIP4P and experimental H_{res} surfaces, (e) difference between GOPAL and experimental H_{res} surfaces	224
5.18	MSRE in H_{vap} reduces by 16% after optimization, however, there is shift of $\simeq 4.5$ kJ/mol. (a) Experimental H_{vap} surface, (b) TIP4P H_{vap} surface, (c) GOPAL H_{vap} surface (d) difference between TIP4P and experimental H_{vap} surfaces, (e) difference between GOPAL and experimental H_{vap} surfaces	225
5.19	MSRE in Cp_{res} reduces by 76% after optimization. (a) Experimental Cp_{res} surface, (b) TIP4P Cp_{res} surface, (c) GOPAL Cp_{res} surface (d) difference between TIP4P and experimental Cp_{res} surfaces, (e) difference between GOPAL and experimental Cp_{res} surfaces	226
5.20	MSRE in κ reduces by 54% after optimization. (a) Experimental κ surface, (b) TIP4P κ surface, (c) GOPAL κ surface (d) difference between TIP4P and experimental κ surfaces, (e) difference between GOPAL and experimental κ surfaces	227
5.21	MSRE in α seems to increase by 74% after optimization. However, this increase is strongly dominated by the large relative error $\simeq 10^3$ near the melting temperature. (a) Experimental α surface, (b) TIP4P α surface, (c) GOPAL α surface (d) difference between TIP4P and experimental α surfaces, (e) difference between GOPAL and experimental α surfaces	228

List of Tables

3.1	Nonbonded interaction parameter values examined in the optimization process.	54
3.2	Predictions and validation $\Delta\Delta G_{EO}$ results for methane solvation match within one and two standard deviations. In column two ΔG and $\Delta\Delta G$ are estimated using samples from benchmark parameter set and re-evaluations done at expensive and optimized parameter sets. In column three we use samples from only one parameter set: either only the benchmark parameter set (B) or only the expensive (E) or only the optimized (O) parameter set. For columns 4-6 we use samples from a pair of parameter sets. Re-evaluation is not done for the remaining parameter sets, so we have no estimate for the unsampled parameter set (labeled as N/A).	86
3.3	Predictions and validation ΔH_{vap} results match for all the three parameter sets within two standard deviations.	87
3.4	Predictions and validation $\Delta\Delta G_{EO}$ results for discharging, charging and complete dipole inversion also match within one and two standard deviations.	88
3.5	Predictions and validation results for anthracene solvation match within one and two standard deviation for $\Delta\Delta G_{EO}$. The predictions that ΔG for expensive and optimized parameter sets are greater than ΔG for benchmark parameter set is correct.	89
3.6	Benchmark, expensive and optimized parameters.	92
3.7	Re-evaluation is more than two orders of magnitude faster than generating fresh samples using MD. The initial optimized parameters are used. . . .	102

3.8	Predicted $\Delta\Delta G_{Ei}$ for GROMACS default parameters, in the bottom right corner, give marginally better convergence compared to the first optimized guess for a slight (10-15%) performance cost. Both satisfy the first criteria of statistical indistinguishability compared to ΔG_E calculations (one standard deviation error shown in column 5).	105
4.1	Force field parameters for the water models used in this study.	125
4.2	$\Delta G_{ij,g}$ (column 1) is calculated analytically and $\Delta G_{ij,\ell}$ (column 2) is calculated using MBAR with mapping. The differences $\Delta\Delta G_{hyd}$ (decoupling) are calculated using direct subtraction and error propagation using data from Table 4.4. $\Delta\Delta G_{hyd}(\text{mapping}) - \Delta\Delta G_{hyd}(\text{decoupling})$ are zero within two and three standard deviations according to the thermodynamic cycle in Eq. 4.22 for all transformations. Subscripts a , b , and c refer to the transformations labeled a , b and c in the first three rows. The result of decoupling cycle in column 5 of the last row is constrained to be identically zero numerically because it consists of quantities $(i - j) + (j - k) + (k - i)$. The result of the mapping cycle in column 4 of the last row is not constrained to be identically zero numerically as it consists of three independent calculations using different simulations; instead, it is in such close agreement with the thermodynamic cycle in Eq. 4.23 because of the high statistical precision of the approach. All free energies are in kJ/mol. . . .	136

4.3	All enthalpies are in kJ/mol and all entropies are in J/mol/K. Decoupling ΔH_{vap} s are calculated using direct subtraction and error propagation using data from Table 4.4. The differences $\Delta S_{ij,\ell}$ are calculated using the relationship $\Delta S = (\Delta H - \Delta G)/T$ for both decoupling and mapping cases, with uncertainties propagated using the covariance calculated with MBAR. Subscripts a , b , and c refer to the transformations labeled a , b and c in the first three rows. The thermodynamic cycle in Eq. 4.23 is satisfied for enthalpy H and entropy S . Enthalpies and entropies calculated with decoupling method agree with the ones calculated using mapping formalism within statistical error.	142
4.4	Solvation free energies, ΔG_{hyd} , and enthalpy of vaporization H_{vap} . H_{vap} estimated using MBAR without mapping (column 3) has half the error as H_{vap} using the standard method of energy averages at the endpoint alone (column 4), as it uses information from nearby intermediate states.	143
4.5	MBAR with mapping requires just 2 states and 1000 samples per state to estimate converged and precise free energy difference between dipoles of very different equilibrium lengths.	146
5.1	The parameter bounds for exploring the SAFT water model parameter space.	198
5.2	The quantum mechanical calculations predict geometry that is close to the experimentally observed gas phase water monomer geometry. In a single point calculation we use user specified molecular geometry to estimate the partial charges.	207
5.3	The parameter bounds for exploring the atomistic water model parameter space.	209

5.4	Optimization converged after 11 simulation iterations and 4100 iterations involving reweighting.	211
5.5	MSREs for optimized parameters compared as a function of iteration from the optimization done using a grid of 110 temperature and pressure points. .	214
5.6	MSRE of all properties derived from first and second derivatives of Gibbs free energy with respect to temperature and pressure decrease for GOPAL. MSRE in G_{res} is statistically insignificant and close to zero for GOPAL. Near the melting temperature, relative errors in α_P are very high because the experimental α_T are very close to zero $\sim 10^{-7} \text{ K}^{-1}$ while the simulated α_P are still $\sim 4 \times 10^{-4} \text{ K}^{-1}$ causing the MSRE to jump three orders of magnitude. At all other temperatures the relative errors in α_P are less than 1. For the rest of the properties there is a statistically significant improvement in the corresponding MSRE. MSRE calculations in this table are done using properties estimated for 210 temperature and pressure combinations. .	218
S1	Predictions and validation results for enthalpy of methane solvation match for expensive and optimal parameter sets within two standard deviations . .	265
S2	Predictions and validation results for enthalpy of dipole inversion match for expensive and optimal parameter sets within two standard deviations . .	266
S3	Predictions and validation results for enthalpy of anthracene solvation match for expensive and optimal parameter sets are within two standard deviations.	267

1 Introduction

1.1 Why do we need efficient ways to estimate thermodynamic properties from molecular simulations?

The field of molecular simulations has come a long way from simulating a few hundred Lennard Jones particles [1] for few picoseconds to simulating an entire viral capsid (1.2 million particles) for microseconds [2]. The gradual advancements in the field have enabled molecular simulations to be used as a potential design tool by reproducing processes occurring at the molecular scale and to help guide experiments. Statistical mechanical tools can be used to quantify the extent of molecular transformations in terms of change in thermodynamic observables to compare simulated results with experiments. Hardware improvements along with improved algorithms have made previously impossible simulation sizes and time scales achievable.

However, complex and lengthy simulations are helpful only if they can reproduce the underlying physics of the system to an acceptable error tolerance. The parameters used to model the potential and kinetic energies of the system under investigation have a significant effect on the thermodynamic and transport properties estimated from simulation. The statistical mechanical approach used to calculate observables from the sampled energies can also contribute to a bias in the predicted observables.

We require a systematic error quantification of the different approaches used for property estimation using molecular simulations. Proper characterization of different choices of model, method and parameters requires very large scale scans over parameter space or force field space which is computationally prohibitive. Even the molecular design and the subsequent process design involves multiple iterations involving property estimation at

each step. With the current molecular simulation methods property estimation becomes the rate limiting step for the entire process. In the following sections we further investigate the problems associated with error quantification and property estimation using molecular simulation.

1.1.1 Challenges in improving reliability and reproducibility in property estimation using molecular simulations

Verification, validation and error quantification of model, method and parameters involved in thermodynamic as well as transport property estimation using molecular simulations will enhance the reliability and the reproducibility of the results generated *in silico*. As part of the Shirts research group efforts my research focuses on improving the utility and reliability of thermodynamic property prediction using molecular simulations. I have performed several important studies that help achieve these goals.

1.1.2 Design of molecular benchmark test set and statistical checks

In my M.S. research, I introduced a molecular benchmark set and a series of statistical checks to systematically characterize equilibrium free energy estimators. We used this molecular benchmark test set to directly compare 10 different equilibrium free energy estimators based on the bias and precision in both the estimated free energy as well as estimated uncertainty [3]. In this work, we quantitatively showed MBAR (Multistate Bennett Acceptance Ratio) [4] was the most efficient as well as accurate and precise thermodynamic property estimator for a given choice of force field, thermostat and barostat.

In the past two years, our lab has created tools to check the thermodynamic ensemble consistency for barostats and thermostats, i.e., whether they sample from the desired ensemble [5]; and studied the effect of parameter choices in the thermostats on transport

properties [6]. My present Ph.D. research focuses on creating tools to quantify and then minimize error in thermodynamic property estimation associated with the choice of the force field and simulation run parameters in molecular simulation. The choice of the atomistic force field parameters is very important in any molecular design problem as the parameters along with the potential model determine the accuracy in reproducing the correct strength and direction of interactions experienced by particles constituting the system under given external conditions of pressure and temperature. The improved accuracy in the atomistic representation of molecular systems will strengthen the confidence in its use as a design tool.

1.1.3 Challenges in molecular design

We can classify molecular design problems into two types. The first type is the forward problem in which for a given molecular system we have to estimate a thermophysical property. For example, if one wants to design a model to study the effect of pollutants on environment one has to know the solvation free energies of the pollutants in different environments i.e. water and air in order to quantify the partitioning of the pollutants in different media. There could be some pollutant species for which the experimental data is not available and thus we cannot parameterize the activity coefficient models to make thermodynamic property predictions. This is where molecular modeling can help, as we can find the solvation free energy *in silico* using molecular simulations. For a given accuracy of the atomistic model parameters, transferability of the force field and proper implementation of barostat and thermostat, we can reduce the bias in the observables due to number of samples and number of intermediate states used for property estimation by choosing MBAR to perform our calculations.

The second type of molecular design problem is the inverse problem in which we wish

to design a molecule which exhibits desired thermophysical property. Examples include drug design, design of new surfactants, new chromatographic surfaces, new solvents, studying phase equilibrium etc. All such designs require scanning over a large, multidimensional but discrete/discontinuous chemical space. There are discrete points in the chemical space represented by different chemical elements. The discrete chemical search space is a subset of continuous, multidimensional and vast atomistic force field parameter space. These different dimensions include nonbonded parameters like charge, Lennard-Jones σ_{LJ} and ϵ_{LJ} , and geometrical parameters like bond length, bond angle, dihedral angle. One could map different molecules from the chemical search space to force field parameters in the parameter space. However, we cannot map all the points from the force field parameter space to a physically possible molecules in chemical space. We are often interested in only a very small portion of this vast, continuous multidimensional force field parameter space, the region corresponding to atomistic models consistent with the desired thermophysical properties. For example, when parameterizing force fields, we scan the model parameter space to find a parameter set which reproduces experimental thermodynamic observables like binding affinity, density, heat of vaporization etc.

The thermodynamic observables are typically estimated using a statistical mechanical approach which almost always requires generation of samples using molecular dynamics or Monte Carlo simulation. To run any molecular simulation, we need to pick a set of simulation parameters, for instance, the nonbonded cutoffs. The choice of these simulation parameters controls the accuracy of Coulomb and Lennard-Jones potential energy calculations. Initially, we don't know which combination of simulation parameters is computationally inexpensive for calculating the thermodynamic property of interest accurately. The only way to determine this is by estimating thermodynamic observables for a large simulation parameter space to select a set of simulation parameters which are fastest for a

given accuracy. However using the current methods the task of exploring the vast combinatorial parameter space was simply impossible. If we assume that we know the correct simulation parameters and force field parameters, we could potentially estimate accurate estimates of the thermodynamic properties using molecular simulations.

1.1.4 Accelerating the force field space scans and simulation parameter space scans

Force field parameter scan and simulation parameter scan require high throughput estimation of thermodynamic observables. However, it can be computationally challenging to evaluate free energies and expectation values of thermodynamic observables over the large, multidimensional space of possible simulation or force field parameters. The sample generation cost for such a high throughput estimation of thermodynamic observables is prohibitively large. Take the case of a rigid 4 site water model. The parameter space comprises of charge q_O , Lennard-Jones $\sigma_{LJ,O}$, $\epsilon_{LJ,O}$ of oxygen, O-H bond length, H-O-H bond angle and distance of the virtual site carrying negative charge from oxygen atom. Even if we choose only 10 values for each parameter to scan the water model parameter space, we will be required to evaluate 10^6 parameter sets. Each parameter set corresponds to an alchemical thermodynamic state. If simulation for a single state takes 20 CPU hrs to generate sufficient samples, simulation for 10^6 states will take 2283 CPU years to complete.

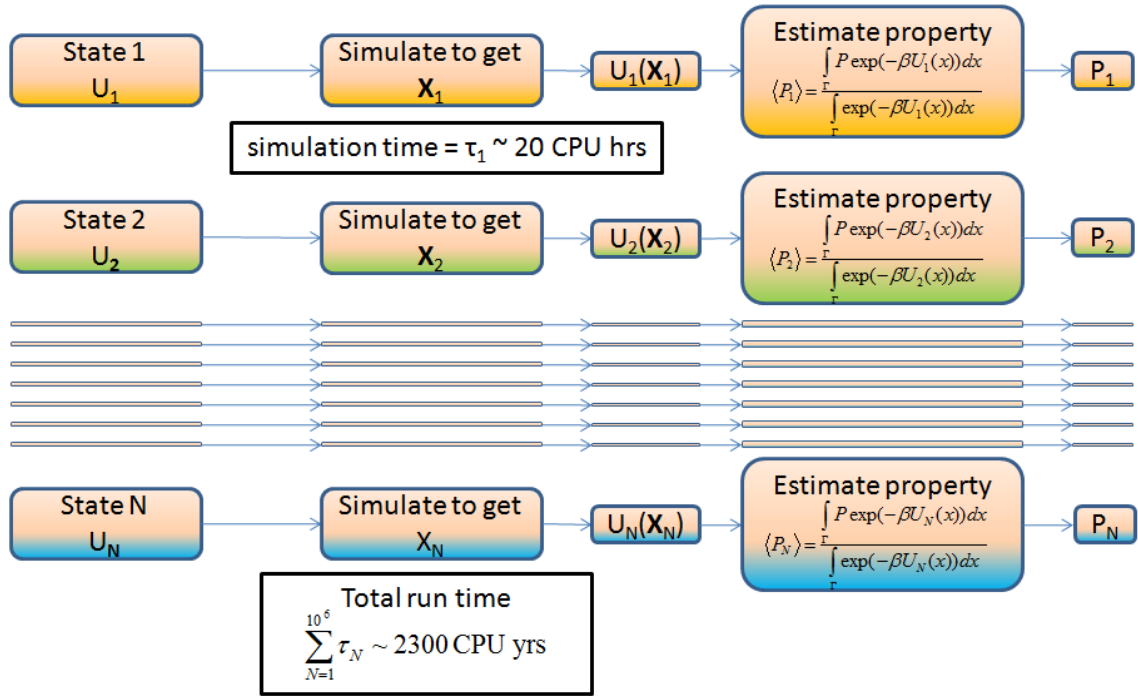


Figure 1.1: The current procedure of estimating properties requires simulation or sampling at every thermodynamic state, which results in impractical computational costs. The total run time is sum over all the simulation time shown vertically above it.

Figure 1.1 shows how combinatorial parameter scans are typically done today. We can reduce the computational cost of the parameter scan if we can reduce the amount of time spent in sampling. We can reduce sampling if we can sample just a few states and predict the observables for the majority of unsampled states. We can thus improve the efficiency of the property estimation process, if we can get the same amount of statistical efficiency while collecting fewer samples.

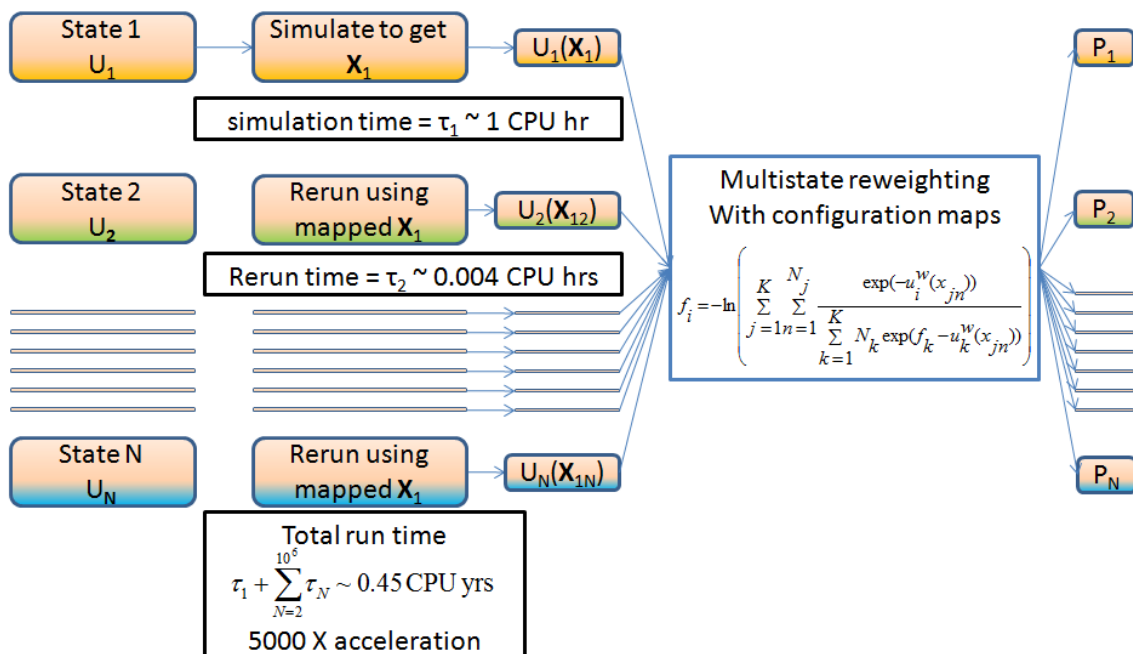


Figure 1.2: We have developed a way in which we simulate at very few states and use only rerun potential energies along with sampled energies to substantially accelerate the property estimation process. The reweighting along with configurational mapping reduces the per state number of samples requirement, thus instead of 20 CPU hrs we need to collect samples for only 1 CPU hr. The rerun does not involve force calculation or integration of molecular dynamics and hence is significantly faster. Rerunning consists in only the last two steps in Figure 2.1.

Multistate reweighting methods such as the multistate Bennett acceptance ratio (MBAR) [4] can help solve this problem by predicting free energies and expectation values of observables at insufficiently sampled or unsampled states using simulations performed at only a few sampled states, together with single point energy reevaluations over the unsampled states.

Figure 1.2 shows the new, faster algorithmic approach we have introduced to bring down the computational costs without losing out on accuracy. In chapter two, we first go through the process of property estimation using molecular simulation and describe

in brief the various choices of model, method and parameters involved at each step. We also explain what multistate reweighting is. We go through the derivation of free energy estimating algorithms in which 1) reweighting with one states is involved (Exponential Averaging) [7] 2) reweighting with two states is involved (Bennett Acceptance Ratio) [8] 3) reweighting with multiple states is involved (Multistate Bennett Acceptance Ratio) [4]. We show through the working equations how accuracy of the free energy estimate is increased by involving information from more and more states.

In chapter three, we demonstrate the power of the multistate reweighting formalism to predict observables for a very large number of unsampled states using information from just a few sampled states. We explore a large combinatorial space of molecular simulation parameters like nonbonded cutoffs, Ewald sum parameters and potential switch distance, using data collected at a single choice of these parameters. Using multistate reweighting, we can quickly identify the computationally least expensive simulation parameters required to obtain a specified accuracy in observables compared to the answer obtained at the most expensive parameters. We specifically examine free energy estimates of three molecular transformations in a benchmark set and the enthalpy of vaporization of TIP3P water. The results not only demonstrate the power of this multistate reweighting approach, but also help identify simulation parameters which can affect free energy calculations and provide guidance to determine the simulation parameters which are both appropriate and computationally efficient for many types of simulation. A simulation parameter space scan described in this chapter would have taken 60 CPU years using conventional methods but reweighting formalism reduced the computational cost to a CPU month.

Standard free energy methods can estimate free energies for alchemical transformations involving only interaction parameters, charge, Lennard-Jones repulsive and attractive terms $C_{12} = 4\epsilon\sigma^{12}$, $C_6 = 4\epsilon\sigma^6$, respectively. However, molecular transformations and parameteri-

zation of force fields require perturbations in molecular geometry as well. It is impossible to calculate free energies using reweighting techniques like free energy perturbation if configurations in a simulation of a state are never seen in simulations of other states. Other techniques for estimating free energies corresponding to changes in molecular geometry are cumbersome and hard to adopt for large scale problems. Thus, estimating free energy of transformations involving a change in molecular geometries is still a big challenge.

In chapter four, we present a new algorithm to calculate free energy differences between geometrically different molecules which have very little or no overlap in the configuration space. The algorithm is built upon the principles of multistate Bennett acceptance ratio (MBAR) and warp bridge sampling. The algorithm is a multistate, minimum variance free energy estimator in which reweighting involves mapping geometries from one state to every other intermediate state in order to facilitate calculation of free energies for transformations involving geometry change. This algorithm is independent of the choice of a reference state. We show its application by calculating 1) free energy differences between non-overlapping, truncated harmonic oscillators, 2) pairwise free energy of transformation for three water models, TIP3P [9], SPC/E [10] and TIP4P [9]. The configuration mapping theory is exact for overlapping truncated harmonic oscillators. The new algorithm, MBAR with mapping, shows a speed up of three orders of magnitude compared to MBAR without mapping. We can thus further reduce the number of samples required for free energy estimation if we use this mapping technique.

Equipped with multistate reweighting and configuration mapping algorithms, we can now build tools required to do force field parameterization or even alchemical molecular design. We show the proof of this concept in chapter five. We not only demonstrate the use of the newly developed computational techniques to explore the rigid water model parameter space but also come up with radically new parameterization schemes. Previous water

models have fit parameters by minimizing error in a single property (density) by sequentially fitting one parameter at a time to a single property (density) at a single temperature and pressure (SPC, SPC/E, TIP3P) or multiple temperatures but single pressure (TIP4P-EW [11], TIP4P/2005) [12]. During the parameterization, geometry parameters, OH bond length r_{OH} , OM bond length r_{OM} where M is the virtual site carrying oxygen's negative charge, HOH bond angle $\angle HOH$, are kept fixed and only interaction parameters ($\sigma_{O,LJ}$, $\epsilon_{O,LJ}$ and q_O) are perturbed one by one. We simultaneously perturb all 6 parameters while fitting to multiple properties at multiple temperature and pressure combinations.

Current force field parameterization protocols involve computationally costly molecular dynamics (MD) simulations at each iteration to estimate the thermodynamic observables of interest. As a result, we are often forced to use the parameters which come from a force field parameterized for entirely different system and external conditions. The force fields are not updated and extended frequently to include new atom types for the same reason. The parameterization is also dependent on the choice of properties to which parameters are fit, the relative weights we put on different properties and the choice of preference function itself.

In chapter five, we also present a parameterization scheme which helps solve the problem of choosing the weights and preference function for different thermodynamic observables. A closer inspection of all the properties reveals that all of them are response functions of Gibbs free energy (G) with respect to changes in temperature and pressure. For example, we can calculate the molar volume or density if we know the change in Gibbs free energy for a small change in pressure at constant temperature ($V = \left(\frac{\partial G}{\partial P}\right)_T$; $\rho = 1/V$). Similarly, if we know the change in Gibbs free energy for a small change in temperature at constant pressure we can estimate enthalpy ($H = -T^2 \left(\frac{\partial G/T}{\partial T}\right)_P$). So, instead of fitting to different property surfaces $\rho(T, P)$, $H(T, P)$, $C_P(T, P)$ etc., we fit to a single $G(T, P)$ surface as

all the property surfaces can be derived from the $G(T, P)$ surface.

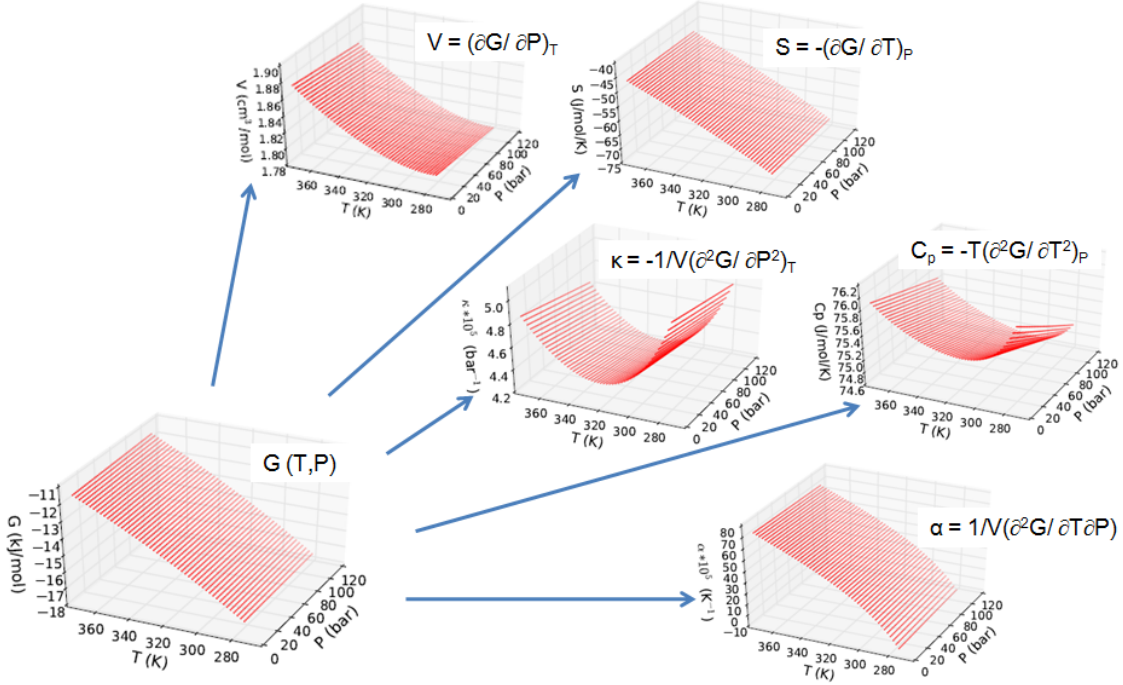


Figure 1.3: Free energy and other thermophysical properties evaluated using the IAPWS95 free energy function for water are shown in this figure. If we can estimate the free energy as a function of temperature and pressure $G(T, P)$, we can estimate any thermophysical property which can be expressed as some function of the first or second derivative of free energy with respect to pressure and/or temperature. All thermophysical property surfaces viz. density $\rho(T, P)$, entropy $S(T, P)$, compressibility $\kappa(T, P)$, heat capacity $C_P(T, P)$ and the thermal expansion coefficient $\alpha(T, P)$ are embedded in the free energy surface $G(T, P)$ and can be easily extracted from it.

Ideally if we could fit our parameters to experimental $G(T, P)$ surface to a very small tolerance, all model property surfaces will automatically fit to experimental property surfaces. This cleaner and more robust parameterization scheme is accelerated as MD is partially replaced with the reweighting and configuration mapping techniques developed in chapter three and four respectively. Even with the acceleration achieved using reweighting and mapping techniques the computational cost for exploring the vast multidimensional

parameter space remains prohibitive. We use an statistical association fluid theory based directly solvable equation of state to guide the more expensive atomistic forcefield optimization for pure fluid.

In chapter six, concepts for force field parameterization based on pure fluid properties developed in chapter five are extended to force field parameterization based on mixture properties. We use parameters derived from force fields parameterized for pure fluid properties to model complex chemically heterogeneous environments such as inside a cell or inside and around a membrane, where there are multiple interfaces. In many cases, the simulations fail to describe the correct physical behavior in a these environments or at interfaces where surface effects start dominating. Parameterization of pure fluids has been well studied but parameterization to get the mixture properties right has not been probed adequately [13]. There are force fields which are parameterized based on solvation free energies[14]. However, solvation free energies correspond to infinite dilution limit whereas chemical engineering applications involve fluids mixtures at finite concentrations. We should be able to estimate mixture properties at various compositions to parameterize force fields based on fluid mixture properties.

Estimating fluid mixture properties, especially excess Gibbs free energy, G^E , at finite concentrations using all-atom molecular dynamics simulation is a difficult problem. Interaction strengths as well as molecular geometries change for multiple molecules in simulations at different compositions. Thus the configurations pertaining to a composition are never visited in the simulations of other compositions which prohibits reweighting and subsequent free energy analysis. Excess enthalpy and volume have been estimated using data from simulation at a single composition but excess free energy using reweighting across different compositions has never been reported previously. Methods based on Gibbs ensemble Monte Carlo can estimate excess chemical potential but do not facilitate

reweighting of configurations and hence are not suitable for high throughput estimation of observables.

We propose a protocol to estimate excess thermodynamic properties, G^E , H^E , V^E and S^E , with the help of reweighting and configuration mapping techniques using an atomistic model of a binary mixture of water and methanol and sampling from an isothermal isobaric ensemble. Different number of water molecules will be mapped to methanol and vice versa as we reweight configurations for different compositions. This exercise lays out the foundation for the parameterization based on thermodynamic properties of binary mixtures at various mole fractions. We will have to fit force field parameters to reproduce not only the pure fluid properties but also the mixture properties at all the compositions correctly.

Mapping between mutually inaccessible configurations and speedup achieved by using reweighting and mapping techniques are critical in accomplishing the studies presented in chapters three, four and five. These studies involve involve very high throughput estimation of thermodynamic observables. Applying reweighting to exploring parameter space will help us better understand the sensitivity of thermodynamic observables with respect to simulation as well as force field parameters. The mapping technique can be applied to not only force field parameterization but to any problem which involves estimation of thermodynamic observables over two or more states having poor or no overlap in configurational space. For example, we could study the phase transition in metals as a function of temperatures. We could study the change in 3D structure in the crystal phase of a drug molecule, which renders it unusable. If we can reliably and efficiently predict the changes in complex molecular structure and the corresponding change in thermophysical properties, we could possibly tailor the molecular makeup to stabilize the structure and/or improve desirable properties. Thus the combination of two techniques should enable accelerated screening of large parameter or chemical design spaces and aid in molecular design.

A chemical product design starts with a molecular design phase in which a macroscopic property of the product is tailored by adjusting the molecular make-up. If successful, the product design is followed by tests in a pilot plant. If the pilot plant tests show promise, a production facility is designed to mass produce the product under environmental and economic constraints. The set-up of a pilot plant as well as the final production unit requires process design. We need accurate and precise process design tools to get reliable estimates of the performance of a certain design under actual process conditions.

1.1.5 Challenges in multiscale process design

At present, chemical engineers design and simulate processes occurring over a wide range of length and time scales. Advances in nanoscale material characterization and the capacity to simulate and tailor properties at the atomistic level have enabled designers to think about process design starting from the building blocks of materials i.e., atoms and molecules. A substantial amount of process engineering research effort is focused on efficient multiscale modeling using a bottom-up design approach as shown in Figure 1.4. This approach involves the design of a molecule having desirable thermophysical properties. Once we have a promising molecular candidate we require a process design for mass producing the product. The process design determines the techno-economic feasibility of the entire project. Reliable designs help making confident decisions and thus accuracy of the design estimates is very important for viability of a project.

The accuracy of a process design heavily depends on the quality of the thermodynamic package being used. Commercially available thermodynamic packages offer thermodynamic information for a limited number of chemical compounds. The parameters regressed for the classical or empirical equations of state like Peng-Robinson (PR) [15], Soave-Redlich-Kwong (SRK)[16] available in these packages are only valid for a specific range

of temperature and pressure and for a specific composition. In some instances, thermodynamic properties are measured with respect to a certain choice of reference state which cannot be reproduced under laboratory conditions (temperature, pressure, toxicity constraints) for the newly developed product [17].

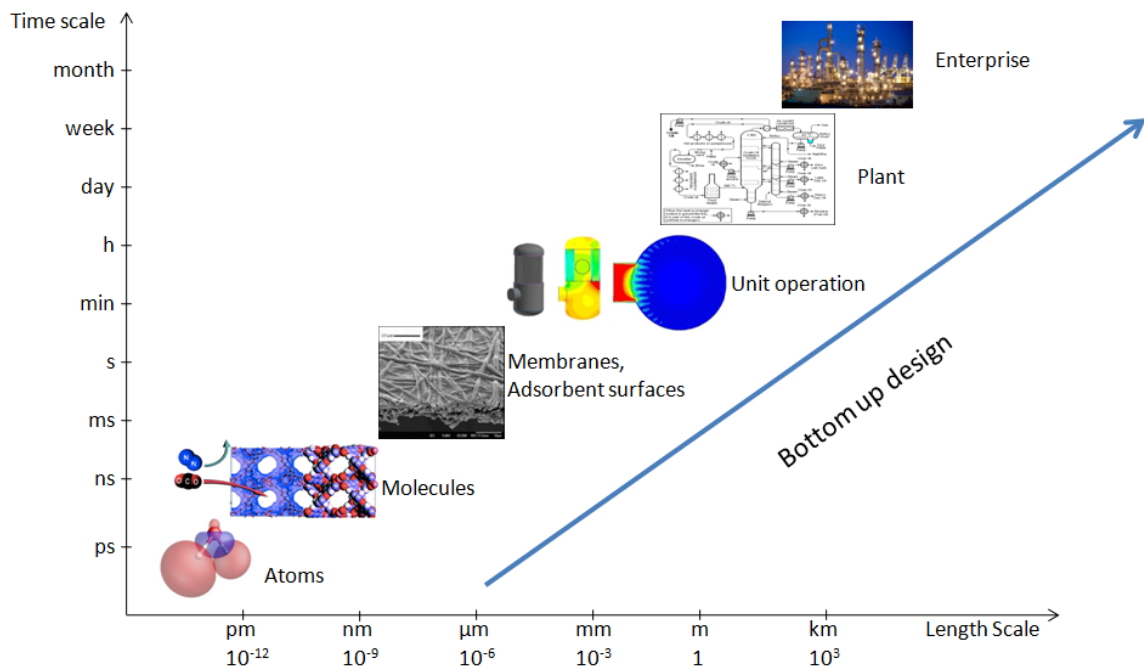


Figure 1.4: Design of a product at the atomistic scale affects the process design and design of process equipments. Design of reaction and separation networks, heat exchange networks, effluent treatment networks, to satisfy environmental constraints, all depend on the product's thermophysical and toxicity properties. Finally, the product and process design both affect the business/enterprise model by determining economic feasibility.

The classical equations of state and activity coefficient models cannot explicitly account for changes in size, shape, interaction of the molecule due to change in temperature, pressure and composition. UNIFAC [18] and UNIQUAC [19] use some information from the atomistic description of molecules but they fail to capture the entropy generated by fluctuations in the configurations of long chain molecules. Statistical association fluid theory

(SAFT) [20] based equations of state use atomistic description as well as configurational information in the form of pair correlation functions, derived from molecular simulations to analytically solve for the properties. However the dependence on the knowledge of pair correlation functions limits the transferability to new unstudied/unsimulated systems. Only an equation of state coming directly from the molecular simulations would capture the characteristics of a complex systems for a wide range of temperatures pressures and compositions. The standard or reference state could also be easily set to a state which is physically realizable and relevant to the problem.

However, the classical equations of state and activity coefficient models are still preferred over molecular simulations because of a huge difference in computational speed. A process design requires hundreds and thousands of iterations of an equation of state. A classical equation of state could do a single iteration in less than a second. The analytical equation of state based on SAFT theory like PC-SAFT [21] takes seconds to estimate a property. On the other hand, molecular simulations would take hours to compute the same property. The primary reason for the slow speed is that for each new temperature, pressure and composition combination a fresh simulation has to be run and properties have to be evaluated using fluctuation formulas. The computational cost for sample generation makes the exercise prohibitive. In this study we, develop tools for accelerating thermodynamic property prediction using molecular simulations and carry out proof of concept studies by exploring large simulation and force field parameter spaces. These techniques in the future should assist as tools for accelerated property predictions required in molecular design and the subsequent process design.

1.1.6 Accelerating multiscale process design

In chapters five and six we show the use of the reweighting technique to tremendously reduce the amount of computational time for property calculation using molecular simulations. We simulate for only a few temperature and pressure combinations and predict properties for a large combination of temperature and pressures. We do not use fluctuation formulas for calculating the thermodynamic properties, but directly derive the properties from the simulated free energy surface $G(T, P)$. In this way, we can not only derive first derivative properties but also second derivative properties fairly easily. The uncertainty propagation in this process is also clear and unambiguous compared to fluctuation formulas.

The multistate reweighting technique enabled estimation of properties at multiple temperatures and pressures by facilitating efficient estimation of the free energy for various combinations of small perturbations in temperature ($\pm\delta T$) and pressure ($\pm\delta P$) around a given T, P in order to numerically calculate the first, second and mixed derivatives of free energy with respect to T and P . We have used 110 temperature and pressure combinations in our water parameterization exercise. For each T and P combination, we had to estimate free energies at the 4 closest points ($T \pm \delta T$ at constant P) and ($P \pm \delta P$ at constant T) to calculate density, enthalpy, heat capacity and isothermal compressibility. Free energy estimates on four more points along the cross diagonal were required to calculate isobaric thermal expansion coefficient. Thus, for estimating properties at 110(T, P) points we needed free energy estimates corresponding to 110×9 temperature and pressure combinations. If a single state simulation for 1.5 ns takes 3 CPU hrs to simulate then the simulation of 990 T and P points would have taken 2970 CPU hrs (123 CPU days) to compute the free energies without the reweighting method. The water model parameterization exercise

done with reweighting required at least 4100 iterations to convergence. The exercise without reweighting would have cost 1544 CPU years. Using reweighting and configuration mapping techniques, the entire parameterization exercise was done in less than eight CPU weeks.

We can estimate properties like density, enthalpy, entropy, heat capacity, and so forth from molecular simulations for a range of temperatures and pressures for once and then we can generate the estimate of any thermodynamic property at any T and P using known interpolation techniques, for example, bi-variate cubic splines as shown in Figure 1.5. Thus, after the initial effort and computational cost of a few hours the computational cost of property estimation from the property surface will be similar to any thermodynamic package as the interpolation or the metamodel execution speeds will be equal to or even greater compared to the solution of classical equations. We could also estimate the transport properties (diffusivity, viscosity etc.) from molecular simulations as well using the reweighting scheme. However, the theory for reweighting transport properties is still not fully developed [22]. An alternate way to predict transport properties at any T and P combination is to estimate the transport properties at several temperature and pressure combinations using molecular simulations and build a surrogate model from the data. The surrogate models are less accurate in prediction compared to thermodynamic reweighting. However, their predictions improve with increasing inputs from the molecular simulations. Thus, we can do process design using the thermodynamic as well as transport property information estimated from the molecular simulations.

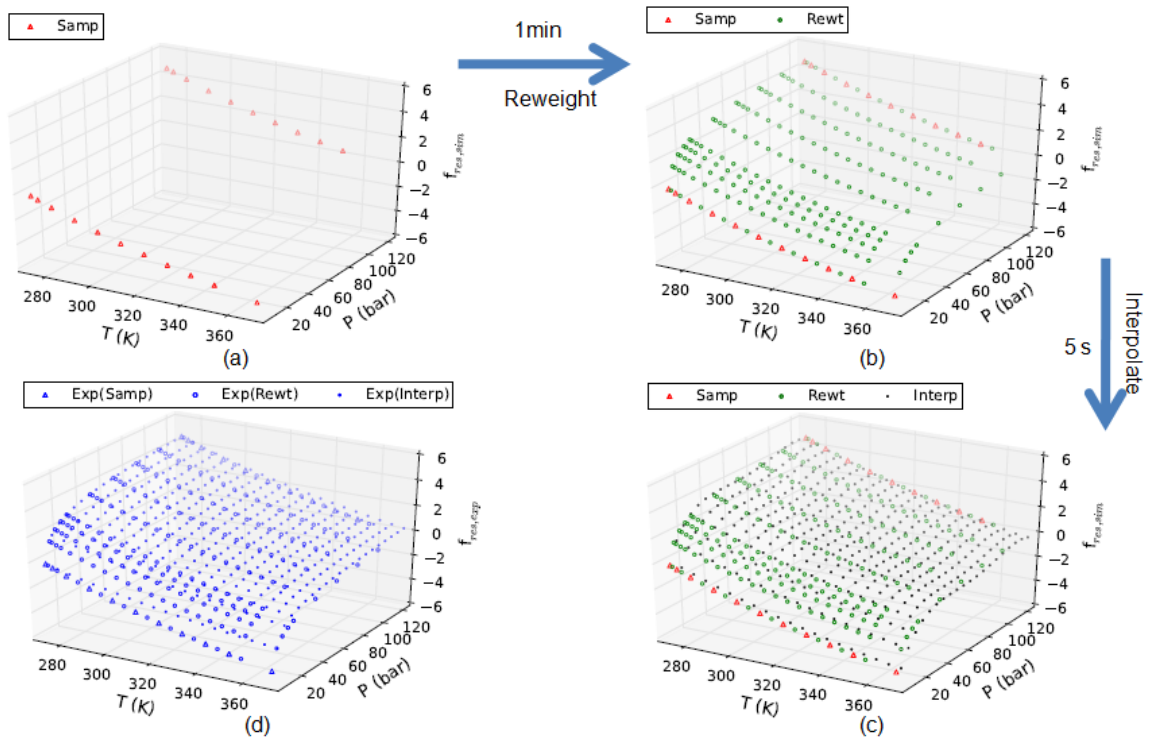


Figure 1.5: A fast method to generate dimensionless residual Gibbs free energy surface for TIP4P water model is shown in sub figures (a)-(c) along with the same property surface generated using IAPWS-95 equation of state shown in sub figure (d). (a) We generate samples at a few temperature and pressure combinations which takes less than an hour. (b) Next we predict properties at intermediate temperatures and pressures using reweighting. Reweighting calculations take less than a minute. (c) We could estimate the property at any temperature and pressure combination using bivariate spline or metamodel generated using the sampled and reweighted data. We used bivariate spline of order 5 in both temperature and pressure direction. On a closer inspection, we see that the interpolation is less accurate compared to reweighting. We could improve accuracy in interpolation by providing a much finer reweighted property mesh.

2 Overview of important theoretical concepts

2.1 Model, method and parameters involved in the process of property prediction using molecular simulations

Figure 2.1 briefly summarizes different parameters and algorithms one has to choose from, before the molecular simulation run to generate samples. These samples are then used to estimate thermodynamic properties like Gibbs free energy, enthalpy etc. using statistical mechanical approaches. To start a molecular simulation, we need an initial guess of co-ordinates of individual atoms and their velocities. Initial co-ordinates for a biomolecular system could be imported from the RCSB Protein Data Bank and solvated in a solvent box of sufficient size to provide three to four solvation shells. For non-biological systems, for example simulation of metals, initial co-ordinates can be generated by placing atoms at regular intervals following a lattice geometry. The initial guess velocities are generated according to the Boltzmann distribution at that temperature. We use an atomistic force field to estimate the forces on each and every atom. A force field is essentially a potential energy model to describe the nonbonded and bonded interactions between individual atoms as a function of inter-atomic distance. The nonbonded potential models the atomistic repulsion/dispersion and electrostatic forces between atoms. The bonded potential model forces experienced by atoms which share a chemical bond with one or more neighboring atoms. The atomistic repulsion and dispersion interactions are usually described by the Lennard-Jones 12-6 potential and the electrostatic interactions are modeled using the Coulomb's law. The bonded interactions are described by harmonic bonds, harmonic angles and dihedral angle potentials. A force field of an atomistic model thus requires specification of parameters like Lennard-Jones σ , ϵ , Coulomb charge q , equilibrium bond length x_o , equi-

librium bond angle θ_o , the corresponding force constants K_b , K_θ etc. These models and model parameters to large extent determine the accuracy with which we can reproduce the correct physics of the system.

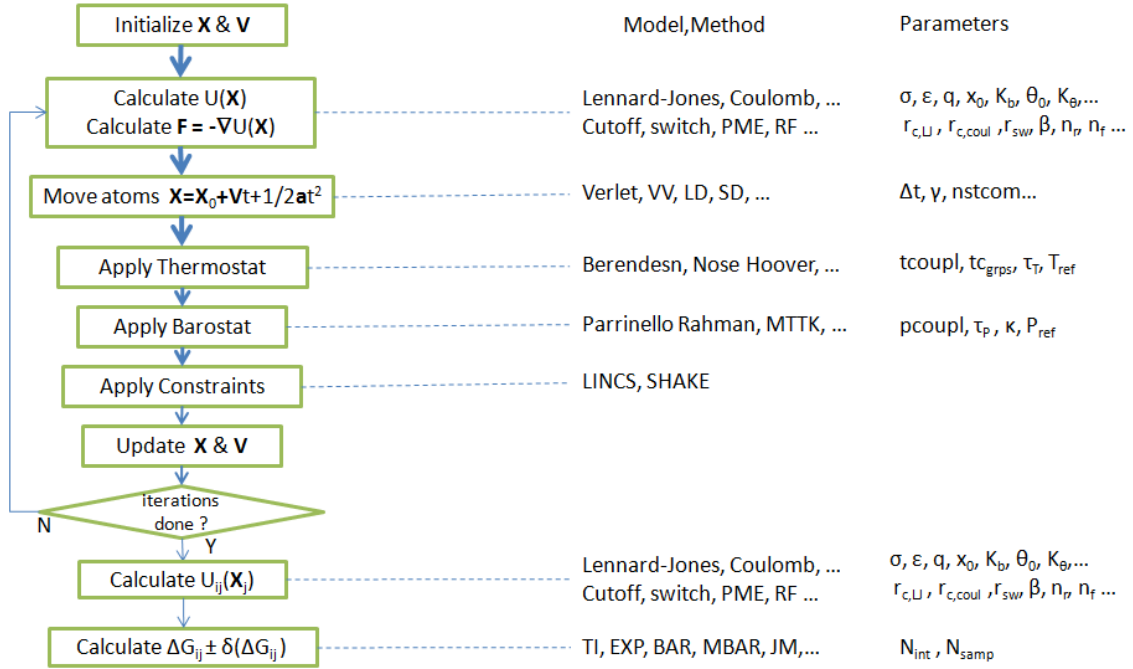


Figure 2.1: Properties estimated using molecular simulation, for example free energy change ΔG_{ij} , involves multiple steps. We have to make a choice of model methods and parameters at each step. All these choices effect the accuracy of the potential energies which eventually affect the accuracy of the estimated property. Frequently, little or no quantitative information is available to know how much each choice of parameter affects the results.

We estimate the forces acting on all atoms to calculate the acceleration. We use these accelerations to obtain new positions for all atoms by integrating Newton's equation of motion for a finite time step Δt , the choice of which depends on the fastest atomistic motion occurring in the system. A very small Δt will make the computation prohibitive whereas a large Δt will lead to energy shifts i.e. unstable system. An optimum Δt would allow fast yet stable evolution of the molecular system with time. The integration could

be done using either the Verlet [23] scheme or leap frog algorithm. If we wish to use Langevin Dynamics instead of the usual Newton’s equation of motion, we need to specify the friction coefficient γ which models the viscous effects of the solvent. The choice of γ should not make the solvent unrealistically thin or viscous. We also need to specify the frequency of center of mass motion removal, `nstcomm`. A higher frequency increases computational cost. However, if center of mass motion removed less frequently, it could result into what is called the flying ice cube effect. The flying ice cube effect is an artifact of numerical integration in which the energy is incorrectly partitioned from high energy degrees of freedom to low energy degrees of freedom or zero energy degrees of freedom, such as translation and rotation of the system.

Most of the chemical and biochemical processes happen at constant temperature and pressure. To reproduce these processes using constant temperature and pressure simulations, we require thermostat and barostat schemes. The thermostat perturbs the velocities to maintain system temperature T_{sys} and the barostat perturbs positions of the atoms and the volume of the system to maintain system pressure P_{sys} , using one of the many available algorithms. The parameters τ_T and τ_P determine the strength of the coupling of the system to the temperature and pressure bath. A strong coupling or weak coupling could result in unrealistic temperature and volume fluctuations. The way we define temperature coupling for different molecular groups affects the way the energy is partitioned from high energetic domains to the low energetic domains affecting the temperature as well as sampling of the system. The choice of thermostat and barostat algorithm and the way we define coupling for different molecular groups also determines whether the samples actually belong to the simulated ensemble.

To accelerate the molecular simulations, we freeze some of the degrees of freedom that do not affect the behavior of the system when observed over long time and length scales.

For example, the bond lengths of bonded hydrogens are constrained using holonomic constraint schemes like SHAKE or LINCS to enable using a larger time step Δt for faster evolution of the system. If not applied appropriately, the application of constraints could lead to unstable systems.

As the system evolves in time we gather snapshots of molecular configurations at regular intervals. These snapshots from the trajectory are used to calculate the potential energy at the sampled state j , $U_j(x_j)$. The potential energy definitions of other states $U_{i,i \neq j}$ could also be used to calculate $U_i(x_j)$. Thus we can estimate $U_{ij}(x_j) = U_j(x_j) - U_i(x_j)$ the pairwise potential energy differences between the sampled state and other thermodynamic states required for free energy estimation. The free energy estimation algorithms like thermodynamic integration, exponential averaging, Bennett acceptance ration, use potential energy differences from sampled and unsampled states using different schemes as explained in the next chapter.

Calculating potential energy, $U_j(x_j)$, is very expensive if done by estimating potential energy contribution due to each atom pair. Thus, $U_j(x_j)$ is estimated as a sum of a long range and short range sums. This scheme of potential energy calculation also involves several parameters like the nonbonded cutoff r_c which separate the long range and short range sums. A larger cutoff gives more accuracy but bumps up the computational cost. A smaller cutoff results in inaccurate potential energies but faster calculations. The potential energy difference $U_{ij}(x_j)$ are used to estimate the thermodynamic observables using a variety of estimators. Each estimator uses different amounts of information from the simulations and thus give results with different accuracy. The choice of the free energy method, number of intermediate states N_{int} and number of samples N_{samp} all effect the free energy estimate. Thus, to accurately estimate thermodynamic properties using molecular simulation, we need to make careful choices of model method and parameters pre- as well as post-

simulation. If we cannot quantitatively predict the variation in simulated properties with change in model, method and parameters, our simulation results will remain questionable and unreliable. Using the multistate reweighting technique we will show that from a combinatorially very large space, we can choose a model, method and parameter based on the estimate of bias and computational cost comparison.

2.2 What is multistate reweighting?

2.2.1 Introduction

There are various equilibrium statistical mechanical estimators which can be used to estimate free energy differences between thermodynamic states with some phase space overlap. Each estimator uses different amounts of information from the sampled states and scheme to estimate the observables. We will see in this section that the simplest form of free energy estimator, exponential averaging algorithm, uses information from just one sampled state to estimate the free energy difference between two states. The Bennett Acceptance Ratio (BAR) improves the accuracy in free energy estimation by including the information from two sampled states. Free energy of an arbitrary transformation can be estimated from initial state to final state (ΔG_{01}) using samples from the initial state. Similarly free energy of the same transformation can be estimated in the reverse direction, from final state to initial state (ΔG_{10}) using samples from the final state. Since we have similar information from two states, we need a way to weigh the information from the two sources to get a single estimate of free energy difference. One way is to take a simple arithmetic average which puts a weight of 0.5 on the free energies estimated in opposite directions. However, Bennett's algorithm picks a weight which minimizes the error in the final free energy estimate.

What if we had information from more than two states? When there is poor overlap between two end states, we introduce multiple intermediate states to bridge the phase space overlap. We could use pairwise BAR which would calculate accurate free energy differences using information from only two states at a time. However, we will not be using information from the non-neighboring intermediate states not included in the free energy calculation. Multistate Bennett acceptance ratio solves this problem by weighing information from multiple states simultaneously to use all the available information from all the sampled states. We have presented in this section a comprehensive derivation of three reweighting algorithms, which is hard to find in the literature. The concept of reweighting multiple states will become clearer as we study the equations that constitute this algorithm.

Let us start by defining the relationship between the molecular partition function and free energy of a system. For the sake of simplicity we choose to work in the canonical ensemble in which the microstate is defined by the positions (\mathbf{x}) and the momenta (\mathbf{p}). The macrostate is defined by the number of particles N , volume of the system V and temperature of the system T . The total internal energy E is a sum of potential energy $U(\mathbf{x})$ and kinetic energy $K(\mathbf{p})$. The partition function Q relates to the Helmholtz free energy A of the system described by the following equation:

$$A = -k_B T \ln(Q) \tag{2.1}$$

The partition function Q can be estimated by the following integral:

$$\begin{aligned}
Q &= \frac{1}{N!h^N} \int_{-\infty}^{\infty} \int_{-\infty}^{\infty} \exp(-\beta E(\mathbf{x}, \mathbf{p})) d\mathbf{x} d\mathbf{p} \\
&= \frac{1}{N!h^N} \int_{-\infty}^{\infty} \exp(-\beta K(\mathbf{p})) d\mathbf{p} \int_{-\infty}^{\infty} \exp(-\beta U(\mathbf{x})) d\mathbf{x} \\
&= \frac{1}{N!\Lambda^{3N}} \int_{-\infty}^{\infty} \exp(-\beta U(\mathbf{x})) d\mathbf{x} \\
&= Q_{tr} Q_{conf} \\
Q_{tr} &= \frac{1}{N!\Lambda^{3N}} \\
Q_{conf} &= \int_{-\infty}^{\infty} \exp(-\beta U(\mathbf{x})) d\mathbf{x}
\end{aligned} \tag{2.2}$$

The partition function Q can be written as a product of the translational partition function Q_{tr} , where Λ is the thermal de Broglie wavelength and the configurational partition function Q_{conf} . We can analytically calculate Q_{tr} ; however, we need simulations to evaluate Q_{conf} . We will therefore refer to Q_{conf} as Q hereafter for the sake of brevity.

We wish to calculate the Helmholtz free energy difference between two thermodynamics states with potentials U_0 and U_1 . In order to avoid confusion in this derivation, both states are maintained at an identical temperature, T .

$$A_{01} = A_1 - A_0 = -k_B T \ln \left(\frac{Q_1}{Q_0} \right) \tag{2.3}$$

The above equation shows that we can calculate the free energy difference A_{01} by estimating the ratio of the partition functions $\frac{Q_1}{Q_0}$. There are different approaches to calculate this ratio. Let us first discuss the simplest one which is called exponential averaging and involves reweighting with one sampled state.

2.2.2 Reweighting Algorithms

2.2.2.1 Reweighting with one sampled state: Exponential Averaging We start by writing the canonical definition of the ratio.

$$\frac{Q_1}{Q_0} = \frac{\int \exp(-\beta U_1(\mathbf{x})) d\mathbf{x}}{\int \exp(-\beta U_0(\mathbf{x})) d\mathbf{x}} \quad (2.4)$$

We then multiply the numerator by $\exp(-\beta U_0(\mathbf{x})) \exp(\beta U_0(\mathbf{x})) = 1$.

$$\begin{aligned} \frac{Q_1}{Q_0} &= \frac{\int \exp(-\beta(U_1(\mathbf{x}) - U_0(\mathbf{x}))) \exp(-\beta U_0(\mathbf{x})) d\mathbf{x}}{\int \exp(-\beta U_0(\mathbf{x})) d\mathbf{x}} \\ &= \langle \exp(-\beta(U_1(\mathbf{x}) - U_0(\mathbf{x}))) \rangle_0 \end{aligned} \quad (2.5)$$

The expression above is the working equation of the exponential averaging algorithm. We can calculate the ratio $\frac{Q_1}{Q_0}$ by simulating a single state, say the starting state, 0. For each sampled configuration \mathbf{x} we evaluate the difference $U_1(\mathbf{x}) - U_0(\mathbf{x})$. The expectation value of the difference taken over the entire trajectory equals the ratio of the partition function from which we can get the free energy difference.

$$\begin{aligned} A_{01} &= -k_B T \ln (\langle \exp(-\beta(U_1(\mathbf{x}) - U_0(\mathbf{x}))) \rangle_0) \\ &= -k_B T \ln (\langle \exp(-\beta(U_{01}(\mathbf{x}))) \rangle_0) \end{aligned} \quad (2.6)$$

We see that exponential averaging uses samples from only one state and potential energy differences in one direction ($0 \rightarrow 1$) to estimate the free energy difference between two states. Often times we need intermediate states between the two end states to increase

phase space overlap in order estimate the free energy difference. If there are N intermediate states then we would have to simulate $N-1$ states and carry out free energy calculation from 0 to 1 , 1 to 2 ... $N-1$ to N . We would have to calculate the expectation values $\langle \exp(-\beta(U_{01}))_0, \dots, \langle \exp(-\beta(U_{N-1,N}))_{N-1}$, all in the forward direction of transformation to get the total free energy difference $\Delta G_{0N} = \Delta G_{01} + \dots + \Delta G_{N-1,N}$. In every pairwise free energy calculation we have samples from the neighboring state. Thus, we can also calculate $\langle \exp(-\beta(U_{10}))_1, \dots, \langle \exp(-\beta(U_{N,N-1}))_N$, all in the reverse direction of the transformation. These expectation values when used in Eq. 2.6 predict free energy difference in the reverse direction $\Delta G_{N0} = \Delta G_{10} + \dots + \Delta G_{N,N-1}$. We could have used the potential energy differences in the two directions to improve the accuracy in the free energy estimate but the nature of exponential averaging algorithm doesn't allow correction based on the free energy differences (for the same transformation), measured in the opposite directions.

2.2.2.2 Reweighting with two states: Bennett Acceptance Ratio Let us now examine the Bennett Acceptance Ratio (BAR), a more complex and more accurate algorithm compared to exponential averaging. We start the derivation with the following identity:

$$\frac{Q_0}{Q_1} = \frac{Q_0}{Q_1} \frac{\int w(\mathbf{x}) \exp(-\beta(U_0(\mathbf{x}) + U_1(\mathbf{x}))) d\mathbf{x}}{\int w(\mathbf{x}) \exp(-\beta(U_0(\mathbf{x}) + U_1(\mathbf{x}))) d\mathbf{x}} \quad (2.7)$$

The above identity is true for any choice of w . We can re-write the above equation in

the following form:

$$\begin{aligned}
\frac{Q_0}{Q_1} &= \frac{\int w(\mathbf{x}) \exp(-\beta(U_0(\mathbf{x}) + U_1(\mathbf{x}))) d\mathbf{x}}{\int w(\mathbf{x}) \exp(-\beta(U_0(\mathbf{x}) + U_1(\mathbf{x}))) d\mathbf{x}} \\
&= \frac{\int w(\mathbf{x}) \exp(-\beta(U_0(\mathbf{x}))) \exp(-\beta(U_1(\mathbf{x}))) d\mathbf{x}}{\int w(\mathbf{x}) \exp(-\beta(U_1(\mathbf{x}))) \exp(-\beta(U_0(\mathbf{x}))) d\mathbf{x}} \\
&= \frac{\langle w \exp(-\beta U_0) \rangle_1}{\langle w \exp(-\beta U_1) \rangle_0}
\end{aligned} \tag{2.8}$$

We could get the free energy difference using the following relation:

$$\beta A_{01} = \ln(\langle w \exp(-\beta U_0) \rangle_1) - \ln(\langle w \exp(-\beta U_1) \rangle_0) \tag{2.9}$$

We see that in the above equation the free energy difference includes potential energy information from both the sampled states. We choose a w which will minimize error in βA_{01} . For the sake of brevity, if we refer to $\langle w \exp(-\beta U_0) \rangle_1$ as x_1 , $\langle w \exp(-\beta U_1) \rangle_0$ as x_0 and βA_{01} as F , then the error $\sigma_{\beta A_{01}}^2$ can be written as:

$$\sigma_{\beta A_{01}}^2 = \frac{1}{n_1} \left| \frac{\delta F}{\delta x_1} \right| \sigma_{x_1}^2 + \frac{1}{n_0} \left| \frac{\delta F}{\delta x_0} \right| \sigma_{x_0}^2 \tag{2.10}$$

Here n_0 and n_1 are the number of samples from simulations of states 0 and 1 respec-

tively. We can solve the partial derivatives in Eq.2.10 and replace $\sigma_{x_0}^2$ and $\sigma_{x_1}^2$ with the variance equation $\text{var}(X) = \langle X^2 \rangle - \langle X \rangle^2$ to get:

$$\begin{aligned}\sigma_{\beta A_{01}}^2 &= \frac{\langle x_1^2 \rangle - \langle x_1 \rangle^2}{n_1 \langle x_1 \rangle^2} + \frac{\langle x_0^2 \rangle - \langle x_0 \rangle^2}{n_0 \langle x_0 \rangle^2} \\ &= \frac{\langle x_1^2 \rangle}{n_1 \langle x_1 \rangle^2} + \frac{\langle x_0^2 \rangle}{n_0 \langle x_0 \rangle^2} - \frac{1}{n_1} - \frac{1}{n_0}\end{aligned}\quad (2.11)$$

Expanding x_0 and x_1 to their original forms we get:

$$\begin{aligned}\sigma_{\beta A_{01}}^2 &= \frac{\langle (w \exp(-\beta U_0))^2 \rangle_1}{n_1 \langle w \exp(-\beta U_0) \rangle_1^2} + \frac{\langle (w \exp(-\beta U_1))^2 \rangle_0}{n_0 \langle w \exp(-\beta U_1) \rangle_0^2} - \frac{1}{n_1} - \frac{1}{n_0} \\ &= \frac{\langle w^2 \exp(-2\beta U_0) \rangle_1}{n_1 \langle w \exp(-\beta U_0) \rangle_1^2} + \frac{\langle w^2 \exp(-2\beta U_1) \rangle_0}{n_0 \langle w \exp(-\beta U_1) \rangle_0^2} - \frac{1}{n_1} - \frac{1}{n_0}\end{aligned}\quad (2.12)$$

We now replace the brackets, $\langle \rangle$, with their corresponding integral forms.

$$\begin{aligned}\sigma_{\beta A_{01}}^2 &= \frac{\frac{\int w^2 \exp(-2\beta U_0) \exp(-\beta U_1) d\mathbf{x}}{n_1 Q_1}}{\frac{\int w \exp(-\beta U_0) \exp(-\beta U_1) d\mathbf{x}}{Q_1^2}} + \frac{\frac{\int w^2 \exp(-2\beta U_1) \exp(-\beta U_0) d\mathbf{x}}{n_0 Q_0}}{\frac{\int w \exp(-\beta U_1) \exp(-\beta U_0) d\mathbf{x}}{Q_0^2}} - \frac{1}{n_1} - \frac{1}{n_0} \\ &= \frac{\int \left(\frac{Q_1}{n_1} \exp(-\beta U_0) + \frac{Q_0}{n_0} \exp(-\beta U_1) \right) w^2 \exp(-\beta(U_0 + U_1)) d\mathbf{x}}{\left(\int w \exp(-\beta(U_0 + U_1)) d\mathbf{x} \right)^2} - \frac{1}{n_1} - \frac{1}{n_0}\end{aligned}\quad (2.13)$$

We notice that the above equation will remain unchanged even if we multiply w with a

constant. Thus we can safely assume the following normalization constant for w :

$$\int w \exp(-\beta(U_0 + U_1)) d\mathbf{x} = \text{constant} \quad (2.14)$$

We minimize the numerator in Eq. 2.13 using the Lagrange multiplier method with the constraint given in Eq. 2.14

$$\text{Minimize } \chi(w) = \int \left(\frac{Q_1}{n_1} \exp(-\beta U_0) + \frac{Q_0}{n_0} \exp(-\beta U_1) \right) w^2 \exp(-\beta(U_0 + U_1)) d\mathbf{x} \quad (2.15)$$

$$\text{Constraint } c(w) = \int w \exp(-\beta(U_0 + U_1)) d\mathbf{x} - \text{constant} \quad (2.16)$$

At the minima the gradient of $\chi(w) - \lambda c(w)$ with respect to w should be zero.i.e.

$$\frac{\delta \chi(w) - \lambda c(w)}{\delta w} = 0 \quad (2.17)$$

Substituting $\chi(w)$ and $c(w)$ in the above differential equation we get:

$$\left(\frac{Q_1}{n_1} \exp(-\beta U_0) + \frac{Q_0}{n_0} \exp(-\beta U_1) \right) 2w \exp(-\beta(U_0 + U_1)) - \lambda \exp(-\beta(U_0 + U_1)) = 0 \quad (2.18)$$

Solving for w in the above equation we get:

$$w = \frac{C_1}{\frac{Q_1}{n_1} \exp(-\beta U_0) + \frac{Q_0}{n_0} \exp(-\beta U_1)} \quad (2.19)$$

Here $C_1 = \lambda/2$ is a constant.

Substituting the above expression for w in Eq: 2.8 we get:

$$\begin{aligned}
\frac{Q_0}{Q_1} &= \frac{\left\langle \frac{C_1 \exp(-\beta U_0)}{\frac{Q_1}{n_1} \exp(-\beta U_0) + \frac{Q_0}{n_0} \exp(-\beta U_1)} \right\rangle_1}{\left\langle \frac{C_1 \exp(-\beta U_1)}{\frac{Q_1}{n_1} \exp(-\beta U_0) + \frac{Q_0}{n_0} \exp(-\beta U_1)} \right\rangle_0} \\
&= \frac{n_1 Q_0}{Q_1 n_0} \left(\frac{\left\langle \frac{1}{1 + \frac{Q_0 n_1}{n_0 Q_1} \exp(-\beta(U_1 - U_0))} \right\rangle_1}{\left\langle \frac{1}{\frac{Q_1 n_0}{n_1 Q_0} \exp(-\beta(U_0 - U_1)) + 1} \right\rangle_0} \right)
\end{aligned} \tag{2.20}$$

Using $\frac{n_1 Q_0}{Q_1 n_0} = \exp(\beta C)$ in the above equation we get:

$$\begin{aligned}
\frac{Q_0}{Q_1} &= \exp(\beta C) \left(\frac{\left\langle \frac{1}{1 + \exp(-\beta(U_1 - U_0 - C))} \right\rangle_1}{\left\langle \frac{1}{\exp(-\beta(U_0 - U_1 + C)) + 1} \right\rangle_0} \right) \\
&= \exp(\beta C) \frac{\langle f(U_0 - U_1 + C) \rangle_1}{\langle f(U_1 - U_0 - C) \rangle_0}
\end{aligned} \tag{2.21}$$

In the above equation, f is the Fermi function $f(x) = \frac{1}{1 + \exp(\beta x)}$. We can get the expectation values of the two Fermi functions in terms of C from the simulations done at

states 0 and 1.

$$\begin{aligned}\langle f(U_0 - U_1 + C) \rangle_1 &= \frac{1}{n_1} \sum_{m=0}^{n_1} f_m(U_0 - U_1 + C) \\ \langle f(U_1 - U_0 - C) \rangle_0 &= \frac{1}{n_0} \sum_{m'=0}^{n_0} f_{m'}(U_1 - U_0 - C)\end{aligned}\tag{2.22}$$

Inserting Eq. 2.22 in Eq. 2.21 and taking log both sides we get

$$\begin{aligned}\ln\left(\frac{Q_0}{Q_1}\right) &= \ln\left(\frac{n_0 \sum_{m=0}^{n_1} f_m(U_0 - U_1 + C)}{n_1 \sum_{m'=0}^{n_0} f_{m'}(U_1 - U_0 - C)}\right) + \ln(\exp(\beta C)) \\ \beta A_{01} &= \ln\left(\frac{\sum_{m=0}^{n_1} f_m(U_0 - U_1 + C)}{\sum_{m'=0}^{n_0} f_{m'}(U_1 - U_0 - C)}\right) + \beta C - \ln\left(\frac{n_1}{n_0}\right)\end{aligned}\tag{2.23}$$

We also know that

$$\begin{aligned}\exp(\beta C) &= \frac{Q_0 n_1}{Q_1 n_0} \\ \ln(\exp(\beta C)) &= \ln\left(\frac{Q_0}{Q_1}\right) + \ln\left(\frac{n_1}{n_0}\right) \\ \beta C &= \beta A_{01} + \ln\left(\frac{n_1}{n_0}\right) \\ \beta A_{01} &= \beta C - \ln\left(\frac{n_1}{n_0}\right)\end{aligned}\tag{2.24}$$

Eq. 2.23 and Eq. 2.24 can be simultaneously true only if

$$\sum_{m=0}^{n_1} f_m(U_0 - U_1 + C) = \sum_{m'=0}^{n_0} f_{m'}(U_1 - U_0 - C) \quad (2.25)$$

So, we sample from both states and calculate the potential energy difference U_{01} in both directions to solve for C using the above equation. The value of C which satisfies the above equation weighs the forward and backward differences to minimize error in the free energy difference. The free energy difference is calculated by inserting C in Eq.2.24. Thus, BAR utilizes information from simulations of states 0 and 1 and reduces bias in the free energy estimate by optimally weighing the potentially energy differences taken in forward and reverse directions to estimate the free energy difference between the two states.

If we had multiple intermediate states, with BAR, we would have used the potential energy differences in the forward and reverse directions only for the two neighboring states. The non-neighboring states corresponding to a sampled state contain useful thermodynamic information which could have been used to improve the accuracy of the free energy estimate but remains unused in BAR. Similar to potential energy differences that can be estimated in forward and reverse directions for a pair of neighboring states we could also calculate the potential energy differences in the forward and reverse directions from a sampled state to a non-neighboring state.

Let us now try to understand how information from a non-neighboring state could improve accuracy in free energy estimates. Say we do simulations at 298 K (state A), 300 K (state B), and 302 K (state C) keeping everything else, potential energy function, constraints etc., unperturbed. Simulations for state A will sample many configurations which would be common to samples generated in simulations of states B and C. Thus samples generated using simulations for state A contain thermodynamic information for both states B and C,

proportionate to the phase space overlap. Similarly simulations done at state B will have thermodynamic information corresponding to states A and C, and simulations done at state C will have thermodynamic information corresponding to states A and B, proportionate to the phase space overlap. We could estimate the free energy difference between states A and B by

1. Estimating ΔG_{AB} with samples from state A, i.e., using $U_{AB}(X_A)$.
2. Estimating $\Delta G_{AB} = -\Delta G_{BA}$ with samples from state B, i.e., using $U_{BA}(X_B)$.
3. Estimating $\Delta G_{AB} = \Delta G_{CB} - \Delta G_{CA}$ with samples from state C, i.e., using $U_{CA}(X_C)$ and $U_{CB}(X_C)$.
4. Estimating $\Delta G_{AB} = \Delta G_{AC} - \Delta G_{BC}$ with samples from states A and B, i.e., using $U_{AC}(X_A)$ and $U_{BC}(X_B)$.

All four methods estimate the free energy difference of the same transformation, $A \rightarrow B$, using thermodynamic information from different simulations so there should be a way to optimally incorporate information from all four methods to minimize error in free energy estimate ΔG_{AB} . BAR can only reweight $U_{AB}(X_A)$ and $U_{BA}(X_B)$ optimally to estimate a free energy difference. However, pairwise potential energy differences from nonneighboring state C, $U_{CA}(X_C)$, $U_{AC}(X_A)$, $U_{BC}(X_B)$ and $U_{CB}(X_C)$ could have been used to improve the accuracy of ΔG_{AB} but are left unused by BAR.

2.2.2.3 Reweighting with multiple states: Multistate Bennett Acceptance Ratio Multistate Bennett Acceptance ratio (MBAR) improves over BAR by incorporating all pairwise potential energy differences to estimate the free energy differences between states. We used a weighing function w in BAR to bridge the information from two states, similarly, we require a multistate bridging function to optimally weight information from multiple states.

Let us first define our thermodynamic variables for a pair of thermodynamic states i , and j . The ratio of partition functions/normalization constants Q_i and Q_j between any two unnormalized probability distributions q_i and q_j defined on the same phase space can be related to the following identity:

$$r = \frac{Q_i}{Q_j} = \left(\frac{\int q_i dx}{\int q_j dx} \right) = \left(\frac{\frac{1}{\int q_j dx}}{\frac{1}{\int q_i dx}} \right) = \left(\frac{\frac{\int q_i \alpha_{ij} q_j dx}{\int q_j dx}}{\frac{\int q_j \alpha_{ij} q_i dx}{\int q_i dx}} \right) = \frac{E_j[q_i \alpha_{ij}]}{E_i[q_j \alpha_{ij}]} \quad (2.26)$$

For physical problems of thermodynamic interest, $q_i = \exp(-\beta U_i(x_i)) = \exp(-u_i(x))$ will be the Boltzmann weight, where $u_i(x) = \beta U_i(x)$. E_i is the statistical expectation value of a system sampled using q_i and α_{ij} is any strictly positive function defined for that same phase space. Identity in Eq. 2.26 is identical to the one used in Eq. 2.7. The only difference is that of the bridging function. In BAR w is the bridging function which optimally weighs(bridges) thermodynamic information between a pair of neighboring states, in MBAR, α_{ij} optimally weighs thermodynamic information between pairs of neighboring as well as nonneighboring states.

We can relate the ratio r directly to the free energy and partition functions of the system.

$$\Delta A_{ij} = -k_B T \ln r = -k_B T \ln \left(\frac{Q_i}{Q_j} \right) \quad (2.27)$$

Although we use the canonical ensemble here, corresponding relationships holds true for other ensembles as well. If we substitute the empirical estimator $N_i^{-1} \sum_{n=1}^{N_j} g(x_{in})$ for the expectations $E_i[g(x_{in})]$ in Eq. 2.26, we can calculate the free energy differences from sim-

ulations.

$$\frac{Q_i}{Q_j} = \frac{\frac{1}{N_j} \sum_{n=1}^{N_j} q_i(x_{jn}) \alpha_{ij}(x_{jn})}{\frac{1}{N_i} \sum_{n=1}^{N_i} q_j(x_{in}) \alpha_{ij}(x_{in})} \quad (2.28)$$

Cross multiplying and summing both sides from $j = 1$ to K in Eq. 2.28.

$$\sum_{j=1}^K \frac{Q_i}{N_i} \sum_{n=1}^{N_i} q_j(x_{in}) \alpha_{ij}(x_{in}) = \sum_{j=1}^K \frac{Q_j}{N_j} \sum_{n=1}^{N_j} q_i(x_{jn}) \alpha_{ij}(x_{jn}) \quad (2.29)$$

The multistate bridging function α_{ij} which minimizes the variance in the free energy estimate has the following form:

$$\alpha_{ij}(x) = \frac{N_j Q_j^{-1}}{\sum_{j=1}^K N_k Q_k^{-1} q_k(x)} \quad (2.30)$$

We can take c_i/N_i out of the summation and then switch the order of summation on the left hand side of Eq. 2.29, and then use the formula for α_{ij} .

$$\frac{Q_i}{N_i} \sum_{n=1}^{N_i} \sum_{j=1}^K \frac{q_j(x_{in}) N_j Q_j^{-1}}{\sum_{k=1}^K N_k Q_k^{-1} q_k(x_{in})} = \sum_{j=1}^K \frac{Q_j}{N_j} \sum_{n=1}^{N_j} \frac{q_i(x_{jn}) N_j Q_j^{-1}}{\sum_{k=1}^K N_k Q_k^{-1} q_k(x_{jn})} \quad (2.31)$$

Eq. 2.31 can now be written as:

$$\frac{Q_i}{N_i} \sum_{n=1}^{N_i} \frac{\sum_{j=1}^K N_j Q_j^{-1} q_j(x_{in})}{\sum_{k=1}^K N_k Q_k^{-1} q_k(x_{in})} = \sum_{j=1}^K Q_j N_j^{-1} \sum_{n=1}^{N_j} \frac{N_j Q_j^{-1} q_i(x_{jn})}{\sum_{k=1}^K N_k Q_k^{-1} q_k(x_{jn})} \quad (2.32)$$

which reduces to:

$$Q_i = \sum_{j=1}^K \sum_{n=1}^{N_j} \frac{q_i(x_{jn})}{\sum_{k=1}^K N_k Q_k^{-1} q_k(x_{jn})} \quad (2.33)$$

Taking negative log on both sides:

$$f_i = -\ln(c_i) = -\ln \left(\sum_{j=1}^K \sum_{n=1}^{N_j} \frac{q_i(x_{jn})}{\sum_{k=1}^K N_k Q_k^{-1} q_k(x_{jn})} \right) \quad (2.34)$$

where f_i is the dimensionless free energy, $\beta_i A_i$. If $q(x) = \exp(-u(x))$ is the Boltzmann weight, we have:

$$f_i = -\ln \left(\sum_{j=1}^K \sum_{n=1}^{N_j} \frac{e^{-u_i(x_{jn})}}{\sum_{k=1}^K N_k e^{f_k - u_k(x_{jn})}} \right) \quad (2.35)$$

OR

$$f_i = -\ln \left(\sum_{j=1}^K \sum_{n=1}^{N_j} \frac{1}{\sum_{k=1}^K N_k e^{f_k - (u_k(x_{jn}) - u_i(x_{jn}))}} \right) \quad (2.36)$$

The above equation when written for all states gives a set of K nonlinear implicit equations in f_i (where $i \in [1...K]$) which can be solved for all f_i , using self consistent iteration or Newton-Raphson root finding method.

So, we see that in MBAR the free energy estimate of a state i includes pairwise potential energy differences from state i to all other states k measured for samples from each of the sampled states j . It has been shown in the paper by Shirts [4] that MBAR for two states

reduces to BAR.

The figure below summarizes the difference between one state reweighting, reweighting with two states and multi-state reweighting.

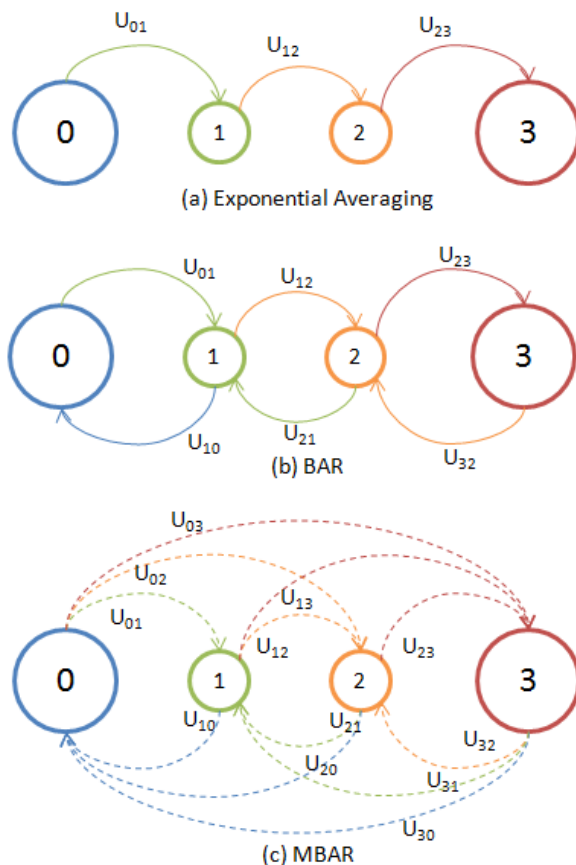


Figure 2.2: Free energy estimates are most accurate when information from multiple states is used with optimal reweighting. (a) Exponential averaging uses potential energy differences measured from only one state reweights using information from only one state. (b) BAR uses potential energy differences measured from two states and optimally reweights to estimate the free energy. (c) MBAR uses pairwise potential energy differences calculated from a state to every other state for multiple states and then optimally reweights to estimate the free energy.

3 Using multistate reweighting to rapidly explore molecular simulation parameters space for nonbonded interactions

3.1 Introduction

In order to understand and predict molecular processes, we frequently need to estimate thermodynamic properties such as free energies, enthalpies, entropies, and ensemble averages of structural quantities. In some cases, we can use statistical mechanical techniques to construct analytic expressions for thermodynamic variables with various levels of approximation. However, for properties that require more molecular detail, we require molecular simulation techniques. Molecular dynamics (MD) simulations and Monte Carlo (MC) simulations are now used for *in silico molecular design* tasks such as engineering molecular recognition [24] and drug design [25, 26, 27, 28]. For such problems, we need methods to directly estimate the true thermodynamic properties of a given model molecular system, as efficiently as possible, with no assumptions beyond those of the model itself.

Tasks such as computing the properties of many similar systems or refining force fields using very large and diverse molecular sets require high throughput calculations which are both accurate and precise [29, 30, 31, 32]. Free energy estimators, for example, typically require collecting samples from every state for which the thermodynamic observables are to be estimated, and potentially non-physical intermediate states as well. As the number of states run into thousands, generating sufficient number of samples for all states becomes impractical.

However, the sampled states contain information about nearby states in parameter space, as they sample the same set of configurations with similar probability as would occur dur-

ing direct simulations of these other choices of similar parameters. Such states are typically referred to as having high phase space overlap. The differences between the probability of any given configuration can be computed exactly using the ratio of the Boltzmann distributions resulting from the choices of parameter set. Standard single reference reweighting techniques can be used to compute free energies and expectation values between thermodynamic states with high phase space overlap [33]. A number of useful methods have been developed around reweighting from a single reference state, [34, 35, 36] though they have clear limitations when used to calculate the properties of states with little phase space overlap from the reference state [3, 30]. However, it is possible to generate significantly improved estimates of thermodynamic observables if reweighting is performed from multiple sampled reference states [37, 4]. For example, the multistate Bennett acceptance ratio (MBAR) [4] is a statistically optimal estimator which reweights samples from all sampled states and predict thermodynamic properties at any of these, or any other unsampled states.

In this study, we demonstrate the power of this multistate reweighting approach by scanning over the space of simulation parameters controlling nonbonded interactions without actually simulating these many alternate states. We scan this space to identify computationally efficient parameter choices which give statistically indistinguishable free energy differences and thermodynamic expectations from those obtained with the most rigorous, computationally expensive parameters. This reweighting is performed using a free energy calculation carried out at a single reference set of parameters. However, it is still multistate reweighting, rather than single state reweighting, since the free energy calculation itself involves simulations at a series of alchemical states interpolating between the two physical end states.

This approach is appropriate for use in other such sensitivity analysis of many parameters simultaneously. For example, this approach is appropriate for computing changes in

free energies with respect to model parameters, as noted in a study of changes in geometry parameters for water [38], although in that case only small numbers of parameters were examined rather than the large-scale scan presented here.

The choice of statistical estimator used to calculate equilibrium expectation values of thermodynamic observables and free energy differences affects both the accuracy and precision of these estimates. [39, 40, 41, 42, 43, 44, 45, 30, 46, 47, 3] The differences in bias and uncertainty in the observables are primarily due to the way each estimator operates on the sampled energies as well as the assumptions made in the algorithm. MBAR estimates of thermodynamic observables generally have lowest bias and provably have the lowest statistical error among all general analysis methods for typical molecular transformations [4, 3]. MBAR is particularly useful for the present study because of its correct treatment of statistical uncertainty, especially when examining differences between quantities that are computed with the same set of sampled data and thus are highly correlated. In this study, we will focus only on issues of sample analysis, rather than sample generation, and so standard molecular dynamics is used to generate the samples.

The accuracy of any thermodynamic property estimator is limited by the quality of potential energy calculations of the samples, as these energies are inputs to the estimator. If the potential energies are not accurately calculated for the model, statistical errors may be swamped by biases due to approximations in the potential. There are of course always approximations in a given model, but there are also approximations in the simulation methods used to generate samples of the model, usually to improve simulation speed, and we must make sure that we avoid errors due to such approximations. Otherwise, simulations of putatively the same model performed with different simulation codes will give different results.

One important caveat is that for our multistate reweighting method (or *any* reweight-

ing method for that matter) to work, we are limited to varying nonbonded parameters that still result in well defined, usually Boltzmann distributions. For molecular dynamics, this means that the approximated forces must still be the gradient of the approximated potential. Approximations such as the convergence tolerance of a self-consistent integrator or a large number of time steps between neighbor-list updates result in a distribution that is not Boltzmann, and thus cannot be treated via reweighting, at least not with Boltzmann distribution statistics. This also means methods such as Berendsen thermostats and barostats, which give incorrect potential energy and volume distributions, [5] are also inappropriate to use when generating samples for single or multistate reweighting applications.

By far the most common type of force field in biomolecular or materials simulations, due to both the computational efficiency and ease of implementation, is a pairwise additive force field. Most commonly, nonbonded energy terms in these force fields consist of fixed partial charges and Lennard-Jones nonbonded interactions. Short-range, bonded terms of a large variety are used to approximate local quantum mechanical behavior. The bonded terms are usually calculated without additional approximations as the cost is negligible. However, to accelerate the calculations, nonbonded interaction potentials are usually evaluated as sums of short range and long range contributions, frequently requiring a number of assumptions, approximations, and tunable parameters to accelerate the long range contribution with acceptable losses of accuracy. What 'acceptable' means in this context must generally be determined by the user and the application of interest.

Considerable research has been done to increase the efficiency and accuracy of Coulomb and Lennard-Jones long range calculations. Efficient algorithms such as particle mesh Ewald (PME) [48, 49], reaction-field [50], and particle-particle-particle-mesh (P3M) [51] accelerate the calculation of Coulomb contributions using different assumptions and approximations. All of these methods have been a matter of significant study. Smith and

Pettitt [52] suggest that for solvents with high relative permittivity, like water, Ewald artifacts are negligible but are more significant for solvents with low permittivity. Mark and Nilson [53] found the PME was more reliable than group based cutoff methods for quantities such as the diffusion co-efficient, radial distribution function, distance-dependent Kirkwood G factor and average potential energy. Henrik[54] found that PME is more computationally efficient at the same level of accuracy than the original Ewald method and the fast multipole methods. However, Hünenberger and McCammon found that Ewald methods can introduce finite-size artifacts by imposing artificial periodicity on systems which are inherently nonperiodic [55]. Overall, despite some potential drawbacks, Ewald methods, especially implementations of PME, seem to be the most robust method to handle long range electrostatics in molecular simulations and have become the most common electrostatics method in molecular simulation.

The long range component of Lennard-Jones dispersion, usually treated using an r^{-6} functional form, is most typically calculated using an analytical correction which assumes the radial distribution function $g(r) = 1$ at long range. A proper treatment of long range dispersion energy is required to get proper enthalpies, densities, and free energies from a simulation. [56] A homogeneous analytical correction is sufficient to properly capture thermodynamic properties for pure fluids and small molecule solvation [56, 47]. However, nonisotropic systems require additional nonisotropic corrections, either as inclusion of very long range interactions at infrequent intervals [47, 57] or Ewald summation in the dispersion term [47, 58].

Less work has gone into the specific choice of the tunable parameters associated with techniques for long range treatment of electrostatic and Lennard-Jones energies. The choice of these parameters can significantly effect the speed and accuracy of the nonbonded potential calculations. Abraham [59] and Wang [60] have proposed strategies for selecting PME

parameters, tuning them by minimizing the computational cost for a given tolerance in force calculations. In both studies, a trajectory is generated with a certain set of nonbonded parameters. The same trajectory is then rerun with different parameters, scanning the entire parameter space until a desired tolerance in the average force calculations is reached. Wang et al. calculate the error estimates using both the analytical and *ik*-differentiation (differentiation in Fourier space) schemes to obtain an optimized set of PME parameters. They observed that the optimization scheme based on force calculation can be unreliable when used for nonhomogeneous systems such as proteins in water or lipid bilayers.

Even fewer papers have looked at the tuning of Lennard-Jones cutoffs. Shirts et al. [47] found that analytical dispersion corrections were very accurate for small molecule solvation or small molecule liquids for cutoffs as low as 0.8 nm, but failed badly for protein-ligand binding calculations for cutoffs as long as 1.5 nm. In't Veld et al. [58] found serious issues in computation of surface tension when using analytical corrections for Lennard-Jones cutoffs at most cutoff lengths.

The effect of these parameters on free energy calculations, which involve simulations at multiple states, has received very little attention in the literature. Errors in potential energy that are dependent on the coupling parameter λ in free energy calculations could have significant effects that may not show up when computing properties at a single end state. Measuring the effects of changing simulation parameters for quantities like ensemble averages and especially free energies can be challenging because the statistical error must be reduced to a low enough level to observe any change between two independent simulations. This can require extremely long simulations to accurately detect small effects. For free energies, these calculations require converging a series of intermediate simulations, rather than just a single simulation. It is therefore unclear exactly how the parameters controlling the long range terms must be treated in order to accurately predict thermodynamic

observables like enthalpy and free energy differences. Given the statistical error in any such computation of observables, are there levels of approximation that give negligible effect on the statistical accuracy but still significantly increase simulation throughput?

To show the power of this multistate reweighting method, we identify the most computationally efficient nonbonded parameters that are statistically indistinguishable from results converged to the effectively infinite cutoff limit, examining both free energies of solvation and enthalpies of vaporization. We calculate these quantities with very high precision by rapidly estimating the difference between the observable estimated using a particular combination of nonbonded simulation parameters and the converged, expensive estimate of the observable over a large multidimensional grid of parameters. Importantly, we find that because of the high overlap in phase space between changes in nonbonded interactions, this calculation can be carried out with samples collected from a single relatively inexpensive set of nonbonded parameters. The information obtained in this process provides quantitative guidance for the choice of Lennard-Jones and PME cutoff parameters.

Varying all the nonbonded simulation parameters independently generates a combinatorially large number of possible settings. We can simplify the process by noting that the optimized Lennard-Jones and Coulomb simulation parameters must both be independently be converged. It may be possible to make choices of the two sets of the parameters with offsetting errors. However, any such offset is likely to be system dependent, involving a balance of the dispersion, repulsion and dipolar density; we should therefore minimize the error for each of the two interaction types independently.

We assume that we can perform the two optimizations serially, first optimizing the electrostatic parameters while keeping Lennard-Jones parameters set at the initial reference choice, and then optimizing the Lennard-Jones parameters. In theory, this process would need to be self-consistently iterated to guarantee statistical convergence. In the end, we

find that a single pass of this two step process converges to an optimized parameter set that is statistically indistinguishable from essentially infinite cutoff parameters, with final refinement that marginally improves performance.

We specifically evaluate free energies for the three molecular transformations proposed in our benchmark set [3] as test systems, as they represent difficult versions of standard problems occurring in small molecule free energy calculations. The three benchmark systems are a) united atom methane solvation in TIP3P water b) the dipole inversion null transformation (switching from $+1/-1$ to $-1/+1$ charges in a diatomic molecule with UA ethane parameters) in TIP3P water and c) united atom anthracene solvation in TIP3P water. The observables we choose to evaluate for this study are (a) the free energy estimate of the molecular transformations in the benchmark molecular set, (b) the enthalpy change during molecular transformations, which for methane and anthracene solvation is simply the enthalpy of solvation and (c) the molar heat of vaporization of TIP3P water. Force field parameters are given in the previous chapter. [3] Because of previous mentioned ambiguities and artifacts in treatment of PME when the total charge changes during the transformation, we do not test parameters for ion solvation because for lack of the correct reference. We validate our predictions by comparing the predictions using only the samples from benchmark states with results generated using samples from simulations run at the expensive and the proposed optimized parameter sets directly.

3.2 Methods

3.2.1 Parameters in short and long range nonbonded interaction calculation

We first describe the details of the different nonbonded interaction parameters involved in the calculation of long range contributions in GROMACS [61, 62]. These details are

generally but not always completely representative of the methods used in other simulation codes; dealing with all possible methods of computing long range interactions is beyond the scope of this study.

Lennard-Jones interactions: Lennard-Jones (LJ) interactions are calculated pairwise for the short range out to $r_{c,LJ}$, the LJ cutoff (in GROMACS, `rvdw`). The long range contribution from $r_{c,LJ}$ to $r = \infty$ is estimated using an analytical correction integrating the pair potential out to infinity by assuming the radial distribution function $g(r) = 1$ beyond the LJ cutoff.

$$\begin{aligned}
U_{LJ} &= U_{r < r_{c,LJ}} + U_{r \geq r_{c,LJ}} \\
&= U_{LJ,short} + \frac{N}{2} \rho \int_{r_{c,LJ}}^{\infty} U(r) g(r) 4\pi r^2 dr \\
&= U_{LJ,short} + 2\pi N \rho \int_{r_{c,LJ}}^{\infty} 4\epsilon \left[\left(\frac{\sigma}{r} \right)^{12} - \left(\frac{\sigma}{r} \right)^6 \right] dr \\
&= U_{LJ,short} + 8\pi N \rho \epsilon \sigma^3 \left[\frac{1}{9} \left(\frac{\sigma}{r_{c,LJ}} \right)^9 - \frac{1}{3} \left(\frac{\sigma}{r_{c,LJ}} \right)^3 \right]
\end{aligned} \tag{3.1}$$

This correction is typically known as the *dispersion correction* as the r^{-12} repulsion contribution to the integral almost completely disappears at typical cutoff distances of 3σ , where σ is the Lennard-Jones radius. The free energy correction is equal to the energy correction for fixed density, as all configurations have the exact same energy correction term. This approximation is easily generalized to systems with multiple LJ sites on the solute or different compositions of solvent. [47]

The dispersion correction must be averaged over all configurations in the case of constant pressure simulations, as each configuration has a different density, and a corresponding correction to the virial must also be added for constant pressure MD algorithms. [56, 47]. For solvation in homogeneous liquids, this analytical correction will generally be suf-

ficient using cutoffs around $3\text{-}5\sigma$ of the largest particles. [47] For heterogeneous systems such as membrane simulations or very large solute molecules, extremely long cutoffs or a more sophisticated long range treatment is required [47, 58], and the optimized parameters derived in this study will not necessarily be applicable in those situations.

Coulomb interactions: Individual Coulombic interactions are proportional to $1/r$ and thus converge slowly with distance. They must be summed over multiple periodic copies of the system because of this slow convergence in order to approximate bulk behavior. This calculation can be accelerated by taking the infinite sum over all periodic copies, and splitting it into a pairwise real space short range contribution and a Fourier space long-range contribution. In the particle mesh Ewald (PME) [48] technique and its smooth variant SPME, [49] the “smeared” long-range charge distribution is interpolated onto a grid where a fast Fourier transform (FFT) can be performed, and the self-interaction portion of the “smearing” is analytically removed.

$$\begin{aligned}
U_{\text{Coulomb}} &= U_{\text{real}} + U_{\text{Fourier}} + U_{\text{self}} \\
U_{\text{Coulomb}} &= \frac{f}{2} \sum_{n_x} \sum_{n_y} \sum_{n_z} \sum_i^N \sum_j^N \frac{q_i q_j}{r_{ij,n}} \\
U_{\text{real}} &= \frac{f}{2} \sum_{i,j}^N \sum_{n_x} \sum_{n_y} \sum_{n_z} q_i q_j \frac{\text{erfc}(\beta r_{ij,n})}{r_{ij,n}} \\
U_{\text{Fourier}} &= \frac{f}{2\pi V} \sum_{i,j}^N q_i q_j \sum_{m_x} \sum_{m_y} \sum_{m_z} \frac{\exp(-(\pi \mathbf{m}/\beta)^2 + 2\pi i \mathbf{m} \cdot (r_i - r_j))}{\mathbf{m}^2} \\
U_{\text{self}} &= -\frac{f\beta}{\sqrt{\pi}} \sum_i^N q_i^2
\end{aligned} \tag{3.2}$$

The primary contribution to the Fourier space sum are the first M_c wave vectors in each of the m_x , m_y and m_z directions [63], corresponding to the longest wavelengths. For PME

calculations, we must specify an order of interpolation of the charge distribution onto a grid (in GROMACS, `pme_order`), typically using a B-spline interpolation function which is smoother and allows higher accuracy with increasing order of interpolation[49]. B-spline interpolation also allows the force expressions to be evaluated analytically by differentiating the real and reciprocal energy equations, rather than using finite difference techniques. While calculating Coulomb potential using the Ewald sums, we assume that the real space sum becomes negligible before the Coulomb cutoff, $r_{c,coul}$ (in GROMACS, `rcoul`). The Ewald tolerance, $etol$ (`ewald_rtol` in GROMACS), is the relative value of the real space potential at the Coulomb cutoff compared to the total electrostatic energy at that distance. The Ewald tolerance parameter used in GROMACS is related to the Gaussian β parameter in Eq. 3.2 used in some other simulation programs by:

$$etol = \operatorname{erfc}(\beta r_{c,coul}) \quad (3.3)$$

A lower tolerance will give a more accurate direct sum but the number of included wave vectors for the reciprocal sum must be increased to compensate. The Fourier spacing is the maximum grid spacing for the fast Fourier transform grid used in PME. In GROMACS, this grid spacing is used to specify the number of grid points in each of the x , y , and z directions.

An additional parameter that must be set in GROMACS is `rlist`, the neighbor list distance. The neighbor list must be larger than the distance between atoms in the same charge group, or errors in energy can appear between neighbor list updates, but has negligible effect on the energy as long as it is longer than this distance. For the systems in this study, a neighbor list 0.2 nm larger than the maximum of the Coulombic and Lennard-Jones cutoffs is sufficient, and does not significantly increase the computation time. This largest

cutoff + 0.2 nm rule for `rlist` is used for all simulations in this study.

Switching functions: In both the Lennard-Jones and Coulomb cases as described above, there is a discontinuity in the short range potential and the force at the cutoff. This abrupt cutoff can lead to errors in the numerical integration, as the force is discontinuous for a particle crossing the cutoff. A switching function in the potential can be introduced at the cutoff for both the Lennard-Jones and Coulomb potentials. A spline of at least third order in the potential is required so that the force is differentiable. In GROMACS, this switching function is quintic:

$$\begin{aligned}
 U_{\text{nonbonded}} &= S(r)U(r) \\
 S(r) &= 1 \quad r < r_{sw} \\
 &= 1 - 10 \frac{(r - r_{sw})^3}{(r_c - r_{sw})^3} + 15 \frac{(r - r_{sw})^4}{(r_c - r_{sw})^4} - 6 \frac{(r - r_{sw})^5}{(r_c - r_{sw})^5} \quad r_{sw} < r \leq r_c \\
 &= 0 \quad r > r_c
 \end{aligned} \tag{3.4}$$

In GROMACS, the switch begins at r_{sw} and ends at r_c , and is specified by `rvdw_switch` and `rcoul_switch` depending on the potential type. We will occasionally refer to a switching distance $r_{dsw} = r_c - r_{sw}$, a switching range.

In the case of Lennard-Jones particles, a complementary switch function can be added to the dispersion correction, meaning no nonbonded energy is lost from the full interaction as long as the radial distribution function is constant outside the start of the switch. In the case of the Coulomb interaction, a short range real space potential switch cannot be directly matched by a compensating switch in the Fourier space potential, so non-negligible switching distances will distort the true $1/r$ potential in the cutoff region. Because *etol* is usually quite low near the cutoff, this energy loss should be fairly small, but has not been

quantified before. A smaller switch width will minimize this distortion of the potential. However, small switch widths also cause moderate spiking in the force at the cutoff, which can potentially affect the kinetics of the system and potentially the stability of the integration. To achieve a balance between the loss in energy without introducing a substantial force spike we must tune the switching distance both for LJ and Coulomb potentials.

It is also possible to eliminate cutoffs using a shifting function, where the potential surface is shifted down to zero at the cutoff, or a combination of the shifts and switches [64, 65]. In this study, we only examine the switching function. A shift affects the entire potential energy surface, and thus causes large effects on ensemble averages such as the enthalpy or the free energy examined in this chapter. On the other hand, properly balanced shift functions eliminate the force spike, and where conformational properties are of most interest, rather than free energies, they may be more appropriate. Additionally, group-based shifts for electrostatics, which are the most common type, have no effect since the shift components cancel for net-neutral groups. In any case, we will find that properly tuned switch functions do not significantly affect free energies or ensemble averages, and at least in this study we will not explore any other the tradeoffs between switching and shifting functions.

The space of all the possible nonbonded simulation parameters is clearly multidimensional. Specifically, we have the order of B-spline interpolation (*order*), tolerance in the real space cutoff (*etol*), the Fourier spacing (*FS*), Coulomb cutoff($r_{c,coul}$), Coulomb switching range ($r_{sw,coul}$), Lennard-Jones cutoff ($r_{c,LJ}$), and Lennard-Jones switching range ($r_{sw,LJ}$). Many of the parameters cannot be set independently for high-quality simulation results, and the PME parameters in particular are interdependent; a good Fourier spacing for one choice of *etol* may not be good for another. Each choice of a set of nonbonded simulation parameter affects the computational cost and accuracy of the thermodynamic

sampling differently. Certain choices of parameters, such as large cutoffs or very fine Fourier spacing significantly increase the simulation time. But beyond a certain point, the increased cost gives limited returns in accuracy, and we seek to identify the speed required for a specified level of accuracy.

The “expensive” reference parameter set we examine includes an Ewald tolerance (*etol*) of 10^{-10} (smaller is more accurate), Fourier grid spacing (*FS*) of 0.04 nm (smaller is more accurate), and a B-spline order of 6 (higher is more accurate). The expensive Coulomb real-space cutoff ($r_{c,coul}$) and Lennard-Jones real-space cutoff ($r_{c,LJ}$) varied with the system, and were both 1.3 nm for methane solvation, 1.5 nm for dipole inversion and 1.4 nm for anthracene solvation, chosen to be the longest possible cutoffs for the respective simulation boxes. Switch distances for the converged PME parameters were chosen to be zero for Coulomb and 0.001 nm for Lennard-Jones; switches only improve the stability of the numerical integration, not the energies themselves. The Lennard-Jones switch distance for comparison was chosen as 0.001 nm, effectively zero, because of implementation-specific constraints on parameter choices in GROMACS.

The order of interpolation range tested was between 3 (the minimum value in GROMACS) and 6, beyond which the potential energy change was negligible for systems of this size for any choice of Coulomb parameters examined. The Fourier spacing range was between 0.04 nm (any smaller became computationally untenable because of expense, but only negligibly changed the energy) to 0.20 nm, which is longer scale than many molecular details. *etol* ranged between 10^{-10} and 10^{-2} , equivalent to a β between approximately 5 and 2 nm^{-1} , thus extending beyond the range of typical values for β . The largest cutoffs possible were limited by the box size for the benchmark molecular set. The lowest cutoff of 0.6 nm for all systems was set to be smaller than for all standard MD simulations.

In the first phase of Coulomb parameter optimization, LJ parameters fixed to those

used in our previous benchmark study [3], which had been selected based on anecdotal experience from previous large scale studies [30, 31, 66]. The selected values used to search through the multidimensional parameter space are given in Table 3.1.

Parameter	Parameter value
Order of interpolation (<i>order</i>)	3, 4, 5, 6
Ewald tolerance (<i>etol</i>)	10^{-2} , 10^{-4} , 10^{-6} , 10^{-8} , 10^{-10}
Fourier spacing (<i>FS</i>) (nm)	0.04, 0.06, 0.08, 0.10, 0.12, 0.14, 0.16, 0.18, 0.20
Coulomb Cutoff ($r_{c,coul}$) (nm)	0.6, 0.7, 0.8, 0.9, 1.0, 1.1, 1.2, 1.3, 1.4, 1.5
Coulomb Switch width (nm) $r_{c,Coul} - r_{sw,coul}$	0.2, 0.18, 0.16, 0.14, 0.12, 0.10, 0.08, 0.06, 0.04, 0.02, 0.01, 0.001
LJ Cutoff ($r_{c,LJ}$) (nm)	0.6, 0.7, 0.8, 0.9, 1.0, 1.1, 1.2, 1.3, 1.4, 1.5
LJ Switch width (nm) $r_{c,LJ} - r_{sw,LJ}$	0.2, 0.18, 0.16, 0.14, 0.12, 0.10, 0.08, 0.06, 0.04, 0.02, 0.01, 0.001

Table 3.1: Nonbonded interaction parameter values examined in the optimization process.

3.2.2 Phase one: Optimization of PME parameters

We first perform the search through Coulomb parameter space, specifically examining the values of the order of B-spline interpolation, the Ewald tolerance, the Fourier spacing, and the Coulomb cutoff. The first portion of search was performed over 180 parameters per $r_{c,coul}$ distance, giving 1440 combinations for methane solvation, 1800 combinations for

dipole inversion and 1620 combinations for anthracene solvation, since each molecule had different box size and therefore a different maximum allowable cutoff.

3.2.2.1 Difference in free energy estimates due to approximations introduced by simulation parameters Samples from equilibrium isobaric-isothermal simulations corresponding to just one parameter set are used to reevaluate energies for different parameter sets. MBAR reweights the sampled energies using the reevaluated energies to estimate the observables at the unsampled parameter set. The variance-minimizing free energy estimating equation for MBAR is:

$$f_i = -\ln \sum_{k=1}^K \sum_{n=1}^{N_K} \frac{\exp[-u_i(x_{kn})]}{\sum_{k'=1}^K N_{k'} \exp[f_{k'} - u_{k'}(x_{kn})]} \quad (3.5)$$

where K is the total number of states and N_k is the total number of uncorrelated samples available from an equilibrium simulation at state k . Each free energy is thus a weighted sum of all samples from all k states. $f_i = \beta G_i$, where G_i is the Gibbs free energy associated with state i . $u_i(x_{kn})$ is the reduced potential energy of the n^{th} sample belonging to equilibrium simulation of state k but evaluated at state i . For the NPT simulations carried out here, the reduced potential $u_i(x_{kn}) = \beta(U_i(x_{kn}) + PV_{kn})$, where P is the applied pressure and V_{kn} is the simulation volume of sample kn .

Equilibrium samples \vec{x}_B were obtained from benchmark simulations from our previous study, with nonbonded simulation parameters P_B listed in Table 3.6. Samples from other simulation parameter sets i are denoted as \vec{x}_i . Samples at the benchmark parameters were obtained from 100 5 ns uncorrelated simulation runs for free energy calculations for the systems in our benchmark study [3], with simulation parameters noted there. The samples were stored as full precision coordinate sets 50 ps apart, which is longer than the maximum

autocorrelation time of 30 ps for the potential energies found in our previous study of the same system. The samples can thus be considered effectively independent. The first 10% (0.5 ns) of data from each run was discarded, leaving a total of 9000 samples at each of the intermediate states from the free energy calculation.

We recalculate potential energies using these samples at a range of parameter sets P_i , with P_E being the most expensive nonbonded simulation parameters discussed above, with expensive “gold standard” reference parameters. Energies were calculated with GRO-MACS 4.5.3 with bug fixes later incorporated into the 4.5.7 and 4.6 versions. [62] $U_i(x_B)$ is therefore the set of potential energies calculated using parameter set P_i with the samples \vec{x}_B , with $U_E(x_B)$ denoting energies evaluated with the expensive parameter set on samples from the simulations done with benchmark parameter set. Benchmark energies were recalculated along with all other energies to maximize consistency of the energies.

To calculate free energy differences and the uncertainties in these free energy differences between P_E and a given choice of P_i using MBAR, we first construct a 3-dimensional matrix U of size $(3K, 3K, N_k)$, where K is the number of states in the free energy simulation performed in the benchmark state. When we re-evaluate energies for expensive and i^{th} trial parameter sets we introduce $2K$ new thermodynamic states, K states for fully converged, “expensive” parameters, and K states for i^{th} trial parameter set. Thus we have a total of $3K$ thermodynamic states defined. In the optimization procedure, only the first K intermediate states simulated using the original benchmark parameters have samples, though more generally for multistate reweighting, all states might include samples. There are $K = 8$ states spanning the initial and final states for methane solvation, 11 for dipole inversion, and 15 for anthracene solvation, with the choice of K for each system discussed in the previous study [3].

We write \mathbf{U} as the 3D matrix:

$$\begin{aligned} \mathbf{U}(3K \times 3K \times N_k) &= \begin{bmatrix} U_0(x_{0,1 \dots N_0}) & \cdots & U_{3K-1}(x_{0,1 \dots N_0}) \\ \vdots & \ddots & \vdots \\ U_0(x_{3K-1,1 \dots N_{3K-1}}) & \cdots & U_{3K-1}(x_{3K-1,1 \dots N_{3K-1}}) \end{bmatrix} \\ &= \begin{bmatrix} \mathbf{U}_B(\mathbf{x}_B) & \mathbf{U}_E(\mathbf{x}_B) & \mathbf{U}_i(\mathbf{x}_B) \\ \mathbf{U}_B(\mathbf{x}_E) & \mathbf{U}_E(\mathbf{x}_E) & \mathbf{U}_i(\mathbf{x}_E) \\ \mathbf{U}_B(\mathbf{x}_i) & \mathbf{U}_E(\mathbf{x}_i) & \mathbf{U}_i(\mathbf{x}_i) \end{bmatrix} \end{aligned} \quad (3.6)$$

Each element of the above matrix is a $K \times K \times N_k$ matrix as it extends out to N_k samples in the third dimension. In these sub-matrices, the subscript to U indicates the parameter set used for energy evaluation. The subscript to X indicates the parameter set with which the sample configurations were generated. The vector \mathbf{N} in Eq. 3.7 contains the number of uncorrelated equilibrium samples collected at each state k .

$$\mathbf{N} = [N_0, \dots, N_{3K-1}] \quad (3.7)$$

The different submatrices of the matrix \mathbf{U} in Eq. 3.6 are:

$$\begin{aligned}
\mathbf{U}_B(\mathbf{X}_B)(K \times K \times N_k) &= \begin{bmatrix} U_0(x_{0,1 \dots N_0}) & \cdots & U_{K-1}(x_{0,1 \dots N_0}) \\ \vdots & \ddots & \vdots \\ U_0(x_{K-1,1 \dots N_{K-1}}) & \cdots & U_{K-1}(x_{K-1,1 \dots N_{K-1}}) \end{bmatrix} \\
\mathbf{U}_E(\mathbf{X}_B)(K \times K \times N_k) &= \begin{bmatrix} U_K(x_{0,1 \dots N_0}) & \cdots & U_{2K-1}(x_{0,1 \dots N_0}) \\ \vdots & \ddots & \vdots \\ U_K(x_{K-1,1 \dots N_{K-1}}) & \cdots & U_{2K-1}(x_{K-1,1 \dots N_{K-1}}) \end{bmatrix} \\
\mathbf{U}_i(\mathbf{X}_B)(K \times K \times N_k) &= \begin{bmatrix} U_{2K}(x_{0,1 \dots N_0}) & \cdots & U_{3K-1}(x_{0,1 \dots N_0}) \\ \vdots & \ddots & \vdots \\ U_{2K}(x_{K-1,1 \dots N_{K-1}}) & \cdots & U_{3K-1}(x_{K-1,1 \dots N_{K-1}}) \end{bmatrix}
\end{aligned} \tag{3.8}$$

Energies computed using these three different simulation input sets, $\mathbf{U}_B(\mathbf{X}_B)$, $\mathbf{U}_E(\mathbf{X}_B)$, $\mathbf{U}_i(\mathbf{X}_B)$ each having K states, is the input for MBAR Eq. 3.5.

These three sets represent a new set of $3K$ thermodynamic states. $U_0(x_{0,n})$ evaluated using $P1[T_B, E_B]$ is different compared to $U_0(x_{0,n})$ evaluated using $P1[T_B, E_E]$. $U_0(x_{0,n})$ evaluated using $P1[T_B, E_E]$ is therefore present in the \mathbf{U} matrix as a different thermodynamic state $U_K(x_{0,n})$. $U_0(x_{0,n})$ evaluated using $P1[T_B, E_i]$ is present as yet another thermodynamic state in the U matrix, $U_{2K}(x_{0,n})$. Similarly $U_{K-1}(x_{0,n})$ evaluated using $P1[T_B, E_B]$ is different compared to $U_{K-1}(x_{0,n})$ evaluated at $P1[T_B, E_E]$ and $P1[T_B, E_i]$, which in the \mathbf{U} matrix appears as different thermodynamic states as $U_{2K-1}(x_{0,n})$ and $U_{3K-1}(x_{0,n})$ respectively. The same holds true for other intermediate states as well and hence we have now a total of $3K$ thermodynamic states.

$$\begin{aligned}
\mathbf{U}_{\mathbf{B}}(\mathbf{X}_{\mathbf{E}})(K \times K \times N_k) &= \begin{bmatrix} U_0(x_{K,1 \dots N_K}) & \cdots & U_{K-1}(x_{K,1 \dots N_K}) \\ \vdots & \ddots & \vdots \\ U_0(x_{2K-1,1 \dots N_{2K-1}}) & \cdots & U_{K-1}(x_{2K-1,1 \dots N_{2K-1}}) \end{bmatrix} \\
\mathbf{U}_{\mathbf{E}}(\mathbf{X}_{\mathbf{E}})(K \times K \times N_k) &= \begin{bmatrix} U_K(x_{K,1 \dots N_K}) & \cdots & U_{2K-1}(x_{K,1 \dots N_K}) \\ \vdots & \ddots & \vdots \\ U_K(x_{2K-1,1 \dots N_{2K-1}}) & \cdots & U_{2K-1}(x_{2K-1,1 \dots N_{2K-1}}) \end{bmatrix} \\
\mathbf{U}_{\mathbf{i}}(\mathbf{X}_{\mathbf{E}})(K \times K \times N_k) &= \begin{bmatrix} U_{2K}(x_{K,1 \dots N_K}) & \cdots & U_{3K-1}(x_{K,1 \dots N_K}) \\ \vdots & \ddots & \vdots \\ U_{2K}(x_{2K-1,1 \dots N_{2K-1}}) & \cdots & U_{3K-1}(x_{2K-1,1 \dots N_{2K-1}}) \end{bmatrix} \\
\mathbf{U}_{\mathbf{B}}(\mathbf{X}_{\mathbf{i}})(K \times K \times N_k) &= \begin{bmatrix} U_0(x_{2K,1 \dots N_{2K}}) & \cdots & U_{K-1}(x_{2K,1 \dots N_{3K-1}}) \\ \vdots & \ddots & \vdots \\ U_0(x_{3K-1,1 \dots N_{3K-1}}) & \cdots & U_{K-1}(x_{3K-1,1 \dots N_{3K-1}}) \end{bmatrix} \\
\mathbf{U}_{\mathbf{E}}(\mathbf{X}_{\mathbf{i}})(K \times K \times N_k) &= \begin{bmatrix} U_K(x_{2K,1 \dots N_{2K}}) & \cdots & U_{2K-1}(x_{2K,1 \dots N_{3K-1}}) \\ \vdots & \ddots & \vdots \\ U_K(x_{3K-1,1 \dots N_{3K-1}}) & \cdots & U_{2K-1}(x_{3K-1,1 \dots N_{3K-1}}) \end{bmatrix} \\
\mathbf{U}_{\mathbf{i}}(\mathbf{X}_{\mathbf{i}})(K \times K \times N_k) &= \begin{bmatrix} U_{2K}(x_{2K,1 \dots N_{2K}}) & \cdots & U_{3K-1}(x_{2K,1 \dots N_{3K-1}}) \\ \vdots & \ddots & \vdots \\ U_{2K}(x_{3K-1,1 \dots N_{3K-1}}) & \cdots & U_{3K-1}(x_{3K-1,1 \dots N_{3K-1}}) \end{bmatrix}
\end{aligned} \tag{3.9}$$

For the optimization procedure, $N_k = 0$ for the $2K$ total states of the free energy calculations carried out with parameter sets P_E and P_i . This means that $\mathbf{U}_{\mathbf{i}}(x_E)$ and $\mathbf{U}_{\mathbf{i}}(x_i)$ for any choice of state i are both undefined and unused in the initial phases of this study.

More generally, we could use this formalism to compute free energies using samples from multiple states simultaneously. In this chapter, we initially restrict ourselves to the case of sampling from a single set of parameters, which we will find will be sufficient to predict thermodynamic properties over the range of simulation parameters of interest. We can then validate the final results with data collected from multiple states.

We also note that there is no specific reason to restrict the property prediction to handling three states (reference, converged and trial) at a time; the multistate reweighting formalism is general enough to perform computations between any number of sampled and unsampled states simultaneously. For example, we could predict the properties of *all* of the unsampled states simultaneously instead of one at a time. However, the memory requirement for the entire matrix of all states becomes prohibitive, and it provides no extra statistical efficiency; the results only change when we change the sampled data, not the order in which the properties at unsampled parameter sets are computed.

Instead we focus on the most flexible and straightforward approach, using the thermodynamic states with energies sampled (in this case, the K benchmark states), the states being used as a reference (in this case, the K expensive parameter states), and the set of states at one other trial parameter set of interest. The process can be made even more efficient if the free energies and weights are saved from the first round of self-consistent iteration, as generating weights for new states with no samples does not require any additional iterations, but for this study, such optimization was not used.

For this optimization process, we can rewrite the matrix as:

$$\mathbf{U}(3K \times 3K \times N_k) = \begin{bmatrix} U_0(x_{0,1 \dots N_0}) & \cdots & U_{3K-1}(x_{0,1 \dots N_0}) \\ \vdots & \ddots & \vdots \\ U_0(x_{K-1,1 \dots N_{K-1}}) & \cdots & U_{3K-1}(x_{K-1,1 \dots N_{K-1}}) \\ 0 & \cdots & 0 \\ \vdots & \ddots & \vdots \\ 0 & \cdots & 0 \end{bmatrix} \quad (3.10)$$

$$= \begin{bmatrix} \mathbf{U}_B(\mathbf{X}_B) & \mathbf{U}_E(\mathbf{X}_B) & \mathbf{U}_i(\mathbf{X}_B) \\ 0 & 0 & 0 \\ 0 & 0 & 0 \end{bmatrix}$$

$$\mathbf{N} = [N_0, \dots, N_{K-1}, 0, 0, \dots, 0, 0] \quad (3.11)$$

The \mathbf{U} matrix and the \mathbf{N} vector in Eqns. 3.10 and 3.11 are the inputs to MBAR (Eqn. 3.5) which is solved using standard optimization techniques [4] for G_i for all $3K$ states. The result is a matrix $\Delta \mathbf{G}$ with all pairwise free energy difference estimates

$$\Delta \mathbf{G}(3K \times 3K) = \begin{bmatrix} G_0 - G_0 = 0 & \cdots & G_{3K-1} - G_0 \\ \vdots & \ddots & \vdots \\ G_0 - G_{3K-1} & \cdots & G_{3K-1} - G_{3K-1} = 0 \end{bmatrix} \quad (3.12)$$

and also a matrix of an estimate of the statistical error $\delta(\Delta G)$ for each of these free energy differences. The uncertainties in the pairwise difference estimates ΔG are estimated using

Eq. 12 in Shirts and Chodera [4].

$$\delta(\Delta \mathbf{G})(3K \times 3K) = \begin{bmatrix} 0 & \cdots & \delta(G_{3K-1} - G_0) \\ \vdots & \ddots & \vdots \\ \delta(G_0 - G_{3K-1}) & \cdots & 0 \end{bmatrix} \quad (3.13)$$

where the diagonal is identically zero as there is no uncertainty in the value of zero for the free energy between a state and itself. For standard molecular transformation calculations, these error estimates are extremely reliable estimates of the true sample standard deviation [3]. The free energy of molecular transformation in the benchmark molecular set, solvation or dipole inversion, is equal to the difference in free energies of the end states, in this case $\Delta G_B = G_{K-1} - G_0$, $\Delta G_E = G_{2K-1} - G_K$, and $\Delta G_i = G_{3K-1} - G_{2K}$.

However, we are most interested in the free energy difference $\Delta\Delta G_{Ei} = \Delta G_i - \Delta G_E$ rather than any of the free energies individually. At first, it may seem that we cannot estimate this difference with any significant degree of precision, because of the uncertainties in the individual free energy estimations. However, the variance estimate of $\Delta\Delta G_{Ei} = \text{var}(\Delta\Delta G_{Ei})$ is not simply the sum of the variances $\text{var}(\Delta G_E)$ and $\text{var}(\Delta G_i)$, because the two free energy estimates are computed from the same samples and are thus are highly correlated. We must instead derive the variance estimate for $\Delta\Delta G_{Ei}$ using the properties of the covariance:

$$\begin{aligned} \text{var}(\Delta\Delta G_{Ei}) &= \text{var}((G_{2K-1} - G_K) - (G_{3K-1} - G_{2K})) \\ &= \text{cov}(G_{2K-1} - G_K, G_{2K-1} - G_K) \\ &\quad + \text{cov}(G_{3K-1} - G_{2K}, G_{3K-1} - G_{2K}) \\ &\quad - 2\text{cov}(G_{2K-1} - G_K, G_{3K-1} - G_{2K}) \end{aligned} \quad (3.14)$$

Where $\text{cov}(x, y)$ is the covariance of the two variables x and y . With repeated application, the above equation yields the following:

$$\begin{aligned}
\text{var}(\Delta\Delta G_{Ei}) = & \text{var}(G_{2K-1}) + \text{var}(G_K) + \text{var}(G_{3K-1}) + \text{var}(G_{2K}) \\
& - 2[\text{cov}(G_{2K-1}, G_K) + \text{cov}(G_{3K-1}, G_{2K}) \\
& + \text{cov}(G_{2K-1}, G_{3K-1}) - \text{cov}(G_{2K-1}, G_K) \\
& - \text{cov}(G_K, G_{3K-1}) + \text{cov}(G_K, G_{2K})]
\end{aligned} \tag{3.15}$$

Each term in the above equation can be straightforwardly extracted from the asymptotic covariance matrix, Θ_{ij} , estimated using Eq. 8 of Shirts and Chodera [4].

We emphasize that this equation, and the resulting ability to calculate the covariances between two observables calculated from the data, is the absolute core of the success of this reweighting approach to estimate *changes* in simulation as well as thermodynamic parameters(temperature and pressure). With it, we can drastically reduce the variance in differences of thermodynamic variables differences. Once we have all the $\Delta\Delta G_{Ei}$, provided the statistical uncertainties $\delta(\Delta\Delta G_{Ei}) = (\text{var}(\Delta\Delta G_{Ei}))^{1/2}$ are low enough, we can find the parameter set for which $\Delta\Delta G_{Ei}$ is less than the desired level of bias in free energy estimate, and then choose the parameter set that are most computationally efficient for that level of bias.

3.2.2.2 Difference in enthalpy of transformation We also calculate the enthalpy of molecular transformation, the difference between the initial and the final state enthalpies $(\langle H \rangle_{\lambda=1} - \langle H \rangle_{\lambda=0}) \pm \delta(\langle H \rangle_{\lambda=1} - \langle H \rangle_{\lambda=0})$. For methane solvation and anthracene solvation, the enthalpy of molecular transformation is the solvation enthalpy.

The expectation value of $H = U_{int} + PV$ is the enthalpy of the simulated state. Each

energy term in the \mathbf{U} matrix, Eq. 3.10, is equal to total internal energy U_{int} plus the pressure times volume term PV . We can therefore use this expression \mathbf{U} as the input matrix of observables to Eqs. 15 and 16 of Shirts and Chodera for expectations of observables. [4] Solving these equations (which requires the weights generated solving for the free energies) yields the equilibrium expectation values of enthalpies at all states and corresponding uncertainties in the expectation values.

$$\langle \mathbf{H} \rangle = \begin{bmatrix} \langle H \rangle_0 \\ \vdots \\ \langle H \rangle_{3K-1} \end{bmatrix}, \delta(\langle \mathbf{H} \rangle) = \begin{bmatrix} \delta(\langle H \rangle_0) \\ \vdots \\ \delta(\langle H \rangle_{3K-1}) \end{bmatrix} \quad (3.16)$$

Where these two vectors are size $(3K \times 1)$, We can also obtain the pairwise difference in expectation values between two states, and associated uncertainties in these differences, which are size $(3K \times 3K)$ arrays.

$$\Delta \langle \mathbf{H} \rangle = \begin{bmatrix} \langle H \rangle_0 - \langle H \rangle_0 = 0 & \cdots & \langle H \rangle_{3K-1} - \langle H \rangle_0 \\ \vdots & \ddots & \vdots \\ \langle H \rangle_0 - \langle H \rangle_{3K-1} & \cdots & \langle H \rangle_{3K-1} - \langle H \rangle_{3K-1} = 0 \end{bmatrix} \quad (3.17)$$

$$\delta(\Delta \langle \mathbf{H} \rangle) = \begin{bmatrix} 0 & \cdots & \delta(\langle H \rangle_{3K-1} - \langle H \rangle_0) \\ \vdots & \ddots & \vdots \\ \delta(\langle H \rangle_0 - \langle H \rangle_{3K-1}) & \cdots & 0 \end{bmatrix} \quad (3.18)$$

We obtain $\Delta \Delta H$ from Eq. 3.17.

$$\Delta \Delta H_{Ei} = (\langle H \rangle_{2K-1} - \langle H \rangle_K) - (\langle H \rangle_{3K-1} - \langle H \rangle_{2K}) \quad (3.19)$$

We derive the error estimate $\delta(\Delta\Delta H_{Ei})$ using the covariance formula, similar to the one used for the error estimate of $\Delta\Delta G_{Ei}$.

$$\begin{aligned}
\text{var}(\Delta\Delta H_{Ei}) &= \text{cov}(H_{2K-1} - H_K) - (H_{3K-1} - H_{2K}), \\
&\quad (H_{2K-1} - H_K) - (H_{3K-1} - H_{2K})) \\
&= \text{var}(H_{2K-1} - H_K) + \text{var}(H_{3K-1} - H_{2K}) \\
&\quad - 2[\text{cov}(H_{2K-1}, H_{3K-1}) - \text{cov}(H_{2K-1}, H_{2K}) \\
&\quad - \text{cov}(H_K, H_{3K-1}) + \text{cov}(H_K, H_{2K})]
\end{aligned} \tag{3.20}$$

The first two variance terms in Eq. 3.20 can be directly read from the matrix in Eq.3.18. Unlike in the case of $\delta(\Delta\Delta G_{Ei})$, the covariance terms cannot be read directly from the covariance matrix Θ corresponding to the expectation values. The estimator of the uncertainty for equilibrium expectation values is given by Eq. 16 in Shirts and Chodera [4]:

$$\delta^2 \hat{A} \equiv \text{cov}(\hat{c}_A/\hat{c}_a, \hat{c}_A/\hat{c}_a) = \hat{A}^2(\hat{\Theta}_{AA} + \hat{\Theta}_{aa} - 2\hat{\Theta}_{Aa}) \tag{3.21}$$

Using Eq. 10 of Shirts and Chodera [4] we can derive an expression for the covariance terms of the form $\text{cov}(\hat{c}_A/\hat{c}_a, \hat{c}_B/\hat{c}_b)$:

$$\text{cov}(\hat{c}_A/\hat{c}_a, \hat{c}_B/\hat{c}_b) = \hat{A}\hat{B}(\hat{\Theta}_{AB} - \hat{\Theta}_{Ab} - \hat{\Theta}_{aB} + \hat{\Theta}_{ab}) \tag{3.22}$$

The four covariance terms in Eq. 3.20 can be calculated using Eq. 3.22. This allows us to compute $\Delta\Delta H_{Ei} \pm \delta(\Delta\Delta H_{Ei})$ between the expensive parameters and any other set of simulation parameters taking into account the correlation between the two measurements. For notational clarity, we will sometimes use $\Delta\Delta G$ and $\Delta\Delta H$ to refer to $\Delta\Delta G_{Ei}$ and $\Delta\Delta H_{Ei}$ in the rest of the chapter.

3.2.2.3 Difference in enthalpy of vaporization of water We calculate the enthalpy of vaporization of water using the estimate of enthalpy of the last alchemical state of methane solvation, which includes water with only a single noninteracting dummy united atom methane molecule. We assume that the enthalpy difference in vapor is negligible between parameter sets, which is exact in the ideal gas limit. The enthalpy of the simulation box after subtracting the kinetic energy of the dummy methane molecule is the enthalpy of liquid TIP3P water. The difference in the enthalpies of vaporization of water evaluated at two different simulation parameter sets, P_E and P_i , will be equal to the difference in the enthalpies of the last state of methane solvation of the two sets, as the PV terms and kinetic energies of the dummy methane molecule cancel out. Thus the difference in the enthalpy of vaporization of water ΔH_{vap} can also be read directly from Eq. 3.17. Similarly, the uncertainty in ΔH_{vap} can be directly read from Eq. 3.18.

$$\begin{aligned}
\Delta H_{vap} &= H_{vap,E} - H_{vap,i} \\
&\approx \langle H_{liq,i} \rangle - \langle H_{liq,E} \rangle \\
&= \langle H \rangle_{3K-1} - \langle H \rangle_{2K-1} \\
\delta(\Delta H_{vap}) &= \delta(\langle H \rangle_{3K-1} - \langle H \rangle_{2K-1})
\end{aligned} \tag{3.23}$$

3.2.3 Phase two: Optimization of the Coulomb switch

Once we have the optimized Coulomb parameters from the first phase of our search, we can investigate how much of a difference Coulomb switch parameters make in the thermodynamic estimates $\Delta\Delta G$, $\Delta\Delta H$ and ΔH_{vap} . Although the switching parameters could have been optimized simultaneously with the other electrostatic parameters, the Coulomb switch was optimized independently to make it easier to identify the effect of this switch on the thermodynamic properties, which is an open question. We construct the input matrix \mathbf{U}

in a similar way as described in previous section. The search proceeds identically, except now varying only the $r_{sw,coul}$. Because the optimized Coulomb cutoff is chosen as 0.9 nm (see the Results section for selection criteria) we calculate $\Delta\Delta G$, $\Delta\Delta H$ and ΔH_{vap} for Coulomb switches starting at 0.7, 0.72, 0.74, 0.76, 0.78, 0.8, 0.82, 0.84, 0.86, 0.88, 0.89 and 0.899 nm, terminating at 0.9 nm.

3.2.4 Phase three: Optimization of the Lennard-Jones parameters

After understanding the behavior of the Coulomb switch, we optimize the Lennard-Jones cutoff $r_{c,LJ}$ and Lennard-Jones switching distance $r_{sw,LJ}$ with fixed Coulomb parameters. Here, we simultaneously optimize both the LJ cutoff and the LJ switching distances. The treatment of the Lennard-Jones switch is somewhat different than in the Coulomb switch case, as in the Lennard-Jones the missing potential energy can be properly treated in the dispersion correction by analytically including the switch function in a way that it cannot be treated in the Fourier space portion of the Coulomb calculation. The maximum cutoffs, set by the box sizes of 1.3 nm for methane solvation, 1.5 nm for dipole inversion and 1.4 nm for anthracene solvation along with optimized PME parameters are chosen as the ‘expensive’ LJ parameter reference. Switch width varies from 0.001 nm to 0.2 nm as shown in Table 3.1.

An important factor in our search is the choice of criteria to by which we decide whether optimized parameters are sufficiently close to the more expensive parameters for general use. We consider two possible choices:

1. A set of parameters is sufficiently close to the converged parameters if $\Delta\Delta G_{Ei} \leq \delta(\Delta G_E)$; in words, the difference in free energies between the two parameter sets is smaller than the uncertainty in a standard calculation, in our case the 10 ns (with 1

ns used for equilibration) calculation used for validation.

2. A set of parameters is sufficiently close to the converged parameters if $\Delta\Delta G_{Ei} \leq \delta(\Delta\Delta G_{Ei})$; in words, the difference in free energies is smaller than the uncertainty in the calculation of this difference.

If calculations are being used for a large scale simulation testing, then likely the first criteria is sufficient; it says that any errors due to the parameters will be statistically indistinguishable from statistical errors. However, to be fully converged, and for the highest precision calculations, then the second criteria would be required. The second criteria is much more stringent, because using reweighting we are able to calculate differences of differences of free energies with extremely high precision.

For the first and second phase of the search, over the Coulomb parameters, we choose the first criteria. For the third, van der Waals phase, we find that all choices already match the first criteria, and then turn to the second criteria, in some cases requiring us to return and perform additional refinement of the Coulombic calculations in order to reach this more stringent second criteria.

Once we have determined which sets of parameters are sufficiently accurate, we identify the parameters that are the most computationally efficient. In all cases, computational expense for a given set of parameters is reported in ns/hr, estimated using 1000 steps of simulation at a single intermediate state run in parallel on 8 cores on the same node. Experimentation showed that 1000 steps of MD is sufficient to eliminate error due to time used in initializing and finalizing simulation runs. Running on different cores may change the tradeoff of expense slightly, but examining all possible combinations of hardware configurations for timings is beyond the scope of this study.

3.3 Results

3.3.1 Optimized PME parameters

The difference in thermodynamic quantities between simulations run with converged PME parameters and the 1440 other parameters examined for methane solvation over the entire multidimensional space is plotted in Figures 3.1–3.3. The $\Delta\Delta G$ for dipole inversion and anthracene solvation, which are qualitatively the same, are shown in Figures 3.5 and 3.7 respectively. Figure 3.1 shows $\Delta\Delta G$ plotted as a function of four PME parameters for methane solvation. The order of interpolation of B-spline varies by columns from 3 on left to 6 on right. The Ewald tolerance varies by rows from 10^{-2} on the top row to 10^{-10} at the bottom row. At a fixed order of interpolation and Ewald tolerance, $\Delta\Delta G$ is plotted in each subplot as a function of Fourier spacing and Coulomb cutoff.

From Figure 3.1, $\Delta\Delta G$ indeed approaches zero for converged PME parameters such as high Coulomb cutoff and small Fourier spacing, providing a sanity check on the procedure. Similar plots for the difference in enthalpy of molecular transformation $\Delta\Delta H$, Figure 3.2, the difference in enthalpy of vaporization of water ΔH_{vap} , Figure 3.3, show expected convergence for expensive parameters.

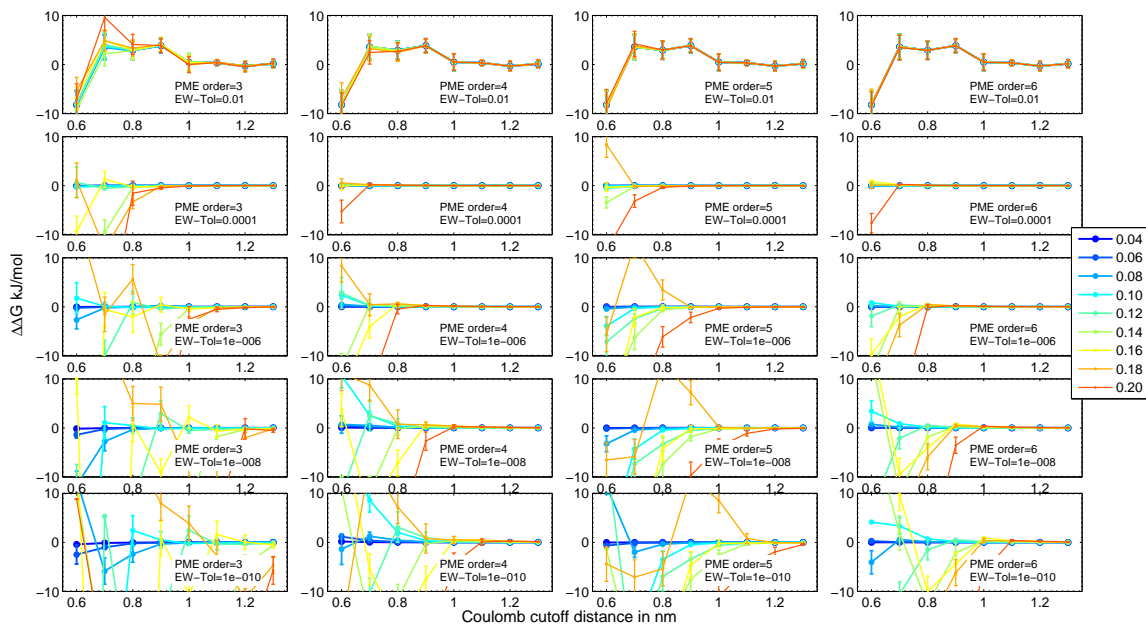


Figure 3.1: $\Delta\Delta G_{Ei}$ for methane solvation between reference expensive PME parameters and a choice of the four PME parameters: Coulomb cutoff (x-axis of each graph), Fourier spacing (color), PME order (graphs arranged left to right), and Ewald tolerance (graphs arranged top to bottom). The difference in free energy differences goes to zero as the reference parameters are approached.

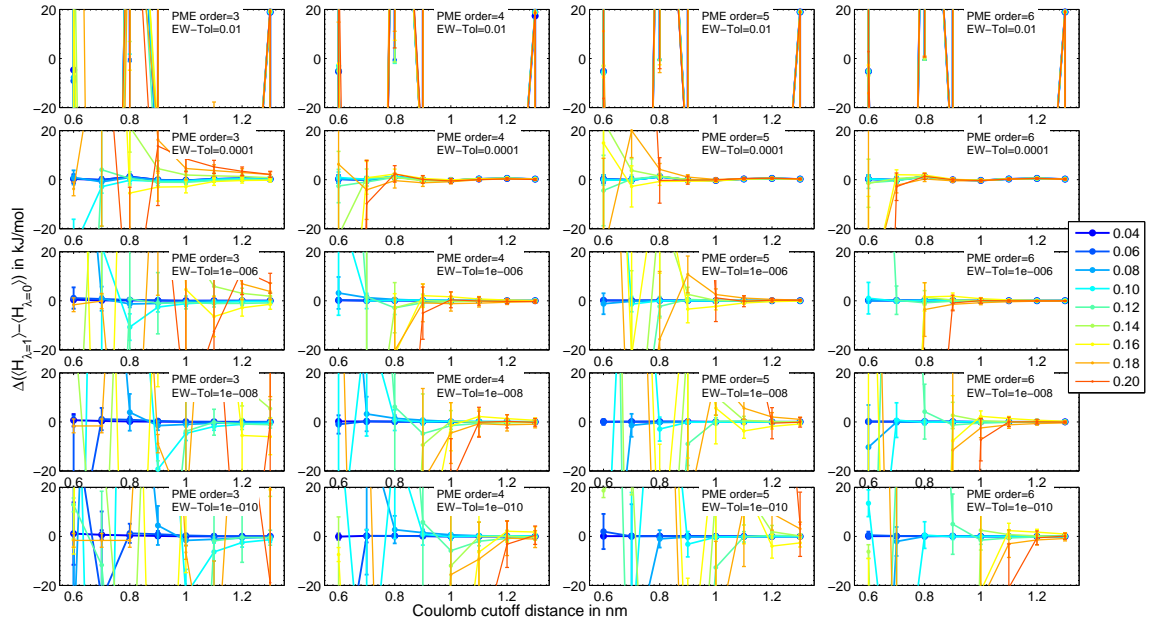


Figure 3.2: Change in enthalpy of methane solvation ($\langle H \rangle_{\lambda=1} - \langle H \rangle_{\lambda=0}$) between expensive reference PME parameters and a choice of the four PME parameters: Coulomb cutoff (x-axis of each graph), Fourier spacing (color), PME order (graphs arranged left to right), and Ewald tolerance (graphs arranged top to bottom). Although we can see the differences go to zero in the limit of the expensive reference parameters, because of the statistical noise in the enthalpy of solvation calculation, the level of bias for any given choice of parameters is difficult to identify.

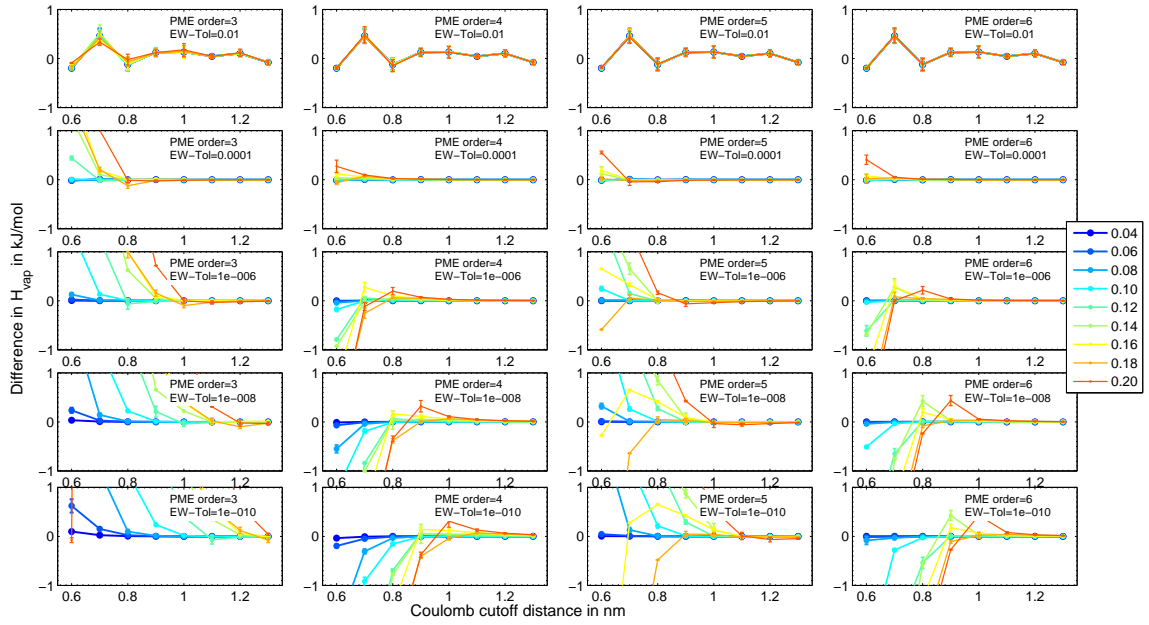


Figure 3.3: Change in enthalpy of vaporization ΔH_{vap} for TIP3P water between expensive reference PME parameters and a choice of the four PME parameters: Coulomb cutoff (x-axis of each graph), Fourier spacing (color), PME order (graphs arranged left to right), and Ewald tolerance (graphs arranged top to bottom) for methane solvation, showing clear convergence to zero for more expensive parameters.

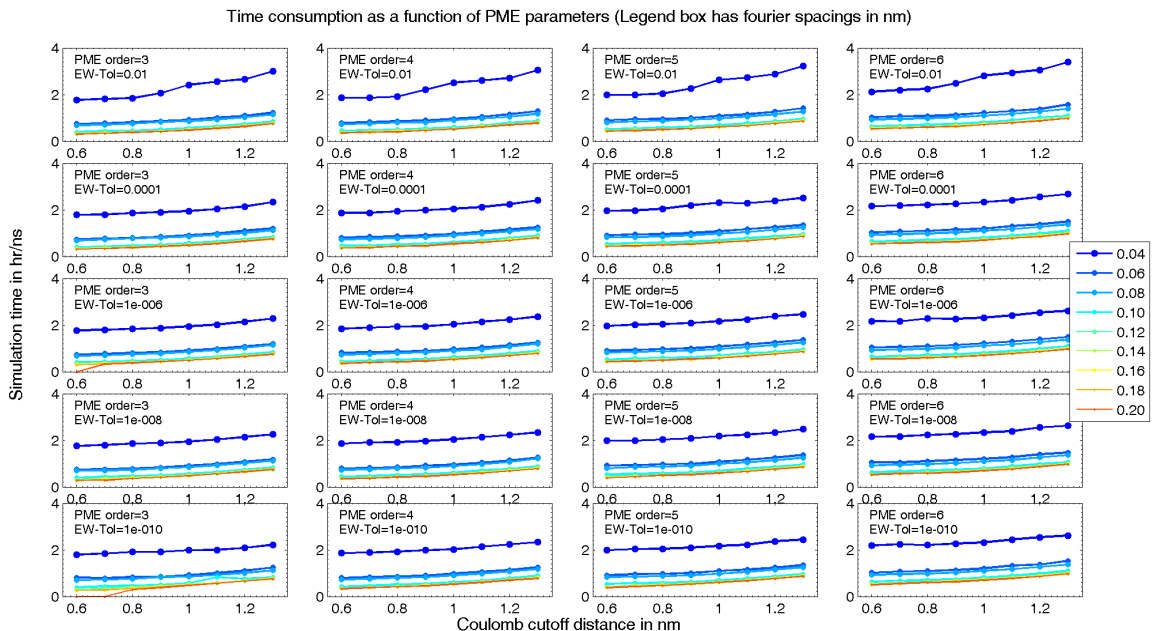


Figure 3.4: Simulation speed for methane solvation as a function of different PME parameters, Coulomb cutoff (x-axis of each graph), Fourier spacing (color), PME order (graphs arranged left to right), and Ewald tolerance (graphs arranged top to bottom). Simulation speed is unaffected by the change in the order of interpolation and Ewald tolerance for high Fourier spacings but it increases with decreasing Fourier spacing and increasing Coulomb cut-off.

Of the three quantities, $\Delta\Delta G$, $\Delta\Delta H$ and ΔH_{vap} , we use only $\Delta\Delta G$ and ΔH_{vap} in our parameter search. The errors $\delta(\Delta\Delta H)$ are larger than the errors $\delta(\Delta\Delta G)$ and $\delta(\Delta H_{vap})$ by more than two orders of magnitude, and thus are not nearly as useful in detecting small changes due to parameterizations. We note that the predictions of $\Delta H_E - \Delta H_O$ are statistically indistinguishable from the validated direct calculations for even the starting benchmark parameters, as can be seen in Tables S1–S3 in the appendix. But since the uncertainties in ΔH are of the order 1-100 kJ/mol, and the uncertainties $\delta(\Delta\Delta H)$ themselves are of the order 1-70 kJ/mol, it is impossible to optimize the fine details of the simulation parameters when including this value in the criteria. This difference in the amount of uncertainty

for these observables is a consequence of enthalpies and entropies being statistically much harder to compute than free energies of the same processes.

The computational speed in ns/hours is plotted as a function of the four PME parameters in Figures 3.4, 3.6 and 3.8 for methane solvation, dipole inversion and anthracene solvation respectively. Several patterns in the computational time required as a function of parameters can be noted. First, the computation time required is essentially independent of *etol*. The computational time increases with increasing order of interpolation for large Fourier spacings 0.12–0.2 nm, but smaller Fourier spacings show no change in computational expense with respect to change in order of interpolation. However, with decreasing Fourier spacing and increasing Coulomb cutoff the computational expense increases significantly. Speed of simulation was essentially identical for all three molecules, as it is determined primarily by the system size in number of atoms, which was roughly equal. Since we can easily determine the difference in thermodynamic properties from the converged estimates as well as computational speed as a function of the four PME parameters, we can easily find which set of parameters reach yield a given error $\Delta\Delta G$, $\Delta\Delta H$ and ΔH_{vap} in the least amount of computational time.

Although the proper choice of parameters depends on the degree of accuracy desired for an application, we propose optimized parameters for which deviations in equilibrium observables satisfy the criteria described in the methods section in minimum time. Using the first criteria, a parameter set i is statistically indistinguishable from the expensive parameter set if $\Delta\Delta G_{Ei} \leq \delta(\Delta G_E)$. $\delta(\Delta G_E)$ is 0.07 kJ/mol for methane solvation, 0.16 kJ/mol for dipole inversion, and 0.13 kJ/mol for anthracene solvation. $\delta(H_{vap,E})$ is 0.002 kJ/mol. Over the collection of all parameter sets i which have $\Delta\Delta G_{Ei}$ less than corresponding $\delta(\Delta G_E)$, the fastest results can be achieved with order of interpolation 4, relative Ewald tolerance 10^{-4} , Fourier spacing 0.12 nm, and Coulomb cutoff 0.9 nm for all three

benchmark systems.

Coulomb cutoffs larger than 0.9 nm or Fourier spacings smaller than 0.12 nm give statistically indistinguishable results from for standard free energy calculations, i.e., within 0.05 kJ/mol for methane solvation and within 0.1 kJ/mol for dipole inversion and anthracene solvation. There are no significant gains in accuracy if we increase Coulomb cutoff or decrease Fourier spacing beyond this point. However, the predicted $\Delta\Delta G_{Ei}$ increases by an order of magnitude when r_{coul} is decreased to 0.8 nm, or for any Fourier spacing larger than 0.12 nm, so we cannot improve the efficiency of the simulation using those parameters without drastically worsening the results.

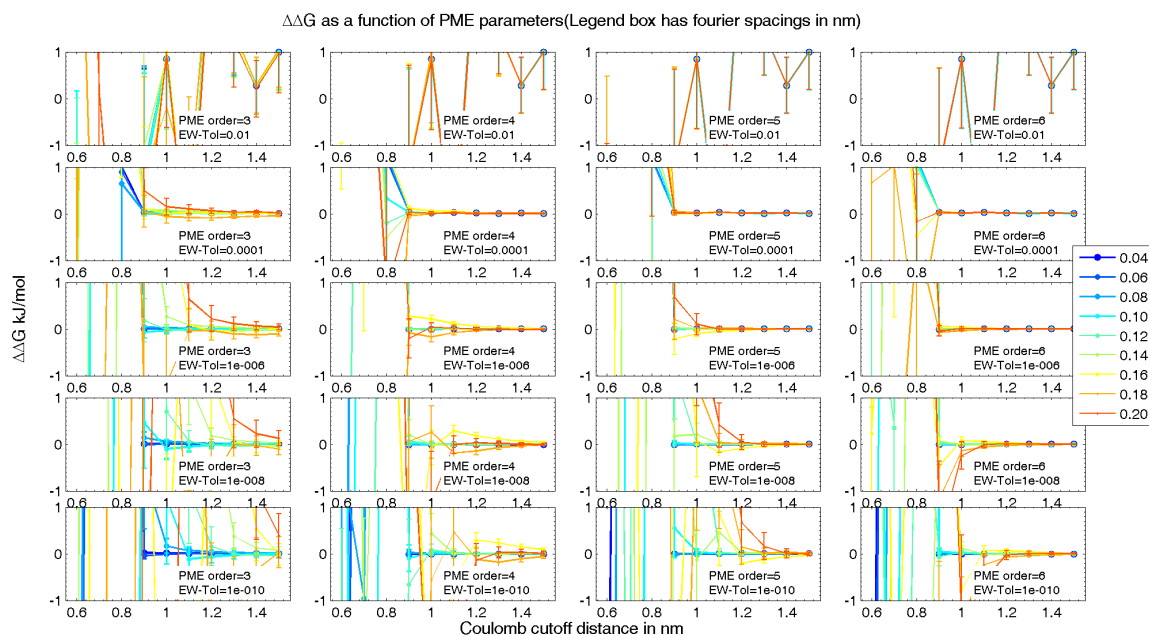


Figure 3.5: $\Delta\Delta G_{Ei}$ for dipole inversion between converged PME parameters and a choice of the four PME parameters Coulomb cutoff (x-axis of each graph), Fourier spacing (color), PME order (graphs arranged left to right), and Ewald tolerance (graphs arranged top to bottom).

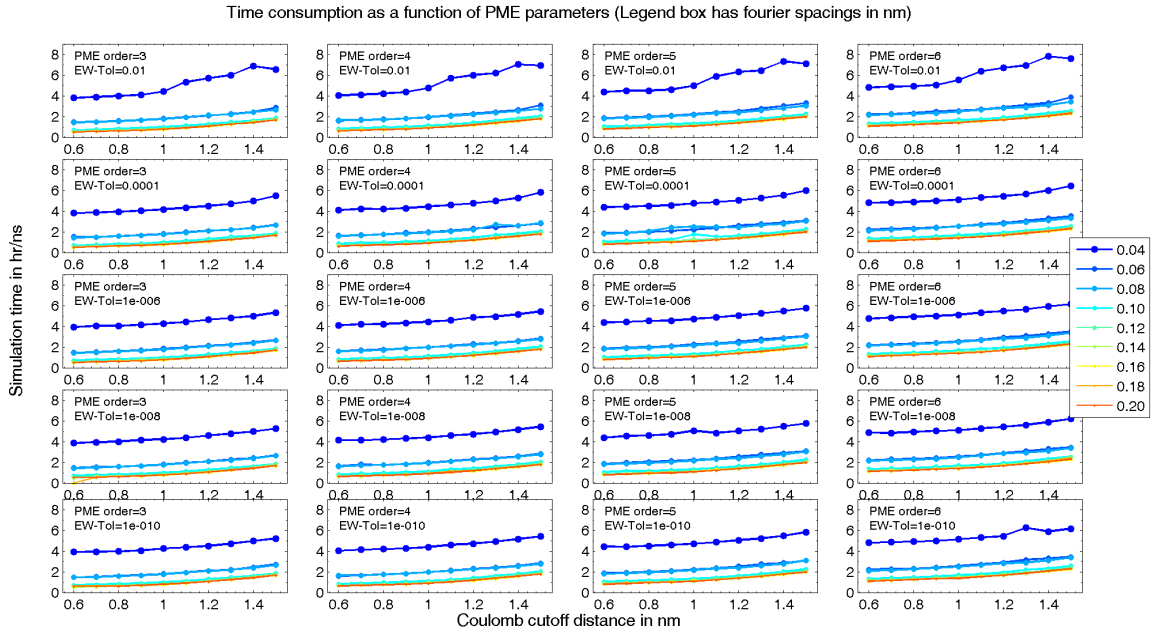


Figure 3.6: Simulation speed for dipole inversion as a function of different PME parameters, Coulomb cutoff (x-axis of each graph), Fourier spacing (color), PME order (graphs arranged left to right), and Ewald tolerance (graphs arranged top to bottom).

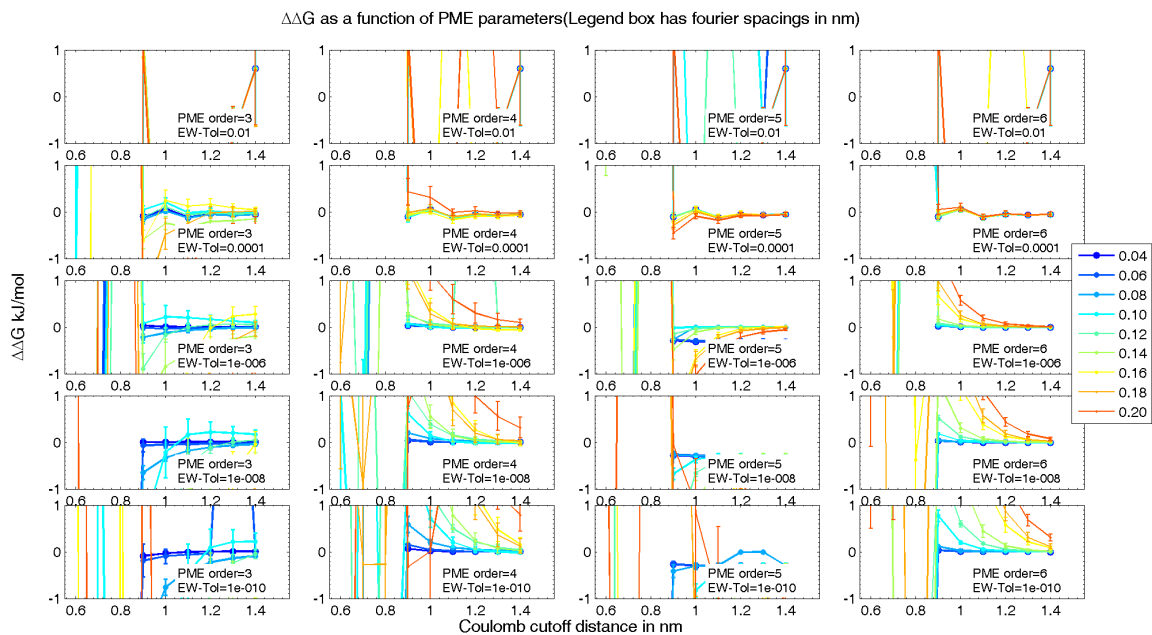


Figure 3.7: $\Delta\Delta G_{Ei}$ for anthracene solvation between converged PME parameters and a choice of the four PME parameters Coulomb cutoff (x-axis of each graph), Fourier spacing (color), PME order (graphs arranged left to right), and Ewald tolerance (graphs arranged top to bottom).

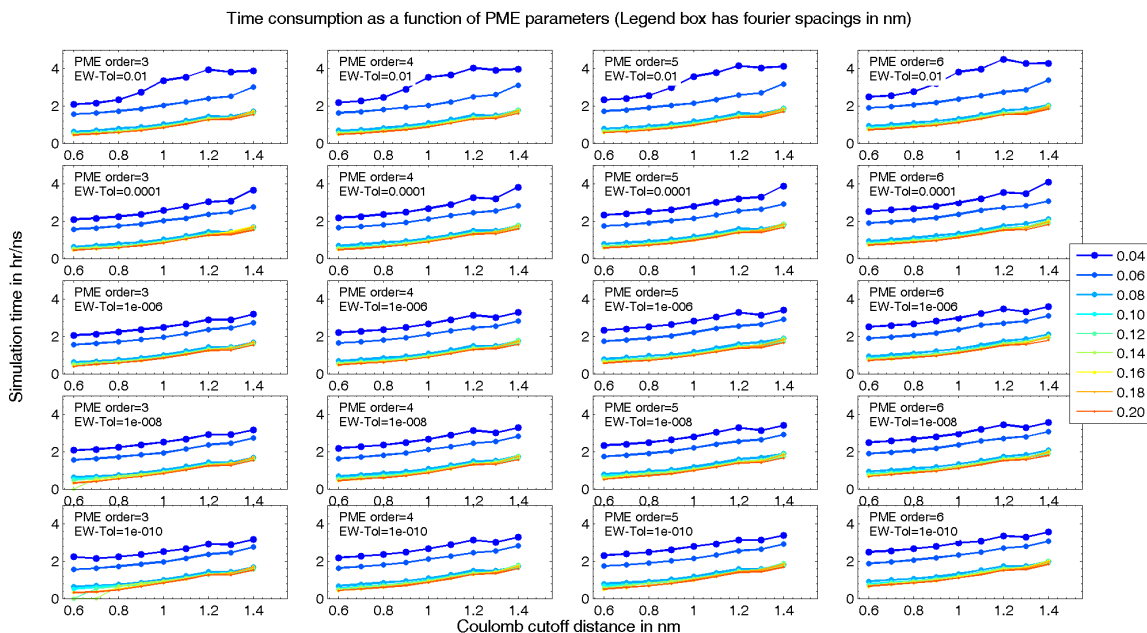


Figure 3.8: Simulation speed for anthracene solvation as a function of different PME parameters, Coulomb cutoff (x-axis of each graph), Fourier spacing (color), PME order (graphs arranged left to right), and Ewald tolerance (graphs arranged top to bottom).

3.3.2 Optimized Coulomb switch

In Figure 3.9 we plot $\Delta\Delta G_{Ei}$ for methane solvation and ΔH_{vap} for TIP3P water for different Coulomb switching distances. Figure 3.12 shows $\Delta\Delta G_{Ei}$ for dipole inversion and anthracene solvation for different Coulomb switching distances. ΔH_{vap} for switching starting points beyond 0.85 nm (for a Coulomb cutoff of 0.9 nm) converge to the switchless values and are within one or two standard deviations of each other. The difference $\Delta\Delta G$ is also within one or two standard deviations for switching distances less than 0.1 nm. $\Delta\Delta G$ for methane solvation and dipole inversion are lower than the first error criteria $\delta(\Delta G_E)$ for all three molecules. ΔH_{vap} is also less than or equal to 0.002 kJ/mol for all Coulomb switches starting at any further than 0.84 nm.

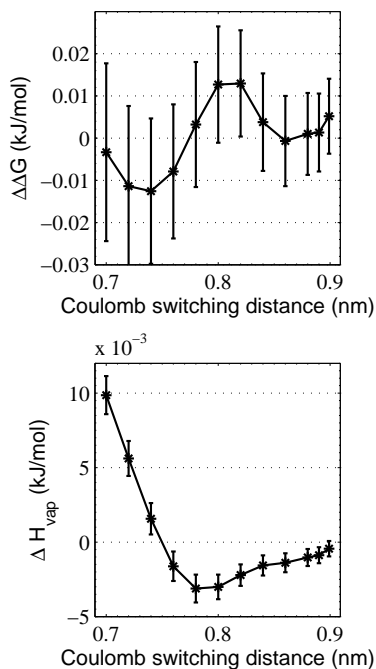


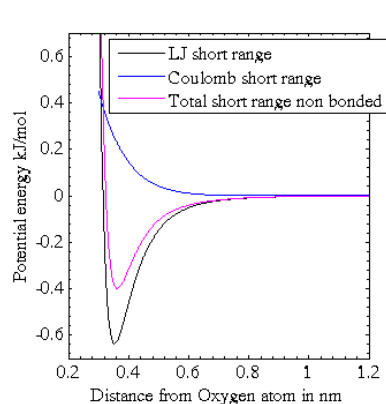
Figure 3.9: $\Delta\Delta G_{Ei}$ for methane solvation and ΔH_{vap} for TIP3P water between reference expensive PME parameters and the value of Coulomb switch width for a optimized Coulomb cutoff of 0.9 nm. Coulomb switch widths of less than 0.1 nm at this cutoff distance and optimized PME parameters are statistically indistinguishable from the reference PME potential. Error bars are one standard deviation.

We should also consider the effect of a switch on the force near the cutoff due to short switching regions. Figure 3.10 shows how the short range nonbonded potentials go to zero at cutoff of 0.9 nm with different choice of switches. A very short switch between 0.899 and 0.9 nm clearly will cause the least distortion of the potential energy. However, the force spiking becomes larger, as seen in Figure 3.11a. We need a rational criterion to decide how large a force spike from a single nonbonded interaction is acceptable. For example, the force for passing through the shift region should not be greater than the force experienced due to a thermal collision. The force F experienced by an atom, with three

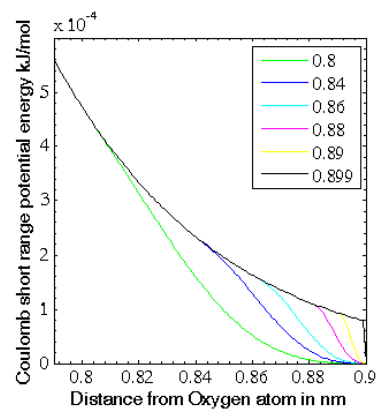
degrees of freedom, during a collision can be estimated by dividing the energy imparted during a collision at temperature T , which equals $\frac{3}{2}k_B T$, where k_B is Boltzmann constant, by a characteristic length, which we choose as the Lennard-Jones radius of oxygen σ_O .

$$F = \frac{3k_B T}{2\sigma_O} \approx 12 \text{ kJ/mol/nm} \quad (3.24)$$

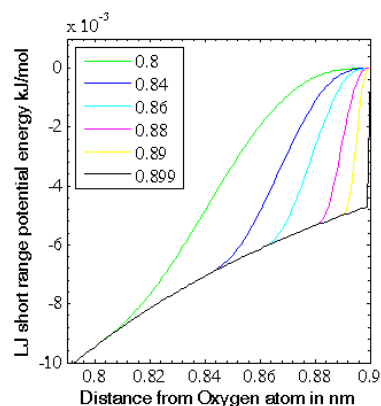
We note that the force spiking calculated here is due to a single nonbonded interaction pair, and that particles will experience forces in all directions. If the solvent is homogeneous, then these radial forces will cancel out on average, so this 12 kJ/mol/nm value might be an overestimate, but serves as a useful baseline motivated by physical criteria.



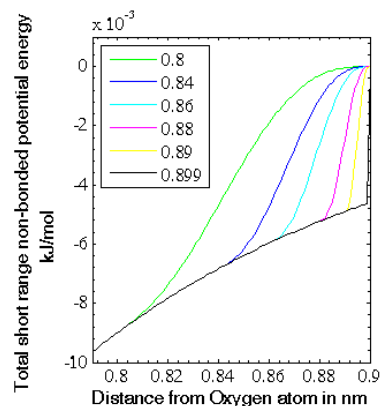
(a) Short range P.E.



(b) Coulomb short range P.E. at cutoff

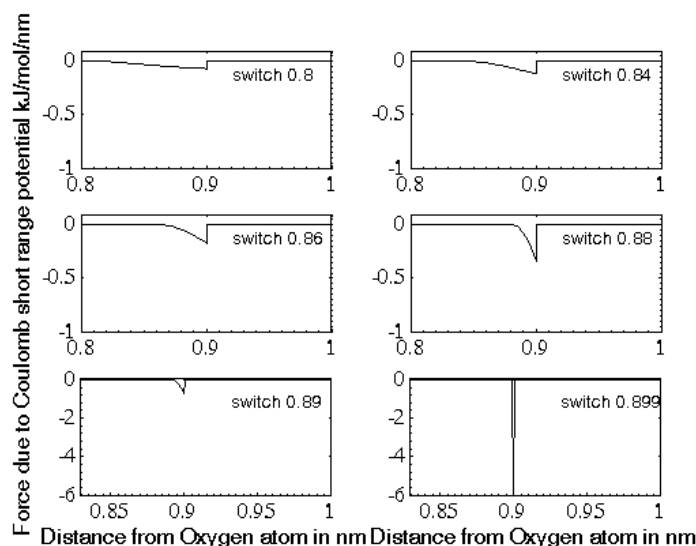


(c) LJ short range P.E. at cutoff

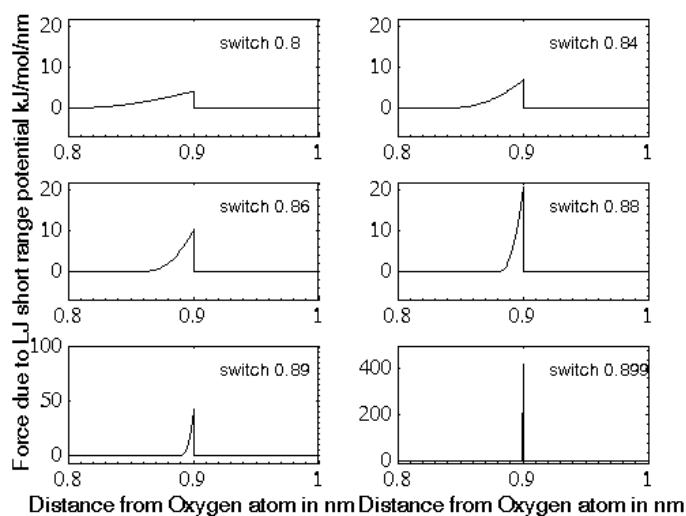


(d) Total (Coulomb + LJ) short range
P.E. at cutoff

Figure 3.10: Short range potential energies at Coulomb and LJ cutoff of 0.9 nm using different switching distances and an Ewald tolerance of 10^{-4} .



(a) Force spikes at cutoff due to Coulomb potential switch



(b) Force spikes at cutoff due to LJ potential switch

Figure 3.11: Force spikes at Coulomb and LJ cutoff of 0.9nm using different switching distances and an Ewald Tolerance of 10^{-4} .

We see in Figure 3.11a that the force spike for all examined Coulomb switches are below 12 kJ/mol/nm; indeed, for any switch width larger than 0.01 nm, the magnitude of any force spike is an order of magnitude below this level. The $\Delta\Delta G$ versus Coulomb

switch plots for dipole inversion and anthracene solvation (Figure 3.12) also show that the $\Delta\Delta G$ for switches between 0.8 and 0.89 are within one to two standard deviations of each other. We therefore choose our optimized Coulomb switch as 0.85 nm, midway between 0.8 and 0.89 nm to balance the effect of force spikes and loss of electrostatic energy, though any switch in that range is statistically identical in thermodynamic properties to free energy calculations carried out without a switch.

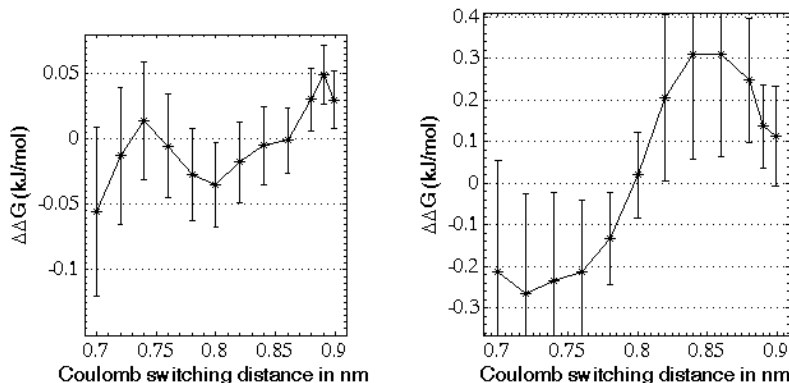


Figure 3.12: $\Delta\Delta G_{\text{solv}}$ for dipole inversion (left) and anthracene solvation (right) as a function of different switching distances for a cutoff of 0.9 nm. Note the large y-axis energy scale for anthracene (approximately $6\times$ the dipole scale).

3.3.3 Optimized LJ cutoff and switch

In the last phase of the search, we examine the effect of varying LJ cutoff and LJ switch using our optimized Coulomb parameters to calculate $\Delta\Delta G$ for all three transformations in the benchmark set and ΔH_{vap} for TIP3P water. As noted above, the initial benchmark parameter choices already satisfy the first criteria. We thus see if we can now obtain the second more stringent criteria, pushing the difference due to deviations in the parameters from converged results below the uncertainty in this calculation of $\Delta\Delta G_{Ei}$ itself, which is 0.01 kJ/mol for methane solvation, 0.02 kJ/mol for dipole inversion, 0.015 kJ/mol for

anthracene solvation, and 0.001 kJ/mol for the enthalpy of vaporization (from Tables 3.2 to 3.5). Figure 3.13 shows $\Delta\Delta G$ for methane solvation, dipole inversion and anthracene solvation as a function of different LJ cutoffs and LJ switches. Figure 3.14 shows ΔH_{vap} for TIP3P water as a function of different LJ cutoffs and LJ switches.

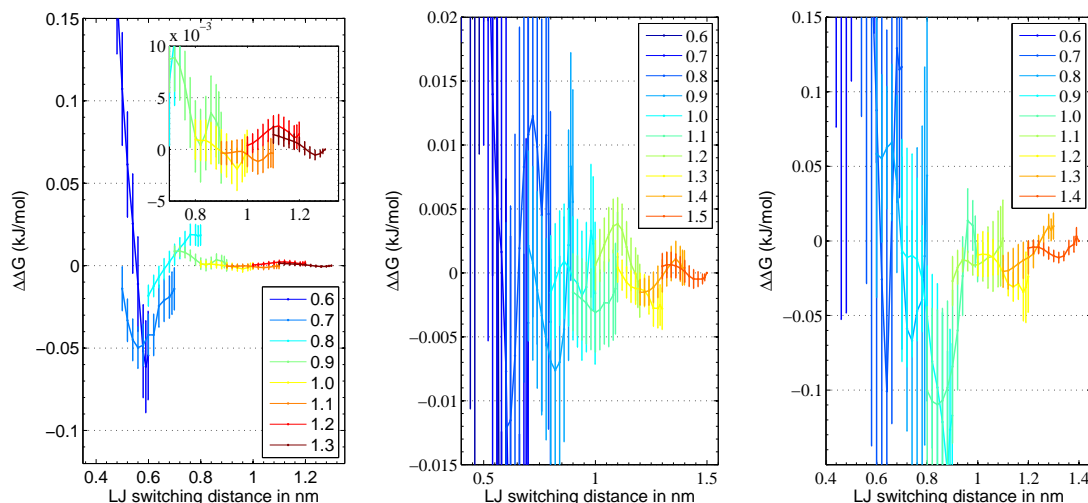


Figure 3.13: $\Delta\Delta G_{\text{solv}}$ for methane solvation (left), dipole inversion (center) and anthracene solvation (right) as a function of different Lennard-Jones switching distances for Lennard-Jones cutoffs in increments of 0.1 nm from 0.6 to the maximum allowed by the box. Each color represents a different cutoff distance, each and line within the color represents the value at a different switching distance, including statistical uncertainty. Note differences in y-axis energy scale, with the dipole inversion scale being approximately $10\times$ smaller than the other two. The inset for methane solvation demonstrates how $\Delta\Delta G$ converges to essentially zero at the largest Lennard-Jones cutoff of 1.3 nm, and below 0.007 kJ/mol for cutoffs of 0.9 nm or greater for any switch width.

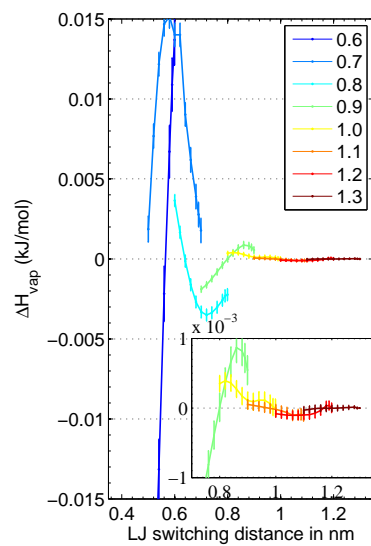


Figure 3.14: ΔH_{vap} for TIP3P water as a function of different Lennard-Jones switching distances for Lennard-Jones cutoffs 0.6–1.3 nm. ΔH_{vap} at and beyond 0.9 nm Lennard-Jones cutoff is less than 0.005 kJ/mol for any switch distance

	Prediction	Validation using			
		One parameter set	Two parameter sets simultaneously		
sampled at \rightarrow	B	B or E or O	B and E	B and O	E and O
ΔG (kJ/mol) for methane solvation					
Benchmark (B)	8.619 \pm 0.069	8.619 \pm 0.069	8.701 \pm 0.049	8.668 \pm 0.049	N/A
Expensive (E)	8.687 \pm 0.071	8.868 \pm 0.069	8.811 \pm 0.049	N/A	8.851 \pm 0.049
Optimized (O)	8.675 \pm 0.072	8.863 \pm 0.069	N/A	8.764 \pm 0.049	8.857 \pm 0.049
$\Delta\Delta G$ (kJ/mol) for methane solvation					
$\Delta G_B - \Delta G_E$	-0.068 \pm 0.019	-0.249 \pm 0.098	-0.109 \pm 0.012	N/A	N/A
$\Delta G_B - \Delta G_O$	-0.057 \pm 0.022	-0.244 \pm 0.098	N/A	-0.096 \pm 0.013	N/A
$\Delta G_E - \Delta G_O$	0.011 \pm 0.011	0.005 \pm 0.098	N/A	N/A	-0.006 \pm 0.006

Table 3.2: Predictions and validation $\Delta\Delta G_{EO}$ results for methane solvation match within one and two standard deviations. In column two ΔG and $\Delta\Delta G$ are estimated using samples from benchmark parameter set and re-evaluations done at expensive and optimized parameter sets. In column three we use samples from only one parameter set: either only the benchmark parameter set (B) or only the expensive (E) or only the optimized (O) parameter set. For columns 4-6 we use samples from a pair of parameter sets. Re-evaluation is not done for the remaining parameter sets, so we have no estimate for the unsampled parameter set (labeled as N/A).

	Prediction	Validation using			
		One parameter set	Two parameter sets simultaneously		
sampled at \rightarrow	B	B or E or O	B and E	B and O	E and O
H_{vap} kJ/mol for TIP3P water					
Benchmark (B)	42.402 \pm 0.002	42.402 \pm 0.002	42.398 \pm 0.001	42.401 \pm 0.001	N/A
Expensive (E)	42.408 \pm 0.002	42.404 \pm 0.002	42.403 \pm 0.001	N/A	42.406 \pm 0.001
Optimized (O)	42.410 \pm 0.002	42.412 \pm 0.002	N/A	42.409 \pm 0.001	42.407 \pm 0.001
ΔH_{vap} kJ/mol for TIP3P water					
$H_{vap\ B} - H_{vap\ E}$	-0.006 \pm 0.001	-0.002 \pm 0.003	-0.005 \pm 0.001	N/A	N/A
$H_{vap\ B} - H_{vap\ O}$	-0.008 \pm 0.001	-0.010 \pm 0.003	N/A	-0.008 \pm 0.001	N/A
$H_{vap\ E} - H_{vap\ O}$	-0.002 \pm 0.001	-0.008 \pm 0.003	N/A	N/A	-0.001 \pm 0.000

Table 3.3: Predictions and validation ΔH_{vap} results match for all the three parameter sets within two standard deviations.

	Prediction	Validation using			
		One parameter set	Two parameter sets simultaneously		
sampled at \rightarrow	B	B or E or O	B and E	B and O	E and O
ΔG (kJ/mol) for complete dipole inversion +e/-e to -e/+e					
Benchmark (B)	-0.079 \pm 0.157	-0.079 \pm 0.157	-0.019 \pm 0.111	0.003 \pm 0.112	N/A
Expensive (E)	-0.120 \pm 0.160	-0.056 \pm 0.158	-0.021 \pm 0.112	N/A	0.030 \pm 0.111
Optimized (O)	-0.092 \pm 0.162	0.088 \pm 0.157	N/A	0.008 \pm 0.112	0.021 \pm 0.111
$\Delta\Delta G$ (kJ/mol) for complete dipole inversion +e/-e to -e/+e					
$\Delta G_B - \Delta G_E$	0.040 \pm 0.035	-0.023 \pm 0.223	0.002 \pm 0.021	N/A	N/A
$\Delta G_B - \Delta G_O$	0.013 \pm 0.041	-0.167 \pm 0.222	N/A	-0.005 \pm 0.023	N/A
$\Delta G_E - \Delta G_O$	-0.028 \pm 0.021	-0.144 \pm 0.223	N/A	N/A	0.009 \pm 0.010
ΔG (kJ/mol) for first half of dipole inversion transformation, discharging the dipole +e/-e to 0e/0e					
Benchmark (B)	93.241 \pm 0.108	93.241 \pm 0.108	93.259 \pm 0.077	93.282 \pm 0.078	N/A
Expensive (E)	93.400 \pm 0.112	93.442 \pm 0.109	93.433 \pm 0.077	N/A	93.483 \pm 0.077
Optimized (O)	93.352 \pm 0.114	93.464 \pm 0.110	N/A	93.393 \pm 0.078	93.418 \pm 0.077
$\Delta\Delta G$ (kJ/mol) for first half of dipole inversion transformation, discharging the dipole +e/-e to 0e/0e					
$\Delta G_B - \Delta G_E$	-0.159 \pm 0.030	-0.201 \pm 0.153	-0.175 \pm 0.018	N/A	N/A
$\Delta G_B - \Delta G_O$	-0.110 \pm 0.035	-0.223 \pm 0.154	N/A	-0.112 \pm 0.020	N/A
$\Delta G_E - \Delta G_O$	0.048 \pm 0.018	-0.022 \pm 0.155	N/A	N/A	0.066 \pm 0.009
ΔG (kJ/mol) for second half of dipole inversion transformation, charging the dipole 0e/0e to -e/+e					
Benchmark (B)	-93.320 \pm 0.109	-93.320 \pm 0.109	-93.277 \pm 0.078	-93.278 \pm 0.077	N/A
Expensive (E)	-93.520 \pm 0.113	-93.498 \pm 0.110	-93.454 \pm 0.078	N/A	-93.453 \pm 0.077
Optimized (O)	-93.444 \pm 0.114	-93.375 \pm 0.109	N/A	-93.385 \pm 0.077	-93.397 \pm 0.077
$\Delta\Delta G$ for second half of dipole inversion transformation, charging the dipole 0e/0e to -e/+e					
$\Delta G_B - \Delta G_E$	0.199 \pm 0.031	0.178 \pm 0.155	0.177 \pm 0.018	N/A	N/A
$\Delta G_B - \Delta G_O$	0.123 \pm 0.036	0.055 \pm 0.154	N/A	0.106 \pm 0.020	N/A
$\Delta G_E - \Delta G_O$	-0.076 \pm 0.018	-0.123 \pm 0.155	N/A	N/A	-0.057 \pm 0.009

Table 3.4: Predictions and validation $\Delta\Delta G_{EO}$ results for discharging, charging and complete dipole inversion also match within one and two standard deviations.

	Prediction	Validation using			
		One parameter set	Two parameter sets simultaneously		
sampled at \rightarrow	B	B or E or O	B and E	B and O	E and O
ΔG (kJ/mol) for anthracene solvation					
Benchmark (B)	-9.624 \pm 0.121	-9.624 \pm 0.121	-9.853 \pm 0.086	-9.823 \pm 0.086	N/A
Expensive (E)	-9.023 \pm 0.125	-9.261 \pm 0.123	-9.267 \pm 0.087	N/A	-9.267 \pm 0.086
Optimized (O)	-8.996 \pm 0.125	-9.205 \pm 0.121	N/A	-9.214 \pm 0.086	-9.237 \pm 0.086
$\Delta\Delta G$ (kJ/mol) for anthracene solvation					
$\Delta G_B - \Delta G_E$	-0.602 \pm 0.029	-0.363 \pm 0.173	-0.585 \pm 0.017	N/A	N/A
$\Delta G_B - \Delta G_O$	-0.628 \pm 0.031	-0.419 \pm 0.171	N/A	-0.609 \pm 0.018	N/A
$\Delta G_E - \Delta G_O$	-0.027 \pm 0.014	-0.056 \pm 0.173	N/A	N/A	-0.030 \pm 0.007

Table 3.5: Predictions and validation results for anthracene solvation match within one and two standard deviation for $\Delta\Delta G_{EO}$. The predictions that ΔG for expensive and optimized parameter sets are greater than ΔG for benchmark parameter set is correct.

In all cases we see that $\Delta\Delta G$ and ΔH_{vap} approaches zero as the LJ cutoff is increased from 0.8 nm. Methane solvation and dipole inversion approach the stricter condition of indistinguishability of parameters at a LJ cutoff of 0.9 nm and switch starting from 0.84 nm, when $\Delta\Delta G$ is equal to or less than 0.01 kJ/mol. $\Delta\Delta G$ for anthracene solvation does not quite reach this level of accuracy until reaching a LJ cutoff of 1.0 nm; at 0.9 nm cutoff $\Delta\Delta G$ anthracene solvation is closer to 0.03 kJ/mol. The predicted $\Delta\Delta G$ for methane solvation and dipole inversion are nearly equal to the error and for anthracene solvation $\Delta\Delta G$ is within twice the error $\delta(\Delta\Delta G_{Ei})$ if we use the optimized parameter set.

For most cases, an error of 0.03 kJ/mol in a few larger molecules and thus a 0.9 nm cutoff might be sufficient. However, we can perform a limited search in the parameter space around this initially optimized parameter set to see if even higher accuracies can be achieved. We discuss this final optimization in the validation section.

$\Delta\Delta G$ and ΔH_{vap} for entire range of LJ switches are all within one and two standard deviations of the unswitched values.

In Figure 3.10c we see that a long LJ switch, 0.7 to 0.8 nm, distorts the potential and a relatively small switch like 0.899 nm will result in large force spikes at the cutoff. Unlike the Coulomb switch, the force spike due to the LJ switch is greater than the 12 kJ/mol/nm mark for switching regions narrower than 0.04 nm, as the magnitude of the potential is larger in the switching region for the Lennard-Jones potential. We therefore select 0.05 nm for the switching width. We note particularly that the free energy and enthalpy results are essentially statistically independent for any value switch distance between 0.1 and 0.001 nm for appropriate cutoff values.

3.3.4 Validation of the optimization procedure

To validate our search process, we must actually perform the simulations at the new parameter values to see if the free energy and enthalpy differences between the optimized parameters and the fully converged reference parameters were correctly predicted. We therefore compare results from our optimized parameter set with results from simulations performed at expensive, converged Coulomb and LJ parameters. We directly validate all stages of optimization in a single comparison, as we only need to validate the individual stages if the final results are incorrect. Validation simulations were performed with GROMACS 4.6.1, which gave identical energies to the bug-fixed GROMACS 4.5.3 but was better optimized. Simulations were run using velocity Verlet with a time step of 2 fs and SETTLE constraints for water [67], with SHAKE/RATTLE [68] with relative tolerance 10^{-12} used to constrain non-water molecules. Temperature and pressure control were obtained using the algorithm of Martyna et al. [69], with $\tau_t = 5.0$ ps at 300 K, and $\tau_p = 5.0$ ps at 1 atm.

The optimized and reference parameters are summarized in the Table 3.6. We find that

to perform the actual simulations at the expensive parameters, rather than just reevaluating the energies of the configurations, we find we needed to make slight modifications. When the LJ and Coulomb cutoffs used are very near to the twice the box length, the estimated free energies are inconsistent, especially for anthracene solvation. This appears to be an artifact of the improper potential energy contribution of periodic images at the box boundaries under box size fluctuations. We therefore chose the “expensive” nonbonded cutoffs to be 0.1 nm less than the most expensive cutoffs, which was determined to have a negligible effect on potential energies of representative configurations. Similarly, a Fourier spacing of 0.06 nm is used instead of 0.04 nm to accelerate the otherwise very slow reference parameter set simulations. The predicted $\Delta\Delta G$ between expensive parameter set used in validation simulations and most expensive parameter set use in reweighting is $4 \times 10^{-5} \pm 5 \times 10^{-5}$ kJ/mol, and thus this approximation is acceptable to any reasonable limit.

Set → Parameter ↓	Benchmark	Expensive		Optimized
		optimization	validation	
Order of interpolation	4	6	6	4
Ewald tolerance	10^{-8}	10^{-10}	10^{-10}	10^{-4} or 10^{-5}
Fourier spacing (nm)	0.12	0.04	0.06	0.12
Coulomb cutoff (nm)	0.9	1.3^a	1.2^a	0.9 or 1.0
		1.5^b	1.4^b	
		1.4^c	1.3^c	
Coulomb switch (nm)	0.88	1.299^a	1.15^a	0.85 or 0.95
		1.499^b	1.35^b	
		1.399^c	1.25^c	
LJ cutoff (nm)	0.9	1.3^a	1.2^a	0.9 or 1.0
		1.5^b	1.4^b	
		1.4^c	1.3^c	
LJ switch (nm)	0.8	1.299^a	1.15^a	0.85 or 0.95
		1.499^b	1.35^b	
		1.399^c	1.25^c	

Parameters marked with a , b , c are parameters for methane solvation, dipole inversion and anthracene solvation respectively, otherwise the parameters are common to all three molecular sets. `rlist` is always 0.2 nm greater than the largest of the two nonbonded cutoff, which is a change from the benchmark. All validations are done for the first optimized parameter set.

Table 3.6: Benchmark, expensive and optimized parameters.

There are two types of computations we can perform to validate these predictions. The

simplest is to use the samples from a simulation corresponding to just one parameter set in our calculations of differences in thermodynamic variables, and compute properties from this simulation alone. In this case, we use sampled energies from simulations performed using the optimized parameter set, a $[K \times K \times N_k]$ matrix of energy differences $\mathbf{U}_O(\mathbf{X}_O)$ to obtain free energy estimates for the optimized parameter set ΔG_O . Similarly, we can use samples from simulation performed using the expensive parameter set, the $[K \times K \times N_k]$ energies $\mathbf{U}_E(\mathbf{X}_E)$, to obtain free energy estimates for the expensive parameter set ΔG_E , and then compute the difference $\Delta\Delta G_{EO} = \Delta G_E - \Delta G_O$. We can easily get the differences in the free energy estimates $\Delta\Delta G$ for other pairs of parameter sets in the same way. The error estimates of $\Delta\Delta G$ will be the square root of the sum of square of errors in individual ΔG being compared, since the two ΔG belong to completely different simulations whose data is uncorrelated. The third column of Tables 3.2-3.5 show $\Delta\Delta G$ calculated using samples corresponding to just one parameter set.

However, it is clear that this standard process for calculating differences in average quantities does not allow us to differentiate very well between the results generated with similar sets of parameters, as the statistical noise is simply too high. We would generally have to run tens of times longer to sufficiently converge our statistics. The much more powerful and statistically efficient way to calculate $\Delta\Delta G$ is by using samples from *both* parameter sets being compared to compute the differences in observables using multistate reweighting.

To compare the expensive and optimized parameter sets, we consider the $[2K \times 2K \times N_k]$ matrix of energy differences $U = [\mathbf{U}_E(\mathbf{X}_E), \mathbf{U}_E(\mathbf{X}_O); \mathbf{U}_O(\mathbf{X}_E), \mathbf{U}_O(\mathbf{X}_O)]$, and use multistate reweighting via MBAR. Now, using data generated using both parameter sets $\mathbf{U}_E(\mathbf{X}_E)$ and $\mathbf{U}_O(\mathbf{X}_O)$, including reevaluation of samples from each parameter set at the other parameter set, $\mathbf{U}_E(\mathbf{X}_O)$ and $\mathbf{U}_O(\mathbf{X}_E)$ we can compute $(\Delta G_E - \Delta G_O) \pm \delta(\Delta G_E -$

ΔG_O), and compare to the estimate of $(\Delta G_E - \Delta G_O) \pm \delta(\Delta G_E - \Delta G_O)$ using data from only the benchmark state obtained during the optimization process. The reevaluation required for this process takes negligible simulation time, since we reprocess only uncorrelated samples. We repeat the same process for the other pairs of simulation data, and show the results in Tables 3.2 to 3.5.

In the course of this study, we found that the simulations in the original benchmark study [3] used a value of `rlist` that truncated the total potential, though did not affect the findings of that study which examined variances. The benchmark free energy estimates for methane solvation, dipole inversion and anthracene solvation differ from the results of our previous study because in this study the benchmark parameter set has a different `rlist`. To be consistent with high precision free energy calculations, we started our search process by performing new calculations with the benchmark study parameters, except using an `rlist` 0.2 nm longer than the longest cutoff. Because free energies are unaffected by any `rlist` greater than this value, we did not include this parameter in our optimization routine. Longer `rlists` have some effect on the total time in GROMACS, and the obvious choice is thus the shortest value of `rlist` that leaves the potential energies and thus free energies unchanged.

We also found that for anthracene, equipartitioning of kinetic energies between solvent and ligand was broken at low coupling of the ligand to the bulk solvent if a global thermostat was used, disrupting both the energy distribution and volume distribution as validated by the *checkensemble* tool [5]. This deviation changed the free energy differences by approximately -3 kJ/mol. To obtain proper equipartitioning we used separate thermostats for the solute and the solvent for anthracene solvation simulations only. No error appeared in the methane solvation case, perhaps because of the much smaller size of the UA methane. Such a problem did not occur in the case of the dipole because all states remain coupled to

the solvent.

For the validation simulations, to match the amount of sampling in this original benchmark study, we performed 10 ns simulations (9 ns postequilibration) at each of the K intermediate states for the expensive and the optimized parameter sets. Each simulation yielded 9000 samples, taking samples every 1 ps. We further subsampled the data using the calculated autocorrelation times of $dH/d\lambda$.

The comparisons to results using samples from two parameter sets at a time are shown in columns 4 (benchmark, expensive), 5 (benchmark, optimized) and 6 (expensive, optimized) in Tables 3.2 to 3.5. For methane solvation in Table 3.2, dipole inversion in Table 3.4, and anthracene solvation in Table 3.5, the predicted $\Delta G_E - \Delta G_O$ in column two agree within one to two standard deviations with the estimates calculating with samples generated using expensive and optimized parameter sets in column 6. We can see that we get remarkably high agreement between predictions of ΔG_{EO} using samples only from the benchmark parameter set and results from simulations actually run with optimized and expensive parameter sets. The statistical convergence is also good, as $\delta(\Delta G_E - \Delta G_O)$ is very low i.e. approximately 0.01 kJ/mol, far closer than would ever be required for molecular simulations, as experimental results for condensed phase data are not that accurate.

Interestingly, even though the sampling at the benchmark state is quite not good enough to predict free energies at these particular alternate (i.e. expensive and optimized) states, it is remarkably able enough to predict *differences* in free energies between these alternate states with dramatically low bias and uncertainty. For methane solvation in Table 3.2 the predicted ΔG_E and ΔG_O by reweighting samples from the benchmark parameter set are 8.687 ± 0.071 kJ/mol and 8.675 ± 0.072 kJ/mol respectively. ΔG_E evaluated using samples generated using the expensive parameter set alone is 8.868 ± 0.069 kJ/mol and ΔG_O evaluated using samples generated using the optimized parameter set alone is 8.863 ± 0.069

kJ/mol. The difference between the predicted and actual ΔG_E is 0.181 ± 0.099 kJ/mol and the difference between the predicted and actual ΔG_O is 0.188 ± 0.099 kJ/mol, at the edge of statistical error. However, the predicted $\Delta G_E - \Delta G_O$, 0.011 ± 0.011 kJ/mol, is within a standard deviation of $\Delta G_E - \Delta G_O$ estimated using the direct difference of estimates from the expensive and optimized sets, 0.005 ± 0.098 kJ/mol, though the statistical error is much larger. When $\Delta G_E - \Delta G_O$ when samples from expensive and optimized sets are used simultaneously, the difference is only -0.006 ± 0.006 kJ/mol, within uncertainty of the predicted value 0.011 ± 0.011 kJ/mol. Importantly, using data from *both* parameter sets allows us to push the uncertainty in differences of ΔG 's down an order of magnitude.

Similarly for dipole inversion and anthracene solvation, the predicted $\Delta G_B - \Delta G_E$ and $\Delta G_B - \Delta G_O$ in column 2, evaluated using only samples generated with the benchmark data, agree with the free energy differences evaluated with the data from the pairs of simulation in column 4, 5, and 6 within error. The difference $\Delta G_E - \Delta G_O$ computed with samples from both the expensive and the optimized simulations agree extremely accurately with the predictions made with samples used from only the benchmark simulations.

We next turn to the agreement of the enthalpy of vaporization. We obtain highly accurate estimates obtained for ΔH_{vap} between the expensive and optimized parameter values, with agreement down to 0.0002 kJ/mol (Table 3.3). The fact that magnitude of $\Delta H_{vap,EB}$ is one to two orders of magnitude smaller than $\Delta \Delta G_{EB}$ indicates that small changes in simulation parameters may influence small molecule free energies more than bulk properties, raising caution about the applicability of parameters optimized for bulk properties to free energy calculations. Here again, reweighting is much more precise than calculating direct differences.

Because the full dipole inversion process could lead to cancellation of errors, we also examine the effect of simulation parameters on the free energy of charging and discharging

separately. Therefore, for dipole inversion we have also reported ΔG and $\Delta\Delta G$ for both halves of the transformation. We notice that $\Delta\Delta G_{EO}$ for the first and the second half of the transformation using data from both the expensive and optimized parameter sets, 0.066 ± 0.009 kJ/mol and -0.057 ± 0.009 kJ/mol, are not zero but the errors do cancel out for the complete dipole inversion. Even in this case, $\Delta\Delta G_{EO}$ for both the first and the second halves satisfy the first criteria of indistinguishability i.e. $\Delta\Delta G_{Ei} \leq \delta(\Delta G_E)$. The $\Delta\Delta G_{EO}$ for the first and the second halves of the dipole inversion do not satisfy the second criteria even at high cutoffs. This could be due to some small artifact of periodic boundary conditions with a total permanent dipole of the system, as small but statistically meaningful difference this does not taper off even when we go out almost to the presumably converged cutoff.

The optimized parameter set also results in good convergence with respect to expensive parameter set. $\Delta\Delta G_{EO}$ for methane solvation and dipole inversion test systems are essentially zero, showing that the optimal parameter set is statistically indistinguishable from the expensive parameter set. For methane solvation $\Delta\Delta G_{EO} = -0.006\pm0.006$ kJ/mol and for dipole inversion $\Delta\Delta G_{EO} = 0.009\pm0.010$ kJ/mol. However for anthracene solvation the predicted value of $\Delta\Delta G_{EO} = -0.027\pm0.014$ kJ/mol. The validated value (in column 6 of Table 3.5) of $\Delta\Delta G_{EO} = -0.030\pm0.007$ kJ/mol using the optimized LJ cutoff of 0.9 nm, which is statistically significant. For most purposes, this small deviation will likely not be relevant, but for complete consistency, slight improvements in these parameters might be necessary.

In our search for optimized PME parameters we used relatively coarse grid spacings for Ewald tolerance, Fourier spacing and the Coulomb cutoff, which already allowed us to come very close to fully converged results. We found that the increasing Coulomb cutoff and decreasing Fourier spacing gave better convergence at the cost of higher computational

expense. However $\Delta\Delta G_{Ei}$ does not change monotonically with Ewald tolerance. For a given Coulomb cutoff and Fourier spacing $\Delta\Delta G_{Ei}$ decreased as Ewald tolerance was increased from 10^{-10} to 10^{-4} and then $\Delta\Delta G_{Ei}$ increased when Ewald tolerance was increased to 10^{-2} , without affecting computational expense. Thus there exists a possibility that slightly improved results could be obtained with $etol = 10^{-5}$ which was not explored in the initial scan.

Perhaps not coincidentally, the GROMACS default parameters determined by the much simpler approach of converging force calculations are Ewald tolerance = 10^{-5} , Coulomb cutoff = LJ cutoff = 1.0 nm, PME order = 4, Fourier spacing = 0.12 nm. These values are close but not exactly the same as our optimized parameters of Ewald tolerance = 10^{-4} , Coulomb cutoff = LJ cutoff = 0.9 nm (with PME order and Fourier spacing the same). We therefore searched the PME parameter space around the our first optimized parameter set, including the GROMACS default parameters among others, to see if we could refine the current optimized parameter set and push the error further down for the test systems. We therefore also tested Ewald tolerance = $[10^{-4}, 10^{-5}]$ and LJ cutoff = Coulomb cutoff = $[0.9, 1.0]$, with PME order = 4, Fourier spacing = 0.12 nm, and switches both of width 0.05 nm.

The results are summarized in the Table 3.8. We found that if we use an Ewald tolerance of 10^{-5} , $rvdw = rcoul = 0.9$ nm, $rvdw-switch$ and $rcoul-switch = 0.85$, predicted $\Delta\Delta G_{Ei}$ for anthracene solvation is reduced from -0.027 ± 0.014 kJ/mol to 0.009 ± 0.007 kJ/mol, predicted $\Delta\Delta G_{Ei}$ for dipole inversion changes from -0.028 ± 0.021 to -0.007 ± 0.012 kJ/mol, $\Delta\Delta G_{Ei}$ for methane solvation changes from 0.011 ± 0.011 to 0.027 ± 0.006 kJ/mol. For all systems $\delta(\Delta\Delta G_{Ei})$ improves by a factor of 2 indicating increased phase space overlap. There was no statistically significant improvement in $\Delta\Delta G_{Ei}$ for methane solvation, full dipole inversion, and anthracene solvation. However, $\Delta\Delta G_{Ei}$

increased with reduced *etol* of 10^{-5} for a cutoff of 0.9 nm, particularly the half-charging calculations, which is surprising, since the electrostatic treatment is presumably getting better. $\Delta\Delta G_{Ei}$ for methane solvation, dipole inversion and anthracene solvation are still less than corresponding $\delta(\Delta G_E)$ and hence follow the first criteria of indistinguishability. The decrease in $\delta(\Delta\Delta G_{Ei})$ seems to indicate that the parameter set with $etol = 10^{-5}$ has a better phase space overlap with the expensive parameter set, although the accuracy in the overall energy may be a bit worse. If we also increased LJ and Coulombic cutoffs to 1.0 nm, with *etol* remaining at 10^{-5} , then as seen in the bottom right corner of the Table 3.8, we obtain even lower error and higher accuracy than the original optimized parameter set for all test systems.

The initial optimized parameter set remains approximately the same speed as the benchmark parameter set (perhaps 3-10% slower) for cutoffs of 0.9 nm, but the accuracy is improved for all molecules. For a slightly higher cost, 10-15% in computational speed depending on the system, we can get slightly more accurate anthracene solvation free energy estimate compared to using a benchmark parameter set.

Our reweighting method, using only samples from the initial free energy calculation, allows us to determine optimized parameters that pass stringent validation tests for methane solvation, dipole inversion and anthracene solvation and predicts the direction of the optimized parameter set correctly for all three test cases. The difference in thermodynamic estimates between the converged and the optimized parameters is of the order of 0.01 kJ/mol for methane solvation, dipole inversion and for anthracene solvation, primarily due to improved choices of PME parameters.

For estimating thermodynamic observables with high accuracy we suggest the simulations be run with B-spline interpolation order 4, Ewald tolerance of 10^{-4} , Fourier spacing of 0.12 nm, Coulomb and LJ cutoff of 0.9 nm, Coulomb and LJ switch between 0.85 nm.

For even higher accuracies and precision with 10-15% reduced speed, Ewald tolerance of 10^{-5} , Coulomb and LJ cutoff of 1.0 nm, Coulomb and LJ switch of 0.95 could be used.

We note that we get the same optimized parameter set for three very different test systems. The molecules were chosen to represent the extremes of small molecule free energy calculations typically attempted, with a large (7 Debye) dipole change and 14 heavy atoms being removed, and thus the results should be transferable across a wide range of free energy calculations. However, there are some limitations to the parameters proposed. We did not examine charging calculations because of difficulties in identifying the proper long range reference when the total charge of the system changes. However, the magnitude of the dipole disappearance (90 kJ/mol) approaches that of a single ion disappearing (250 kJ/mol), suggesting that magnitude of such free energy changes are supported by these parameters.

Additionally, for nonhomogeneous simulations, such as in the case of ligand binding or membrane simulations, it is clear that short Lennard-Jones cutoffs are not sufficiently accurate [47]. Binding free energies differ by 0.8–1.2 kcal/mol when evaluated with shorter (0.8 nm) vs. very long (2.5 nm) cutoffs. However, short cutoffs with some reweighted information from longer cutoffs (only one configuration every 200 ps) can give cutoff-independent results [47]. This suggests that at least for ligand binding, a twin range scheme that only occasionally uses much longer cutoffs may be required. Ewald schemes for dispersion interactions are also possible [58].

Larger box sizes would not result in loss of accuracy of the thermodynamic observables with the parameters described. However, computational speed would drop because of the increased number of interaction sites, which would perhaps require an increase of real space cutoffs to balance an increasing Fourier space cost, requiring additional optimization. In cases where researchers suspect these parameters are may not be transferable, then the

detailed presentation of methods in this chapter for validating parameters should allow those situations to be tested.

3.4 Conclusions

In this chapter we describe the use of multistate reweighting, using the MBAR formalism, to estimate thermodynamic observables for a large range of unsampled states using the configurations from only a few sampled states. We demonstrate the utility of this procedure by performing a multidimensional search in the space of nonbonded interaction simulation parameters to identify an optimized set of simulation parameters. These optimized parameters are chosen to give statistically indistinguishable results to those generated with fully converged nonbonded parameters, but with lower computation time. Careful ordering of the parameter search reduced the final number of parameter sets to be compared to approximately 5200. For each of these parameter sets, we reevaluate the energies of 9000 uncorrelated samples from each simulation performed for the different alchemical states in the original free energy calculations, a much faster procedure than performing full simulations. Specifically, reevaluating every 500th step takes approximately 0.4% of the simulation time of an equivalent MD simulation. Table 3.7 compares actual MD sample generation rate versus the rate at which re-evaluations can be done. Since the GROMACS version 4.5.3 did not support parallel rerun for re-evaluation for velocity Verlet this comparison was performed using a single processor for both molecular dynamics and trajectory reruns.

System	Parameter set	MD (hr/ns)	Re-evaluation (hr/ns)
Methane solvation	Benchmark	3.620	0.013
	Expensive	9.212	0.028
	Optimized	3.721	0.013
Dipole inversion	Benchmark	6.935	0.026
	Expensive	22.292	0.073
	Optimized	7.582	0.026
Anthracene solvation	Benchmark	4.629	0.022
	Expensive	13.268	0.055
	Optimized	5.123	0.024

Table 3.7: Re-evaluation is more than two orders of magnitude faster than generating fresh samples using MD. The initial optimized parameters are used.

Performing 10 ns of simulation for approximately 60,000 thermodynamic states (5200 parameter sets \times the number of alchemical states) with 3 million observables estimated in the optimization process would have taken over 60 years of CPU time. In this study, the calculations took less than a month of CPU time, resulting in a time savings of almost three orders of magnitude.

Estimates of $\Delta\Delta G_{EO}$ calculated using only samples from the initial benchmark states agree with the estimates calculated directly using samples from the optimized and expensive parameter set within statistical error. Remarkably, this agreement is usually of the order of 0.01 kJ/mol, with statistical error equally low both for predictions and validations. Both the level of agreement of predictions with the validation calculations and the high precision of all results is quite surprising and demonstrates the power of this multi-

state reweighting approach. The final computational cost of the optimized parameters is approximately the same as was used in previous benchmarking studies, but with substantial improvements in the accuracy of free energy calculations with respect to the previous benchmark calculations for anthracene, and statistically significant accuracy improvements for methane solvation and dipole inversion.

The fact that the optimal parameters for these thermodynamic calculations were similar to the default parameter previously chosen to minimize errors in the force evaluation is encouraging, showing that very different simulation observables have similar dependence on these cutoff parameters, and suggests general transferability of these parameters. The fact that the benchmark set used in this study included fairly large changes (such as the disappearance of a 7 Debye dipole or removal of 14 heavy atoms) suggest that the results should be relatively transferable to other molecules, with the caveats for heterogeneous systems analyzed above. Errors in free energies of solvation for suboptimal parameters were larger than errors in the bulk enthalpy, suggesting the importance of examining multiple types of observables when performing optimization of force field parameters.

Interestingly, even in the case of lower overlap between the sampled states and unsampled thermodynamic states, we obtained highly accurate $\Delta\Delta G$ results between pairs of unsampled states that did share overlap with each other. The key factor leading to these accurate estimations of the statistical uncertainty in $\Delta\Delta G$ and $\Delta\Delta H$ values is the use of MBAR to correctly propagate the correlated uncertainty in differences between two ΔG values.

This reweighting process using MBAR could easily be further extended to any other type of parameter sensitivity analysis, such as the evaluation of free energies at a different temperatures or for different force field parameters for which samples are not available because no new simulations are done at the new conditions. The only constraint is that the

new unsampled thermodynamic states should not be particularly far away in phase space from the sampled states. Determining exactly the tradeoff between distance in parameter space and amount of error is a topic for further research. It is somewhat difficult to relate the statistical uncertainty in calculated observables to the phase space overlap for even a single state, [70, 71, 72, 73] and interpreting overlap in multistate reweighting is even more complicated. However, the very low errors obtained in the present study indicate that the effects of at least moderate changes in parameters on thermodynamic observables should be easily measurable with at most moderate statistical errors.

Cutoff	System	$\Delta\Delta G$ (kJ/mol)		$\delta(\Delta G_E)$ (kJ/mol)
		10^{-4}	10^{-5}	
		High accuracy		
0.9	Methane solvation	0.011 ± 0.011	0.027 ± 0.006	0.071
	Full dipole inversion	-0.028 ± 0.021	-0.007 ± 0.012	0.160
	Discharging	0.048 ± 0.018	0.117 ± 0.010	0.112
	Charging	-0.076 ± 0.018	-0.124 ± 0.010	0.113
	Anthracene solvation	-0.027 ± 0.014	0.009 ± 0.07	0.125
	H_{vap}	-0.002 ± 0.001	0.004 ± 0.000	0.002
			Very high accuracy	
1.0	Methane solvation	0.013 ± 0.011	0.004 ± 0.003	0.071
	Full dipole inversion	0.005 ± 0.020	-0.001 ± 0.006	0.160
	Discharging	0.060 ± 0.018	0.069 ± 0.006	0.112
	Charging	-0.054 ± 0.018	-0.070 ± 0.006	0.113
	Anthracene solvation	-0.009 ± 0.014	-0.002 ± 0.004	0.125
	H_{vap}	0.002 ± 0.001	0.002 ± 0.000	0.002

Table 3.8: Predicted $\Delta\Delta G_{Ei}$ for GROMACS default parameters, in the bottom right corner, give marginally better convergence compared to the first optimized guess for a slight (10-15%) performance cost. Both satisfy the first criteria of statistical indistinguishability compared to ΔG_E calculations (one standard deviation error shown in column 5).

4 Free energy calculation for alchemical transformations involving changes in molecular geometry using MBAR and extended warp bridge sampling.

4.1 Introduction

Computer-aided molecular design problems like drug design, [28] solvent design [74] and molecular recognition [24] require high throughput screening of a large library of chemical compounds. Thermodynamic properties of interest such as solvation free energy or binding free energy thus must be calculated over a large multidimensional chemical space which may involve significant geometrical changes within molecules. Similarly, refining force field parameters based on solvation free energies requires high throughput thermodynamic calculations over a large multidimensional parameter space made of both interaction and geometry parameters.

For a given accuracy of atomistic force fields, there are major challenges that stand in the way of free energy calculations from becoming a mainstream tool for *in silico* molecular design. The current high computational costs associated with generating samples from simulation makes free energy calculations impractical for screening large numbers of compounds using molecular dynamics or Monte Carlo simulations. This is especially true for structurally different compounds, for which methods to calculate free energy differences exist but are not straightforward to implement in a high throughput manner.

In this study, we show that for problems involving changes of molecular geometry, we can reduce the computational sample generation costs of calculating free energies and other properties by up to five orders of magnitude by adapting the reweighting formalism of multistate Bennett acceptance ratio (MBAR) [4] to include phase space mapping. MBAR

can predict thermodynamic properties for poorly sampled or even unsampled states using data from only a few sampled states. However, the present form of MBAR cannot be used to estimate free energy and expectation value differences between geometrically different molecules which have little or no overlap in configuration space because of these geometrical differences. In this chapter, we demonstrate how to extend multistate reweighting such as MBAR to perform free energy calculations for molecules of different geometries and demonstrate the significant computational efficiencies that can be achieved.

Methods to compute free energies and expectations based on potential reweighting, such as exponential averaging, [7] the Bennett acceptance ratio method, [8] and MBAR [4] require that all samples from the ensemble of configurations generated from one thermodynamic state should be observed with nonzero probability in the configurational ensemble of the other thermodynamic states of interest for the calculations to converge to the correct answer. When there is poor overlap, many samples are required to eliminate bias from the calculation and the calculations will have large statistical uncertainty. When there is zero overlap in configuration space, no amount of sampling results will give an unbiased free energy difference. For example, if we wish to calculate the free energy difference between a SPC/E [10] and a TIP3P [9] water molecule, we will never see a rigid TIP3P molecular configuration in rigid SPC/E simulation. Thus, reweighting methods would fail and we will get incorrect free energy differences and in most cases, large uncertainties as well.

One approach to overcome this problem of non-overlapping phase spaces is to perform sampling with a potential that explicitly includes phase space overlap with both ends of the free energy calculation. For example, Oostenbrink and van Gunsteren developed a single step perturbation method allowing efficient calculation of free energy differences between sufficiently similar molecules. [75] This method involves choosing a reference structure, R , such that simulations of R share phase space with both end state structures A

and B . The free energy difference ΔG_{AB} can be calculated as difference between ΔG_{AR} and ΔG_{BR} . However, the selection and design of reference states for large number of compounds or reaction coordinates is a complicated problem with no clear comprehensive solution. More general investigations of designing intermediates with phase space overlap have been explored by Kofke and co-workers. [70, 71, 72, 73]

Straatsma, Zacharias and McCammon [76] proposed a potential of mean force approach using thermodynamic integration (TI) and includes holonomic constraints. They calculated the free energy along a chosen reaction coordinate using the constraint forces evaluated from the SHAKE [77] coordinate correction. The method has been successfully used in a number of free energy calculation applications. [78, 79, 80, 81, 82] Such TI-based free energy calculations make use of analytical constraint derivatives with respect to one or two reaction coordinates. [83]

Other methods to calculate free energy differences for geometrically diverse compounds, both rigid and nonrigid, have been proposed based on constructing phase space mappings between two end states. [76, 84] With this approach, a coordinate transformation is defined between each point in the phase space of each molecular system. Since all free energies and expectation values are calculated by integrals over the respective phase space, the coordinate transformations result in Jacobian terms that can be integrated into the free energy difference calculations.

Several other types of mathematical transformations between the phase spaces of two molecular states have been proposed in order to improve the efficiency of calculations for free energies and other ensemble observables. For example, Voter [85] introduced a translational shift in the integration variable to map between two energy distributions in order to estimate free energies for states separated in configurational space. Voter's method, however, only works for spatially translated distributions. Ytreberg and Zuckerman generalized

Voter’s method to include translations of internal coordinates as well as incorporate them into Bennett’s acceptance ratio [86].

To deal with more complex and general transformations, Jarzynski [84] proposed the targeted free energy perturbation approach, using an invertible transformation of the phase space A which maps to a new phase space A' such that A' has significant overlap with the phase space of the target distribution B , and later extended this to time-dependent mappings. [87, 88] Jarzynski applied this method to calculate the free energy associated with the expansion of cavity in a fluid. He envisioned his technique could be used for free energy estimation over different molecular geometries. However, a way to use this formalism for molecular problems was not explicitly laid out. The general approach described by Jarzynski is similar to that of Severance, Essex, and Jorgensen, [89] where a Jacobian factor was included to account for phase space contributions to the free energy of changing bond lengths, but only for unidirectional perturbation formulas.

Tan, Schultz, and Kofke applied this formalism to a realistic molecular problem, [90] studying the temperature dependence of solid phase free energies by combining Jarzynski’s targeted free energy method with the Bennett acceptance ratio. [8] Because the harmonic portion of the potential is dominant, configurations observed at different temperatures could therefore be mapped to each other with respect to deviation from a temperature dependent harmonic reference potential, and the much smaller differences from this temperature-dependent harmonic reference potential could be calculated with lower uncertainty.

Similar configuration mapping methods have been investigated by researchers in statistics as well. MBAR itself can be seen as application of extended bridge sampling. [91, 4] Meng and Shilling [92] developed a set of methods similar to Jarzynski’s mapping technique to estimate the ratio of normalizing constants, which they called “warp bridge sam-

pling.” They proposed three types of warp-bridge mapping. Warp-I maps distributions by shifting the integration variable. Voter’s method therefore belongs to Warp-I category. Warp-II involves mapping the variance as well as the mean, which is equivalent to Tan et al.’s use of harmonically targeted temperature perturbation to achieve phase space overlap. Warp-III involves mapping mean, spread and skewness of the distributions.

We propose a general algorithm inspired by these previous mapping approaches, specifically combining mapping of configurations via a change of variables with the multistate Bennett acceptance ratio (MBAR), the minimum variance multistate reweighting method. MBAR is provably the most efficient method to estimate free energies and expectation values [4] (although if carefully handled, the drawbacks of other standard methods can be minimized), and has been demonstrated to have lower bias than thermodynamic integration in the limit of fewer alchemical intermediate states. [3]

Using MBAR with configuration mapping allows the use of data from every sampled state to estimate free energy difference between any two given states, even when these states differ in the geometry. The configurations at any sampled state are mapped to geometries of the other states, creating phase space overlap in the configurational space. A Jacobian factor due to the change of variables is required from the mapping, but can usually be computed in a postprocessing step.

The advantage of MBAR with mapping is that it is easy to handle multiple geometries once pairwise maps implementing the invertible transformations are known. Free energy differences and other physical properties can then be efficiently estimated for a large number of thermodynamic states having different geometries without modifying anything in the simulation code used for sample generation by postprocessing the simulation data.

We demonstrate this approach to free energy calculations by applying it to a toy model (truncated harmonic oscillators) as well to realistic rigid water models, specifically trans-

formations between SPC/E, [10] TIP3P [9] and TIP4P, [9] and to the change in equilibrium bond length of a dipole formed by partial charges separated by a harmonic bond.

In the harmonic oscillator example, we vary two parameters, the force constant k and the equilibrium position μ , between different states. Because these harmonic oscillators are truncated, there is exactly zero phase space overlap between any two systems. However, despite this lack of overlap, free energy differences and expectation values can be calculated to exact agreement with analytical results with any number of samples by explicitly constructing a mapping between the oscillators.

Similarly, rigid water models sample from completely different configuration spaces, as we will never see a TIP3P geometry while performing a simulation of TIP4P. However, we can construct a one-to-one mapping between configurations of any three- or four-point water model which preserves the center of mass of the molecule. Indeed, such a mapping can be constructed between any rigid water model sharing the same symmetry, regardless of how many interaction sites are included. Although the phase spaces sampled by the different water molecules do not have sufficiently large overlap to perform this transformation in a single step, we can construct a series of intermediate states that have reversible maps to each of the end states and each other, linearly interpolating all other parameters, and then compute free energies and thermodynamic property differences using data from all the intermediates simultaneously. We examine an increasing number of intermediates, and find we can calculate unbiased results with very high precision with as few as one to three intermediate states.

Finally, we calculate the free energy difference between two dipoles of equal charge but different equilibrium bond length and show that even for flexible molecules these mapping calculations can drastically increase the efficiency of such transformation calculations.

In all cases, we can construct thermodynamic cycles to check the results that show

complete cancellation to within the calculated errors. Overall, we find that we can drastically improve the estimates of differences in properties between the molecular models. This improvement is so great that it becomes practically impossible to validate the errors by running standard free energy simulations because of the $N_{samp}^{-1/2}$ dependence of the statistical error on the number of samples N_{samp} collected. The alternate approach we present is simply that much more efficient.

4.2 Methods

We define a reduced energy $u_i(q) = \beta_i(H_i(q, p) + P_i V - \sum_k \mu_{k,i} N_k)$, corresponding to state i with Hamiltonian H_i , pressure P_i , chemical potentials of k species $\mu_{k,i}$, multidimensional coordinates and velocities q and p , volume V , and species numbers N_k . The thermodynamics state i is defined by the allowed microstate configurations $x = \{p, q, V, N_k\}$ defined over the phase space volume Γ_i with microstate probabilities determined by the Boltzmann probability distribution $P_i(x) \propto \exp(-u_i(x))$.

We define a mapping T_{ij} which takes a configuration x_i sampled from the phase space Γ_i of thermodynamic state i to $T_{ij}(x_i)$, a sample contained in the phase space Γ_j of thermodynamic state j . To emphasize, the convention we use is that T_{ij} carries from initial phase space i to final phase space j . We assume that this map is completely invertible, such that $T_{ij}^{-1} = T_{ji}$ exists, and that it is bijective, i.e. it is one-to-one and onto between phase space Γ_i and Γ_j . T_{ij} is allowed to depend on x_i (and likewise T_{ji} on x_j) though our examples will use linear maps that do not depend on the coordinates x_i or x_j . The transformation T_{ij} will have an associated Jacobian matrix $J_{ij}(x_i)_{kl} = \frac{\partial(T_{ij}(x_i))_k}{\partial x_{il}}$, where $(T_{ij}(x_i))_k$ is the k component of the transformation matrix, and x_{il} is the l th component of the x_i coordinate space.

This matrix may be a function of x_i , the coordinates of the domain, and because the transformation is invertible, we will have the relationship $J_{ij}(x_i) = J_{ji}^{-1}(x_j)$.

Our central finding is that if we define a “warped reduced energy” term which includes the Jacobian term:

$$u_{ij}^w(x_j) = u_i(T_{ji}(x_j)) - \ln |J_{ji}(x_j)| \quad (4.1)$$

all the multistate reweighting identities derived in previous chapters in the context of the multistate Bennett acceptance ratio method will hold. We can then re-write the multistate reweighting equation in terms of warped reduced energy terms,

$$f_i = -\ln \left(\frac{\sum_{j=1}^K \sum_{n=1}^{N_j} \frac{\exp(-u_{ij}^w(x_{jn}))}{\sum_{k=1}^K N_k \exp(f_k - u_{kj}^w(x_{jn}))} \right), \quad (4.2)$$

regaining the same form as the original multistate Bennett’s acceptance ratio as shown in the derivation below.

4.2.1 Derivation of multistate mapping formalism

The ratio r of normalization constants c_i and c_j between any two unnormalized probability distributions q_i and q_j defined on the same phase space can be related to the identity Eq. 4.3,

$$r = \frac{c_i}{c_j} = \frac{E_j[q_i \alpha_{ij}]}{E_i[q_j \alpha_{ij}]} \quad (4.3)$$

Where E_i is the statistical expectation value of a system sampled using q_i and α_{ij} is any strictly positive function defined on that same phase space, as derived in previous work on multistate reweighting techniques. [4]

For physical problems of thermodynamic interest, then $q_i = \exp(-u_i(x))$ will be the Boltzmann weight, using the same definition of the reduced potential $u_i(x)$ as in [4] to incorporate external parameters such as temperature, pressure, and chemical potentials. We can relate this ratio directly to the free energy and partition functions of the system.

$$\Delta A_{ij} = -k_B T \ln r = -k_B T \frac{Q_i}{Q_j} \quad (4.4)$$

Although we use the canonical ensemble here, corresponding relationships hold for other ensembles. If we substitute the empirical estimator $N_i^{-1} \sum_{n=1}^{N_j} g(x_{in})$ for the expectations $E_i[g(x_{in})]$ in 4.3, we can calculate these free energy differences from simulations.

$$r = \frac{\frac{1}{N_j} \sum_{n=1}^{N_j} q_i(x_{jn}) \alpha_{ij}(x_{jn})}{\frac{1}{N_i} \sum_{n=1}^{N_i} q_j(x_{in}) \alpha_{ij}(x_{in})} \quad (4.5)$$

We now define a map T_{ij} which maps a configuration x_i sampled from the phase space Γ_i of state i to $T_{ij}(x_i)$, which is a sample contained in the phase space Γ_j of state j (again, the convention is that T_{ij} carries from phase space i to phase space j). Assume that this map is completely invertible, such that $T_{ij}^{-1} = T_{ji}$ exists and is one-to-one between phase space Γ_i and Γ_j . T_{ij} may depend on x_i (and likewise T_{ji} on x_j though our examples will not use this fact. The transformation will have an associated Jacobian factor J_{ij} , which also may be a function of x_i , and because the transformation is invertible, we will have $J_{ij}(x_i) = J_{ji}^{-1}(x_j)$.

We can sample from the unnormalized probability distribution function for j by per-

forming sampling from state i , since:

$$q_j = e^{-u_j(x_j)} = e^{-u(T_{ij}(x_i))} \quad (4.6)$$

And the partition function will be

$$Q_j = \int_{\Gamma_j} e^{-u(x_j)} dx_j = \int_{\Gamma_i} e^{-u(T_{ij}(x_i))} |J_{ij}(x_i)| dx_i \quad (4.7)$$

Based on similar arguments, Meng and Schilling derived the equation for ratio r under the transformation for two states in the general statistical context. The equation from their paper can be rewritten for any pair of states i and j as:

$$\frac{Q_i}{Q_j} = \frac{\frac{1}{N_j} \sum_{n=1}^{N_j} q_i(T_{ji}(x_{jn})) |J_{ji}(x_{jn})| \alpha_{ij}(x_{jn})}{\frac{1}{N_i} \sum_{n=1}^{N_i} q_j(T_{ij}(x_{in})) |J_{ij}(x_{in})| \alpha_{ij}(x_{in})} \quad (4.8)$$

Here, the n th sample from the j state x_{jn} is mapped into the i th phase space using the map T_{ji} , and visa versa. Cross multiplying and summing both sides for $j = 1$ to K in Eq. 4.8.

$$\begin{aligned} \sum_{j=1}^K \frac{Q_i}{N_i} \sum_{n=1}^{N_i} q_j(T_{ij}(x_{in})) |J_{ij}(x_{in})| \alpha_{ij}(x_{in}) \\ = \sum_{j=1}^K \frac{Q_j}{N_j} \sum_{n=1}^{N_j} q_i(T_{ji}(x_{jn})) |J_{ji}(x_{jn})| \alpha_{ij}(x_{jn}) \end{aligned} \quad (4.9)$$

Without the variable transformation, then the choice of α_{ij} that minimizes the variance if

this estimate has the following form. [4]

$$\alpha_{ij}(x) = \frac{N_j Q_j^{-1}}{\sum_{k=1}^K N_k Q_k^{-1} q_k(x)} \quad (4.10)$$

Using the definition of the transformed probability function, we can re-write α_{ij} using the transformations as

$$\alpha_{ij}(x_i) = \frac{N_j Q_j^{-1}}{\sum_{k=1}^K N_k Q_k^{-1} q_k(T_{ki}(x_i)) |J_{ki}(x_i)|} \quad (4.11)$$

Following, [4] we can take c_i/N_i out of the summation and then switch the order of summation on the left hand side of Eq. 4.9, and then use our formula for α_{ij} to include the transformations.

$$\begin{aligned} & \frac{Q_i}{N_i} \sum_{n=1}^{N_i} \sum_{j=1}^K \frac{q_j(T_{ij}(x_{in})) |J_{ij}(x_{in})| N_j Q_j^{-1}}{\sum_{k=1}^K N_k Q_k^{-1} q_k(T_{ik}(x_{in})) |J_{ik}(x_{in})|} \\ &= \sum_{j=1}^K \frac{Q_j}{N_j} \sum_{n=1}^{N_j} \frac{q_i(T_{ji}(x_{jn})) |J_{ji}(x_{jn})| N_j Q_j^{-1}}{\sum_{k=1}^K N_k Q_k^{-1} q_k(T_{jk}(x_{jn})) |J_{jk}(x_{jn})|} \end{aligned} \quad (4.12)$$

Eq. 4.12 can now be written as:

$$\begin{aligned}
& \frac{Q_i}{N_i} \sum_{n=1}^{N_i} \frac{\sum_{j=1}^K N_j Q_j^{-1} q_j(T_{ij}(x_{in})) |J_{ij}(x_{in})|}{\sum_{k=1}^K N_k Q_k^{-1} q_k(T_{ik}(x_{in})) |J_{ik}(x_{in})|} \\
&= \sum_{j=1}^K Q_j N_j^{-1} \sum_{n=1}^{N_j} \frac{N_j Q_j^{-1} q_i(T_{ji}(x_{jn})) |J_{ji}(x_{jn})|}{\sum_{k=1}^K N_k Q_k^{-1} q_k(T_{jk}(x_{jn})) |J_{jk}(x_{jn})|}
\end{aligned} \tag{4.13}$$

which reduces to:

$$Q_i = \sum_{j=1}^K \sum_{n=1}^{N_j} \frac{q_i(T_{ji}(x_{jn})) |J_{ji}(x_{jn})|}{\sum_{k=1}^K N_k Q_k^{-1} q_k(T_{jk}(x_{jn})) |J_{jk}(x_{jn})|} \tag{4.14}$$

Taking negative log on both sides:

$$f_i = -\ln(Q_i) = -\ln \left(\sum_{j=1}^K \sum_{n=1}^{N_j} \frac{q_i(T_{ji}(x_{jn})) |J_{ji}(x_{jn})|}{\sum_{k=1}^K N_k Q_k^{-1} q_k(T_{jk}(x_{jn})) |J_{jk}(x_{jn})|} \right) \tag{4.15}$$

where f_i is the dimensionless free energy. Assuming that $q(x) = \exp(-u(x))$ is the Boltzmann weight, we have:

$$f_i = -\ln \left(\sum_{j=1}^K \sum_{n=1}^{N_j} \frac{e^{-u_i(T_{ji}(x_{jn}))} |J_{ji}(x_{jn})|}{\sum_{k=1}^K N_k e^{f_k - u_k(T_{kj}(x_{jn}))} |J_{kj}(x_{jn})|} \right) \tag{4.16}$$

We can define a “warped potential energy” term which includes the Jacobian term:

$$u_{ij}^w(x_{jn}) = u_i(T_{ji}(x_{jn})) - \ln(|(J_{ji}(x_{jn}))|) \quad (4.17)$$

Note specifically that the reduced potential includes a factor of β_i , while the Jacobian term does not. Note also that we must transform the samples from the j th thermodynamic state before evaluating the potential function in state i . We can then re-write the multistate reweighting equation in terms of warped potential energy terms:

$$f_i = -\ln \left(\frac{\sum_{j=1}^K \sum_{n=1}^{N_j} \exp(-u_{ij}^w(x_{jn}))}{\sum_{k=1}^K N_k \exp(f_k - u_{kj}^w(x_{jn}))} \right) \quad (4.18)$$

Regaining the same form for multistate Bennett’s acceptance ratio.

We next turn to expectation values of other observables computing using reweighting. This translation is trivial, because all other results will follow directly the equations above. We have previously shown [4] that expectations can be treated as probability distributions with no samples, and that if there are no samples collected, the math does not require that these quasi-probability distributions be nonnegative. The only caution that must be followed is that observables must be computed using the transformed coordinates, $A(T_{ij}(x_i))$, which may require non-negligible extra computation for each sampled configuration.

Once we define the mappings and have the $K \times K \times N_k$ warped energies $u_{ij}^w(x_j)$ we can then solve Eq. 4.2 self-consistently to find all free energies using methods already introduced. [4] Expectation values of arbitrary functions can be computed using the same formalism. Indeed, all multistate reweighting formulas developed by Shirts and Chodera re-

main valid, [4]. This result is not totally unexpected; as we have discussed, similar single state reweighting formulas written in terms of a “warped” potential as described in Eq. 4.1 have been developed for analyzing molecular simulations, and a similar multistate formulation has been observed in statistics, as discussed in the introduction. However, this is the first full generalization of this idea to calculations involving multiple thermodynamics states, and we demonstrate for the first time that the combined multistate plus configuration space mapping approach can make previous challenging problems of computing differences in observables as a function of molecular transformation much easier.

4.2.2 Models

4.2.2.1 Truncated harmonic oscillators We first examine the problem of calculating the free energy difference between a system of truncated (or censored) harmonic oscillators with spring constants k_i , truncated at one standard deviation $\sigma_i = k_i^{-1/2}$ from their mean value μ_i , with the potential becoming infinite (and probability zero) with any larger displacement, so that

$$U_i(x) = \begin{cases} \frac{1}{2}k_i(x - \mu_i)^2 & |x - \mu_i| < \sigma_i \\ \infty & |x - \mu_i| > \sigma_i \end{cases}$$

We assume that the spring constants k_i are chosen sufficiently large and harmonic oscillator potential centers μ_i are chosen sufficiently far apart that there is no phase space overlap between any two oscillators. In this case, no amount of sampling will allow the calculation of the free energy differences between these oscillators by any reweighting method.

We now approach this problem with the assistance of the mapping formalism. We first must define our maps T_{ij} . A general approach to construct pairwise maps is to construct

each map T_{ij} implicitly by constructing maps T_i to a reference state, and composing maps to obtain maps $T_{ij}(x_i) = T_j^{-1}T_i(x_i)$. Although this problem is simple enough not to require this approach, we will use it for pedagogical purposes, as it becomes useful for more complicated problems. For this toy problem, we use a reference state with zero mean and unit variance for the underlying Gaussian that is then truncated, and we map by shifting and rescaling:

$$\begin{aligned} T_i(x_i) &= \frac{x_i - \mu_i}{\sigma_i} \\ T_{ij}(x_i) &= T_j^{-1}(T_i(x_i)) = \left(\frac{x_i - \mu_i}{\sigma_i} \right) \sigma_j + \mu_j \end{aligned} \tag{4.19}$$

This transformation $T_{ij}(x_i)$ translates the sample by $-\mu_i$, rescales by σ_j/σ_i and then translates by $+\mu_j$. The Jacobians J_{ij} and J_{ji} for this map are:

$$\begin{aligned} J_{ij} &= \frac{\partial T_{ij}(x_i)}{\partial x_i} = \frac{\sigma_j}{\sigma_i} \\ J_{ji} &= \frac{\partial T_{ji}(x_j)}{\partial x_j} = \frac{\sigma_i}{\sigma_j} \end{aligned} \tag{4.20}$$

In this case the maps and the corresponding Jacobians are independent of the position coordinate.

Calculation of $u_i(x_{jn})$ is not possible without the mapping since x_{jn} is never seen in the i^{th} simulation. The warped reduced energy $u_{ij}^w(x_{jn})$ using the mapping and Jacobian

terms is:

$$\begin{aligned}
u_{ij}(x_{jn}) &= \beta \frac{1}{2} K_i (T_{ji}(x_{jn}) - \mu_i)^2 - \ln \frac{\sigma_i}{\sigma_j} \\
&= \beta \frac{1}{2} K_i \left(\frac{\sigma_i(x_{jn} - \mu_j)}{\sigma_j} + \mu_i - \mu_i \right)^2 - \ln \frac{\sigma_i}{\sigma_j} \\
&= \beta \frac{1}{2} K_i \left(\sqrt{\frac{K_j}{K_i}} (x_{jn} - \mu_j) \right)^2 - \ln \frac{\sigma_i}{\sigma_j} \\
&= u_j(x_{jn}) - \ln \frac{\sigma_i}{\sigma_j}
\end{aligned} \tag{4.21}$$

These energies can then be used in Eq. 4.2, including Jacobian term, and free energies estimated and validated against the analytical estimates of free energies. The analytical estimate of the Helmholtz free energy of a truncated harmonic oscillator at constant temperature depends only on the force constant with $A_{i,\text{analytical}} = -k_B T \ln (\sqrt{2\pi}\sigma_i \text{erf}(2^{-1/2}))$.

In this particular case, the free energy differences between two harmonic oscillators is simply $A_i/A_j = -k_B T \ln \sigma_i/\sigma_j$. We note that the potential energy will not change after mapping from x_j to $T_{ji}(x_j)$, so the potential energy contribution to the free energy from all sampled points will be zero, leaving simply the Jacobian contribution. We therefore require exactly zero samples in order to correctly predict the free energy, since we have an exact phase space mapping which takes each sample to a sample having equal Boltzmann weight as before the mapping. This exact phase space mapping for our truncated harmonic oscillators is an example of the ‘‘Warp-II’’ strategy of Meng and Schilling, with a transformation scaling both the coordinates and the variance of the distribution of energies.

Multistate reweighting using MBAR also makes it possible to evaluate not only free energies but expectations at state i , using the sampling performed at all of the K states, rather than calculating expectation values at state i using only samples taken from state i . When using multistate reweighting with mapping for this truncated harmonic oscillator problem,

the statistical uncertainty of any given observable (such as average potential energy or RMS fluctuation around the mean position) scales as $(\sum_i N_i)^{-1/2}$, the total number of samples collected among all states, rather than the number of samples N_i collected at each state, because each sample, from any state, contributes equal information to ensemble averages at all other states. This is because the phase space mapping is perfect; each point in phase space, after mapping, has the same energy, and thus same Boltzmann weight. If the mapping is not perfect then, the error in the expectation values will have some intermediate efficiency, scaling better than $N^{-1/2}$ but not as good as $(\sum_i N_i)^{-1/2}$.

In almost all cases of real physical relevance, such an exact mapping cannot be constructed. Although one-to-one mappings between spaces can be easily constructed in many cases (as we will show), they very rarely map between points with equal Boltzmann weight. However, this mapping technique can be used to create overlap where this overlap did not exist before. For example, if the harmonic oscillators were truncated at an arbitrary distance C_k for all oscillators rather than at 1 standard derivation for all states, then a new map $T_{ij}(x) = \left(\frac{x_j - \mu_j}{C_i}\right) C_j + \mu_i$ with Jacobian C_i/C_j can be used. The potential energies will change under such a transformation, but there will be a moderate amount of phase space overlap as long as the force constants are not very different, allowing MBAR to be used to calculate free energies and expectation values efficiently.

Alternatively, mappings can be used to increase overlap where less overlap initially existed. For example, if we had standard harmonic oscillators, without any truncation, then there will always exist some nonzero overlap between any two probability distributions, as the normal distribution is nonzero (if small) everywhere. However, because of the poor phase space overlap if the harmonic oscillators have high spring constants, or are separated by a large distance, it can take a very large number of samples to calculate free energy differences with a moderate degree of precision. In this case, if we happen to use the same

$T_{ij}(x)$ defined in the case of truncated harmonic oscillators, we will again have an exact mapping, meaning free energy differences require no collection of samples, and samples collected at any state will be equally good for calculating expectation values for all states.

4.2.2.2 Water models We next demonstrate how multistate reweighting with mapping can be used to drastically improve the efficiency of molecular transformation calculations. We calculate the pairwise difference in the Gibbs free energy of hydration $\Delta\Delta G_{hyd}$ as well as differences in enthalpy and entropy between three water models using both standard multistate reweighting and multistate reweighting with mapping. The thermodynamic cycle shown in Figure 4.1 relates these quantities. For concreteness, it is shown for TIP4P to TIP3P, but same cycle can be constructed for any pair of rigid water models (such as TIP3P to SPC/E or SPC/E to TIP4P).

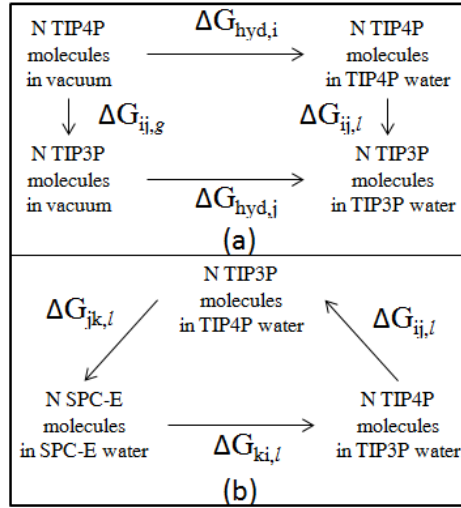


Figure 4.1: The difference between analytically calculated free energy $\Delta G_{ij,g}$ and free energy calculated using MBAR with mapping $\Delta G_{ij,\ell}$ should be consistent with the difference in the solvation free energies calculated using MBAR without mapping for thermodynamic cycle (a) according to Eq. 4.22 for the three transformations. $\Delta G_{ij,\ell}$, $\Delta G_{jk,\ell}$ and $\Delta G_{ki,\ell}$ should add up to zero in thermodynamic cycle (b) according to Eq. 4.23.

In this thermodynamic cycle $\Delta G_{ij,g}$ is the Gibbs free energy of mutating N water molecules of model i to N molecules of model j in the ideal gas state. Interaction between molecules in the ideal gas state is zero. Thus the reduced warped potential in Eq. 4.1 will simply be equal to the PV term minus the Jacobian term $|J_{ji}|$.

$\Delta G_{i,hyd}$ in the thermodynamic cycle (a) is the free energy of hydration of N molecules of model i . The solvation free energy of N molecules is N times the chemical potential $\mu_{i,\ell}$ (the solvation free energy for a single molecule of model i in pure liquid), using the ideal gas reference state. $\Delta G_{ij,\ell}$ is the free energy of mutating N water molecules of model i to N molecules of model j in the liquid state. $\Delta G_{ij,\ell}$ is calculated using the MBAR with mapping formalism. $\Delta G_{ij,\ell}$, $\Delta G_{i,hyd}$, $\Delta G_{j,hyd}$ and $\Delta G_{ij,g}$ follow a thermodynamic cycle given by Eq. 4.22.

$$\Delta G_{i,hyd} - \Delta G_{j,hyd} = \Delta G_{ij,\ell} - \Delta G_{ij,g} \quad (4.22)$$

Dividing the entire Eq. 4.22 by N gives the difference in free energy changes for a single molecule.

Finally, we note that we can validate the $\Delta \Delta G_{ij,\ell}$ calculations by constructing the cycle for transformations between three models TIP4P, TIP3P and SPC/E represented by i , j , k , which must satisfy:

$$\Delta G_{ij,\ell} + \Delta G_{jk,\ell} + \Delta G_{ki,\ell} = 0 \quad (4.23)$$

In our calculations, the free energy change $\Delta G_{ij,\ell}$ is estimated along the path linearly varying all interaction (oxygen charge q , Lennard-Jones parameters C_6 and C_{12}) and geometry (bonds, bond angles and location of the virtual charge site) parameters between models i and j .

Water model \rightarrow		SPC/E	TIP3P	TIP4P
Parameter \downarrow	units			
C_6	$\text{kJ/nm}^6/\text{mol}$	2.616907×10^{-3}	2.489480×10^{-3}	2.55224×10^{-3}
C_{12}	$\text{kJ/nm}^{12}/\text{mol}$	2.633237×10^{-6}	2.435088×10^{-6}	2.5104×10^{-6}
$q(O)$	e	-0.8476	-0.834	-1.040
$q(H)$	e	0.4238	0.4170	0.5200
$\angle\text{HOH}$	deg	109.47	104.52	104.52
r_{OH}	nm	0.1	0.09572	0.09572
r_{OM}	nm	0.000	0.000	0.015
r_{HH}	nm	0.16330	0.15139	0.15139

Table 4.1: Force field parameters for the water models used in this study.

All force field parameters for the water models used are given in Table 4.1. We define a λ parameter which varies linearly from zero to one. A force field parameter set P for a state intermediate to two end states i and j can be defined as $P(j, i, \lambda) = P_i(1 - \lambda) + P_j(\lambda)$. We must then define mappings T_{ji} between any two states with parameters $P(j, i, \lambda)$ which we describe in the case of specific transformations between water models as described below.

4.2.2.3 Maps between water models

4.2.2.3.1 Mapping for TIP4P to TIP3P transformation In this transformation the $\angle\text{HOH}$ and $d(\text{OH})$ remain same throughout the transition. Only $d(\text{OM})$ changes, from 0.015 to 0.0 nm, as seen in Fig. 4.2a. For each λ dependent state, we use the TIP3P configuration as the reference state. First, we map geometry of a state j to geometry of TIP3P model and then from TIP3P model to state i 's geometry. The transformation matrix is defined below.

$$\begin{aligned}
T_{ji} = T_i^{-1}(T_j(\mathbf{X}_{\text{jn}})) &= \begin{bmatrix} 1 & 0 & 0 & 0 \\ 0 & 1 & 0 & 0 \\ 0 & 0 & 1 & 0 \\ 1 - a_{\lambda_i} - b_{\lambda_i} & a_{\lambda_i} & b_{\lambda_i} & 0 \end{bmatrix} \times \left(\begin{bmatrix} 1 & 0 & 0 & 0 \\ 0 & 1 & 0 & 0 \\ 0 & 0 & 1 & 0 \\ 1 & 0 & 0 & 0 \end{bmatrix} \times \begin{bmatrix} \mathbf{X}_{\text{jn}}(\text{O}) \\ \mathbf{X}_{\text{jn}}(\text{H1}) \\ \mathbf{X}_{\text{jn}}(\text{H2}) \\ \mathbf{X}_{\text{jn}}(\text{M}) \end{bmatrix} \right) \\
T_i^{-1}(T_j) &= \begin{bmatrix} 1 & 0 & 0 & 0 \\ 0 & 1 & 0 & 0 \\ 0 & 0 & 1 & 0 \\ 1 - a_{\lambda_i} - b_{\lambda_i} & a_{\lambda_i} & b_{\lambda_i} & 0 \end{bmatrix} \\
a_{\lambda_i} &= \frac{d(\text{OM})_i}{2d(\text{OH})_i \cos(\angle \text{HOH}_i/2)} \\
b_{\lambda_i} &= a_{\lambda_i} \\
J_{ji}(\mathbf{X}_{\text{jn}}) &= \det|T_i^{-1}(T_j)|
\end{aligned} \tag{4.24}$$

Notice that $\mathbf{X}_{\text{jn}}(\text{M})$ can be expressed in terms of $\mathbf{X}_{\text{jn}}(\text{O})$, $\mathbf{X}_{\text{jn}}(\text{H1})$ and $\mathbf{X}_{\text{jn}}(\text{H2})$ and hence is not an independent variable. Thus it does not appear in the partition function integral. Since $\mathbf{X}_{\text{jn}}(\text{O})$, $\mathbf{X}_{\text{jn}}(\text{H1})$ and $\mathbf{X}_{\text{jn}}(\text{H2})$ do not undergo any transformation the Jacobian for this transformation is 1.

4.2.2.3.2 Mapping for SPC/E to TIP3P transformation The invertible mapping between the various intermediate states between SPC/E and TIP3P is derived using three conditions without going through a common intermediate state. The first condition is that the center of mass of a water molecule should not change upon transformation of the coordinates. In Fig. 4.2b, if \mathbf{X}_{1j} , \mathbf{X}_{2j} , \mathbf{X}_{3j} represent coordinates of oxygen and the two

hydrogens and \mathbf{X}_{1i} , \mathbf{X}_{2i} , \mathbf{X}_{3i} represent transformed coordinates of oxygen and the two hydrogen, then:

$$\frac{m_O(\mathbf{X}_{1i}) + m_H(\mathbf{X}_{2i}) + m_H(\mathbf{X}_{3i})}{M} = \frac{m_O(\mathbf{X}_{1j}) + m_H(\mathbf{X}_{2j}) + m_H(\mathbf{X}_{3j})}{M} \quad (4.25)$$

$$M = m_O + 2m_H$$

In the above equation, m_O is the atomic mass of oxygen 15.9994 g/mol, m_H is 1.008 g/mol, the atomic masses of hydrogens H1 and H2.

The second condition for mapping is that the unit vector joining the center of mass of the two hydrogens to the oxygen does not change upon transformation

$$\frac{\mathbf{X}_{1i} - (\mathbf{X}_{2i} + \mathbf{X}_{3i})/2}{d(\text{OH})_i \cos(\theta_i)} = \frac{\mathbf{X}_{1j} - (\mathbf{X}_{2j} + \mathbf{X}_{3j})/2}{d(\text{OH})_j \cos(\theta_j)}$$

$$\theta_i = \frac{\angle \text{HOH}_i}{2}; \theta_j = \frac{\angle \text{HOH}_j}{2}$$

$$K_{ij} = \frac{d(\text{OH})_i \cos(\theta_i)}{d(\text{OH})_j \cos(\theta_j)} \quad (4.26)$$

$$\mathbf{X}_{1i} - \frac{(\mathbf{X}_{2i} + \mathbf{X}_{3i})}{2} = K_{ij} \left(\mathbf{X}_{1j} - \frac{(\mathbf{X}_{2j} + \mathbf{X}_{3j})}{2} \right)$$

Third and final condition is that the old unit vector $(\mathbf{X}_{2j} - \mathbf{X}_{3j})/d(\text{HH})_j$ is equal to the new unit vector $(\mathbf{X}_{2i} - \mathbf{X}_{3i})/d(\text{HH})_i$ after a certain translation. $d(\text{HH})_i$, $d(\text{HH})_j$ are the distances between the two hydrogens in model i and j respectively.

Let us translate vector $\mathbf{X}_{2j} - \mathbf{X}_{3j}$ such that it coincides with new vector $\mathbf{X}_{2i} - \mathbf{X}_{3i}$.

$$\begin{aligned}\mathbf{X}'_{2j} &= \mathbf{X}_{2j} + \left(\frac{(\mathbf{X}_{2i} + \mathbf{X}_{3i})}{2} - \frac{(\mathbf{X}_{2j} + \mathbf{X}_{3j})}{2} \right) \\ \mathbf{X}'_{3j} &= \mathbf{X}_{3j} + \left(\frac{(\mathbf{X}_{2i} + \mathbf{X}_{3i})}{2} - \frac{(\mathbf{X}_{2j} + \mathbf{X}_{3j})}{2} \right)\end{aligned}\quad (4.27)$$

\mathbf{X}'_{2j} and \mathbf{X}'_{3j} are the translated coordinates.

Equating the translated unit vector to the unit vector of the transformed geometry gives:

$$\begin{aligned}\frac{\mathbf{X}_{2i} - \mathbf{X}_{3i}}{d(\text{HH})_i} &= \frac{\mathbf{X}'_{2j} - \mathbf{X}'_{3j}}{d(\text{HH})_j} \\ \mathbf{X}_{2i} - \mathbf{X}_{3i} &= \frac{d(\text{HH})_i}{d(\text{HH})_j} (\mathbf{X}_{2j} - \mathbf{X}_{3j})\end{aligned}\quad (4.28)$$

We can write the three conditions in a matrix form

$$\begin{aligned}T_i^{-1}(T_j(\mathbf{X}_{jn})) &= \begin{bmatrix} \frac{m_O}{M} & \frac{m_H}{M} & \frac{m_H}{M} \\ 1 & \frac{-1}{2} & \frac{-1}{2} \\ 0 & 1 & -1 \end{bmatrix}^{-1} \times \begin{bmatrix} \frac{m_O}{M} & \frac{m_H}{M} & \frac{m_H}{M} \\ K_{ij} & \frac{-K_{ij}}{2} & \frac{-K_{ij}}{2} \\ 0 & \frac{d(\text{HH})_i}{d(\text{HH})_j} & \frac{-d(\text{HH})_i}{d(\text{HH})_j} \end{bmatrix} \times \begin{bmatrix} \mathbf{X}_{jn}(\text{O}) \\ \mathbf{X}_{jn}(\text{H1}) \\ \mathbf{X}_{jn}(\text{H2}) \end{bmatrix} \\ T_i^{-1}(T_j) &= \begin{bmatrix} \frac{m_O}{M} + (1+c)K_{ij} & \frac{m_H}{M} - (1+c)\frac{K_{ij}}{2} & \frac{m_H}{M} - (1+c)\frac{K_{ij}}{2} \\ \frac{m_O}{M} + (c)K_{ij} & \frac{m_H}{M} - (c)\frac{K_{ij}}{2} + \frac{d(\text{HH})_i}{2 d(\text{HH})_j} & \frac{m_H}{M} - (c)\frac{K_{ij}}{2} - \frac{d(\text{HH})_i}{2 d(\text{HH})_j} \\ \frac{m_O}{M} + (c)K_{ij} & \frac{m_H}{M} - (c)\frac{K_{ij}}{2} - \frac{d(\text{HH})_i}{2 d(\text{HH})_j} & \frac{m_H}{M} - (c)\frac{K_{ij}}{2} + \frac{d(\text{HH})_i}{2 d(\text{HH})_j} \end{bmatrix} \\ c &= -\frac{m_O}{M} \\ J_i(T_j(\mathbf{X}_{jn})) &= \det|T_i^{-1}(T_j)|\end{aligned}\quad (4.29)$$

4.2.2.3.3 Mapping TIP4P to SPC/E transformation The mapping for TIP4P to SPC/E transformation can be derived by combining the mapping of the previous two trans-

formations:

$$T_i^{-1}(T_j) = \begin{bmatrix} 1 & 0 & 0 & 0 \\ 0 & 1 & 0 & 0 \\ 0 & 0 & 1 & 0 \\ 1 - a_{\lambda_i} - b_{\lambda_i} & a_{\lambda_i} & b_{\lambda_i} & 0 \end{bmatrix} \times \dots$$

$$\dots \begin{bmatrix} \frac{m_O}{M} + (1.0 + c)K_{ij} & \frac{m_H}{M} - (1 + c)\frac{K_{ij}}{2.0} & \frac{m_H}{M} - (1 + c)\frac{K_{ij}}{2} & 0 \\ \frac{m_O}{M} + (c)K_{ij} & \frac{m_H}{M} - (c)\frac{K_{ij}}{2} + \frac{d(HH)_i}{2d(HH)_j} & \frac{m_H}{M} - (c)\frac{K_{ij}}{2} - \frac{d(HH)_i}{2d(HH)_j} & 0 \\ \frac{m_O}{M} + (c)K_{ij} & \frac{m_H}{M} - (c)\frac{K_{ij}}{2} - \frac{d(HH)_i}{2d(HH)_j} & \frac{m_H}{M} - (c)\frac{K_{ij}}{2} + \frac{d(HH)_i}{2d(HH)_j} & 0 \\ 0 & 0 & 0 & 0 \end{bmatrix}$$

(4.30)

Here again, because $\mathbf{X}_{jn}(\mathbf{M})$ is not an independent variable, the Jacobian is equal to the determinant of a 3×3 submatrix corresponding to change in $\mathbf{X}_{jn}(\mathbf{O})$, $\mathbf{X}_{jn}(\mathbf{H1})$ and $\mathbf{X}_{jn}(\mathbf{H2})$.

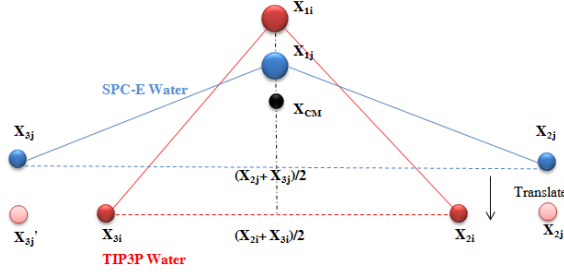
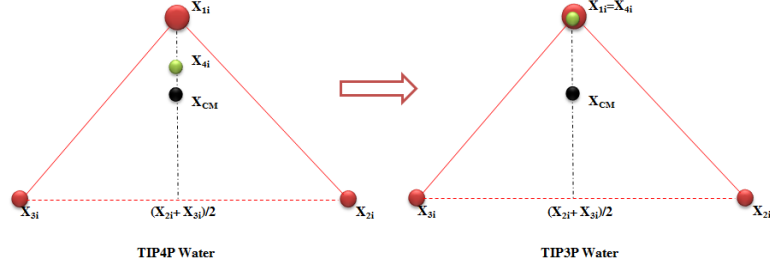


Figure 4.2: (a) TIP4P to TIP3P transformation and (b) SPC/E to TIP3P transformation

For all simulations, we use Ewald order of interpolation of 4, Ewald tolerance of 10^{-4} , Fourier spacing of 0.09 nm, Coulomb and Lennard-Jones cutoffs of 0.9 nm with a switch starting at 0.85 nm for both interactions as well as a short range neighbor list cutoff (rlist) of 1.1 nm, and a Fourier spacing of 0.1 nm. A Nosé-Hoover [93] thermostat was used with a time constant of 5 ps. Pressure was kept constant at 1.01325 bar (1 atm) using Martyna-Tuckerman-Tobias-Klein [69] barostat with time constant of 5 ps and compressibility of $4.5 \times 10^{-5} \text{ bar}^{-1}$. The time step was 0.002 ps, and bonds constrained using the SETTLE algorithm. [67]

A cubic box $2.5 \times 2.5 \times 2.5 \text{ nm}^3$ containing 521 water molecules was used for each of the three water transformations. We performed 10 ns of NPT simulations at each of $K = 41$ different equally spaced physical states for each transformation. Each of the $K - 2$ intermediate states have force field parameters linearly interpolated between the two end state

water models as described above. We record coordinates every 1 ps to create a trajectory of 10,000 coordinate samples, which are sufficiently far apart to have uncorrelated energies. We then have K trajectories worth of samples, \mathbf{X}_{jn} 's, $j = 1 \dots K$ from these simulations at all states. A Gromacs trajectory conversion template was used to build a tool in C for operating directly on binary trajectory files to map the geometries of the simulated states to the trajectory of $K - 1$ other states according to the transformation matrix defined in the equations above. This creates a matrix of $K \times K$ trajectories consisting of samples $T_{ji}(\mathbf{X}_{jn})$. We then evaluate the energies of these trajectories using `mdrun` in rerun mode at the mapped geometries $U_i(T_{ji}(\mathbf{X}_{jn}))$ to generate the $\mathbf{U}[K \times K \times N_k]$ matrix of potential energies required for multistate reweighting calculations. The transformation $T_{ji}(\mathbf{X}_{jn})$ and the subsequent rerun for a state i takes less than 5 minutes on a single processor, which is negligibly small compared to computational cost to generate \mathbf{X}_{jn} . From this process, we obtain $\Delta G_{ij,\ell} \pm \delta(\Delta G_{ij,\ell})$ for N molecules. The molar value for the Gibbs free energy of transformation is $\Delta G_{ij,\ell}/N$, which means that the uncertainty will be $\delta(\Delta G_{ij,\ell})/N$, i.e. dividing by N and not by $N^{1/2}$, since changes in the molar value of each molecule are not independent.

For all water models, samples for estimating hydration free energies using standard alchemical methods by decoupling a single water molecule are generated for 21 intermediate states to solvate a water molecule in corresponding bulk liquid. These simulations are run for 20 ns to produce free energy of transfer estimates with useful uncertainties. Solute-solvent Coulomb interactions are decoupled linearly and the Lennard-Jones interactions are decoupled using a soft core interaction potential. [3]

4.2.2.4 Dipole transformation We used water models to test the mapping algorithm for estimating free energy differences between dissimilar rigid molecular geometries. In that

case, part of the efficiency gain in computing the differences in free energies of solvation came from the fact that we were simulating pure liquid properties, and could divide by the number of molecules. We now wish to test the MBAR plus configurational mapping techniques for the free energy change for single molecule free energy differences. We also investigate whether the approach would work for dissimilar but still flexible geometries. We therefore also use this approach to compute the free energy difference between dipoles with different equilibrium lengths, and thus different dipole moment. In this case, there is some possibility of observing a dipole of a given equilibrium bond length in a simulation of a different equilibrium bond length, but the frequency is likely to be low if the equilibrium bond lengths are too different on the scale of the bond length fluctuations.

In this test, we calculate the free energy change for a change in the equilibrium bond length of a dipole solvated in TIP3P water while keeping all nonbonded interactions and the force constant of the harmonic bond unchanged. To model a dipolar solute, we consider a flexible dimer of two Lennard-Jones spheres (OPLS-UA ethane parameters) connected by a harmonic bond, where charges of +1 and -1 are localized on the Lennard-Jones sites. This model is the same as the dipole model considered our previously developed molecular benchmark set. [3]

Again, the results from the standard alchemical decoupling approach for the difference in solvation free energy are compared to the results obtained by using MBAR with mapping between configurational ensembles. The configurations of the dipole corresponding to an equilibrium bond length are mapped to other equilibrium bond lengths according to a center of mass preserving transformation described in the next section. fractional deviation from the equilibrium length preserved.

The equilibrium bond length of dipole used in the initial state is 0.144 nm and in the final state is 0.164 nm, with force constant fixed at 224262.4 kJ/mol/nm². The estimated

standard deviation in the distribution of bond lengths for this force constant is 0.0033 nm, so the equilibrium bond length difference between end states is 61 standard deviations. We simulate with nine equally spaced equilibrium dipole bond lengths intermediate to 0.144 and 0.164 to enable ample configurational space overlap so that free energy estimation using standard MBAR without any configurational mapping is possible. Mapping and re-evaluation of energies are done using the trajectories of the individual state simulations as described in the water models section. Each state was simulated for 10 ns. Other simulation parameters are the same as for the water models. In the case of the dipole exercise the exact same simulations are performed for both standard and mapped calculations; only the postprocessing analysis is different.

4.2.2.4.1 Mapping Dipole with different bond lengths We scale the coordinates of the dipole by the ratio of equilibrium bond lengths, d_j and d_i to map from state j geometry to state i geometry as shown in Figure 4.3.

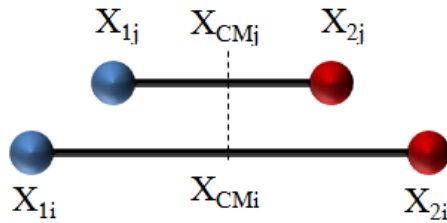


Figure 4.3: Transformation of equilibrium bond lengths in dipole

$$\begin{aligned} X_{1j} &= X_{CMj} + (X_{1j} - X_{CMj}) \frac{d_i}{d_j} \\ X_{2j} &= X_{CMj} + (X_{2j} - X_{CMj}) \frac{d_i}{d_j} \end{aligned} \tag{4.31}$$

We can write these conditions in the form of a matrix

$$\begin{aligned}
T_i^{-1}(T_j(\mathbf{X}_{\text{jn}})) &= \begin{bmatrix} \frac{1}{2} - \frac{d_i}{2d_j} & \frac{1}{2} + \frac{d_i}{2d_j} \\ \frac{1}{2} + \frac{d_i}{2d_j} & \frac{1}{2} - \frac{d_i}{2d_j} \end{bmatrix} \times \begin{bmatrix} \mathbf{X}_{\text{jn}}(1) \\ \mathbf{X}_{\text{jn}}(2) \end{bmatrix} \\
T_i^{-1}(T_j) &= \begin{bmatrix} \frac{1}{2} - \frac{d_i}{2d_j} & \frac{1}{2} + \frac{d_i}{2d_j} \\ \frac{1}{2} + \frac{d_i}{2d_j} & \frac{1}{2} - \frac{d_i}{2d_j} \end{bmatrix}
\end{aligned} \tag{4.32}$$

4.3 Results

4.3.1 Water models

4.3.1.1 Free energy differences We start with results for water model transformations, as the harmonic oscillator results are exact and were presented in the section on the models. In Table 4.4 the hydration free energy $\Delta G_{i,hyd}$ is calculated using MBAR without mapping for a single water molecule, using the decoupling method, for all three water models. Uncertainties in free energies are around 0.05 kJ/mol, and uncertainties in H_{vap} are around 0.002 kJ/mol, in both cases much smaller than experimental error. This high precision partly due is due to the large amount of simulation data used, nearly 400 ns in total for each water molecule free energy, a nontrivial amount even for a small water box of about 500 molecules. The heat of vaporization endpoint calculations use only the fully coupled simulation, thus only 20 ns of simulation. The uncertainty in the heat of vaporization calculation using MBAR, utilizing the same data from the free energy calculations, is about half that of the enthalpy of vaporization using simulations only of the coupled endpoint. This is because simulations with similar potentials will have many configurations with nonnegligible Boltzmann weight in the ensemble we are calculating our statistics at. Because error scales as $N_{samp}^{-1/2}$ with N_{samp} the number of samples, it means that we are ef-

fectively extracting $3\times$ extra samples from the 21 intermediates that can be used to compute expectation averages at the fully coupled endpoint.

In Table 4.2, we directly compare the results for the $\Delta\Delta G_{i,hyd}$ generated using the standard single molecule decoupling cycle in Table 4.4 to the mapping cycle presented in this study, contrasted in columns 4 and 5 respectively, via the thermodynamic cycle in Eq. 4.22. Clearly the mapping cycle calculations are far more efficient, with uncertainties at least two orders of magnitude lower. The differences between the two cycles for the calculation are shown in the last column, and are all well within two standard deviations. Since the statistical error is essentially entirely in the alchemical results, we need additional ways of validating the high predicted precision of these mapping based calculations.

Transformation	$\Delta G_{ij,g}$	$\Delta G_{ij,\ell}$	$\Delta\Delta G_{hyd}$ (mapping)	$\Delta\Delta G_{hyd}$ (decoupling)	$\Delta\Delta G_{hyd}$ (mapping) - $\Delta\Delta G_{hyd}$ (decoupling)
a) TIP4P \rightarrow TIP3P	0	-0.0410 \pm 0.0002	-0.0410 \pm 0.0002	0.021 \pm 0.063	0.062 \pm 0.063
b) TIP3P \rightarrow SPC/E	-0.4570	-4.4575 \pm 0.0001	-4.0005 \pm 0.0001	-3.948 \pm 0.063	-0.073 \pm 0.063
c) SPC/E \rightarrow TIP4P	0.4570	4.4984 \pm 0.0002	4.0414 \pm 0.0002	3.927 \pm 0.066	0.094 \pm 0.066
$\Delta G_a + \Delta G_b + \Delta G_c$	0		0.0001 \pm 0.0003	0	

Table 4.2: $\Delta G_{ij,g}$ (column 1) is calculated analytically and $\Delta G_{ij,\ell}$ (column 2) is calculated using MBAR with mapping. The differences $\Delta\Delta G_{hyd}$ (decoupling) are calculated using direct subtraction and error propagation using data from Table 4.4. $\Delta\Delta G_{hyd}$ (mapping) - $\Delta\Delta G_{hyd}$ (decoupling) are zero within two and three standard deviations according to the thermodynamic cycle in Eq. 4.22 for all transformations. Subscripts a , b , and c refer to the transformations labeled a , b and c in the first three rows. The result of decoupling cycle in column 5 of the last row is constrained to be identically zero numerically because it consists of quantities $(i - j) + (j - k) + (k - i)$. The result of the mapping cycle in column 4 of the last row is not constrained to be identically zero numerically as it consists of three independent calculations using different simulations; instead, it is in such close agreement with the thermodynamic cycle in Eq. 4.23 because of the high statistical precision of the approach. All free energies are in kJ/mol.

We therefore examine the cyclic transformation between the three water models described in thermodynamic cycle in Eq. 4.23 for the mapped results in column 4 of the last row, and see that it is zero with extremely high statistical precision; within 3×10^{-4} kJ/mol, demonstrating the extremely low estimated statistical errors, all near 10^{-4} kJ/mol, are in fact accurate. The result of alchemical cycle in column 5 of the last row is constrained to be identically zero numerically because it consists of quantities $(i - j) + (j - k) + (k - i)$. However, the result of the mapping cycle in column 4 of the last row is not constrained to be identically zero numerically, as it consists of numbers generated from three independent simulations; instead, it is in such close agreement with the thermodynamic cycle in Eq. 4.23 because of the efficiency of the method.

Figure 4.5 shows the free energy differences as a function of distance along the coupling term between states. Figure 4.4 shows convergence of free energy estimate using different number of intermediate states, with a fixed amount (10 ns) of sampling. In both cases, we see that the results converge to the correct value qualitatively with only one intermediate state; even with no intermediate states, the free energies are quite close to the limit with more states. More quantitatively, Figure 4.5 shows that the value is indistinguishable to the final results with only five intermediate states.

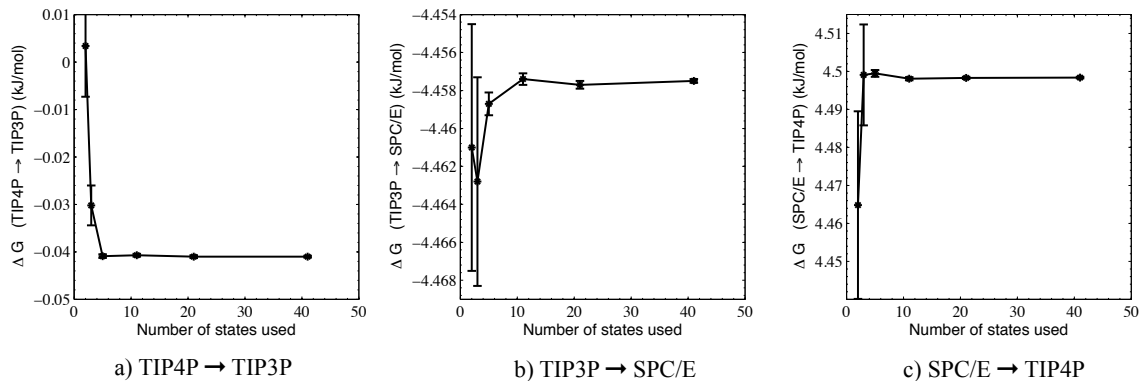


Figure 4.4: Free energy estimates converge with just five intermediate states for all the transformations.

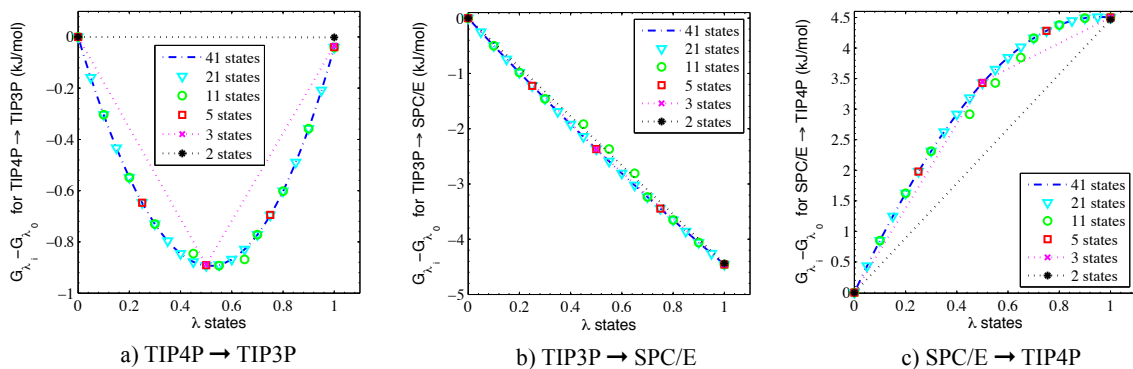


Figure 4.5: Free energies differences along the transformation coordinate are plotted for the three water transformations. Three intermediate states are sufficient to accurately estimate the free energy difference, or a single intermediate state if less precision is required. Uncertainties are the same size as or smaller than the symbols.

Clearly, in most cases there is no need to compute free energies to within 10^{-4} kJ/mol. Instead, these more efficient methods can be used to calculate thermodynamics properties with far less sampling, either reducing the number of intermediates or reducing the length of simulations, drastically improving the throughput of calculations. In Figure 4.6a, we compare both of the methods as a function of the number of samples used and the number

of states along the path simulated for the SPC/E to TIP4P calculation.

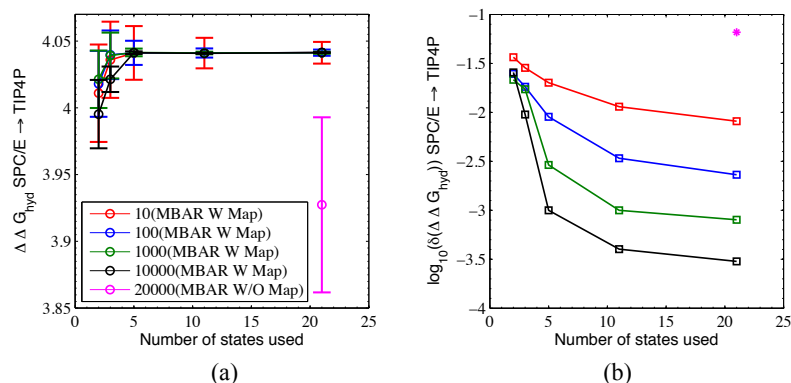


Figure 4.6: $\Delta\Delta G_{hyd}$ for SPC/E–TIP4P estimated using MBAR with mapping with different number of states (2, 3, 5, 11, 21) and number of samples per state (10, 100, 1000, 10 000) has 2–3 orders lower uncertainty compared with $\Delta\Delta G_{hyd}$ for SPC/E–TIP4P estimated using MBAR without mapping with 21 states and 20 000 samples per state.

We examine calculations with 2, 3, 5, 11 and 21 states and 10, 100, 1000 and 10 000 samples per state to calculate $\Delta\Delta G_{hyd}$ between SPC/E and TIP4P models using MBAR with mapping. For all combinations of number of states and number of samples per state, uncertainty in $\Delta\Delta G_{hyd}$ using MBAR with mapping is 2–3 orders of magnitude lower compared to the lowest uncertainty when MBAR without mapping (magenta) is used as seen in Figure 4.6a. This $\Delta\Delta G_{hyd}$ (from Table 4.2, column 5, row 3) is the highest precision decoupling result, using all the available data. In Figure 4.6b, we plot the log of the statistical uncertainty of the calculations. If we consider 0.01 kJ/mol as a useful target uncertainty amount, we can achieve this with only five states and 100 samples per state; if 0.05 kJ/mol is sufficient, the level achieved by standard decoupling methods, then we only require only ten samples using either one or no intermediates (though the bias becomes approximately the same size as the uncertainty in the case of no intermediates).

We can quantify this improvement in efficiency by estimating the number of samples

required of method A to achieve similar precision as method B, assuming that we are in the large sample regime so that the statistical uncertainty scales as $N^{-1/2}$. In this case, then we can express an efficiency of method A compared to method B in terms of the number of samples N_A required to reach the same precision as method B which used N_B samples, via the equation:

$$\frac{N_A}{N_B} = \left(\frac{\delta(\Delta\Delta G_{hyd})_B}{\delta(\Delta\Delta G_{hyd})_A} \right)^2 \quad (4.33)$$

In Figure 4.7 we plot the log of the ratio, $\log_{10}(N(\text{decoupling})/N(\text{mapping}))$, as a function of number of states and number of samples per state. We clearly see that MBAR with mapping is statistically more efficient compared to the standard decoupling calculations without mapping by 2–5 orders of magnitude, and in most cases, closer to five orders of magnitude.

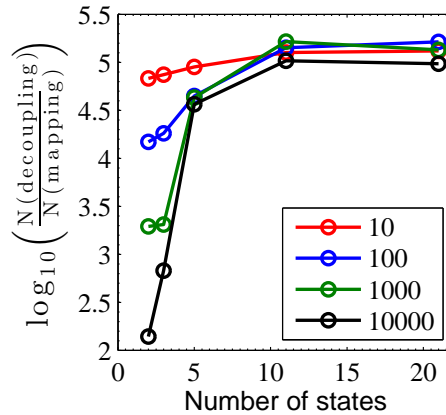


Figure 4.7: Ratio of samples required for MBAR without remapping vs. with remapping to achieve a target statistical uncertainty. Mapping and reweighting approaches requires 10^2 – 10^5 times fewer samples compared to MBAR without mapping to achieve the same precision in $\Delta\Delta G_{hyd}$.

4.3.1.2 Enthalpy and entropy differences Estimation of equilibrium observables using information from all intermediate states, of very different geometries, is also possible using MBAR with mapping. In this study, we specifically calculate the difference in enthalpy of vaporization and the difference in entropy of solvation for all three transformations. The difference in enthalpy of vaporization between two water models is equal to enthalpy of transformation, $\Delta H_{ij,\ell}$, since our transformations only involve water at both end states. We neglect analytical correction factors that can be used to increase the accuracy of comparison to experiment, [11] as they do not affect the statistical uncertainty.

In Table 4.3 column 2, $\Delta H_{vap} = \Delta H_{ij,\ell}$ is evaluated using MBAR with mapping. In Table 4.3 column 3, ΔH_{vap} is calculated by subtracting the heats of vaporization in Table 4.4 evaluated by MBAR. Interestingly, unlike the case of $\Delta\Delta G_{hyd}$, we see that ΔH_{vap} using the mapping and alchemical approaches agree within statistical error, with no improvement in the uncertainties for the mapping transformation. Part of the reason the efficiency of calculating $\Delta\Delta G_{hyd}$ was so high is that the mapping techniques allowed us to use a transformation where we can calculate molar values, and divide the result by N molecules, which was not possible with standard decoupling techniques. However, for H_{vap} , we are already taking advantage of this efficiency gain.

Transformation	ΔH_{vap} = $\Delta H_{ij,\ell}$ (mapping)	ΔH_{vap} (decoupling)	$\Delta S_{ij,\ell}$ (mapping)	$\Delta S_{ij,\ell}$ (decoupling)
a) TIP4P \rightarrow TIP3P	-1.3074 ± 0.0034	-1.3049 ± 0.0027	-4.221 ± 0.011	-4.42 ± 0.21
b) TIP3P \rightarrow SPC/E	6.6674 ± 0.0028	6.6632 ± 0.0025	35.560 ± 0.010	35.37 ± 0.21
c) SPC/E \rightarrow TIP4P	-5.3587 ± 0.0031	-5.3583 ± 0.0028	-31.334 ± 0.010	-30.95 ± 0.22
$\Delta H_a + \Delta H_b + \Delta H_c$	0.0013 ± 0.0054	0		
$\Delta S_a + \Delta S_b + \Delta S_c$			0.005 ± 0.018	0

Table 4.3: All enthalpies are in kJ/mol and all entropies are in J/mol/K. Decoupling ΔH_{vap} s are calculated using direct subtraction and error propagation using data from Table 4.4. The differences $\Delta S_{ij,\ell}$ are calculated using the relationship $\Delta S = (\Delta H - \Delta G)/T$ for both decoupling and mapping cases, with uncertainties propagated using the covariance calculated with MBAR. Subscripts a , b , and c refer to the transformations labeled a , b and c in the first three rows. The thermodynamic cycle in Eq. 4.23 is satisfied for enthalpy H and entropy S . Enthalpies and entropies calculated with decoupling method agree with the ones calculated using mapping formalism within statistical error.

Water Model	ΔG_{hyd} (kJ/mol)	H_{vap} (MBAR) (kJ/mol)	H_{vap} (endpoint) (kJ/mol)
TIP4P	-25.375 ± 0.047	43.7589 ± 0.0021	43.7515 ± 0.0042
TIP3P	-25.354 ± 0.043	42.4540 ± 0.0017	42.4507 ± 0.0035
SPC/E	-29.302 ± 0.046	49.1172 ± 0.0018	49.1132 ± 0.0042

Table 4.4: Solvation free energies, ΔG_{hyd} , and enthalpy of vaporization H_{vap} . H_{vap} estimated using MBAR without mapping (column 3) has half the error as H_{vap} using the standard method of energy averages at the endpoint alone (column 4), as it uses information from nearby intermediate states.

There are other reasons that expectation values cannot be improved as much by increases in overlap as the free energies. As we see in the case of harmonic oscillators, improvements in the efficiency of expectation averages (such as the enthalpy) were due to the increase of effective numbers of samples at each state due to the nonnegligible Boltzmann weighted contributions to the average from samples at nearby states. With the perfect mapping in the harmonic oscillator case, all samples contributed to expectation values at all thermodynamics states. This is not the case with water, however, as the overlap between intermediate states is much lower.

For endpoint reweighting methods, increasing the overlap between the two phase spaces by a factor of 10 decreases the variance roughly by the same factor of 10. [8] If the Boltzmann weights are initially 1%, then the effective contribution of samples from one state to the expectation values at neighboring states using reweighting is only 1% of the samples at the state itself. Increasing the overlap, and thus the Boltzmann weights of neighboring states 10% only increases the effective number of samples by 10%, for a total efficiency gain of $1.10/1.01 = 1.09$ in expectations rather than a factor of 10 improvement for free

energies. Expectation values cannot therefore be improved by as much as free energies can by increasing overlap between neighboring states. Because the exact quantification of overlap integrals in multistate simulations is an ongoing topic of research, it is not possible to make more quantitative comparisons, but the qualitative trend is clear.

Additionally, the neighboring states contributing to the endpoint averages are somewhat different in the mapping case and in the decoupling case. In the decoupling case, intermediate states have $N-1$ identical water molecules, and one water molecule being turned off; in the mapping case, intermediates have all of the molecules changing types slightly, with a mapping to increase phase space overlap. In the limit of fewer intermediates, which clearly is possible, then there will be reduced overlap between alchemical intermediate states. In the case of mapping, when the number of intermediates drops to five, then the ΔH_{vap} results are statistically indistinguishable from using only the endpoints. Fortunately, these endpoint results are already very accurate.

The entropy of transformation is calculated using the relationship $\Delta S = (\Delta H - \Delta G)/T$, with uncertainties in ΔH and ΔG propagated using MBAR. In Table 4.3 columns 4 and 5, the entropy of transformation $\Delta S_{ij,\ell}$ estimated using MBAR with mapping agrees within statistical error, with the entropy of transformation estimated using decoupling methods, for all three transformations. The uncertainty in entropy of transformation using mapping is an order of magnitude lower compared to the single molecule decoupling methods. We only use the MBAR enthalpy differences, because only when using MBAR are we able to accurately compute the correlations between the uncertainties in the free energies and the uncertainties in the enthalpies to propagate into uncertainties in the entropy. Clearly, these uncertainties are not independent, as they are calculated from the same data.

Although enthalpies have not changed significantly by adding mapping, the lower uncertainty of free energies estimated using mapping helps significantly in lowering the un-

certainty in entropy of transformation. In standard procedures for calculating the entropy, obtaining low statistical error can be challenging because of the loss of statistical precision that occurs when subtracting free energies from enthalpies, which may be of similar magnitude, in order to obtain entropies directly. Similar loss of precision occurs when performing finite difference calculations of free energies carried out at two close temperatures, as these free energies are certainly of the same magnitude. However, the case of our study, because of the extremely high precision of both enthalpy and entropy differences, we are able to extract entropy differences between water models with very low uncertainties, only 0.01 J/mol/K, with relatively little computational effort. The thermodynamic cycle in Eq. 4.23 is not only applicable for free energy of transformation but also for other state variables like enthalpy and entropy of transformation. The last two rows in Table 4.3 demonstrate this fact by applying Eq. 4.23 for enthalpy and entropy of transformation and simultaneously validate these results.

We note that the hydration free energies using the decoupling methods do not involve transformation of all the molecules, and the uncertainties are therefore not scaled by the number of molecules. Part of the increase in efficiency using mapping is allowing us to use information from all of the molecules transforming, i.e. changing which cycle we calculate, and not solely using mapping to improve the convergence of a given cycle. Decoupling all the molecules simultaneously to the ideal gas state would have resulted in crossing a phase boundary during the transformation, which would lead to essentially zero overlap and poor efficiency. So although only part of the efficiency gain results *directly* from the mapping, the mapping between states also makes it possible to perform calculations not otherwise possible. One alternate method that could also take advantage of all-molecule transformation would have been a thermodynamic integration of all N molecules between states. However, as thermodynamic integration is not generally as efficient as MBAR, [3]

and also requires an additional calculation of the change of holonomic constraints, such an approach was not pursued in this study.

4.3.2 Dipole transformation

We next examine the results of the free energy of dipole length change. Figure 4.8 and Table 4.5 shows free energies between dipoles of different equilibrium bond lengths calculated using MBAR without mapping (Fig. 4.8a) and MBAR with mapping (Fig. 4.8b). In Fig. 4.8c we see that the MBAR with mapping shows significant improvement in the accuracy as well as precision in the free energy estimates over standard approach for same number of states and number of samples. The free energy differences are calculated using different number of states (2, 3, 5, 11) and different numbers of samples per state (10, 100, 1000, 10 000).

state →	2		11	
samples ↓	(mapping)	(no mapping)	(mapping)	(no mapping)
10,000	-18.337±0.027	-17.986±0.496	-18.316±0.015	-18.227±0.050
1000	-18.333±0.092	-18.351±1.197	-18.334±0.040	-18.224±0.189
100	-18.342±0.257	-18.450±3.512	-18.323±0.158	-18.264±0.469
10	-18.308±1.074	-18.107±7.158	-18.317±0.927	-18.244±1.323

Table 4.5: MBAR with mapping requires just 2 states and 1000 samples per state to estimate converged and precise free energy difference between dipoles of very different equilibrium lengths.

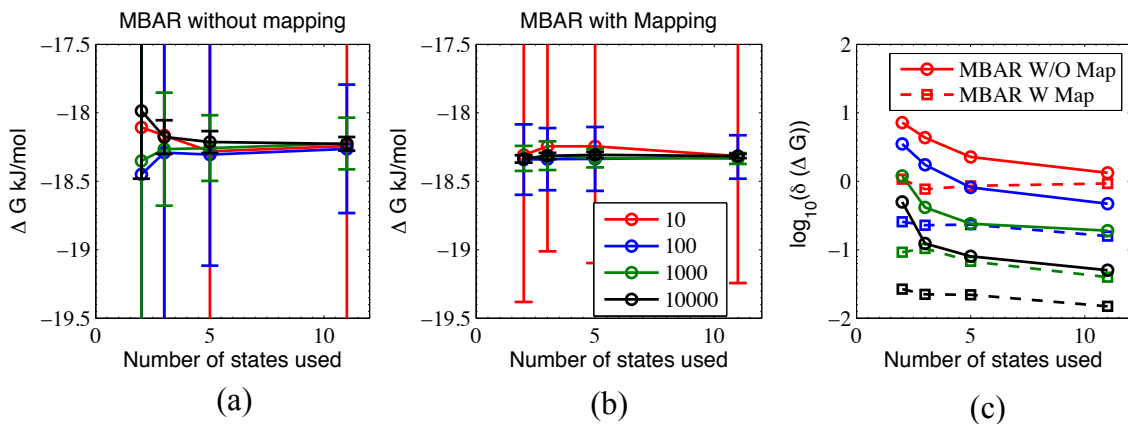


Figure 4.8: The free energy differences between dipoles of different equilibrium lengths are calculated using two approaches: (a) MBAR without mapping and (b) MBAR with mapping. Different number of states (2, 3, 5, 11) and number of samples in each state (10, 100, 1000, 10 000) are used to estimate the free energies. MBAR with mapping estimates converged free energies with low uncertainty using only 2 states and 100 to 1000 samples per state where as MBAR without mapping gives unconverged free energy estimate with high uncertainty unless many intermediates are used. In subplot (c) we see that the uncertainty in free energy using MBAR with mapping is an order lower compared to uncertainty in free energy estimated using MBAR without mapping using the same amount of sampling.

We next compare the statistical efficiency of MBAR with mapping against MBAR without mapping for each combination of number of states and samples per state in Figure 4.9, using Eq. 4.33. We plot the log of ratio of samples required for a given precision $\log_{10}(N(\text{no mapping})/N(\text{mapping}))$ as a function of number of states and number of samples per state.

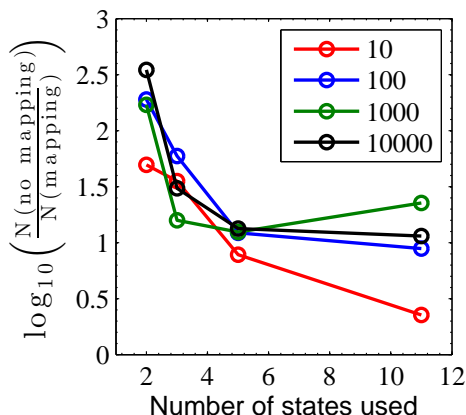


Figure 4.9: Log ratio of samples required for MBAR without remapping vs. with remapping to achieve a target statistical uncertainty for the free energy difference between dipoles of different lengths. Phase space remapping combined with MBAR requires 3–300 times fewer samples compared to MBAR without mapping to achieve the same precision in estimating free energies between dipoles of different length.

Depending on the precise choice of intermediates states, for this calculation MBAR with mapping will require 3–300 times fewer samples compared to MBAR without mapping for the same precision in ΔG . In this case, we see statistical efficiency improvements between 0.5 - 2.5 orders of magnitude, compared to 2–5 orders of magnitude in the case of hydration free energies. In this case, the gain in efficiency is solely because of mapping; the simulations are used for both calculations. For a 0.1 kJ/mol level of uncertainty, we see that 1000 samples with only the two end states is sufficient using mapping; it would require more than 250 000 samples using standard techniques. For 0.25 kJ/mol, or about 0.06 kcal/mol uncertainty, which is frequently the level of experimental precision for accurate solvation free energies, only 100 samples are required with just the two endpoint states.

4.4 Discussion and Conclusions

In this study, we have extended the capacity of multistate reweighting to estimate thermodynamic observables for alchemical transformations involving changes in geometry. The multistate Bennett acceptance ratio method (MBAR) is coupled with configuration mapping to derive the new approach. The approach has been validated and tested using a toy model of truncated harmonic oscillators, the interconversion of SPC/E, TIP3P and TIP4P water models, and the free energy difference of change in equilibrium bond length of a dipole. Mapping between mutually inaccessible configurations and speedup achieved by using reweighting combined with mapping can enable very high-throughput thermodynamic property prediction required for exploring large parameter and chemical spaces.

The mapping algorithm estimates the free energy between the truncated harmonic oscillators with zero error, independent of the number of samples. Estimates of free energy, enthalpy and entropy of transformation of water molecules are verified by the thermodynamic cycles within two to three standard deviations. Estimates of free energy of transformation of dipole equilibrium bond length also agree with results obtained from alchemical approach within two to three standard deviations. In both the water model and dipole examples, we require very few samples and intermediate states if we use mapping with multistate reweighting. The mapping algorithm improves the statistical efficiency of thermodynamic property estimation by up to five orders of magnitude compared to standard decoupling approaches, with the advantage most pronounced for free energies and entropies.

The mapping technique can potentially be applied to force field parameterization or to any problem which involves estimation of thermodynamic observables over two or more states having poor or no overlap in configurational space, as long as an appropriate mapping can be constructed. For example, one could compute the free energy difference between

a coarse grained potential with the same number of degrees of freedom; for example, the free energy difference between a rigid phenyl ring and a three or four site model with the same symmetry. One could compute the free energies and enthalpies of transformation between serine and cystine, or between chloro- and bromo- halogenates with very little error, using mapping to account for bond length differences. It would be less useful for transformations where the changes in the energy terms are large enough to dominate the weightings of individual states even when the geometries are similar. For example, the change from dipole to monopole would likely dominate the computation of free energy differences when morphing a water molecule to a ion.

Deriving an appropriate invertible mapping is a limiting factor but simplicity in implementation, high efficiency of information usage and tremendous reduction in number of samples required for analysis should encourage future applications of this approach. Generally, molecular mappings that maintain the center of mass will be more straightforward, as the center of mass and intramolecular partition functions will be separable. Mappings that minimize changes in excluded volume will also increase the overlap, so shifts of atoms by only 10–20% of the Lennard-Jones radii will be more efficient than mappings that drastically change excluded volume potentials. Aligning atomic sites in the end states is therefore recommended. We had outlined in detail the transformation process used to map between water models and dipoles of different lengths as examples.

We emphasize that this analysis technique does not alter the collection of data at all, only the analysis. The time required to sample each new uncorrelated samples when performing simulations remains unchanged. If uncorrelated samples cannot be obtained at all, this method will still have bias. The reduction of error is because the number of correlated samples required to converge the physical quantity of interest is greatly decreased.

We also emphasize that this approach works well when the end state configuration en-

sembles differ explicitly in the geometric parameters used to define the states, such as bond lengths and angles. In the case of representing a complex many body system evolving on a multidimensional landscape in a mean field way, the identification of a proper coordinate transformation, if any, is generally an intractable problem. Most mean field approaches use an approximate function that has a simplified energy function, but not necessarily different geometric configurations. Standard energy reweighting methods would be the most appropriate in those cases.

A number of avenues are possible to explore further using this formalism. Improving the estimation of observables between phase spaces with different discrete symmetries or that have changing numbers of degrees of freedom are beyond the scope of this chapter, but would be very interesting to address with this formalism. The extension to differences in discrete symmetries would be likely be straightforward, through the inclusion of proper symmetry factors, though the mapping between different degrees of freedom would not be as simple.

In this study, we have also restricted ourselves to coordinate independent transformations that preserve the center of mass. However, we could use transformations that are coordinate dependent, for example, a map between dihedral angle distributions of different amino acid side chains. The only difference is that since these transformations are coordinate dependent, the term must be directly added before performing multistate reweighting, instead of being added on after the analysis. Another possibility would be transformations of the locations of the molecular centers of mass, which would make it possible to construct maps between molecular systems of different average densities, or between NVT simulations performed at different volumes. Additional transformations beyond those discussed here are likely to yield even more interesting and effective approaches to estimating differences in thermodynamic properties as a function of molecular transformation.

5 Using the multistate reweighting and mapping algorithm to identify and optimize models in water-like model parameter space

5.1 Introduction

Classical force field parameterization is computationally intensive [94]. Bonded parameters such as bond length, bond angle and dihedral angle, are estimated using quantum chemical calculations and/or fit to spectroscopic data. However, the nonbonded parameters, especially Lennard-Jones (LJ) parameters, are usually difficult to determine from first principles calculation or from experiments [95, 96, 97, 98].

The nonbonded parameters, charge q and LJ σ , ϵ are generally fit to reproduce experimental observables [96, 99]. The fitting procedure involves computationally expensive molecular simulations to estimate observables at each iteration. The new set of parameters is either guessed based on a trial and error approach [100] or is generated by simplex or gradient based optimization [94]. The time spent in either case is dominated by evaluation of the objective function which requires fresh generation of samples for a new guess of parameter set. Hence, we can accelerate the force field parameterization process if we can reduce the time spent in sampling at each iteration.

In this chapter we present an accelerated force field parameterization scheme. We gain speed by skipping several steps of molecular simulation, replacing these runs using reweighting techniques to estimate the observables with well-bounded precision. The reweighting formalism requires re-evaluation of the energies with the new set of parameters using the configurations generated in simulations run with the initial guess set of parameters. The time required to estimate observables using re-evaluated energies is orders of

magnitude less compared to a fresh simulation. Chaimovich and Shell [101] have recently proposed an reweighting-based coarse-graining parameterization scheme. Their scheme, however, does not use multistate reweighting or configuration mapping tools.

Re-weighting works well as long as there is sufficient phase space overlap between the iterated and the sampled parameter sets [4, 30, 8]. Each parameter set represents a distinct alchemical thermodynamic state. We need molecular simulations when or if phase space overlap between two states decreases to a level that makes the uncertainties unacceptable. The increase in uncertainty in the estimated thermodynamic quantities indicates decreasing phase space overlap between two states. Large uncertainty makes the comparison between the observables between two iterations difficult, requiring additional simulation data. To verify the simulations, we must also perform fresh simulations whenever the error is minimized, to ensure that our predicted ensemble has not deviated too much from the true ensemble that would be generated with those parameters.

We will have to use the configurational mapping algorithm introduced in Chapter 4 as we iterate over geometry parameters in order to create phase space overlap between these states. It has been shown in previous chapter that we require very few samples to calculate accurate and precise expectation values and free energy estimates for parameter perturbations in water models. By implementing a combination of reweighting and the mapping techniques we should be able to get substantial reductions in computational costs involved in parameterization based on free energy estimates and other thermodynamic observables.

In this chapter, we demonstrate the applicability of the parameterization scheme by modeling liquid water. In the process, we also explore the multidimensional water model parameter space to set bounds on each dimension. The different parameters in a water model as shown in Figure 5.1 are: charge q_O , LJ σ and ϵ of oxygen, OH bond length, HOH bond angle, OM distance between the virtual site (carrying the negative charge) and

oxygen atom. The charge on both the hydrogens is necessarily $+q_O/2$. The LJ σ and ϵ of both hydrogens are chosen in this family of models to be zero. We effectively then have six parameters $\{q_O, \sigma_O \text{ and } \epsilon_O, r_{OH}, \angle HOH, r_{OM}\}$ which are varied to identify regions in parameter space for water-like models.

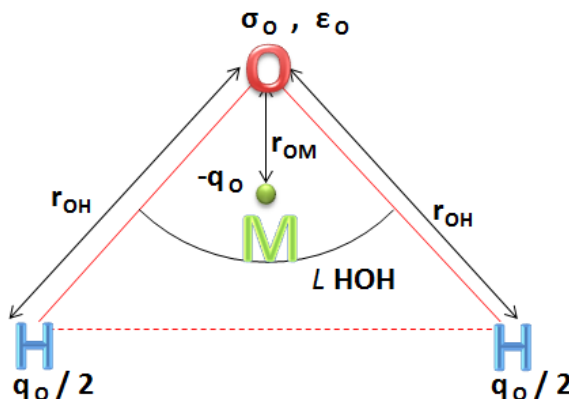


Figure 5.1: There are three nonbonded parameters, σ_O , ϵ_O , and q_O and three geometry or bonded parameters r_{OH} , $\angle HOH$, and r_{OM} in water model. σ and ϵ for hydrogen are zero and once q_O is fixed we also know the partial charge on the two hydrogens.

We model liquid water for a temperature range of 273–373 K and pressure range of 1–120 atm. Although the parameterization can be done to span the entire phase equilibrium of water, it is very hard to sample near phase boundaries because of density fluctuations and sampling is especially hard in solid state [102] where the kinetics is slow. The large phase space separation of liquid and vapor phase spaces prohibits reweighting between these states and the subsequent calculation of observables using molecular dynamics simulations of one phase to predict the other phase. shifts in the center of mass of the molecules in the box. Configurational mapping over different phases is a subject for future study. In this study, we apply configurational mapping in a single phase to parameterize the water model.

There are a large number of water models which were parameterized in different ways with different optimization goals, and we discuss some of the most common models here.

TIP, TIP3P and TIP4P models were parameterized to reproduce structural and energetic results for water dimer and density of liquid water at a single temperature 298 K [103]. TIP4P-Ew was parameterized by fitting the parameters to experimental density and heat of vaporization for a range of temperatures [11]. SPC-E [10] includes corrections due to self-polarization and cannot give good results for protein based force field which does not account for the polarization effects [104]. Because of this, the self-solvation free energy for SPC-E is 4.8 kJ/mol greater than the other water models. This can cause errors in calculation and interpretation of solvation free energy (excess chemical potential) of small molecules which are parameterized with respect to TIP3P water model. The polarizable water models [105, 106] also do not combine well with biomolecular force fields which neglect polarization effects. Accounting for the polarization can significantly increase the computational costs. Because of this, researchers prefer not to use polarization if possible. It is also hard to parameterize these models, since the most appropriate form of the polarization contribution for a given problem isn't properly understood. We thus do not introduce polarization in modeling water in this study.

The flexible water models, MCYL [107], SPC-F1, SPC-F2 [108] satisfactorily reproduce energetics and dynamics of water but are computationally more costly and can even introduce artifacts [104]. Glättli [104] et al. proposed the need for a better parameterized rigid, non-polarizable water model. Glättli et al. used a trial and error approach to change $\angle\text{HOH}$, LJ sites, charge, bond length to improve structural, dielectric thermodynamic and transport properties.

A more holistic parametric search method was proposed by Horn [11] et al. which they used to design TIP4P-Ew model. They searched through the parameter space by minimizing the square of the residual between simulated and experimental density at various temperatures and at 1 atm pressure. But their algorithm perturbed only σ_O , ϵ_O and q_O for

a fixed same vapor phase geometry. Horn et al. adopted the assumptions made in TIP4P model for geometrical parameters that the liquid phase molecular geometry of the water molecule should not be very different from that of the experimentally observed gas phase geometry. However, the effect of this assumption was never examined. In fact, all the TIPnP water models use the experimental gas phase OH bond length (r_{OH}), and HOH bond angle ($\angle HOH$), and only parameterize oxygen's LJ parameters σ_O , ϵ_O and charge q_O for 3 site models. In 4 site rigid water models, the distance between the virtual site which carries negative charge of the oxygen atom, (r_{OH}), in the plane of the water molecule, along the angle bisector of $\angle HOH$ is also optimized.

In this study, we instead perform a multidimensional optimization in all six dimensions and fit to multiple properties for a range of temperatures and pressures by fitting the full simulated residual free energy surface $G_{res,sim}(T, P, \mathbf{x})$, \mathbf{x} being the vector of parameters, to the experimental residual free energy surface $G_{res,exp}(T, P)$. In the methods section, we show the development of this powerful new forcefield parameterization scheme.

In this study, we also use an analytical model of water derived using Wertheim's thermodynamic perturbation theory to guide the design of our objective function. These analytically solvable models are popularly called statistical association fluid theory (SAFT) models. A SAFT model includes atomistic energy and geometry parameters. The contributions due to the Lennard-Jones, coulombic and hydrogen bond interactions to the residual Helmholtz energy are estimated with respect to an ideal gas reference state. The residual Helmholtz free energy-based equation of state derived for a SAFT model is a much quicker way to estimate a vector of thermodynamic properties $\mathbf{F}(\mathbf{x})$ as a function of atomistic parameter set \mathbf{x} , compared to running atomistic simulations, though the vector of molecular parameters may behave differently in the two models.

This large scale parameterization of water models is made possible by the previous two

studies which dramatically increase the efficiency of free energy calculations for a very large number of thermodynamic states [3] with little or no configurational map [38]. Like all other parameterizations our scheme also involves iterations to convergence. Marco [94] et al. have proposed a gradient based parameterization work flow for the automated development of molecular models. But Marco et al. use the standard computationally expensive molecular simulation to estimate properties at each iteration. One could use direct methods like Nelder-Mead simplex [109] instead of gradient methods but such more robust direct methods converge slowly. We cannot use simplex or gradient-based method because the simplex algorithm does not support multiobjective optimization and in gradient based methods the use of the gradient with very small step length, when optimal step length is not known, makes the convergence very slow. Calculation of optimal step length or the use of Hessian based method is computationally prohibitive. Instead, we use a mesh adaptive direct search [110, 111] method which appears best suited for our problem type. We discuss the efficacy of different optimization methods and compare them further in the methods section. We replace the time-consuming MD step by a faster reweighting plus configuration mapping step to estimate properties at each iteration. The configurational mapping reduces the amount of samples, which have to be generated using the initial set of parameters and the reweighting reduces the need to generate new samples at new iterated sets of parameters.

5.2 Methods

5.2.1 Property estimation

5.2.1.1 Water properties from experimentally fitted equation of state The International Association for the Properties of Water and Steam 1997 formulation, IAPWS97, [112]

uses an empirically fitted Gibbs free energy based equation of state to derive thermodynamic properties. We require the experimental residual Gibbs free energy contribution of the total Gibbs free energy to parameterize our atomistic water model. However, the residual and ideal gas contributions are not reported separately for the liquid phase region in the IAPWS97 formulation. So we use IAPWS95 [113] formulation which gives both the residual and the ideal gas Gibbs free energy contributions for liquid water regime. Similar to IAPWS97, in IAPWS95 the Helmholtz free energy based equation of state is fitted to reproduce experimentally observed water properties. Additionally, IAPWS95 is more accurate compared to IAPWS97 as IAPWS97 was primarily designed for faster calculations and sacrifices some accuracy. We have implemented and validated the IAPWS95 formulation in a Python script to reduce heterogeneity in the computational pipeline set up for the project and is available for future use as well. IAPWS95 is a pressure-explicit equation of state, i.e. properties are expressed as a function of density and temperature. However, generating the reweighted ensemble as a function of both temperature and pressure using molecular dynamics is much easier if we have properties as a function of pressure and temperature. We therefore back-calculated a density giving the desired pressure at a given temperature and used this density and temperature to estimate properties from IAPWS95 equation of state. Specifically, we find a density which would give $P_{simulation} - P_{IAPWS95}(\rho, T) = 0$ using 1000 kg/m^3 as an initial guess density. The root is found using the fsolve scipy module which is actually a wrapper around MINPACK's hybrd and hybrj algorithms.

5.2.1.2 Water properties from SAFT based equation of state

5.2.1.2.1 SAFT water model description There exist various flavors of SAFT water models in the literature [114, 115]. They differ primarily in the way the Lennard-Jones,

electrostatic and hydrogen bond association interactions are modeled. Clark et al. [115] give a nice overview of the history and development of the SAFT water models. In their current state the SAFT water models use square well potential to model the LJ and electrostatic interactions. However, in atomistic simulation we model Lennard-Jones as 12-6 potential and electrostatics by a Coulomb potential.

Muller and Gubbins' [116] SAFT water model comes closest to our atomistic water model. They model water as a Stockmayer fluid in which there is an attractive-repulsive Lennard-Jones core along with the dipole for accounting electrostatic interactions. The hydrogen bonding association interaction is estimated using Wertheim's first order perturbation theory and is modeled using square well potential.

The intermolecular SAFT potential can therefore be written as a sum of a medium range Lennard-Jones interaction ϕ_{LJ} , a short range hydrogen bonding potential ϕ_{HB} and a long range dipole potential, ϕ_{DD} .

$$\phi_{SAFT} = \phi_{LJ} + \phi_{DD} + \phi_{HB} \quad (5.1)$$

5.2.1.2.2 Property estimation from SAFT model The power of SAFT models lies in mapping molecular interaction parameters to an analytically solvable equation of state. All the interactions contribute to the residual free energy. All the interactions are modeled as a function of temperature and density so the natural choice of free energy function is the Helmholtz free energy. The analytical estimation of the residual Helmholtz free energy contributions are done with a system of reduced units commonly used in SAFT models.

$$\begin{aligned}
\rho^* &= \rho \sigma_{LJ}^3 \\
T^* &= \frac{k_B T}{\epsilon_{LJ}} \\
P^* &= \frac{P \sigma_{LJ}^3}{\epsilon_{LJ}} \\
\mu^{*2} &= \frac{\mu^2 \sigma_{LJ}^3}{\epsilon_{LJ}} \\
U^* &= \frac{U}{N \epsilon_{LJ}} \\
A^* &= \frac{A}{N \epsilon_{LJ}}
\end{aligned} \tag{5.2}$$

In the above set of equations ρ is system density at temperature T . For a given ρ and T the system exhibits a pressure P . The molecular dipole is μ , while σ_{LJ} and ϵ_{LJ} are the Lennard-Jones parameters. U is the potential energy of the system and A is the Helmholtz free energy of the system. The different contributions to the residual Helmholtz free energy for reference fluid are:

$$A_{res} = A_{res}^{LJ} + A_{res}^{DD} + A_{res}^{HB} \tag{5.3}$$

A_{res}^{LJ} is contribution due to LJ potential as described in Kolafa and Nezbeda's paper [117].

A_{res}^{DD} is contribution due to dipole dipole interaction as explained by Gray and Gubbins [118]. The

sum of A_{res}^{LJ} and A_{res}^{DD} is estimated using the Padé approximation for the free energy.

$$\begin{aligned} A_{res}^p &= A_{res}^{LJ} + A_{res}^{DD} \\ &= A_{res}^{LJ} + A_2 \left[1 - \frac{A_3}{A_2} \right]^{-1} \end{aligned} \quad (5.4)$$

In the above equation A_{res}^{LJ} is the residual Helmholtz free energy for a pure Lennard-Jones fluid. Polynomial equations exist to estimate A_{res}^{LJ} . The first order perturbation term vanishes. A_2 and A_3 are the second and the third order perturbation terms. A_2 and A_3 are estimated using the following equations.

$$\begin{aligned} A_2^* &= - \frac{2\pi}{3} \frac{\rho^* \mu^{*4}}{T^*} J \\ A_3^* &= - \frac{32\pi^3}{135} \left(\frac{14\pi}{5} \right)^{1/2} \frac{\rho^{*2} \mu^{*6}}{T^{*2}} K \end{aligned} \quad (5.5)$$

J and K are the integrals over the two and three body correlation functions of Lennard-Jones fluid. A_{res}^{HB} is contribution due to hydrogen bond interaction as modeled in Muller

and Gubbins's paper.

$$\begin{aligned}
A_{HB}^* &= T^*(\ln X_a^4 - 2 * X_a + 2) \\
X_a &= \frac{-1 + (1 + 8\rho\Delta)^{1/2}}{4\rho\Delta} \\
\Delta &= 4 * \pi F_{HB} K_{HB} I \\
F_{HB} &= \exp(\epsilon_{HB}/k_B T) - 1 \\
I &= \frac{1}{24b^2\sigma_{LJ}^3} \int_{2b-\sigma_{HB}}^{2b+\sigma_{HB}} g(r)(\sigma_{HB} + 2b - r)^2(2\sigma_{HB} - 2b + r)rdr
\end{aligned} \tag{5.6}$$

$g(r)$ is the LJ pair correlation function. The integral I can be evaluated numerically for a given σ_{HB} , the diameter of the square well association site, and the distance between the center of the square well site and the LJ center, b . K_{HB} is the association constant fit to reproduce experimental properties. X_a is the fraction of molecules not bonded at site a . From the Equations 5.4 - 5.6 we see that the SAFT water model consists of following six parameters. σ_{LJ} , ϵ_{LJ} , μ , K_{HB} , σ_{HB} , ϵ_{HB} .

For a given SAFT parameter set if we can estimate A_{res} as a function of ρ and T , we essentially have an equation of state from which all thermodynamic properties can be estimated. Using the SAFT model we can estimate residual Helmholtz free energy A_{res} , residual internal energy $U_{res} = \frac{\delta(A/T)}{\delta(1/T)}$, pressure $P = \rho T + \rho^2 \frac{\delta A}{\delta \rho}$ and residual chemical potential $\mu_{res} = A_{res} + \frac{P}{\rho} - T$ which are sufficient for doing any phase equilibrium calculation.

We modified an implementation provided by Prof. Eric Muller to use in our study. Prof. Muller's implementation was designed to calculate properties as a function of density and temperature, whereas, we needed a SAFT implementation which estimated properties as a function of pressure and temperature. We did this by first calculating the density which

resulted in system pressure at a given temperature using the SAFT equation of state. However finding the correct density to reproduce the correct pressure was **not** trivial problem as it was in IAPWS equation of state, as for a random set of SAFT parameters we don't know what is the corresponding approximate liquid density at a given temperature. For example, if we pick random values for σ_{LJ} , ϵ_{LJ} , at a given temperature we cannot say how different the SAFT compressed liquid density will be from experimental compressed liquid density at NTP. Thus picking a suitable initial guess for compressed liquid density for a set of SAFT parameters at a given temperature makes the problem challenging. However, we know that the compressibility of water (both true water and SAFT-modeled) is very small, there is a very little difference between the saturated liquid density and the compressed liquid density for pressures greater than the saturation pressure at a given temperature. We used this fact to arrive at the initial guess for the density in solving the problem. We first did a two phase calculation for the given set of SAFT parameters \mathbf{x}_{SAFT} at a given temperature to get the saturated liquid density. We used this saturated liquid density as the initial guess to start a bisection root method with upper and lower bounds defined as $\pm 10\%$ of the initial guess to find the correct density which would satisfy $P - P_{SAFT}(\rho, T, \mathbf{x}_{SAFT}) = 0$. The original SAFT model by Prof. Muller and the reconfigured SAFT model are Fortran executables which can be called through Python scripts.

5.2.1.3 Water properties from an atomistic model

5.2.1.3.1 Atomistic model description There are many existing water models [9, 10, 11] with varying levels of complexity. Bertrand Guillot [119] gives a good review of a lot of water models. The web resource <http://www.lsbu.ac.uk/water/models.html> maintained by Martin Chaplin is also a useful guide to the efforts made

historically to model water atomistically. The most popular water models are the ones which are simple to implement and are computationally less expensive. So a vast array of polarizable water models and flexible water models are not included in the design space. We focus on rigid water models. The TIP4P water models, especially the TIP4P-Ew and other more recent variations reproduce experimental densities better than other water models.

We therefore use a basic framework of four site TIP4P water model in which there is single LJ site on the oxygen atom. There are positive partial charges on the two hydrogens and the negative partial charge of oxygen lies on the angle bisector of the HOH angle. The partial charges sum to zero to make the molecule electrostatically neutral. The OH bonds are symmetric in length and the entire molecule is rigid i.e. all vibrational degrees of freedom are frozen. The total potential energy comprises of a Lennard-Jones potential and electrostatic potential contributions as there are no bonded interactions. The short range Lennard-Jones is modeled by a 12-6 potential and the long range dispersion is analytically estimated only for the attractive part since the dispersion correction for the repulsive part is negligibly small. The electrostatic potential is modeled using Coulomb potential. The pairwise Coulomb contribution is estimated using a Particle Mesh Ewald sum. More description on the estimation of the Lennard-Jones and the Coulomb contributions can be found in our previous chapter.

5.2.1.3.2 Property estimation from molecular simulations Density, isobaric and isometric heat capacities, isothermal and adiabatic compressibilities, isobaric thermal expansion coefficient and thermal pressure coefficient are well-studied response functions for fluids [120, 121]. Of these density, isobaric heat capacity, isothermal compressibility, and isobaric thermal expansion coefficient, along with the heat of vaporization are most com-

monly used to characterize water models [11, 122]. In this study, we examine the less commonly used residual Gibbs free energy of water (which is also equal to hydration free energy of a water molecule) in the list of properties used to parameterize a water model.

We can estimate the properties either using a) fluctuation formulas based on ensemble averages or b) derivatives of Gibbs free energy with respect to temperature and pressure. Almost all water model studies [121, 11, 122] use fluctuation formulas to calculate properties. However, we will use the derivatives of free energy using finite difference using reweighting, as we can propagate the error more easily than can be done with the fluctuation formulas. Derivatives of free energy with respect to pressure or temperature can be computed numerically and the calculation is made trivially cheap by reweighting, since reweighting at different temperatures and pressures requires no additional energy calculations.

Bulk density ρ

$$\langle \rho \rangle = \frac{N_{water} M_{water}}{N_A \langle V \rangle}; \delta(\langle \rho \rangle) = \langle \rho \rangle \frac{\delta \langle V \rangle}{\langle V \rangle} \quad (5.7)$$

Alternately we can find density by:

$$\rho = \frac{N_{water} M_{water}}{N_A V} = \frac{N_{water} M_{water}}{N_A \left(\frac{\partial G}{\partial P} \right)_{T,N}} \quad (5.8)$$

N_{water} is the number of water molecules in the simulation box, N_A is the Avogadro's number, M_{water} is the molecular mass of water.

Heat of vaporization H_{vap} At a given pressure and temperature

$$H_{vap} = H_{gas} - H_{liq} \quad (5.9)$$

$$\approx (U_{gas} + K_{gas} + PV_{gas}) - (U_{liq} + K_{liq} + PV_{liq}) + C$$

For ideal gas, $U_{gas} = 0$ and molecular kinetic energies are identical in the gas and liquid. Several water models apply corrections C to incorporate vibrational (C_{vib}), polarization (C_{pol}), non ideal gas (C_{ni}) and pressure effects (C_x) as explained by Horn et al. [11] in Eqs. 21–27 in their paper.

$$C(T, P) = C_{vib}(T) + C_{pol} + C_{ni}(T, P_{vap}) + C_x(T, P) \quad (5.10)$$

The heat of vaporization expression finally has the following form:

$$H_{vap} \approx -\langle U_{liq} + PV_{liq} \rangle + k_B T + C \quad (5.11)$$

Here we have replaced PV_{gas} with $k_B T$, pushing deviations from ideality into C .

Isobaric heat capacity C_P

There are three ways we can calculate enthalpy.

1. By the enthalpy fluctuation formula

$$C_P = \frac{\langle H^2 \rangle - \langle H \rangle^2}{Nk_B T^2} \quad (5.12)$$

2. By the first derivative of enthalpy with respect to temperature

$$C_P = \left(\frac{\partial \langle H \rangle}{\partial T} \right)_{P,N} \quad (5.13)$$

The derivative could be numerically calculated by reweighting configurations sampled at temperature T for new temperatures $T - \delta T$ and $T + \delta T$ at constant pressure.

3. By second derivative of Gibbs free energy.

$$C_P = -T \left(\frac{\partial S}{\partial T} \right)_{P,N} = -T \left(\frac{\partial^2 G}{\partial T^2} \right)_{P,N} \quad (5.14)$$

The second derivative can also be calculated numerically by reweighting configurations sampled at temperature T for new temperatures $T - \delta T$ and $T + \delta T$ at constant pressure.

We will use the third formula to estimate C_P due to reasons described before.

Isothermal compressibility κ_T

The volume fluctuation formula to compute κ_T is:

$$\kappa_T = \frac{\langle V^2 \rangle - \langle V \rangle^2}{k_B \langle T \rangle \langle V \rangle} \quad (5.15)$$

Alternately we can also find κ_T using the following formula:

$$\kappa_T = -\frac{1}{V} \left(\frac{\partial V}{\partial P} \right)_{T,N} = -\frac{\left(\frac{\partial^2 G}{\partial P^2} \right)_{T,N}}{\left(\frac{\partial G}{\partial P} \right)_{T,N}} \quad (5.16)$$

We can get all the differences by reweighting the configurations sampled at pressure P for new pressures $P + \delta P$ and $P - \delta P$ at constant temperature. We will use this formula to compute κ_T .

Isobaric thermal expansion coefficient α_p The enthalpy volume fluctuation formula to estimate α_p is.

$$\alpha_p = \frac{\langle VH \rangle - \langle V \rangle \langle H \rangle}{k_B \langle T \rangle^2 \langle V \rangle} \quad (5.17)$$

However, we calculate α_p using the following formula:

$$\alpha_p = \frac{1}{V} \left(\frac{\partial V}{\partial T} \right)_{P,N} = - \frac{\left(\frac{\partial^2 G}{\partial P \partial T} \right)}{\left(\frac{\partial G}{\partial P} \right)_{T,N}} \quad (5.18)$$

5.2.1.4 Relationship between simulated and IAPWS95 residual Gibbs free energies

From simulations we get Gibbs free energies corresponding to NPT ensemble, whereas IAPWS95 gives Gibbs free energies corresponding to a NVT ensemble. The difference lies in the ideal gas reference states since $G_{id}(T, P)$ in the NPT ensemble is not equal to $G_{id}(T, \rho)$ in the NVT ensemble. This difference will become more clear as we go through the statistical mechanical derivation of $G_{id}(T, P)$ and $G_{id}(T, \rho)$. Using explicit statistical mechanical definitions of the latter two terms we will then derive the relationship between the simulated and IAPWS95 residual Gibbs free energies.

Let us start with the NVT ensemble. Molar Helmholtz free energy, a , in a NVT ensemble can be expressed as a sum of residual molar Helmholtz free energy, a_{res} , and ideal gas molar Helmholtz free energy, a_{id} . This sum assumes ideal gas as the standard state in which all the intermolecular interactions are zero. Any non-zero intermolecular interaction contributes to a_{res} .

$$a = a_{res} + a_{id} \quad (5.19)$$

From statistical mechanics Helmholtz free energy can be written down in terms of the

canonical partition function $Q(N, V, T)$.

$$\begin{aligned}
a &= \frac{-k_B T}{N} \ln(Q(N, V, T)) \\
Q(N, V, T) &= \frac{1}{N! h^{3N}} \int_{x=-V^{1/3}/2}^{x=V^{1/3}/2} \int_{p=-\infty}^{p=\infty} \exp(-\beta(U(x) + K(p))) dp^{3N} dx^{3N} \\
&= \frac{1}{N! h^{3N}} \int_{p=-\infty}^{p=\infty} \exp(-\beta K(p)) dp^{3N} \int_{x=-V^{1/3}/2}^{x=V^{1/3}/2} \exp(-\beta U(x)) dx^{3N} \\
&= Q_{tr} Q_c
\end{aligned} \tag{5.20}$$

Thus we can estimate the translational and configurational contribution to canonical partition function.

$$\begin{aligned}
Q_{tr} &= \frac{1}{N! h^{3N}} \int_{p=-\infty}^{p=\infty} \exp(-\beta K(p)) dp^{3N} \\
&= \frac{1}{N! \Lambda^{3N}} \\
Q_c &= \int_{x=-V^{1/3}/2}^{x=V^{1/3}/2} \exp(-\beta U(x)) dx^{3N}
\end{aligned} \tag{5.21}$$

Here Q_{tr} is the translational partition function contribution. For brevity, we do not consider rotational and vibrational partition function contributions. However, the absence of rotational and vibrational partition function does not change our findings. Q^c is the configurational partition function contribution.

The ideal gas partition function can be calculated by putting $U(x)=0$.

$$\begin{aligned}
a_{id} &= \frac{-k_B T}{N} \ln(Q_{id}(N, V, T)) \\
Q_{id}(N, V, T) &= \frac{1}{N! h^{3N}} \int_{p=-\infty}^{p=\infty} \exp(-\beta K(p)) dp^{3N} \int_{x=-V^{1/3}/2}^{x=V^{1/3}/2} dx^{3N} \\
&= Q^{tr} * V^N \\
Q_{id}^c &= V^N
\end{aligned} \tag{5.22}$$

So the residual molar Helmholtz free energy a_{res} can be found by the difference of a and a_{id}

$$\begin{aligned}
a_{res} &= a - a_{id} \\
&= \frac{-k_B T}{N} \ln(Q(N, V, T)) + \frac{-k_B T}{N} \ln(Q_{id}(N, V, T)) \\
&= \frac{-k_B T}{N} \ln\left(\frac{Q^c}{Q_{id}^c}\right)
\end{aligned} \tag{5.23}$$

Similarly molar Gibbs free energy g for the NPT ensemble can be expressed as a sum of residual molar Gibbs free energy g_{res} and ideal gas molar Gibbs free energy g_{id} . This sum also assumes ideal gas as the standard state in which all the intermolecular interactions are zero. Any non zero intermolecular interaction contributes to g_{res} .

$$g = g_{res} + g_{id} \tag{5.24}$$

From statistical mechanics the Gibbs free energy can be written in terms of isothermal isobaric partition function $\Xi(N, P, T)$. $V^{1/3}$ is equal to the side L of a cubical box so we

will use L in place of $V^{1/3}$.

$$\begin{aligned}
g &= \frac{-k_B T}{N} \ln(\Xi(N, P, T)) \\
\Xi(N, P, T) &= \int_{V=0}^{V=\infty} (Q(N, V, T) \exp(-\beta PV)) dV \\
&= \int_{V=0}^{V=\infty} \left(\frac{1}{N! h^{3N}} \int_{x=-L/2}^{x=L/2} \int_{p=-\infty}^{p=\infty} \exp(-\beta(U(x) + K(p))) dx^{3N} dp^{3N} \right) \exp(-\beta PV) dV \\
&= \frac{1}{N! h^{3N}} \int_{p=-\infty}^{p=\infty} \exp(-\beta K(p)) dp^{3N} \int_{V=0}^{V=\infty} \int_{x=-L/2}^{x=L/2} \exp(-\beta U(x)) dx^{3N} \exp(-\beta PV) dV \\
&= \Xi^{tr} \cdot \Xi^c
\end{aligned} \tag{5.25}$$

Thus we can estimate the translational and configurational contribution to isothermal isobaric partition function.

$$\begin{aligned}
\Xi^{tr} &= \frac{1}{N! h^{3N}} \int_{p=-\infty}^{p=\infty} \exp(-\beta K(p)) dp^{3N} \\
&= \frac{1}{N! \Lambda^{3N}} \\
\Xi^c &= \int_{V=0}^{V=\infty} \left(\int_{x=-L/2}^{x=L/2} \exp(-\beta U(x)) dx^{3N} \right) \exp(-\beta PV) dV
\end{aligned} \tag{5.26}$$

The ideal gas partition function can be calculated by setting $U(x)=0$.

$$\begin{aligned}
g_{id} &= \frac{-k_B T}{N} \ln(\Xi_{id}(N, P, T)) \\
\Xi_{id}(N, P, T) &= \frac{1}{N! h^{3N}} \int_{p=-\infty}^{p=\infty} \exp(-\beta K(p)) dp \int_{V=0}^{V=inf} \left(\int_{x=-L/2}^{x=L/2} dx^{3N} \right) \exp(-\beta PV) dV \\
&= \Xi^{tr} \int_{V=0}^{V=\infty} V^N \exp(-\beta PV) dV \\
\Xi_{id}^c &= \int_{V=0}^{V=\infty} V^N \exp(-\beta PV) dV \\
&= \frac{N!}{(\beta P)^{N+1}}
\end{aligned} \tag{5.27}$$

So the residual molar Gibbs free energy g_{res} can be found by the difference of g and g_{id}

$$\begin{aligned}
g_{res} &= g - g_{id} \\
&= \frac{-k_B T}{N} \ln(\Xi(N, P, T)) + \frac{-k_B T}{N} \ln(\Xi_{id}(N, P, T)) \\
&= \frac{-k_B T}{N} \ln \left(\frac{\Xi^c}{\Xi_{id}^c} \right)
\end{aligned} \tag{5.28}$$

The difference in residual molar gibbs free energy between states i and j at temperature and pressure T_i, P_i and T_j, P_j can be expressed as:

$$\begin{aligned}
g_{res,ij} &= g_{res,j} - g_{res,i} \\
&= \frac{-k_B T_j}{N} \ln \left(\frac{\Xi^{c,j}}{\Xi_{id}^{c,j}} \right) - \frac{-k_B T_i}{N} \ln \left(\frac{\Xi^{c,i}}{\Xi_{id}^{c,i}} \right)
\end{aligned} \tag{5.29}$$

Let us define a dimensionless Gibbs free energy $f_i = \beta_i g_i$. We can rewrite the above

equation in terms of dimensionless free energies.

$$\begin{aligned}
g_{res,ij} &= g_{res,j} - g_{res,i} \\
&= \frac{1}{\beta_j} (f_{res,j}) - \frac{1}{\beta_i} (f_{res,i}) \\
&= \frac{1}{\beta_j} (f_j^c - f_{j,id}^c) - \frac{1}{\beta_i} (f_i^c - f_{i,id}^c)
\end{aligned} \tag{5.30}$$

We can get f_{ij}^c from MBAR and estimate $f_{ij,id}^c$ analytically. The superscript c denotes the configurational part of the partition function.

$$\begin{aligned}
f_{res,ij} &= f_{res,j} - f_{res,i} \\
&= (f_j^c - f_{j,id}^c) - (f_i^c - f_{i,id}^c) \\
&= (f_j^c - f_i^c) - (f_{j,id}^c - f_{i,id}^c)
\end{aligned} \tag{5.31}$$

Only for states which have same temperatures, $\beta_i = \beta_j$ and differ only in pressure $P_i \neq P_j$, there exists a relation between $g_{res,ij}$ and $f_{res,ij}$ which is:

$$f_{res,ij} = \beta_i g_{res,ij} \tag{5.32}$$

However $f_{res,ij}$ has a more complicated relationship with $g_{res,ij}$ for free energies at different temperatures. However, they both contain the same thermodynamic information, as both are uniquely defined by T and P alone, and either can be used for optimization. The experimental dimensionless residual free energies $f_{res,exp}$ from the IAPWS95 equation of state are functions of V and T . However, the dimensionless residual free energies from the molecular simulations have P and T as natural variables.

The NVT ideal gas reference is different from the NPT ideal gas reference. To compare $f_{res,exp}(N,V,T)$ with $f_{res,sim}(N,P,T)$ we need to estimate the difference in the NPT and NVT ideal gas references, which we do as follows:

$$\begin{aligned}
G_{res,exp}(N, V, T) &= G(N, V, T) - G_{id}(N, V, T) \\
G_{res,sim}(N, P, T) &= G(N, P, T) - G_{id}(N, P, T) \\
G_{res,exp}(N, V, T) &= G_{res,sim}(N, P, T) + G_{id}(N, P, T) - G_{id}(N, V, T)
\end{aligned} \tag{5.33}$$

Multiplying throughout by β gives dimensionless free energies.

$$f_{res,exp}(N, V, T) = f_{res,sim}(N, P, T) + f_{id}(N, P, T) - f_{id}(N, V, T) \tag{5.34}$$

Molar ideal gas dimensionless free energies can be expressed in terms of their partition functions.

$$\begin{aligned}
f_{id}(P, T) - f_{id}(V, T) &= -\frac{1}{N} (\ln(\Xi_{id}(NPT)) - \ln(Q_{id}(NVT))) \\
&= \frac{1}{N} \ln \left(\frac{Q_{id}(NVT)}{\Xi_{id}(NPT)} \right)
\end{aligned} \tag{5.35}$$

We know that

$$\begin{aligned}
Q_{id}(NVT) &= \frac{V^N}{N! \Lambda^{3N}} \\
\Xi_{id}(NPT) &= \frac{1}{\Lambda^{3N} (\beta P)^{N+1}}
\end{aligned} \tag{5.36}$$

So

$$f_{id}(P, T) - f_{id}(V, T) = \frac{1}{N} \ln \left(\left(\frac{P}{k_B T} \right)^{N+1} V^N / N! \right) \quad (5.37)$$

For large number of molecules, N

$$\begin{aligned} f_{id}(P, T) - f_{id}(V, T) &= \ln \left(\frac{PV}{k_B T} \right) - \ln(N) + 1 \\ &= \ln(Z) - \ln(N) + 1 \end{aligned} \quad (5.38)$$

Where Z is the compressibility factor $= \frac{PV}{k_B T}$. Eq. 5.38 is very similar to Eq.4.2.27 derived by O'Connell and Haile except for the term $-\ln(N) + 1$. This term however vanishes once we consider difference in the free energies between two states i and j .

$$f_{id,ij}(P, T) - f_{id,ij}(V, T) = \ln(Z_{ij}) \quad (5.39)$$

Thus the relationship between simulated and experimental dimensionless residual free energies will be

$$f_{res,exp,ij}(N, V, T) = f_{res,sim,ij}(N, P, T) + \ln(Z_{ij}) \quad (5.40)$$

We will have to add $\ln(Z_{ij})$ to the free energy differences estimated using NPT simulations to be able to compare them with the free energy differences estimated using IAPWS95 equation of state. The residual enthalpy and internal energy don't have to be corrected as residual enthalpy and internal energy for ideal gas remains unchanged for NVT and NPT ensembles. However the residual entropy estimated using NPT simulations have to be corrected for the difference in NVT and NPT ideal gas entropies for comparison with

IAPWS95 entropy differences. Using the expression $S = k_B(\beta H - f)$ we can calculate the correction for entropy.

$$S_{res,exp,ij}(N, V, T) = S_{res,sim,ij}(N, P, T) - \ln(Z_{ij}) \quad (5.41)$$

5.2.1.5 Estimating properties using free energies estimated using MBAR First reviewing definitions, of general terms:

$$\begin{aligned} \beta &= \frac{1}{k_B T} \\ f &= \beta G \\ u &= \beta(U + PV) \\ &= \beta(P.E. + K.E. + PV) \\ &= -k_B \beta^2 \end{aligned} \quad (5.42)$$

We use $u = \beta(P.E + PV)$ to estimate the Boltzmann weight as we are interested in estimating only the configurational part of the partition function. The configurational part of the residual Gibbs free energy will be used to calculate the properties corresponding to partial derivatives of Gibbs free energy with respect to pressure, for example density, molar volume, compressibility. The residual Gibbs free energy can be easily extracted by subtracting the ideal gas configurational free energy from the total configurational free energy.

$$f_{res,ij} = f_{ij}^c - f_{id,ij}^c \quad (5.43)$$

Difference in residual free energies can be estimated as described in the previous section using Eq. 5.30.

All thermodynamic properties of interest can be expressed as derivatives of configurational or residual free energy with respect to pressure and β . This makes the computation of the derivatives easy and clearer. The partial derivatives with respect to pressure and β are estimated using finite difference formula requiring estimation of residual free energy differences $f_{res,ij}$ or configurational free energy differences, f_{ij}^c , both of which can be estimated using MBAR.

Molar Volume:

$$\begin{aligned} v_i &= \frac{\partial G}{\partial P} \\ &= \frac{1}{\beta} \frac{\partial f}{\partial P} \\ &= \frac{1}{\beta} \frac{\partial f^c}{\partial P} \end{aligned} \quad (5.44)$$

Residual molar volume:

$$v_{res,i} = v_i - k_B T_i / P_i. \quad (5.45)$$

Molar Density:

$$\rho = \frac{1}{v} \quad (5.46)$$

Enthalpy:

$$H = -T^2 \left(\frac{\partial G/T}{\partial T} \right)_P = \frac{\partial f}{\partial \beta} \quad (5.47)$$

For estimating residual enthalpy, H_{res} all we have to do is replace f by f_{res} .

Potential Energy or residual internal energy:

$$U_{res,ij} = H_{res,ij} - PV_{res,ij} \quad (5.48)$$

Residual Entropy:

$$S_{res,ij} = k_B(\beta_j H_{res,j} - \beta_i H_{res,i} - f_{res,ij}) \quad (5.49)$$

Heat of Vaporization:

$$H_{vap} = -H_{res} \quad (5.50)$$

While estimating the heat of vaporization we do not add corrections. We assume ideal state for vapor state and estimate the difference in enthalpy between liquid and enthalpy of ideal gas. This difference is equal to the negative of residual enthalpy of the liquid.

Heat capacity:

$$C_p = \frac{\partial H}{\partial T} = \left(\frac{\partial^2 f}{\partial \beta^2} \right) (-k_B \beta^2) \quad (5.51)$$

For estimating residual heat capacity $C_{P,res}$ we can replace f by f_{res} .

Isothermal compressibility:

$$\kappa = -\frac{\frac{\partial^2 G}{\partial^2 P}}{\frac{\partial G}{\partial P}} = -\frac{\frac{\partial^2 f^c}{\partial^2 P}}{\frac{\partial f^c}{\partial P}} \quad (5.52)$$

Isobaric thermal expansion coefficient:

$$\begin{aligned} \alpha &= \frac{\frac{\partial^2 G}{\partial T \partial P}}{\frac{\partial G}{\partial P}} \\ &= -k_B \left(\frac{\beta^2 \left(\frac{\partial^2 f}{\partial \beta \partial P} \right) - \beta \left(\frac{\partial f}{\partial P} \right)}{\frac{\partial f}{\partial P}} \right) \end{aligned} \quad (5.53)$$

5.2.1.6 Uncertainty in the property estimates Uncertainty in the experimental IAPWS95 properties are negligibly small. The mean square relative error in enthalpy, entropy and Gibbs free energy for IAPWS95 equation is less than $\sim 10^{-9}$. We assume that the uncertainty in the ideal gas part of the property (derived analytically) does not contribute to the total uncertainty. Thus the total uncertainty in experimental properties, however small, comes from the residual part.

The uncertainty in the SAFT EOS derived properties is zero as the SAFT model is an analytical model. The uncertainty calculation for the difference in the SAFT and IAPWS95 derived properties is omitted as the only contributions are from the IAPWS95 uncertainties which are negligibly small.

The uncertainty in the properties estimated using atomistic simulations are estimated by propagating the uncertainties for the free energy terms involved in the calculation of

the property. The method of propagation of the uncertainties using the covariance matrix has been already described in the third chapter. Only the uncertainties of the properties estimated from the simulations contribute to the uncertainty calculation for the difference in the atomistic and IAPWS95 derived properties as the IAPWS95 uncertainties are very small.

5.2.2 Defining the objective function

5.2.2.1 Objective function originally proposed We had proposed to find water model parameters which minimized the normalized residual, Eq. 5.54, or error between the experimental and simulated properties.

$$\xi = \sum_{k=1}^{N_P} \sum_{j=1}^{N_T} \sum_{i=1}^{N_f} \left(\frac{F_{sim,i}(T_j, P_k, \mathbf{x}) - F_{exp,i}(T_j, P_k)}{F_{exp,i}(T_j, P_k)} \right)^2 \quad (5.54)$$

Here $F_{sim}(T, P, \mathbf{x})$ is set of simulated properties for a set of model parameters \mathbf{x} at some temperature T and pressure P . Similarly, $F_{exp}(T, P)$ is the corresponding set of experimental properties for the same temperature T and pressure P . N_f is the number of experimental water properties we want model parameters to fit to. N_T is the number of temperatures at which we want parameters to fit. N_P is the number of pressures at which we want parameters to fit.

$$\begin{aligned} F_{sim}(T, P, \mathbf{x}) &= \{\rho, H_{vap}, \Delta G_{solv}, \kappa, \alpha_p\} \\ \mathbf{x} &= \{\sigma_O, \epsilon_O, q_O, r_{OH}, \angle HOH, r_{OM}\} \\ F_{exp}(T, P) &= \{\rho, H_{vap}, \Delta G_{solv}, \kappa, \alpha_p\} \end{aligned} \quad (5.55)$$

In this objective function, we are equally weighting relative errors of all properties. It is

not clear exactly what sorts of models will emerge from this equal weighting. We first tried different weights for density and heat of vaporization, for example $[w_\rho, w_{H_{vap}}] \in \{[1,0], [0.9,0.1], [0.5,0.5], [0.1,0.9], [0,1]\}$. The optimization for some choice of weights $\{[1,0], [0.9,0.1], [0.5,0.5], [0.1,0.9]\}$ was biased towards getting only the density right and for $[w_\rho, w_{H_{vap}}] = [0,1]$ only the error in heat of vaporization was minimized at the cost of increased error in density. However, we were not able to find a set of weights which could simultaneously minimize errors in both the properties in a single optimization run.

Because of this failure, we decided to first revise our objective function such that the parameterization would result in water model parameters which would simultaneously reduce deviation between all simulated and experimental thermophysical properties of water.

5.2.2.2 Revised objective function Almost all water models studies have treated the water parameterization exercise as a multiobjective optimization exercise. However, almost all of them place the entire weight on a single property, density (ρ), and at the end adjust parameters to incorporate enthalpy of vaporization corrections. There are several problems associated with the latter approach. The model parameters minimize a linear weighted sum of water properties. The weighted sum approach is only a linear approximation of the preference function which aims to model liquid water. We don't have a good understanding as to what combination of weights and which form of preference function, linear or non linear, would result in model parameters which will reproduce properties of liquid water. Most of the water models parameterizations use equal weights for density and heat of vaporization. Such a choice will make the optimization to spend most of the time reducing the errors in density. If we use Pareto optimal weights, the optimization will be unbiased with respect to any property but we will still be unsure if the combination of Pareto weights will properly model liquid water.

The heat of vaporization H_{vap} is the enthalpy difference between the liquid and the gas phase. This implies that H_{vap} may not be the best choice of parameters for a model because it is not a pure liquid phase property. For H_{vap} , the gas phase enthalpy is approximated by first assuming an ideal gas state and later adding corrections to account for non-ideality. The enthalpy change is then corrected for self-polarization when transferring to liquid water. Horn et al. [11] also correct for the classical approximation of water molecule by adding quantum corrections to both liquid phase property and properties involving phase change. The overall effect of including heat of vaporization is that the parameterization is not for pure liquid phase and the parameterization also becomes sensitive to the accuracy of the corrections and assumptions involved in the both liquid and vapor phase property calculations.

The previous rigid water model parameterizations were done by minimizing deviation between simulated and experimental densities, which is equivalent to minimizing deviation between simulated and experimental molar volume. However, it is cleaner to minimize the MSE in molar volumes because the molar volume is the partial derivative of residual Gibbs free energy with respect to pressure.

$$V_{sim} - V_{exp} = \left(\frac{\partial G_{sim}(T, P)}{\partial P} \right)_T - \left(\frac{\partial G_{exp}(T, P)}{\partial P} \right)_T \quad (5.56)$$

The simulated free energy $G_{sim}(T, P)$ and can be written in terms of individual components.

1. $G_{sim,conf}(T, P)$ (Configurational free energy as a function of pressure and temperature)
2. $G_{sim,trans}(T)$ (Translational free energy as a function of temperature)

3. $G_{sim,rot}(T)$ (Rotational free energy as a function of temperature)

There is no vibrational contribution for the rigid water model.

Similarly experimental free energy $G_{exp}(T, P)$, $G_{exp}(T, P)$ and can be written in terms of individual components.

1. $G_{exp,conf}(T, P)$ (Configurational free energy as a function of pressure and temperature)
2. $G_{exp,trans}(T)$ (Translational free energy as a function of temperature)
3. $G_{exp,rot}(T)$ (Rotational free energy as a function of temperature)
4. $G_{exp,vib}(T)$ (Vibrational free energy as a function of temperature)

$$V_{sim} - V_{exp} = \left(\frac{\partial(G_{sim,conf}(T, P) + G_{sim,trans}(T) + G_{sim,rot}(T))}{\partial P} \right)_T - \left(\frac{\partial(G_{exp,conf}(T, P) + G_{exp,trans}(T) + G_{exp,rot}(T) + G_{exp,vib}(T))}{\partial P} \right)_T \quad (5.57)$$

At pressures we are parameterizing the water model 1–120atm vibrational energies do not depend on pressure. This kind of separation is feasible for molecules as rotational KE and PE are not related. Terms that depend on temperature alone, i.e., translational, rotational, vibrational Gibbs free energies, do not contribute to the partial derivative of the total Gibbs free energy with respect to pressure at constant temperature. Thus the difference in simulated and experimental Gibbs free energy reduces to difference in corresponding configurational Gibbs free energies.

$$V_{sim} - V_{exp} = \left(\frac{\partial G_{sim,conf}(T, P)}{\partial P} \right)_T - \left(\frac{\partial G_{exp,conf}(T, P)}{\partial P} \right)_T \quad (5.58)$$

The configurational Gibbs free energy can be written as a sum of ideal gas configurational Gibbs free energy and the residual Gibbs free energy.

$$V_{sim} - V_{exp} = \left(\frac{\partial(G_{sim,res}(T, P) + G_{id,conf}(T, P))}{\partial P} \right)_T - \left(\frac{\partial(G_{exp,res}(T, P) + G_{id,conf}(T, P))}{\partial P} \right)_T \quad (5.59)$$

Since the experimental and simulated ideal gas configurational Gibbs free energies are the same they cancel out. In the end we find that the difference in the experimental and simulated molar volumes is equal to the difference in the partial derivatives of the residual Gibbs free energies with respect to pressure at constant temperature.

$$\begin{aligned} V_{sim} - V_{exp} &= \left(\frac{\partial G_{sim,res}(T, P)}{\partial P} \right)_T - \left(\frac{\partial G_{exp,res}(T, P)}{\partial P} \right)_T \\ &= \left(\frac{\partial f_{sim,res}(T, P)}{\partial \beta P} \right)_T - \left(\frac{\partial f_{exp,res}(T, P)}{\partial \beta P} \right)_T \end{aligned} \quad (5.60)$$

Here f_{res} is the dimensionless residual Gibbs free energy, with as usual $\beta = (k_B T)^{-1}$. Similarly all the liquid phase properties density, residual enthalpy, residual heat capacity, isothermal compressibility and thermal expansion coefficient can be expressed as some function of partial derivatives of residual Gibbs free energy or configurational Gibbs free energy with respect to temperature and pressure.

Previous parameterization efforts have already tried to fit to the experimental density and heat vaporizations [103, 10, 11]. Deviations between experimental and simulated density can be expressed in terms of first derivative of Gibbs free energy with respect to pressure. Deviations between experimental and simulated H_{vap} (which is approximately equivalent to H_{res} in magnitude if vapor state is assumed to be ideal) can be expressed in terms of first derivative of Gibbs free energy with respect to temperature using the Gibbs-Helmholtz

equation. If we try to include the properties estimated using the second derivatives, specifically residual heat capacity, isothermal compressibility and thermal expansion coefficient in order improve the liquid phase parameterization we will use information redundantly as the information about the second derivatives is already contained in the change of the first derivatives over temperature and pressure ranges. If the Gibbs free energy surface is “rigid” i.e., parameter changes shift the entire free energy surface equally, then in principle we will not achieve significant improvements by including these properties, especially since the first derivatives vary very smoothly and gradually with respect to temperature and pressure. However, if the first derivatives fluctuated a significantly with temperature and pressure then inclusion of the second derivative properties can make significant contributions.

All derivative properties are contained in the fundamental thermodynamic function of Gibbs free energy $G(T, P)$. Thus if we wish to improve thermodynamic agreement between our model and real water it in theory should be sufficient match $G_{sim}(T, P)$ and $G_{exp}(T, P)$ i.e. fit the water model parameters by minimizing the difference between the experimental and simulated Gibbs free energy surfaces as a function of temperature and pressure.

However, there is a problem if we try to fit the parameters of a rigid water model to reproduce $G_{exp}(T, P)$. As we will show, what we wish to minimize is difference between experimental and simulated residual Gibbs free energy, $G_{res}(T, P)$. To see this, let us examine the partition function of the model water Q_{sim} and the partition function for experimental/real water Q_{exp} .

$$\begin{aligned}\exp(-\beta G_{sim}) &= Q_{sim} = Q_{tr,sim} Q_{rot,sim} Q_{conf,sim} \\ \exp(-\beta G_{exp}) &= Q_{exp} = Q_{tr,exp} Q_{rot,exp} Q_{vib,exp} Q_{conf,exp}\end{aligned}\tag{5.61}$$

$Q_{tr,sim}, Q_{rot,sim}, Q_{conf,sim}$ are the translational, rotational, and configurational partition function respectively for the simulated rigid water model. $Q_{tr,exp}, Q_{rot,exp}, Q_{vib,exp}, Q_{conf,exp}$ are the translational, rotational, vibrational and configurational partition function of the real water. The minimization of MSE $\sum_T \sum_P (G_{sim} - G_{exp})^2$ will lead to an increase in $Q_{conf,sim}$ to compensate for the missing vibrational partition function in Q_{sim} .

We know that density can be estimated using the partial derivative of the configurational Gibbs free energy with respect to pressure at constant temperature.

$$\begin{aligned} \rho = v^{-1} &= \left(\frac{\partial G_{sim}(T, P)}{\partial P} \right)_T^{-1} \\ &= \left(\frac{\partial (G_{sim,conf}(T, P) + G_{sim,trans}(T) + G_{sim,rot}(T))}{\partial P} \right)_T^{-1} \\ &= \left(\frac{\partial G_{sim,conf}(T, P)}{\partial P} \right)_T^{-1} \end{aligned} \quad (5.62)$$

The parameterization done by fitting to total Gibbs free energy will have incorrect $G_{sim,conf}(T, P)$. Therefore, we will never be able to reduce the error in density or even interaction energies from a rigid water model parameterized to fit experimental total Gibbs free energy. Instead if we try to minimize the error in residual Gibbs free energy $\sum_T \sum_P (G_{res,sim} - G_{res,exp})^2$ the parameters will be fit to reproduce at least the correct intermolecular interactions as residual Gibbs free energy arises purely from the intermolecular interactions. The liquid water model thus parameterized will reproduce the intermolecular interactions of the experimental liquid water.

We need a Gibbs free energy based equation of state (EOS) fitted using experimental properties of liquid water. Fortunately there exists a high accuracy EOS from IAPWS95 which can be used to estimate Gibbs free energy of water for various ranges of temperatures and pressures. The errors in the thermodynamic properties estimated using the IAPWS95

equation of state are two to three orders smaller compared to statistical uncertainties in the simulated properties and therefore are not taken into account while comparing the simulated and experimental properties. But before comparing the experimentally derived IAPWS95 free energies and simulated free energies we need to take care of three issues.

The first issue is that the ideal gas partition function contribution to the simulated free energies and IAPWS95 free energies do not match. The difference occurs due to the difference in degrees of freedom. In the experimental ideal gas partition function there are 3 translational, 3 rotational, 3 vibrational degrees of freedom. However, the vibrational degrees of freedom are absent in the classical rigid water model. Also the heat capacity estimates from IAPWS95 ideal gas free energies show temperature dependence. This effect cannot be captured using a classical rigid model with no internal degrees of freedom, since rigid models must have an ideal gas heat capacity that is independent of temperature. The temperature dependence of the heat capacity thus makes any analytical correction insufficient to makeup for the missing degrees of freedom in the simulated free energies to compare with IAPWS95 free energies directly. Figure 5.2 compares the ideal gas heat capacity of a rigid water model with the ideal gas heat capacity of real water estimated using IAPWS95 EOS.

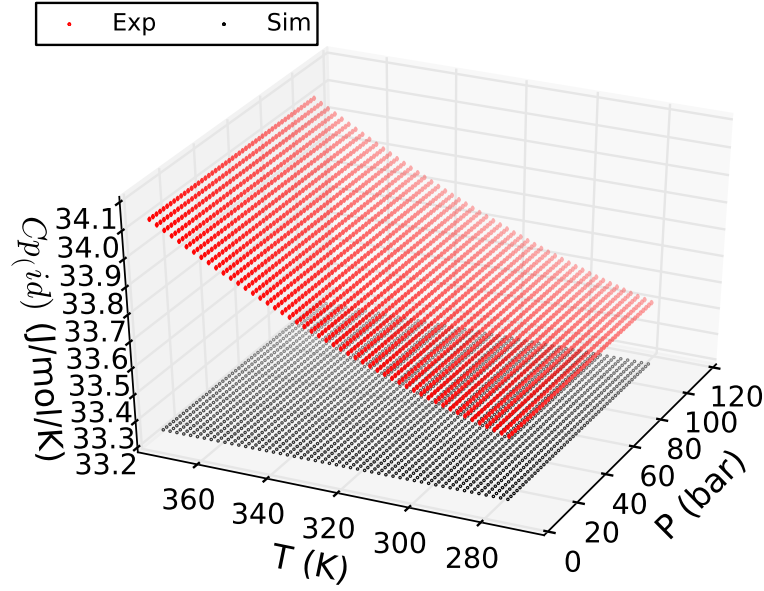


Figure 5.2: The isobaric specific heat capacity of rigid water model in ideal gas state (in black) is constant compared to a temperature dependent ideal gas heat capacity for real water (in red).

The second issue is that the IAPWS95 free energies are referenced with respect to the saturated liquid phase internal energy and entropy at the triple point. In the IAPWS95 formulation, the ideal gas free energy part is scaled such that the internal energy and entropy are zero at the reference state. It is impossible to set the triple point of water as a reference state for the simulated Gibbs free energies, both because we specifically do not expect our water model to be valid at the triple point, and because convergence times will be very long at the triple point because of convergence problems between phases.

However, we notice that residual Gibbs free energy contribution in IAPWS95 formulation is unaffected by the choice of the reference state. Thus, we don't have to treat the residual free energy estimated using IAPWS95 formulation for comparing with the simulated residual Gibbs free energy. Once we have the mean square error of the simulated and

experimental residual Gibbs free energy surfaces for a range of temperatures and pressures, we can optimize water model parameters for a given objective function.

If we could match the experimental $G_{res,exp}$ and simulated $G_{res,sim}$ surfaces with very small tolerance then the partial first derivatives of G_{res} with respect to T - and P -containing properties, density and H_{res} and the partial second derivative of G_{res} with respect to T - and P -containing properties, compressibility and $C_{P,res}$ should also match. This hypothesis is based on the assumption that the $G_{res}(T, P)$ surface is such that a tilt or rotation at one point rotates the entire function. However, we will find this assumption fails, because $G_{res}(T, P)$ surface is found to be prone to local deformation according to the constraints and objective function to which it is fit.

The third issue is that the residual free energies estimated using a pressure explicit EOS (in IAPWS95 volume and temperature are variables), $G_{res,exp}$ are functions of V and T , whereas the residual free energies estimated using atomistic simulations (where pressure and temperature are variables), $G_{res,sim}$ are functions of P and T . This can be overcome by explicitly calculating the relationship between the residual Gibbs free energies, $G_{res,exp}(V, T)$ and $G_{res,exp}(P, T)$, explained later in the chapter.

The dimensionless residual Gibbs free energy $f_{res,ij}$ is a different function compared to molar residual Gibbs free energy $g_{res,ij}$, but either can be used for parameterization, as both contain the same information, as $\beta g = f$. We use $f_{res,ij}$ in our parameterization as MBAR outputs $f_{res,sim,ij}$, referenced such that the first state is set as the reference with $f_{res,0} = 0$. $f_{res,sim,i}$ for parameterization. As a shorthand, we will sometimes refer to the individual thermodynamic state variables $f_{res,exp,i}$ as $f_{res,exp}$ and $f_{res,sim,i}$ as $f_{res,sim}$ for defining the objective functions.

We first started by minimizing just the MSE in $f_{res,sim}$. All $f_{res,sim}$ and $f_{res,exp}$ are calculated with same reference state, which could be user selected temperature T_r and

pressure P_r .

$$\begin{aligned}
& \underset{\mathbf{x}}{\text{minimize}} \quad \xi(x) = \frac{1}{N_{TP}} \sum_{i=1}^{i=N_P} \sum_{j=1}^{j=N_T} (f_{res,sim}(P_i, T_j, \mathbf{x}) - f_{res,exp}(P_i, T_j))^2 \\
& \text{subject to} \quad f_{res,sim}(P_r, T_r, \mathbf{x}) = f_{res,exp}(P_r, T_r) = 0
\end{aligned} \tag{5.63}$$

We used already existing water models (SPC, SPC/E, TIP4P, TIP4P-EW, TIP4P-2005) as our initial guesses for the optimization run with COBYLA [123] optimization routine. We chose COBYLA as it is a derivative-free optimization algorithm and can handle constraints in the objective function. To observe the effect of optimization on the first derivative properties of f_{res} with respect to T and P we observed the changes in the errors in $H_{res} = (\partial(f_{res})/\partial(\beta))$ and $\rho (= 1/(\partial(f_{conf})/\partial(\beta P)))$. For the models which have large deviations in H_{res} (absolute error ≈ 5 kJ/mol) but very good densities (absolute error $\approx 1-3$ Kg/m³), such as TIP4P-EW, the optimization tends to drastically decrease the fit to the density when improving the H_{res} correct in order to best match the simulated G_{res} surface to the experimental G_{res} surface. Thus, although this procedure minimizes the distance between experimental and simulated free energy surfaces, it does not give particularly good water properties across all parameters of interest.

For the models which have moderate deviations in H_{res} (abs error ≈ 1 kJ/mol) and moderately good densities (abs err $\approx 5-21$ Kg/m³), for example, TIP4P and SPC, the optimization tends to improve densities at higher temperatures (where the deviations are large) and worsen densities at lower temperatures (where deviations are small) and effect on H_{res} is very small.

These observations suggest that the optimization process per se is working effectively. However, we need to modify our objective function such that the difference in experimental

and simulated f_{res} surfaces is minimized without significantly reducing the accuracy in the properties.

A possible solution is to minimize deviation in $f_{res,sim}$ surface by “pinning” the partial derivatives of $f_{res,sim}$ with respect β and P or alternately pinning density and H_{res} at three locations: high moderate and low temperatures at 1 atm. Since the surface is smooth, continuous and assumed to be rigid, we anticipate the constraints will make sure that the simulated $f_{res,sim}$ surface achieves minimum deviation from experimental surface without deteriorating either of the two properties. This suggest the minimization function:

$$\begin{aligned} \underset{\mathbf{x}}{\text{minimize}} \quad & \xi(x) = \frac{1}{N_{TP}} \sum_{i=1}^{i=N_P} \sum_{j=1}^{j=N_T} (f_{res,sim}(P_i, T_j, \mathbf{x}) - f_{res,exp}(P_i, T_j))^2 \\ \text{subject to} \quad & |H_{res,sim}(x) - H_{res,exp}| - 0.01 < 0 \\ & \text{at [T=274 K, P=1atm], [T=298 K, P=1atm], [T=372 K, P=1atm]} \end{aligned} \quad (5.64)$$

The deviations $\pm 1 \text{ kg/m}^3$ in density and $\pm 0.01 \text{ kJ/mol}$ in $H_{res,sim}$ are arbitrary/ user based. At the pinning points constraints were respected and every where else density was sacrificed to get $H_{res,sim}$ correct.

Then we pinned the $f_{res,sim}$ surface at low moderate and high temperature and at low and high pressures by introducing density and H_{res} constraints. Again, at the constraints the errors in density were minimum compared to else where. However, this time the optimization completely ruined the density versus temperature behavior as the density rose and fell multiple times with the increasing temperature around the pinning points. Importantly, the $f_{res,sim}$ surface looked smooth as shown in Figure 5.3, meaning that these errors in first derivative properties did not appear significant in the overall surface.

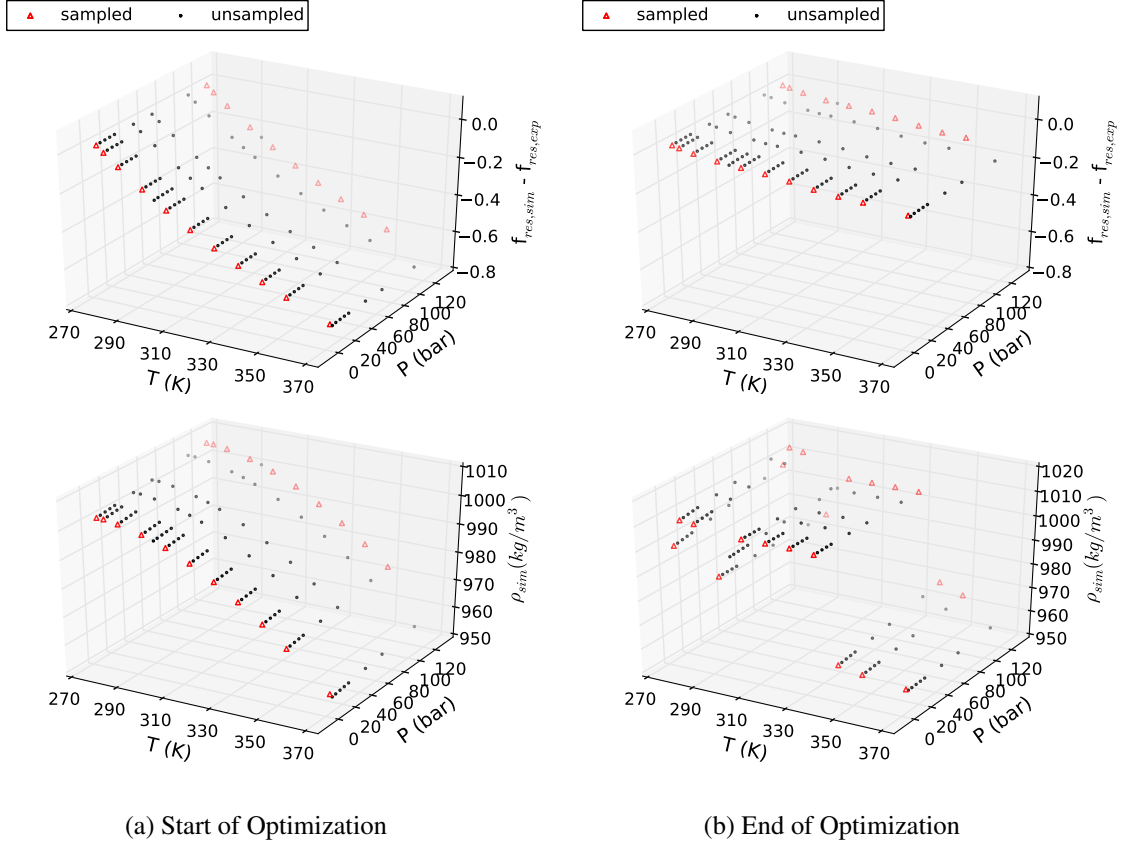


Figure 5.3: We start the minimization with TIP4P-2005 water model parameters. Even though we minimize error in residual free energy, the density versus temperature behavior gets totally distorted. We see that at $[T=274 \text{ K}, P=1\text{atm}]$, $[T=298 \text{ K}, P=1\text{atm}]$, $[T=372 \text{ K}, P=1\text{atm}]$ the constraints on density are followed however around the constraint points the curve rises and falls multiple times.

At this point, we have found that the optimization of MSE in $f_{res,sim}$ alone does not preserve either the first or the second derivative of $f_{res,sim}$ in T or P direction. We have also observed that a relatively smooth surface of $f_{res,sim}$ exhibits anomalous first and second derivatives behavior when constrained at individual temperature and pressure points. From the experiments in which we introduced constraints it is clear that the constraints at individual points results in anomalous behavior of first and second derivatives. Thus, we must

set up our optimization such that the minimization of MSE in $f_{res,sim}$ improves MSE in density and $H_{res,sim}$. This indicates the need of a surface-wide constraint on the properties which come from first derivative of $f_{res,sim}$ with respect to T and P for the optimization.

$$\begin{aligned}
& \underset{\mathbf{x}}{\text{minimize}} \quad \xi(x) = \frac{1}{N_{TP}} \sum_{i=1}^{i=N_P} \sum_{j=1}^{j=N_T} (f_{res,sim}(P_i, T_j, \mathbf{x}) - f_{res,exp}(P_i, T_j))^2 \\
& \text{subject to} \quad (1) \frac{1}{N_{TP}} \sum_{i=1}^{i=N_P} \sum_{j=1}^{j=N_T} (\rho_{sim}(P_i, T_j, \mathbf{x}) - \rho_{exp}(P_i, T_j))^2 - 1 < 0 \\
& \quad \quad \quad (2) \frac{1}{N_{TP}} \sum_{i=1}^{i=N_P} \sum_{j=1}^{j=N_T} (H_{res,sim}(P_i, T_j, \mathbf{x}) - H_{res,exp}(P_i, T_j))^2 - 0.01 < 0
\end{aligned} \tag{5.65}$$

Using SPC water model (which has the lowest MSE($f_{res,sim}$ among water models) as the starting guess, the best feasible solution using the objective function 5.65 results in worsened MSE($f_{res,sim}$) without substantial improvements in either MSE in density or in $H_{res,sim}$. For TIP4P-2005 as the starting point MSE($f_{res,sim}$) and MSE($H_{res,sim}$) reduced compared to the starting value but then the worsening MSE (ρ_{sim}) becomes greater than 100 kg/m³.

Interestingly, we observed that the parameterization generally minimizes error in $f_{res,sim}$ by correcting $H_{res,sim}$ without improving the accuracy in ρ . We thus next attempt to switch

places of $f_{res,sim}$ with that of MSE (ρ_{sim}) as shown below.

$$\begin{aligned}
& \underset{\mathbf{x}}{\text{minimize}} \quad \xi(x) = \frac{1}{N_{TP}} \sum_{i=1}^{i=N_P} \sum_{j=1}^{j=N_T} (\rho_{res,sim}(P_i, T_j, \mathbf{x}) / \rho_{res,exp}(P_i, T_j) - 1)^2 \\
& \text{subject to} \quad (1) \frac{1}{N_{TP}} \sum_{i=1}^{i=N_P} \sum_{j=1}^{j=N_T} (f_{res,sim}(P_i, T_j, \mathbf{x}) / f_{res,exp}(P_i, T_j) - 1)^2 - 10^{-6} < 0 \\
& \quad \quad \quad (2) \frac{1}{N_{TP}} \sum_{i=1}^{i=N_P} \sum_{j=1}^{j=N_T} (H_{res,sim}(P_i, T_j, \mathbf{x}) / H_{res,exp}(P_i, T_j) - 1)^2 - 10^{-6} < 0
\end{aligned} \tag{5.66}$$

We wish the optimization to get the densities and the density versus temperature behavior correct while keeping the errors in $f_{res,sim}$ and $H_{res,sim}$ within user specified bounds, which we have set to 10^{-6} . We realized that instead of mean square errors, mean square relative errors will reduce any confusion in error comparison due to choice of units. So in objective function in Eq. 5.66 we replaced the mean square errors (MSE) with mean square relative errors (MSRE).

The best feasible solution (minimum violation to the constraints) using the objective function defined in Eq. 5.66 could reduce the $\text{MSRE}(\rho_{sim}(\mathbf{x}))$ but could never fully satisfy the constraints. In the process of approaching $\text{MSRE}(f_{res,sim}(\mathbf{x})) < 10^{-6}$ the optimization run tries to minimize error in density and $H_{res,sim}$. However the improvements in $\text{MSRE}(f_{res,sim}(\mathbf{x}))$ hits a hard wall as the density does not improve beyond a certain point. $H_{res,sim}$ can be written as sum of potential energy U and PV_{res} . So the improvement in $H_{res,sim}$ also hits a hard wall when the errors in V_{res} or density dominate.

This bottleneck in the objective function in Eq. 5.66 forced us to give a fresh look at the

fundamental thermodynamic function of Gibbs free energy G_{res} .

$$\begin{aligned}
G_{res} &= H_{res} - TS_{res} \\
&= U_{res} + PV_{res} - TS_{res} \\
&= U_{res} + P \left(\frac{\partial G_{res}}{\partial P} \right)_T + T \left(\frac{\partial G_{res}}{\partial T} \right)_P
\end{aligned} \tag{5.67}$$

In the above equation we see that for a given T and P the residual Gibbs free energy is a combination of the following state functions: the residual internal energy U_{res} (which is equal to the potential energy of the system for a rigid water model), the residual molar volume $V_{res} = \left(\frac{\partial G_{res}}{\partial P} \right)_T$ and the residual entropy $S_{res} = \left(\frac{\partial G_{res}}{\partial T} \right)_P$.

By this argument, we could have multiple combination of forcefield parameters which give a correct G_{res} but have cancelling errors U_{res} , V_{res} and S_{res} . For a given fluid, there exists a unique combination of U_{res} , V_{res} and S_{res} which gives specific residual Gibbs free energy at given T and P . Initially, we were trying to fit to the experimental G_{res} , T , P surface and observed that we were not able to obtain the correct fluid properties meaning the corresponding simulated $U_{res,sim}$, $V_{res,sim}$ and $S_{res,sim}$ did not match with experimental $U_{res,exp}$, $V_{res,exp}$ and $S_{res,exp}$ for water. The optimization was reducing the error in $G_{res,sim}$ but was not fixing to the unique $U_{res,sim}$, $V_{res,sim}$ and $S_{res,sim}$ of water. This could be the numerical reason why our optimization runs with just the free energy alone were not working.

The above reasoning prompted us that we should fit to the experimental G_{res} surface (or f_{res} surface), making sure that the simulated $U_{res,sim}$, $V_{res,sim}$, and $S_{res,sim}$ correspond to that of the experimental water. We will be fitting to the residual free energy surface of water but with a greater confidence, since the objective function will give free energy with the correct combination of U_{res} , V_{res} and S_{res} i.e. corresponding to water. Thus, we have

the following new objective function:

$$\begin{aligned}
& \underset{\mathbf{x}}{\text{minimize}} \quad \xi(x) = \frac{1}{N_{TP}} \sum_{i=1}^{i=N_P} \sum_{j=1}^{j=N_T} (v_{sim}(P_i, T_j, \mathbf{x})/v_{exp}(P_i, T_j) - 1)^2 \\
& \text{subject to} \quad (1) \frac{1}{N_{TP}} \sum_{i=1}^{i=N_P} \sum_{j=1}^{j=N_T} (U_{res,sim}(P_i, T_j, \mathbf{x})/U_{res,exp}(P_i, T_j) - 1)^2 < 10^{-6} \\
& \quad (2) \frac{1}{N_{TP}} \sum_{i=1}^{i=N_P} \sum_{j=1}^{j=N_T} (S_{res,sim}(P_i, T_j, \mathbf{x})/S_{res,exp}(P_i, T_j) - 1)^2 < 10^{-6} \\
& \quad (3) \frac{1}{N_{TP}} \sum_{i=1}^{i=N_P} \sum_{j=1}^{j=N_T} (f_{res,sim}(P_i, T_j, \mathbf{x})/f_{res,exp}(P_i, T_j) - 1)^2 < 10^{-6}
\end{aligned} \tag{5.68}$$

Minimizing error in $U_{res,sim}$ will make sure that the model results in a realistic water potential energy and that there is minimum shift between experimental and simulated $G_{res}(T, P)$ surfaces. Minimizing error in V_{res} and S_{res} will ensure that the gradients of simulated $G_{res}(T, P)$ surfaces in the temperature and the pressure directions closely match with those of the experimental $G_{res}(T, P)$ surface. Thus, we not only match the points on the $G_{res}(T, P)$ surface but we also make sure that the shape of the surface around every T and P point also matches with experimental counterpart. These conditions will ensure that the combination of U , S and V that minimizes error in G which actually corresponds to that of liquid water.

There could be multiple sets of force field parameters what could produce similar $G_{res}(T, P)$ surfaces but with very different $U_{res}(T, P)$, $S_{res}(T, P)$ and $V_{res}(T, P)$ surfaces. The constraints on $U_{res}(T, P)$, $S_{res}(T, P)$ and $V_{res}(T, P)$ surfaces will help reduce the false $G_{res}(T, P)$ surfaces and drive the parameterization towards a better water model. Thus, the parameterization with objective function defined in Eq. 5.68 should show better conver-

gence compared to parameterization with objective function defined in Eq. 5.66. We can test the convergence by doing multiple optimization runs with different initial guess set of parameters using the two objective functions in Eq. 5.68 and Eq. 5.68 and compare. However, running multiple optimizations using reweighting is computationally very expensive.

Optimization even with reweighting does not reduce the computational cost (time as well as memory) enough to allow hundreds of simultaneous optimization run to convergence. This is where SAFT model can help. A SAFT water model has similarities to the atomistic water model and yet computationally much cheaper to evaluate. Similar to the water atomistic water model, the SAFT water model we chose has a 12-6 LJ potential which describes repulsive and dispersion interactions and the Coulomb contribution are estimated using an analytical Pade approximation. SAFT models posit a configuration integral that is used to estimate the association interactions which describe hydrogen bond forces. Apart from the association parameters (K_{hb} , σ_{hb} , ϵ_{hb}), SAFT model requires σ_O , ϵ_O and molecular dipole μ which can be mapped to atomistic model parameters σ_O , ϵ_O , q_O , r_{OH} , r_{OM} and $\angle HOH$. Thus, the response of the property surface to the change in SAFT model parameters will be qualitatively similar to the response of the property surface to the change in atomistic model parameters. Thus, the objective function that works well for parameterizing SAFT model should also work for atomistic model parameterization. We could run hundreds of SAFT model parameter optimizations with random starting parameter sets and compare the convergence for objective functions in Eq. 5.68 and Eq. 5.68. To make random initial guesses we need to set bounds on the SAFT model parameters such that a random value is picked between the upper and lower bound, as shown in Table 5.1, to create an initial guess set of parameters to start the optimization. The bounds are chosen such that even the worst parameters (which give very large error in SAFT estimated properties) are inclusive.

Parameter	(units)	Range [lower bound , upper bound]
σ_{LJ}	(nm)	[0.28,0.35]
ϵ_{LJ}	(kJ/mol)	[0.332,3.327]
μ	(D)	[1.9,3.1]
ϵ_{hb}	(kJ/mol)	[6.653 , 16.633]
K_{hb}	()	[1 , 200]
σ_{hb}/σ_{LJ}	()	[0.02 , 0.4]

Table 5.1: The parameter bounds for exploring the SAFT water model parameter space.

COBYLA searches for a local minima only in the neighboring multidimensional function space. However, we wish to use an optimization routine that attempts to search through the entire variable space defined by the parameter bounds to arrive at a minima. So, we tested the convergence of objective functions in Eq. 5.66 and Eq. 5.68 using the SAFT equation of state with mesh adaptive direct search (MADS) algorithm [110] with progressive barriers [111] approach for handling constraints instead of COBYLA.

For Eq. 5.66 we ran 1000 SAFT optimizations with random initial starting guesses. In Figure 5.4 we can observe that the parameters like σ , ϵ show zones which represent water like models. However, there is no distinct minima. Some of the optimizations drift to the parameter boundaries in search of the minima for example we found many optimizations got stuck at the lower end of μ . The error in H_{res} did not go below 2.4 kJ/mol and the error in G_{res} did not go below 0.2 kJ/mol. The error in density fluctuates between 40 kg/m³ to 400 kg/m³

For Eq. 5.68 we ran 500 SAFT optimizations with random initial starting guesses. In Figure 5.5 we can see that for all runs the optimizations converged to a single distinct $\epsilon \simeq$

1 kJ/mol and to a single band of $\sigma \simeq 3.2$. The error in U_{res} and G_{res} can be reduced to 0.02 kJ/mol, the error in S_{res} goes down to 0.04 J/mol/K and the error in V or V_{res} is less than $4 \times 10^{-6} \text{ m}^3/\text{mol}$ which corresponds to an error of 286 kg/m³ which is very large. From this exercise we can learn that errors in Gibbs free energy and density cannot be simultaneously reduced. There will be a point when error in density will start increasing sharply with the decreasing error in residual Gibbs free energy. At this point we will have to make a decision to lower the tolerance in the residual Gibbs free energy error to get acceptable error in densities.

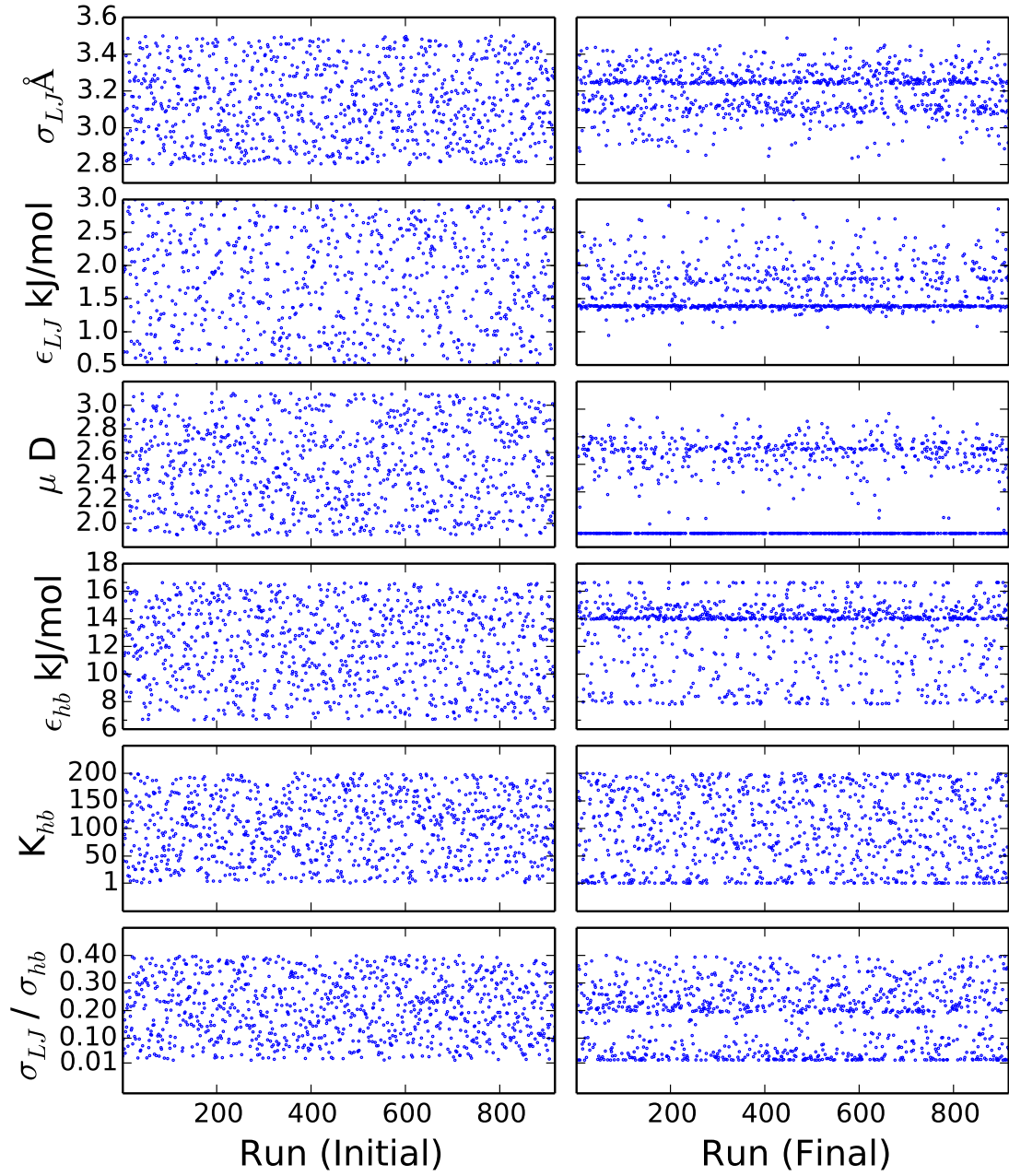


Figure 5.4: Subplots on the left show the values of the parameters at the start of the optimization; Subplots on the right show the values of the parameters at the end of optimization from 1000 SAFT model optimization runs using the objective function definition in Eq. 5.66. We see bands forming indicating possible location of a water like model however there is no prominent minima.

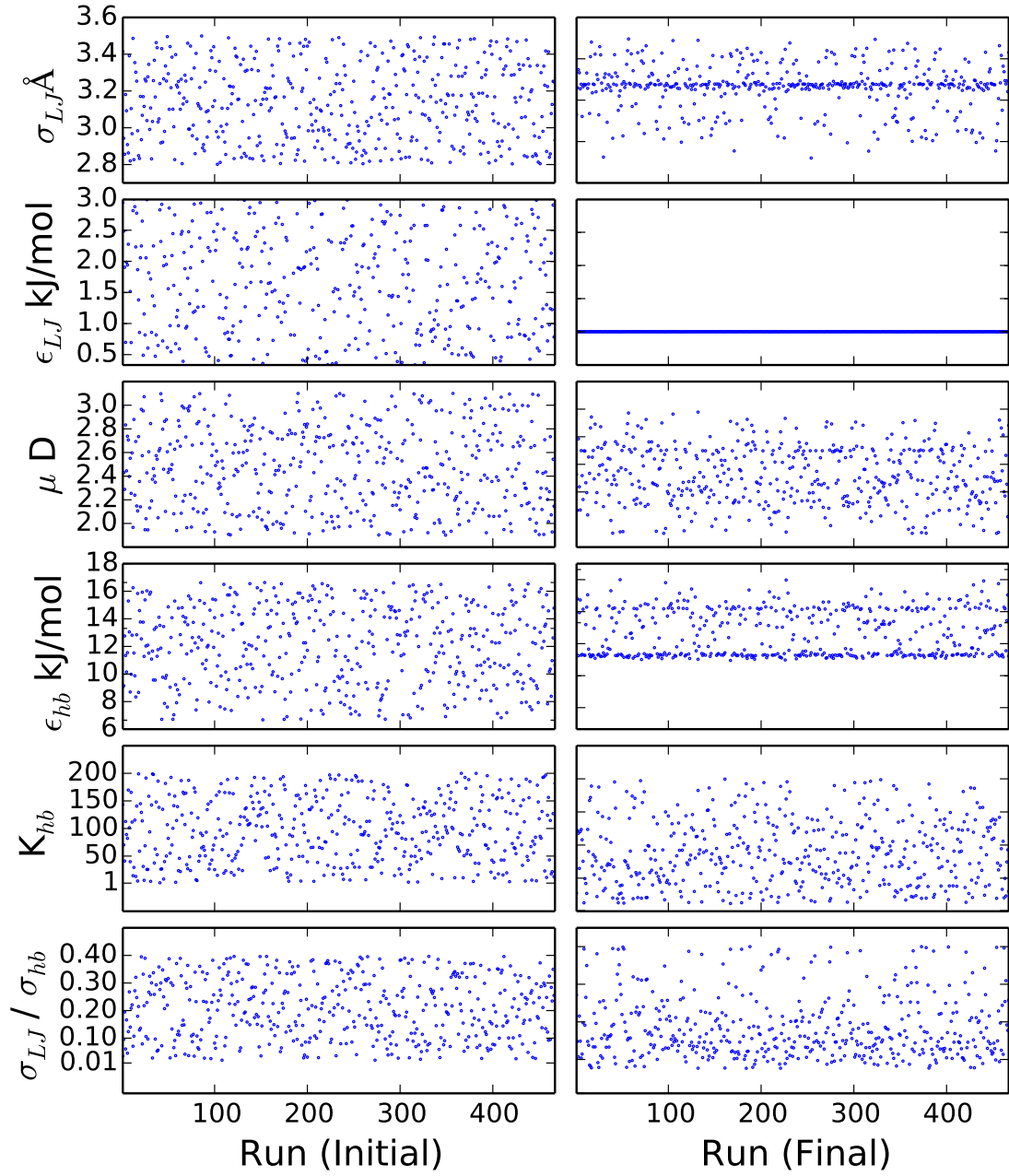


Figure 5.5: Subplots on the left show the values of the parameters at the start of the optimization; Subplots on the right show the values of the parameters at the end of optimization from 500 SAFT model optimization runs using the objective function definition in Eq. 5.68. We see a distinct value for ϵ and a single band of allowed values for σ

We plotted the association parameters and σ , ϵ and μ together to see if there exist a lower dimensional submanifold relating these parameters. In Figure 5.6, in the top left subplot we see that the association parameters fall on a surface. In the top right sub plot we see that σ , ϵ and μ also have specific regions where all constraints in U_{res} , S_{res} , and G_{res} are satisfied.

The bottom sub plots in Figure 5.6 include only those parameter combinations for which mean square error in molar volume is less than 0.01, and mean square error in internal energy, entropy and free energy is also less than 0.01. These parameters fall on a straight line. The sieve excludes those combinations which have low MSE in internal energy, entropy and free energy but high MSE in density. The sieved combinations of σ , ϵ and μ fall along a line.

We plot σ_{LJ} against ϵ_{LJ} in Figure 5.7. The sieved σ_{LJ} against ϵ_{LJ} combinations fall on a line which has slope almost equal to zero which suggests that there is a strong sharp minima in σ for the SAFT model. ϵ_{LJ} can vary between 120.1 and 120.5 K indicating a minima over a small range.

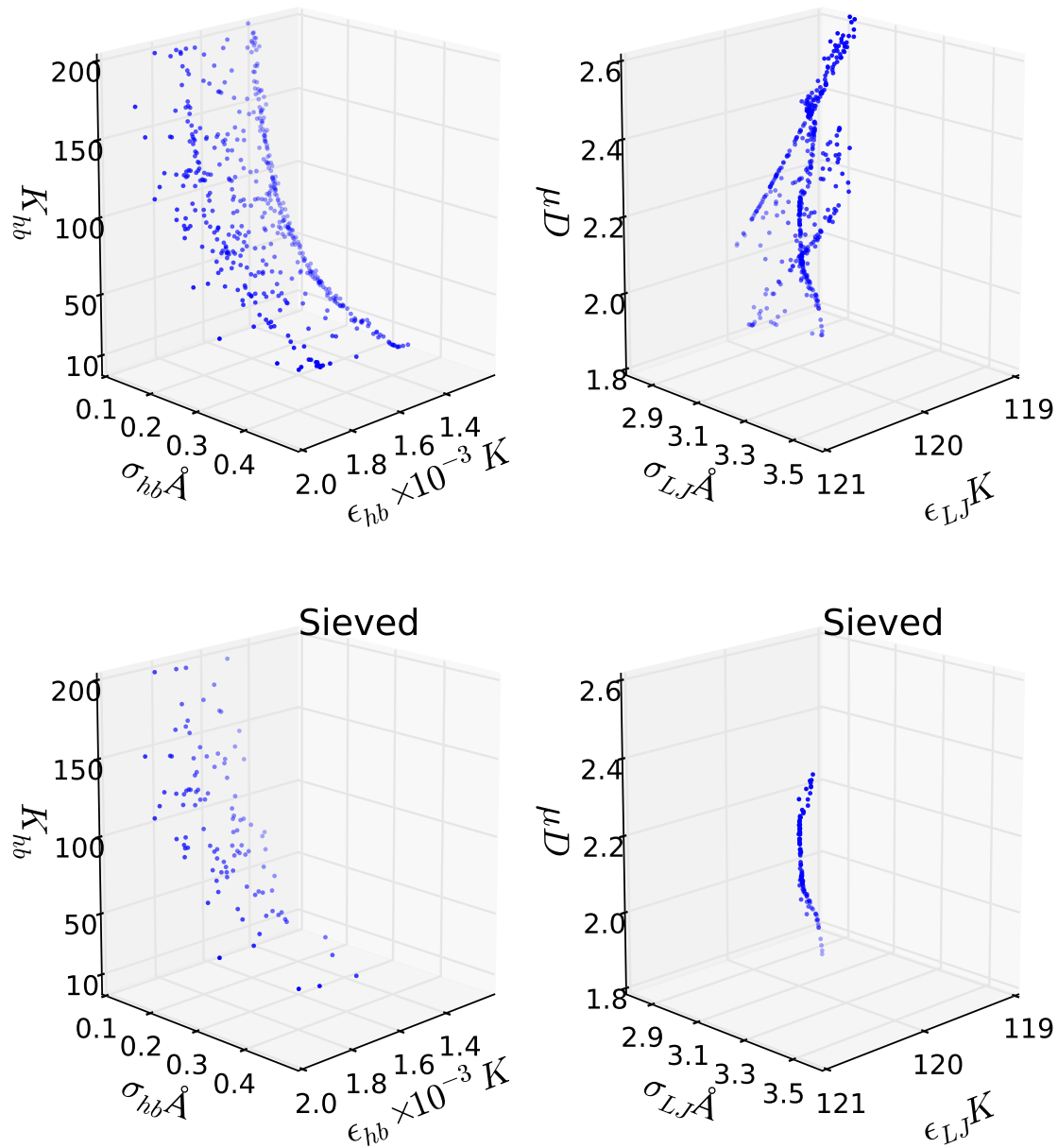


Figure 5.6: There exist low dimensional submanifolds which relate the SAFT model parameters. The association parameters K_{hb} , σ_{hb} , and ϵ_{hb} for which the mean square errors in molar volume, residual internal energy, residual entropy and residual Gibbs free energy is lower than 0.01 fall on a surface and the corresponding Lennard-Jones and coulomb parameters σ_{LJ} , ϵ_{LJ} and μ fall on a line.

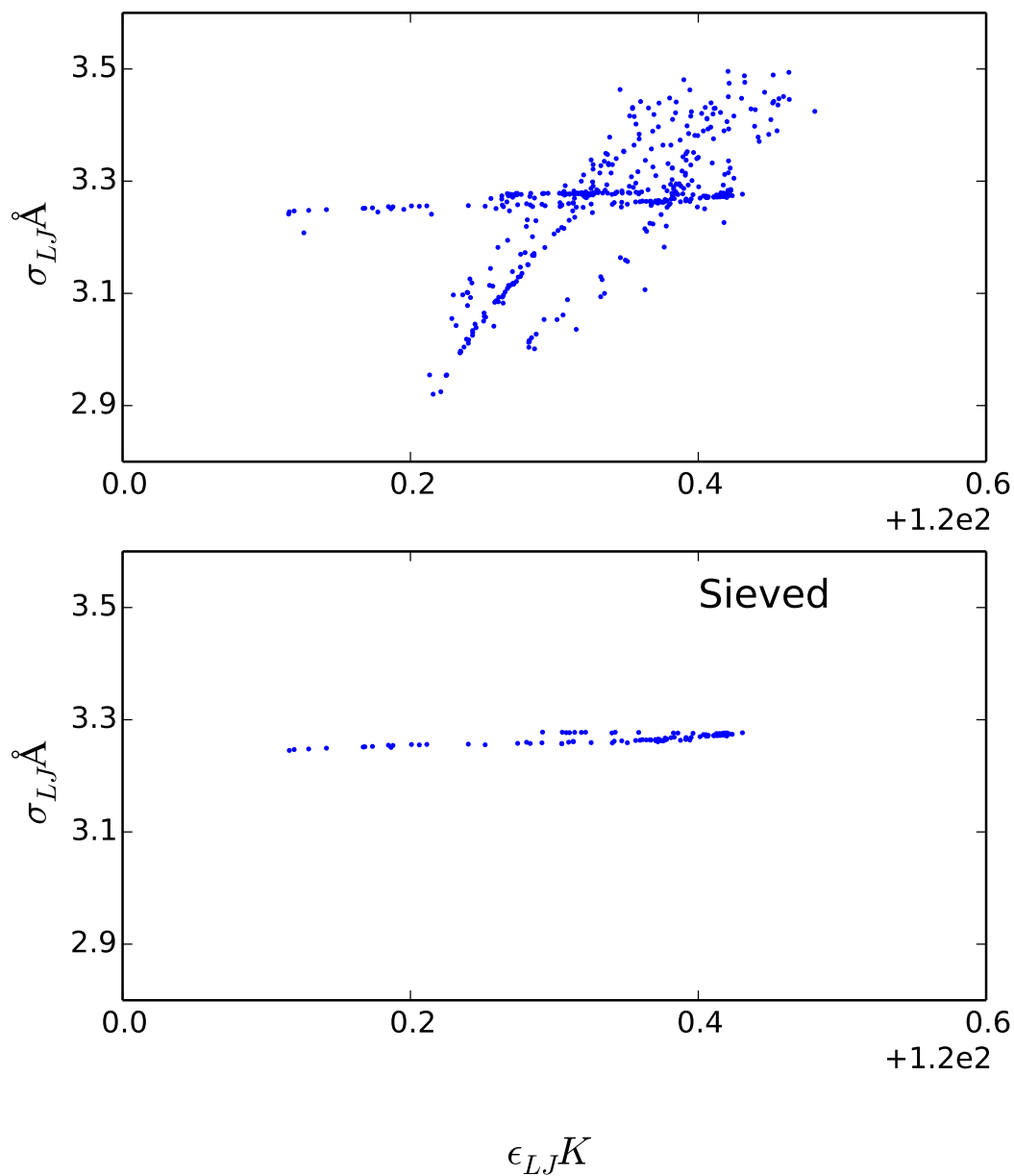


Figure 5.7: This plot shows that in a two dimensional infinite space of σ_{LJ} , and ϵ_{LJ} parameters, there is a very small portion, a small and thin line, which corresponds to SAFT model parameters which reproduce experimental molar volume, residual internal energy, residual entropy and residual Gibbs free energy with a mean square error of 0.01.

We could have explored the results from the convergence tests a little more by studying the correlation between parameters and property surfaces, checking for any parameter degeneracies and if we could converge the parameters further by restarting the optimization using the converged parameter sets from the previous run as the initial guess. However, we had sufficient qualitative information from the convergence characteristics of the objective function with SAFT water model using the MADS algorithm to initiate optimization of the atomistic water model parameters. Optimization based on the MADS (Mesh adaptive direct search) algorithm allows application of constraints as progressive barriers and shows better convergence (lower minimum and adherence to constraints) compared to hard constraints as implemented as COBYLA and also performs searches within set bounds on parameter space. The progressive barrier approach of dealing with the constraints is better than the extreme barrier approach in which the infeasible solutions are rejected straight away. Progressive barrier results in better and faster convergence even when a starting feasible point is unknown, which is very beneficial for our problem. MADS facilitates both progressive as well as extreme barriers. We thus use MADS for all our subsequent optimizations.

An iteration using MADS algorithm involves evaluation of the objective function $\text{Obj}(x)$ and constraint violation function $h(x)$ defined over N_c constraint functions $c_j(x) < 0$ ($j \in [1 \dots N_c]$):

$$h(x) = \infty \quad \text{if } x \notin X_b \quad (5.69)$$

$$= \sum_{j=1}^{j=N_c} (\max(c_j(x), 0))^2 \quad \text{if } x \in X_b \quad (5.70)$$

X_b is the set of the upper and lower bounds for all the variables in x .

The optimization starts from the initial supplied guess point. A mesh is created around the initial point for the search step according to user specified mesh generation algorithm,

a mesh size parameter within the user specified bounds of the parameter. A feasible point is one which has $Obj_k(x) < Obj_{k-1}(x)$ and $h_k(x) = 0$ i.e. all the constraints are satisfied. If all the constraints are not satisfied (for an infeasible point) then the optimization will span a mesh for the POLL step, according to a poll size parameter around the current point to perform a more local exploration. If a better solution, having lower value of $h(x)$, is found using either SEARCH or POLL steps the optimization updates x with the new feasible point and makes the mesh coarser. If a better solution is not found then the optimization does not update x and refines the mesh. This process is carried out till all the constraints are progressively satisfied. Once the optimization trajectory lands in the space of feasible solutions, minimization of $f(x)$ is again resumed.

We use a progressive barrier on the three constraints defined in Eq. 5.68. In addition, we also have two extreme barrier constraints imposed on the dipole moment of the water model. Studies have shown that the water model should have dipole moment between 2D and 3D to reproduce the correct dielectric constant of water. We constrained the dipole of the water model to be between 1.9D and 3.1D such that the dipole moment of the model is always greater than the gas phase dipole moment (1.85D) and is less than 3.1D which is an arbitrarily set upper limit to include all existing water models.

5.2.2.3 Setting the water model parameter exploration space To search the water model parameter space for a better water model using the MADS algorithm, we will have to set parameter bounds. The bounds are set such that the probability of finding a water model outside the space set by these bounds is negligible. We propose that the liquid phase geometry should not be very different from the gas phase. Therefore, we start by defining the parameter search space for molecular geometry by estimating geometry of water molecule in the vapor phase using quantum mechanics. *ab initio* quantum mechanical

(QM) methods can give the geometry and charges which minimize the potential energy for a water molecule in gas phase 5.2.

Parameter (units)	Experimental [124]	QM optimized	Single point calculation using experimental geometry
r_{OH} (nm)	0.09572	0.09474	0.09572
$\angle HOH$ (deg)	104.52	105.538	104.52
$q(O)$ (e)	-	-0.8688	-0.8655

Table 5.2: The quantum mechanical calculations predict geometry that is close to the experimentally observed gas phase water monomer geometry. In a single point calculation we use user specified molecular geometry to estimate the partial charges.

A potential energy scan for different OH bond lengths and HOH bond angles around the QM minima showed that the gas phase water molecule potential energy surface has a definite minimum as shown in Figure 5.8. All quantum mechanical calculations were done using Gaussian03 package [125]. We chose restricted Hartree Fock method using 6-31G(d) basis set.

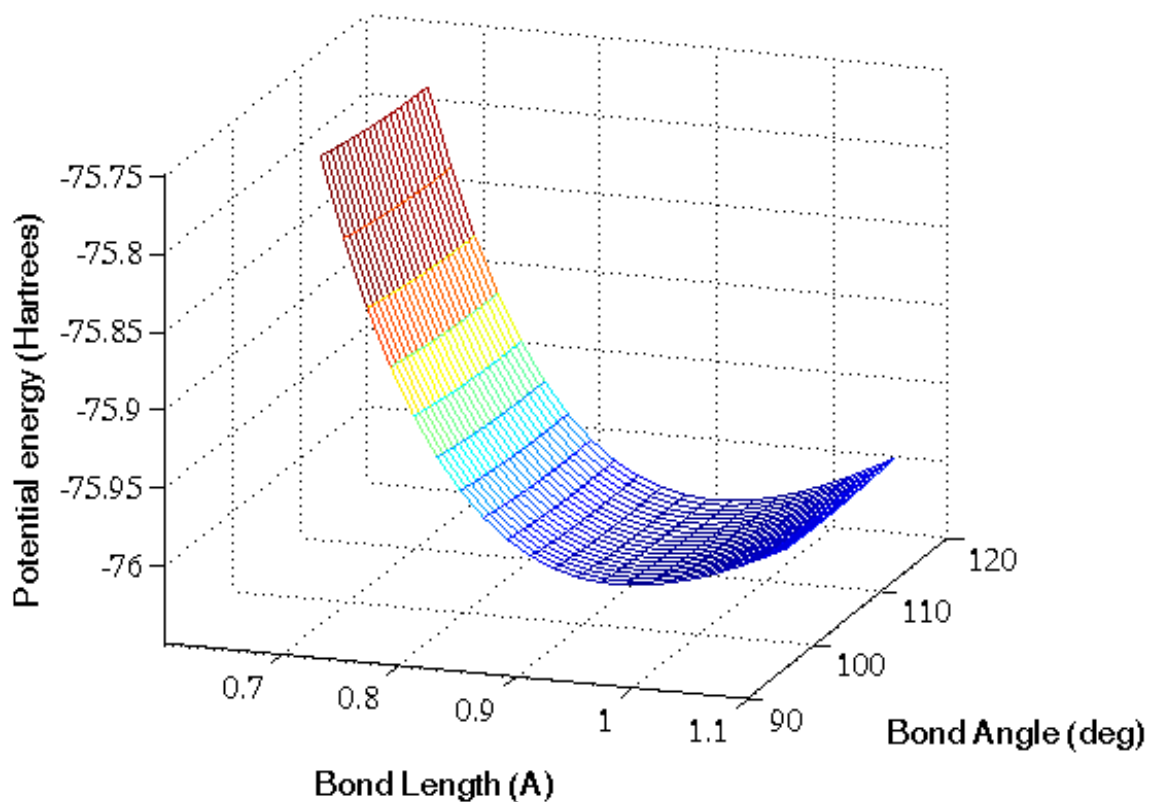


Figure 5.8: There exists a single, distinct minima both with respect to bond length and bond angle in the potential energy surface of a water molecule in gas phase.

Also the dipole moment of liquid water is debated to be between 2.6–3.0 D [126, 119]. The QM minimized geometry and charges give dipole close to 2.6 D [127]. However, there could be multiple geometry and charge combinations which could give dipole moment in the range 2.6–3.0 D. We also browsed through the literature for different water models to get the upper and lower bounds for each parameter. We define our parameter search space such that these bounds include all popular water models and are around the QM minima. These bounds are listed in the Table 5.3.

Parameter	(units)	Range [lower bound , upper bound]
ROH	(nm)	[0.08572 , 0.10572]
AHOH	(rad)	[1.685 , 1.964]
ROM	(nm)	[-0.025 , 0.025]
σ	(nm)	[0.26,0.35]
ϵ	(kJ/mol)	[0.332,2.495]
q(O)	(e)	[-1.3,-0.6]

Table 5.3: The parameter bounds for exploring the atomistic water model parameter space.

5.2.2.4 Work flow for the parameterization. Figure 5.9 shows the work flow for the optimization routine. The initial guess parameter set is input to a re-evaluation and estimation module. The re-evaluated energies along with the sampled energies are used to predict the properties $F_{sim}(T, P, \mathbf{x}_i)$. ξ is estimated using the simulated properties for the input set. ξ is checked against a convergence criteria, if it passes the criteria the iteration is stopped, if not then the parameter set \mathbf{x}_i is passed to a gradient based or direct optimization routine to get a parameter set for the next iteration. Optimization involves multiple function calls to the re-evaluation and the estimation module.

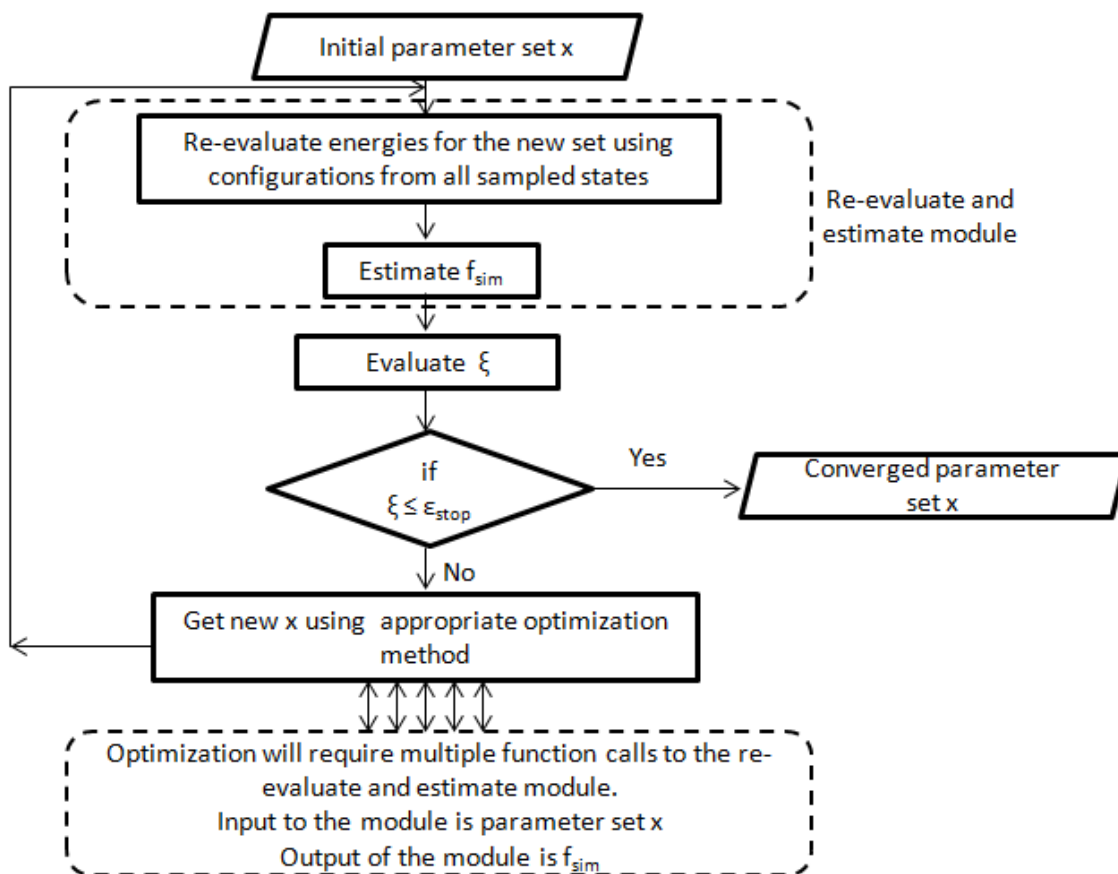


Figure 5.9: The workflow for the optimization. The thermodynamic observables are estimated using reweighting as opposed to running new molecular simulations. This should speed up the iterations in the workflow.

5.3 Results

Table 5.4 contains the starting TIP4P parameters and the final optimized parameters. We call the set of optimized parameters as Gibbs Optimized Parameters for Atomistic Liquid simulation, GOPAL. As predicted the optimized geometry is very close to the experimentally derived geometry also used by TIPnP models. This finding for the first time quantitatively proves the assumption to be true.

Model	r_{OH} nm	$\angle HOH$ Rad	r_{OM} nm	q_O e.s.u	σ_O nm	ϵ_O kJ/mol
1) TIP4P	0.0957	1.8242	0.0150	-1.0400	0.3154	0.6487
2)	0.0945	1.8337	0.0136	-1.0519	0.3158	0.6638
3)	0.0945	1.8283	0.0134	-1.0450	0.3139	0.7380
4)	0.0946	1.8371	0.0126	-1.0371	0.3138	0.7733
5)	0.0946	1.8395	0.0119	-1.0265	0.3125	0.8462
6)	0.0945	1.8465	0.0122	-1.0300	0.3110	0.9365
7)	0.0957	1.8639	0.0122	-1.0220	0.3126	0.8920
8)	0.0956	1.8613	0.0127	-1.0280	0.3128	0.8484
9)	0.0958	1.8567	0.0132	-1.0281	0.3131	0.8115
10)	0.0958	1.8568	0.0131	-1.0275	0.3130	0.8120
11) GOPAL	0.0958	1.8569	0.0131	-1.0276	0.3130	0.8122

Table 5.4: Optimization converged after 11 simulation iterations and 4100 iterations involving reweighting.

In Table 5.5 we can see that the optimization starting with TIP4P parameters as initial guess brings down the mean square relative error (MSRE) in molar volume V , potential energy or residual internal energy, U_{res} , residual entropy, S_{res} , as well as residual Gibbs free energy, f_{res} . We started the optimization with TIP4P parameters and used reweighting to estimate the objective function and constraint function at new iterations. After several iterations parameters perturbations became very small and MSRE stopped improving. The parameter set at which reached this intermediate convergence was reached, was used to generate fresh samples and restart the optimization process. The optimization converged to the final answer after 11 such fresh simulations starts, and a total of 4100 reweighting

iterations. The ten parameter sets shown in Table 5.5 are the ones which we had to simulate. We used 11 temperatures $\{1, 4, 10, 20, 30, 40, 50, 60, 70, 80, 98\}^{\circ}\text{C}$ and 2 pressures $[1.01325, 121.01325]$ bar to generate the fresh samples. This gave 22 sampled pressure and temperature states. We used 88 intermediate temperature and pressure combinations i.e., a total of 110 temperature and pressure combinations to generate the property surfaces.

We used a tolerance of 10^{-6} in the constraint functions of U_{res} , S_{res} and f_{res} for parameter sets 1-5 in Table 5.5, however, from the 6th set we had to relax the tolerance to 10^{-4} , 5^{-3} and 10^{-4} to prevent MSRE V from further deteriorating. The constraints are always satisfied from this point onwards, the optimization stops minimizing MSRE in U_{res} , S_{res} and f_{res} (to satisfy the constraints) and focuses solely on minimizing MSRE V . We can observe this change visually in Figure 5.10. After we relax the tolerance at the 6th set, MSRE in V decreases at the cost of increasing MSRE in U_{res} , S_{res} and f_{res} .

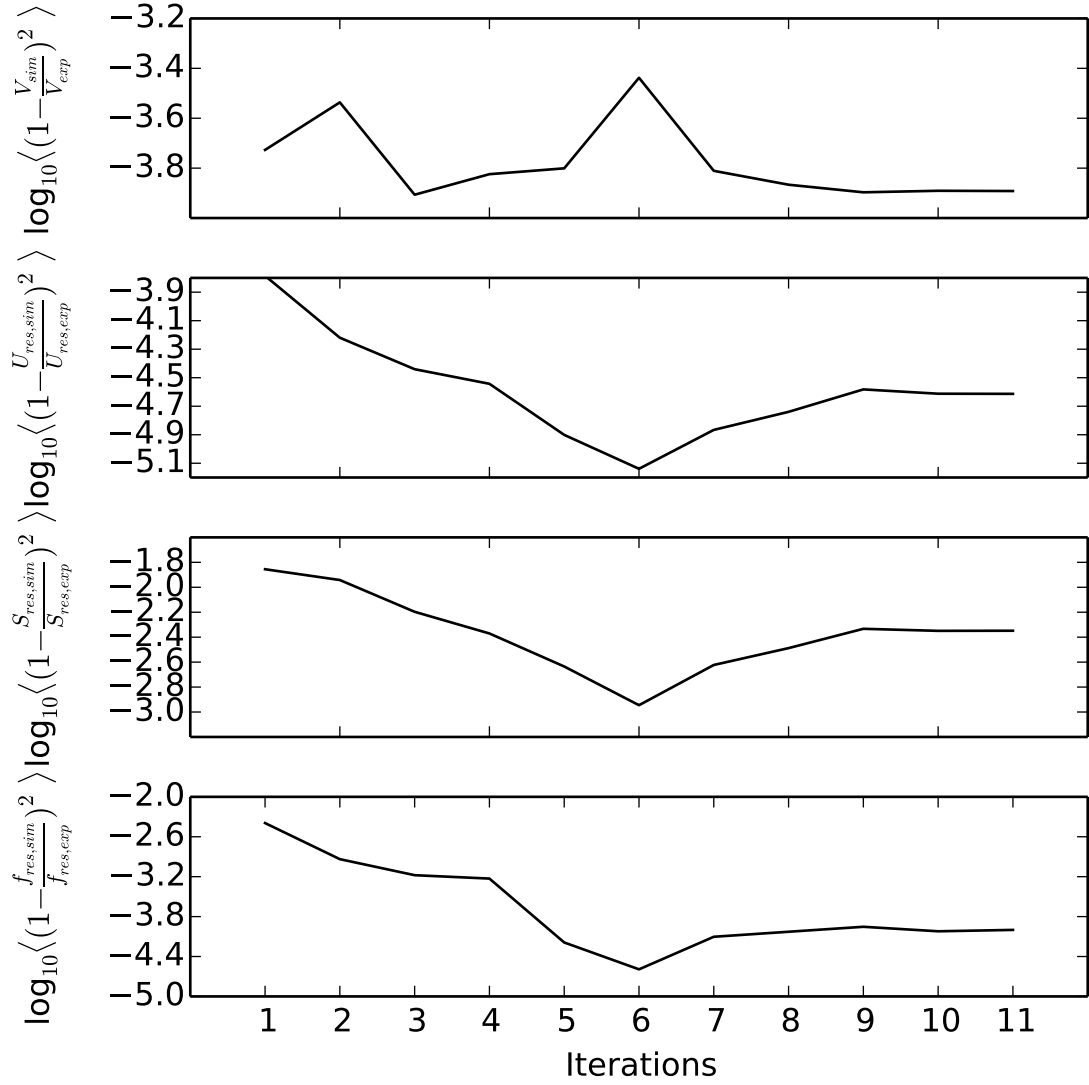


Figure 5.10: MSRE in V , U_{res} , S_{res} and f_{res} cannot simultaneously decrease indefinitely. MSRE in U_{res} , S_{res} and f_{res} has to be sacrificed to get reduction in MSRE in V

We found the observation from the SAFT runs that we cannot reduce the error in Gibbs free energy and density simultaneously to be true in the atomistic simulations also. This limitation could be due to the rigid geometry and fixed charge model of water. One way to

improve the agreement is to vary the hardness and dispersion of the Lennard Jones model. Instead of a 12-6 model we could make the repulsion and dispersion exponents variables in our optimization and estimate which powers better model water.

Model	MSRE V	MSRE U_{res}	MSRE S_{res}	MSRE f_{res}
1) TIP4P	1.875×10^{-4}	1.640×10^{-4}	1.395×10^{-2}	4.036×10^{-3}
2)	2.908×10^{-4}	6.031×10^{-5}	1.143×10^{-2}	1.157×10^{-3}
3)	1.240×10^{-4}	3.628×10^{-5}	6.359×10^{-3}	6.644×10^{-4}
4)	1.499×10^{-4}	2.866×10^{-5}	4.262×10^{-3}	5.908×10^{-4}
5)	1.582×10^{-4}	1.256×10^{-5}	2.317×10^{-3}	6.473×10^{-5}
6)	3.649×10^{-4}	7.261×10^{-6}	1.134×10^{-3}	2.554×10^{-5}
7)	1.546×10^{-4}	1.361×10^{-5}	2.383×10^{-3}	7.883×10^{-5}
8)	1.360×10^{-4}	1.822×10^{-5}	3.253×10^{-3}	9.380×10^{-5}
9)	1.268×10^{-4}	2.618×10^{-5}	4.646×10^{-3}	1.114×10^{-4}
10)	1.286×10^{-4}	2.442×10^{-5}	4.474×10^{-3}	9.532×10^{-5}
11) GOPAL	1.283×10^{-4}	2.436×10^{-5}	4.484×10^{-3}	9.997×10^{-5}

Table 5.5: MSREs for optimized parameters compared as a function of iteration from the optimization done using a grid of 110 temperature and pressure points.

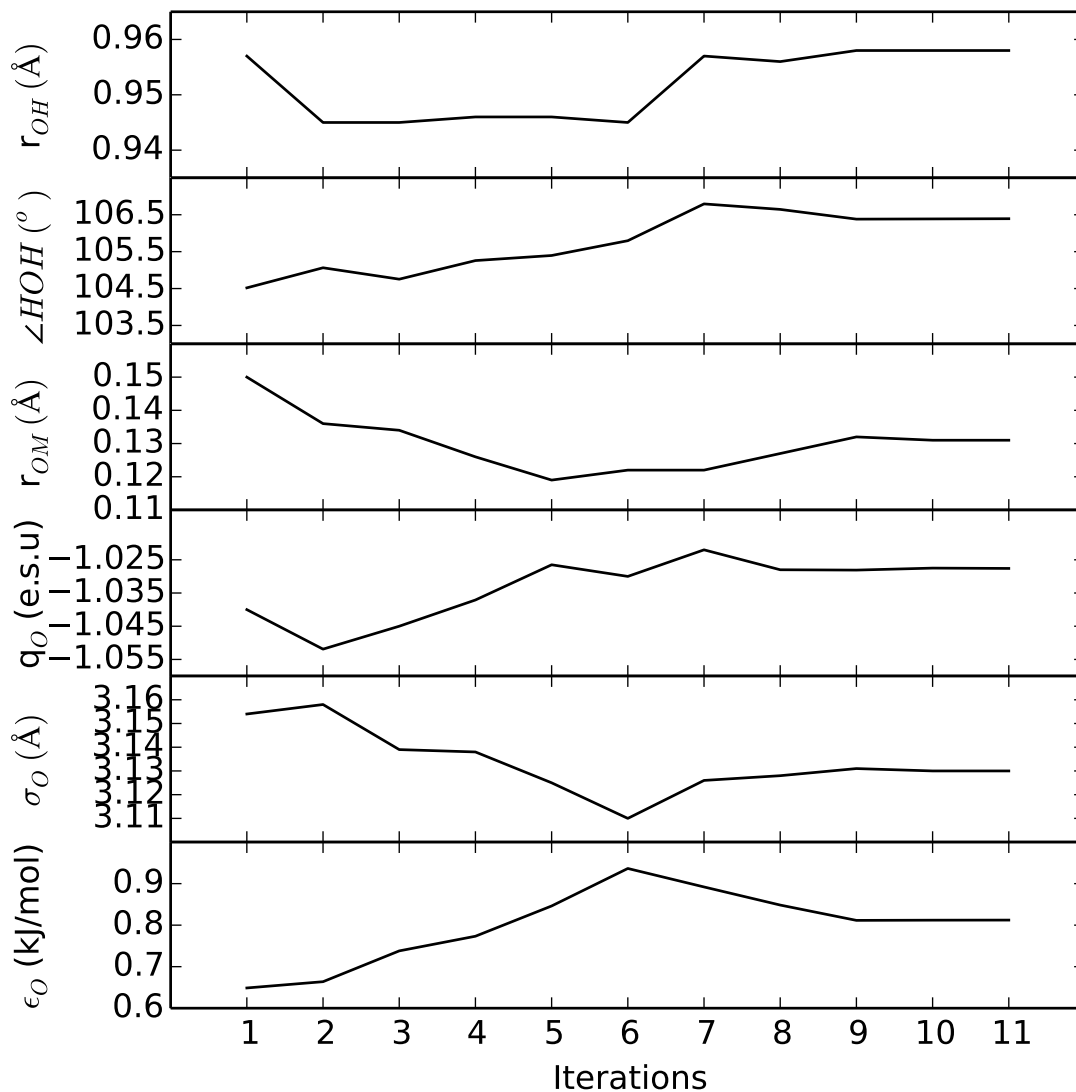


Figure 5.11: After we relax the tolerances in U_{res} , S_{res} and f_{res} at the sixth sampled set we see that all the parameters converge to a value for which MSRE in V is minimum.

We increased the number of grid points from 110 to 210 for the final comparison between TIP4P and GOPAL to capture any inconsistencies in the property surface with the finer grid spacing. Figures 5.12 - 5.21 show property surfaces

- (a) estimated using experimental equation of state, IAPWS95,
 - (b) estimated using atomistic simulations with TIP4P parameters,
 - (c) estimates using atomistic simulations with GOPAL parameters,
- and also the difference between experimental and simulated property surface
- (d) difference between TIP4P and experimental property surface,
 - (e) difference between GOPAL and experimental property surface.

In all the plots triangles represent the sampled states and the dots represent the reweighted states.

All simulated property surfaces except $C_{P,res}$ look similar to experimental property surface in shape and form for both TIP4P and GOPAL parameter sets. It is only when we look at the difference from the experimental property surface we find that the property estimates using GOPAL parameter set have improved agreement with the experimental properties. For example, we can see that TIP4P has small deviation from experimental f_{res} at low temperatures and large deviations in f_{res} at higher temperatures. GOPAL has low deviations in f_{res} at both high and low temperatures. The H_{vap} surface, although shifted by almost 4.6 kJ/mol (since we do not include the self polarization correction) has lower deviation at higher temperatures. Similarly, the experimental and simulated U_{res} and S_{res} , H_{res} estimates using GOPAL parameter set have better agreement than TIP4P. TIP4P densities have large errors, 27 kg/m³ at high temperatures and low error at lower temperatures 4 kg/m³. GOPAL shows equal deviations at lower and higher temperatures of about 16 kg/m³. Although the TIP4P and GOPAL $C_{P,res}$ surfaces do not match in form when compared to experimental $C_{P,res}$ surface we can easily see that the deviations from experimental $C_{P,res}$ surface is lower for GOPAL compared to TIP4P. This is due to lowering of error in the

residual entropy surface with GOPAL parameters. The deviations in estimates of compressibility and thermal expansion coefficients seem to show no improvement. However, the magnitude of deviation and the uncertainty in the deviation are of the same magnitude which makes any comparison difficult. This is not the case for U_{res} and S_{res} , H_{res} , f_{res} for which the uncertainty in deviation is one to two orders lower compared to magnitude of deviation itself. Thus the differences are statistically significant.

In Table 5.6 we see that there is a statistically significant improvement in almost all thermodynamic properties if we use GOPAL parameter set. The largest percentage decrease in MSRE is in $G_{res} \sim 99\%$.

Property	TIP4P MSRE1 $\pm\delta$ (MSRE1)	GOPAL MSRE2 $\pm\delta$ (MSRE2)	Percent decrease $\frac{MRSE1-MRSE2}{MRSE1} \times 100$
U_{res}	$1.843 \times 10^{-4} \pm 4.497 \times 10^{-6}$	$2.677 \times 10^{-5} \pm 1.472 \times 10^{-6}$	85
S_{res}	$9.283 \times 10^{-3} \pm 1.466 \times 10^{-3}$	$2.990 \times 10^{-3} \pm 7.698 \times 10^{-4}$	68
V	$2.158 \times 10^{-4} \pm 7.274 \times 10^{-6}$	$1.354 \times 10^{-4} \pm 4.885 \times 10^{-6}$	37
G_{res}	$4.468 \times 10^{-2} \pm 4.588 \times 10^{-3}$	$5.658 \times 10^{-4} \pm 3.108 \times 10^{-4}$	99
ρ	$2.063 \times 10^{-4} \pm 6.755 \times 10^{-6}$	$1.341 \times 10^{-4} \pm 4.707 \times 10^{-6}$	35
H_{res}	$1.609 \times 10^{-4} \pm 3.900 \times 10^{-6}$	$2.379 \times 10^{-5} \pm 1.285 \times 10^{-6}$	85
H_{vap}	$1.204 \times 10^{-2} \pm 2.892 \times 10^{-5}$	$1.007 \times 10^{-2} \pm 2.477 \times 10^{-5}$	16
$C_{P,res}$	$1.044 \times 10^{-2} \pm 4.557 \times 10^{-3}$	$2.466 \times 10^{-3} \pm 2.419 \times 10^{-3}$	76
κ_T	$8.116 \times 10^{-2} \pm 2.097 \times 10^{-1}$	$3.697 \times 10^{-2} \pm 1.408 \times 10^{-1}$	54
α_P	$6.846 \times 10^3 \pm 1.114 \times 10^4$	$1.192 \times 10^4 \pm 1.335 \times 10^4$	-74

Table 5.6: MSRE of all properties derived from first and second derivatives of Gibbs free energy with respect to temperature and pressure decrease for GOPAL. MSRE in G_{res} is statistically insignificant and close to zero for GOPAL. Near the melting temperature, relative errors in α_P are very high because the experimental α_T are very close to zero $\sim 10^{-7} \text{ K}^{-1}$ while the simulated α_P are still $\sim 4 \times 10^{-4} \text{ K}^{-1}$ causing the MSRE to jump three orders of magnitude. At all other temperatures the relative errors in α_P are less than 1. For the rest of the properties there is a statistically significant improvement in the corresponding MSRE. MSRE calculations in this table are done using properties estimated for 210 temperature and pressure combinations.

GOPAL water model parameters have the lowest error in f_{res} compared to any TIPnP water models, SPC and SPC/E water models. Thus, GOPAL water model parameters do a better job in modeling the intermolecular interactions of liquid water. However, the GOPAL water model parameters are unable to reproduce the correct density maximum and the compressibility minimum for water.

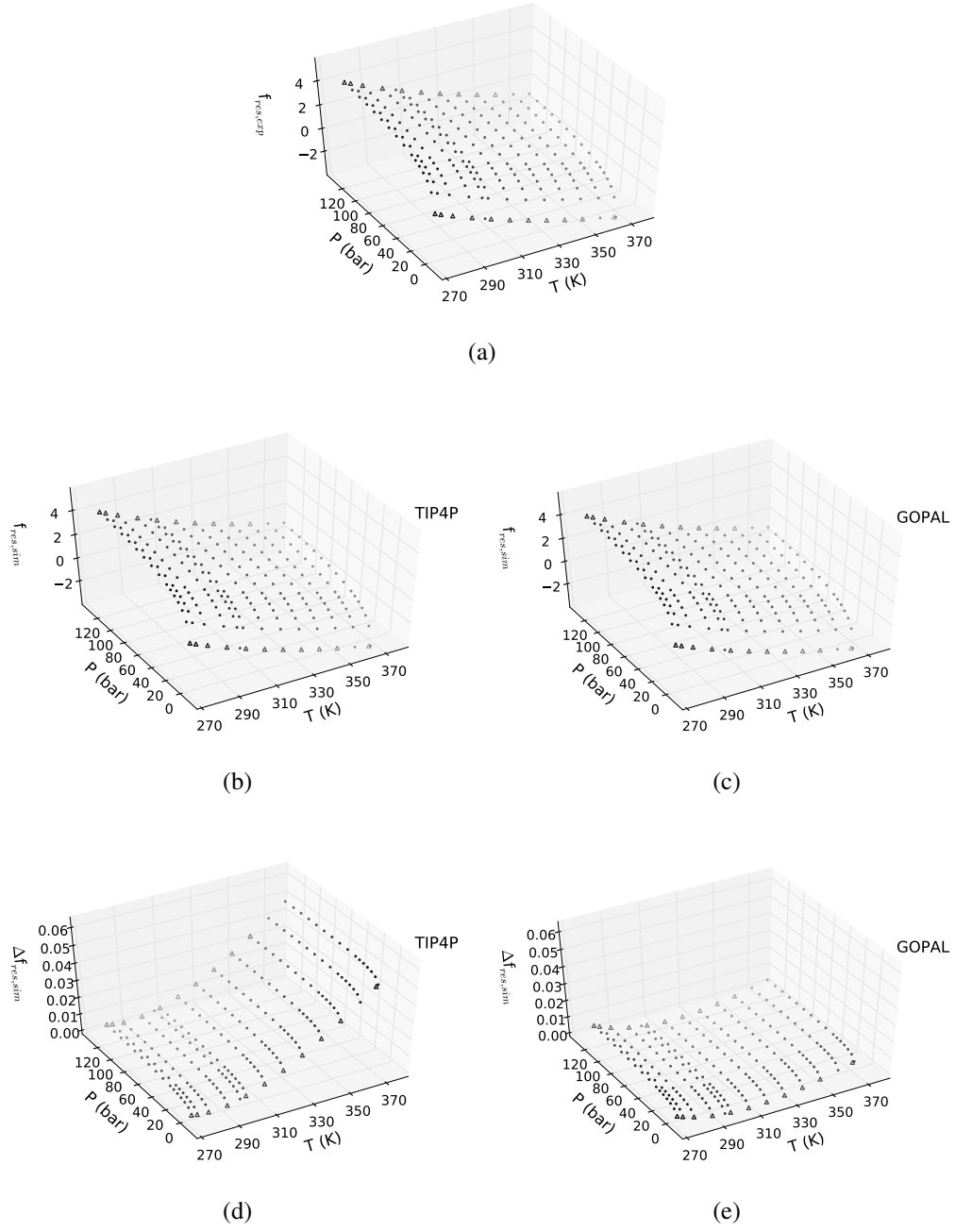


Figure 5.12: MSRE in f_{res} reduces by 99% after optimization. (a) Experimental f_{res} surface, (b) TIP4P f_{res} surface, (c) GOPAL f_{res} surface (d) difference between TIP4P and experimental f_{res} surfaces, (e) difference between GOPAL and experimental f_{res} surface

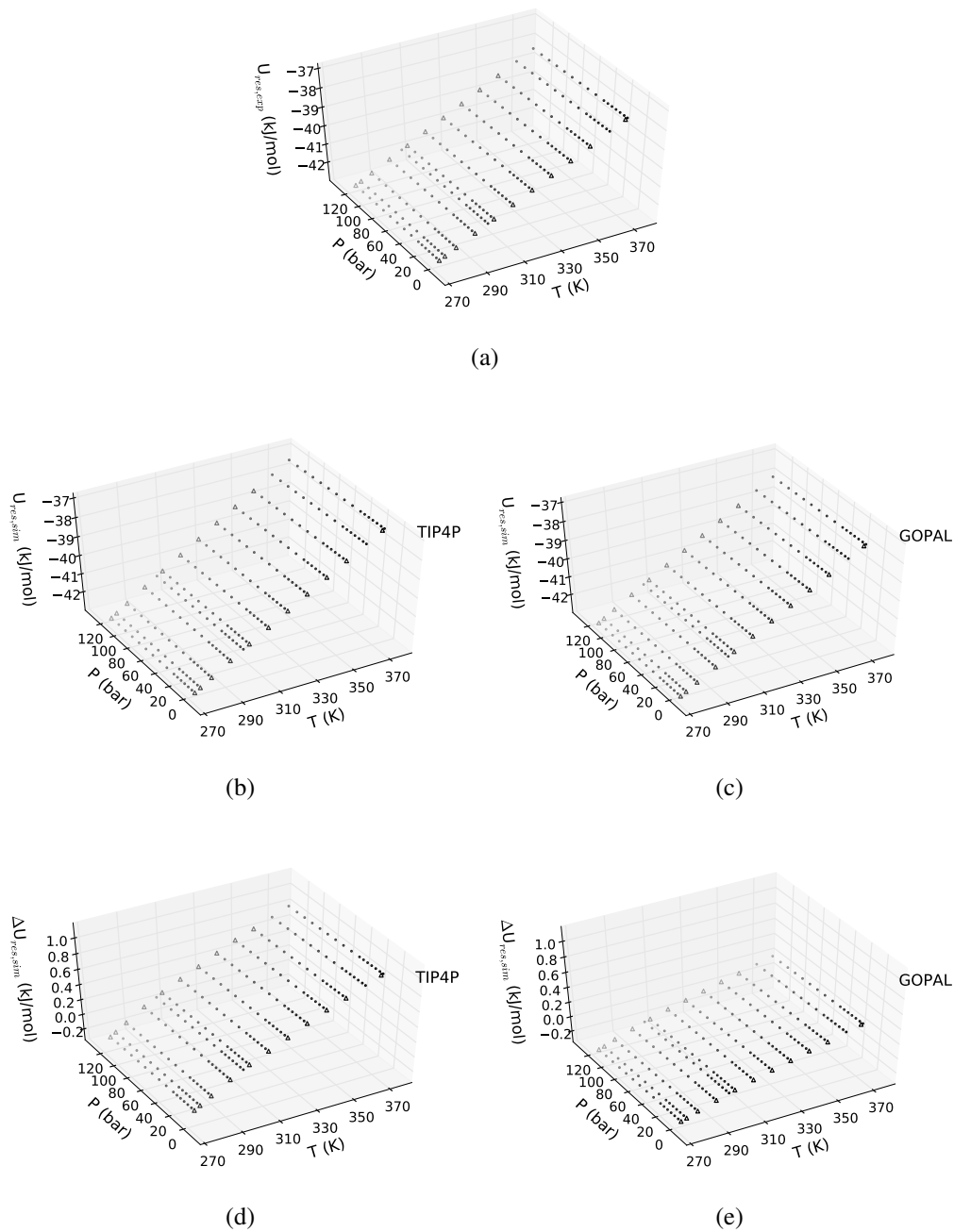


Figure 5.13: MSRE in U_{res} reduces by 85% after optimization. (a) Experimental U_{res} surface, (b) TIP4P U_{res} surface, (c) GOPAL U_{res} surface (d) difference between TIP4P and experimental U_{res} surfaces, (e) difference between GOPAL and experimental U_{res} surfaces

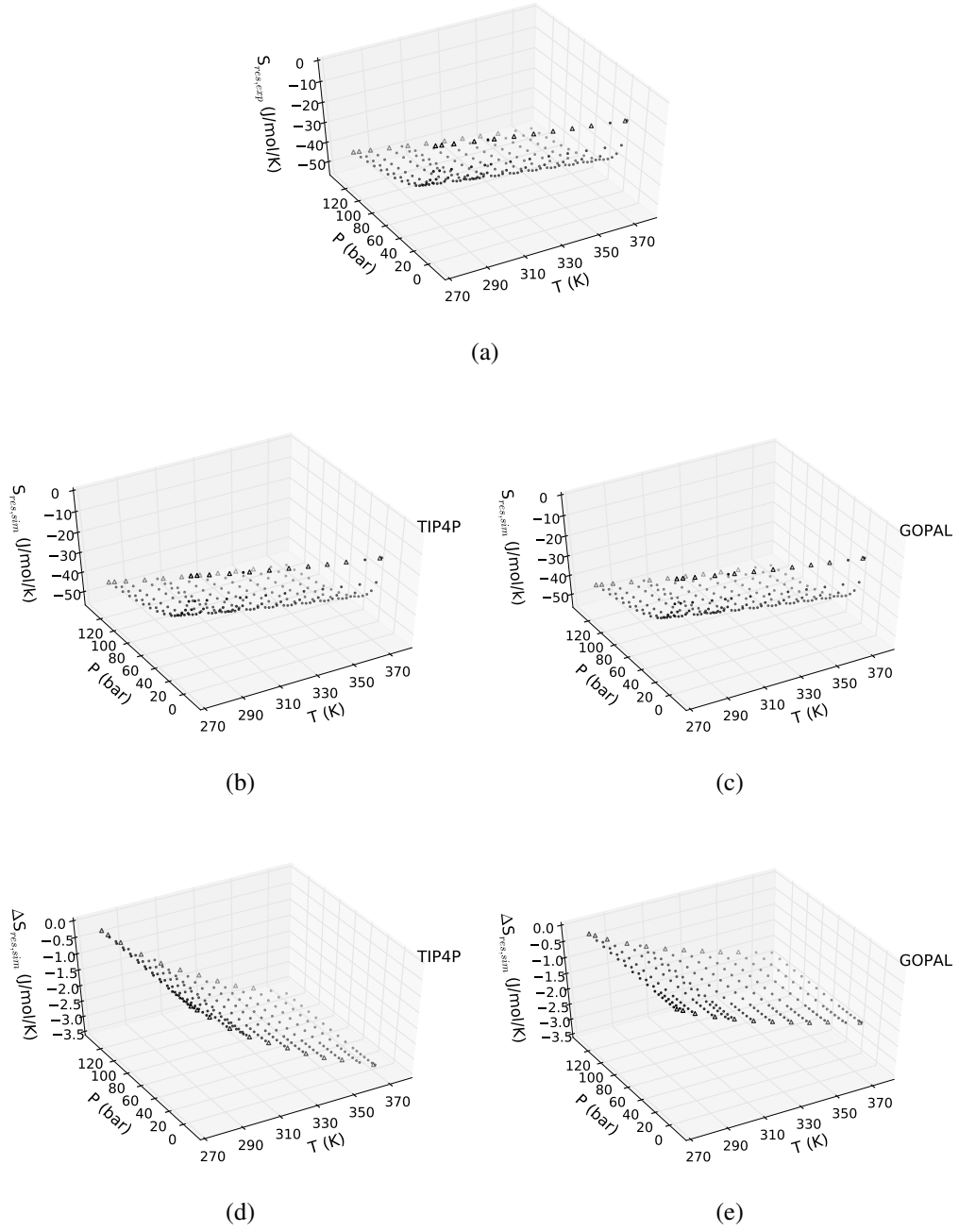


Figure 5.14: MSRE in S_{res} reduces by 68% after optimization. (a) Experimental S_{res} surface, (b) TIP4P S_{res} surface, (c) GOPAL S_{res} surface (d) difference between TIP4P and experimental S_{res} surfaces, (e) difference between GOPAL and experimental S_{res} surfaces

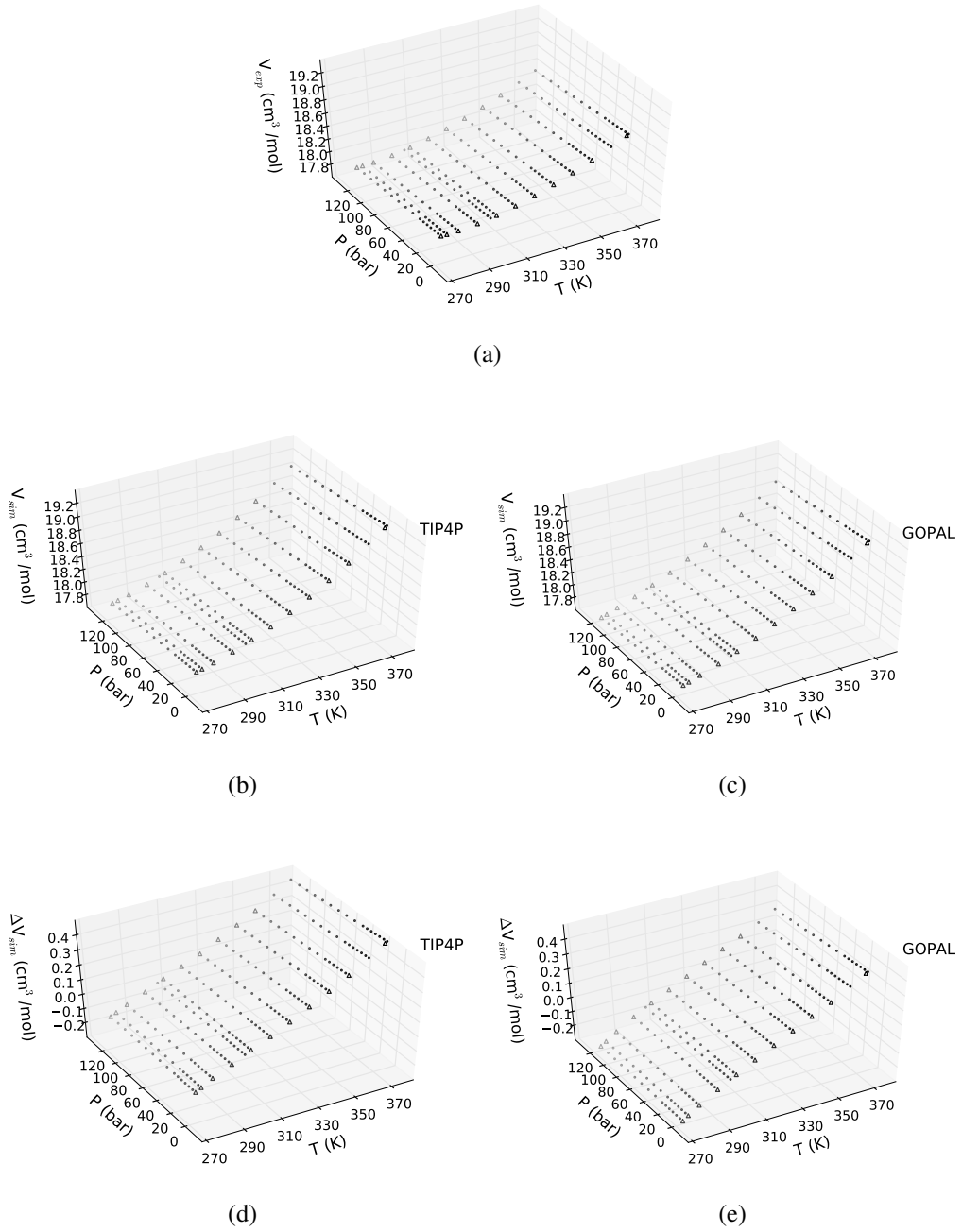


Figure 5.15: MSRE in V reduces by 37% after optimization. Error in V gets redistributed evenly around $T = 310$ K after optimization. (a) Experimental V surface, (b) TIP4P V surface, (c) GOPAL V surface (d) difference between TIP4P and experimental V surfaces, (e) difference between GOPAL and experimental V surfaces

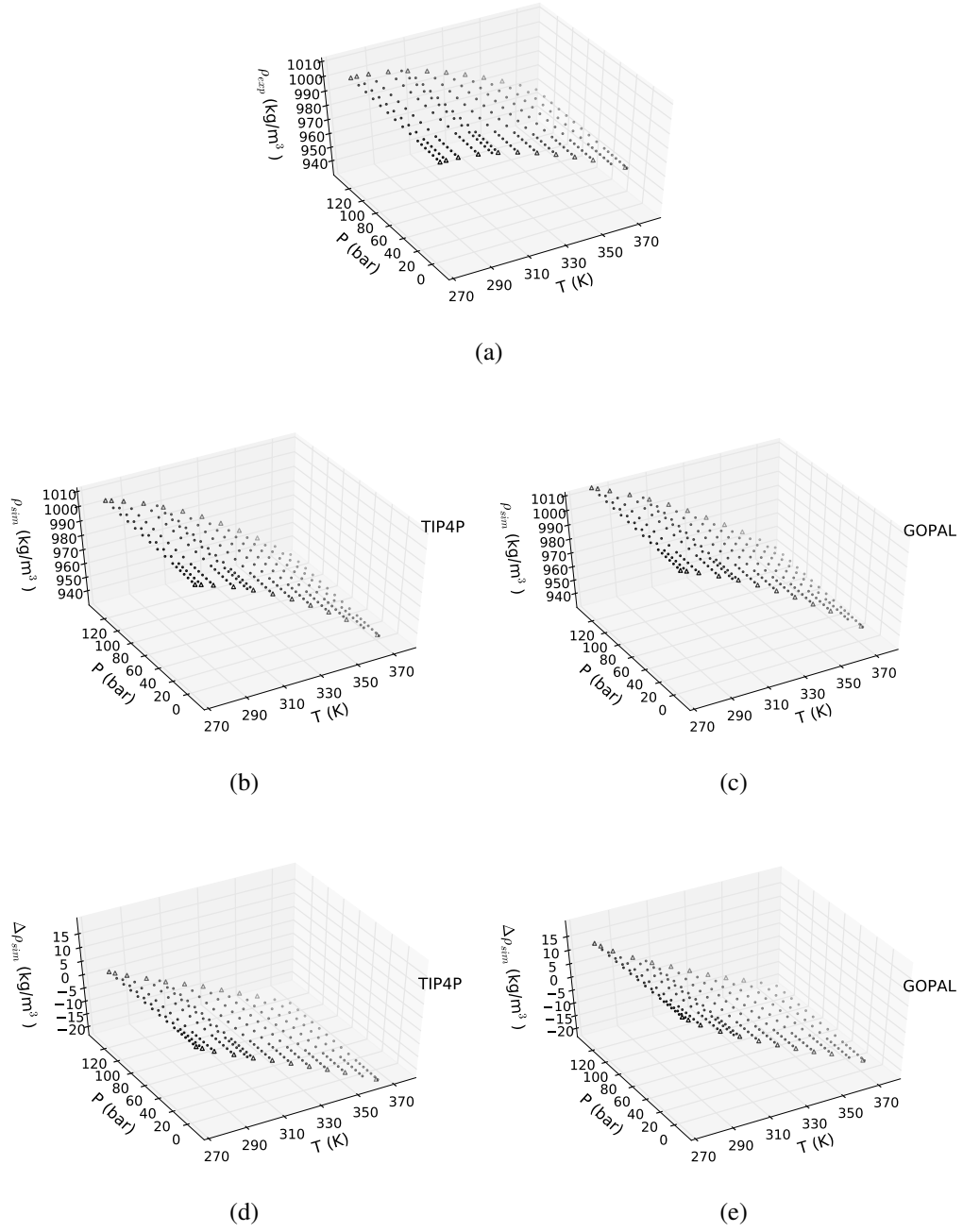


Figure 5.16: MSRE in density reduces by 35% after optimization. Error in density also gets redistributed evenly around $T = 310$ K after optimization. (a) Experimental density surface, (b) TIP4P density surface, (c) GOPAL density surface (d) difference between TIP4P and experimental density surfaces, (e) difference between GOPAL and experimental density surfaces

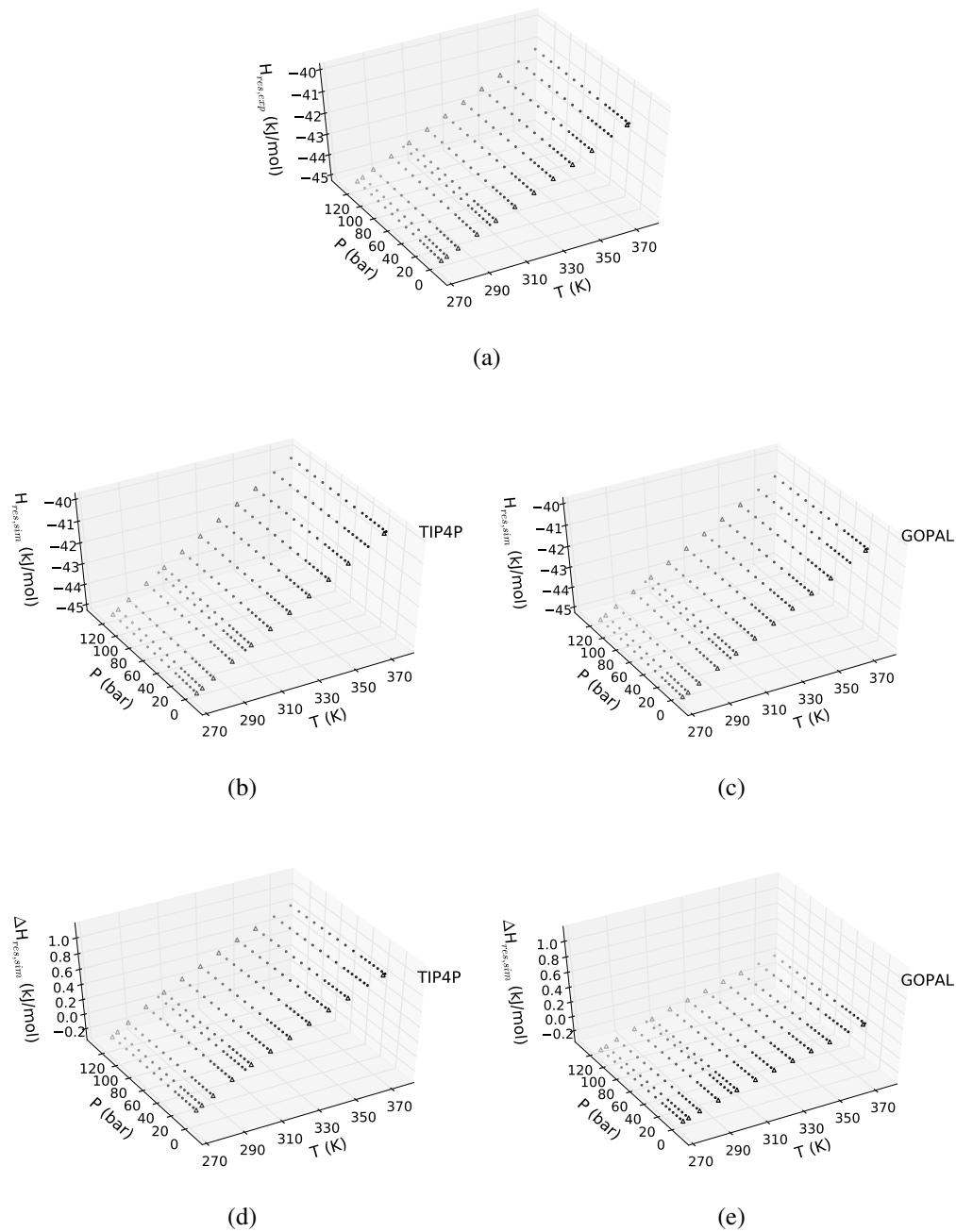


Figure 5.17: MSRE in H_{res} reduces by 85% after optimization. (a) Experimental H_{res} surface, (b) TIP4P H_{res} surface, (c) GOPAL H_{res} surface (d) difference between TIP4P and experimental H_{res} surfaces, (e) difference between GOPAL and experimental H_{res} surfaces

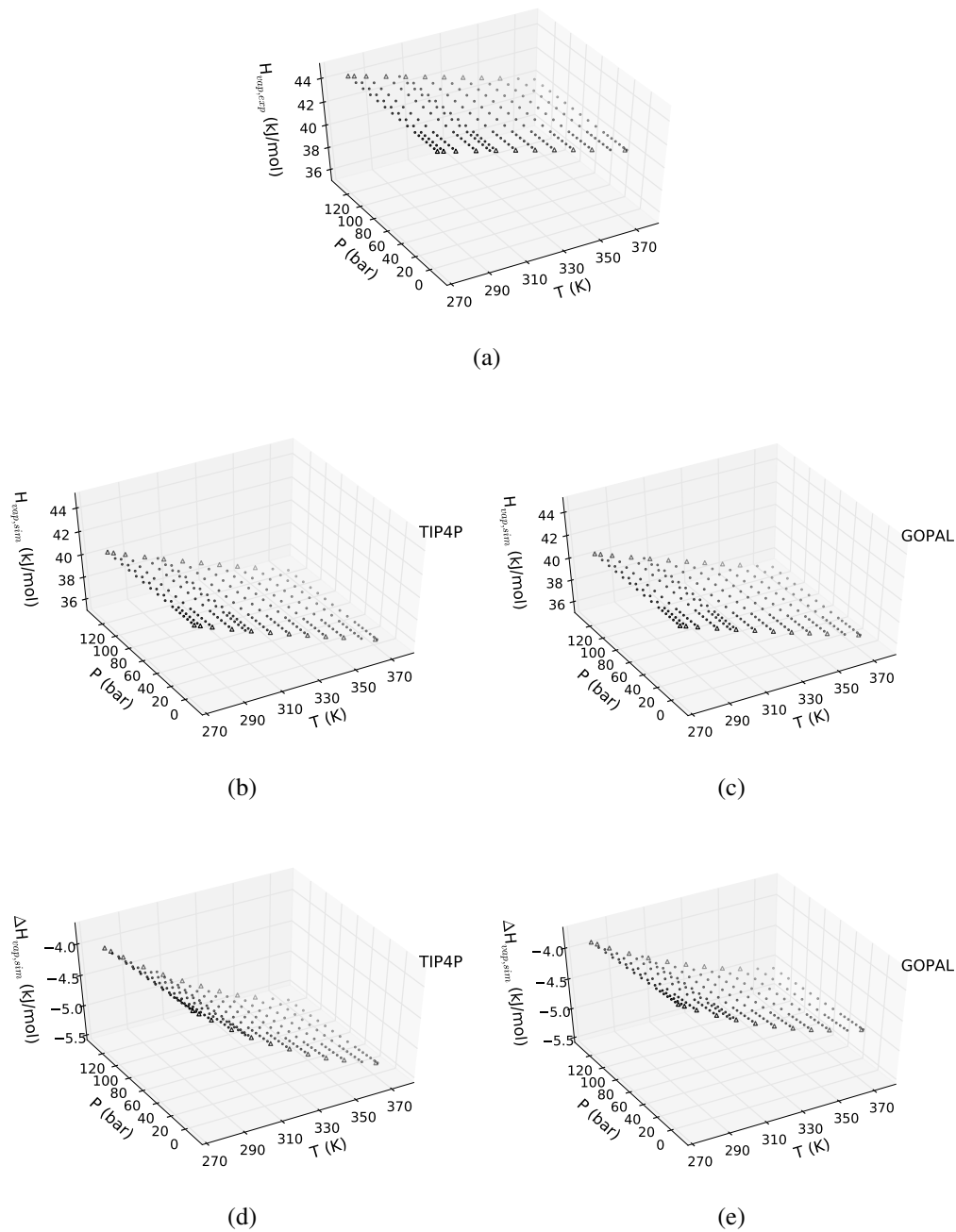


Figure 5.18: MSRE in H_{vap} reduces by 16% after optimization, however, there is shift of $\simeq 4.5$ kJ/mol. (a) Experimental H_{vap} surface, (b) TIP4P H_{vap} surface, (c) GOPAL H_{vap} surface (d) difference between TIP4P and experimental H_{vap} surfaces, (e) difference between GOPAL and experimental H_{vap} surfaces

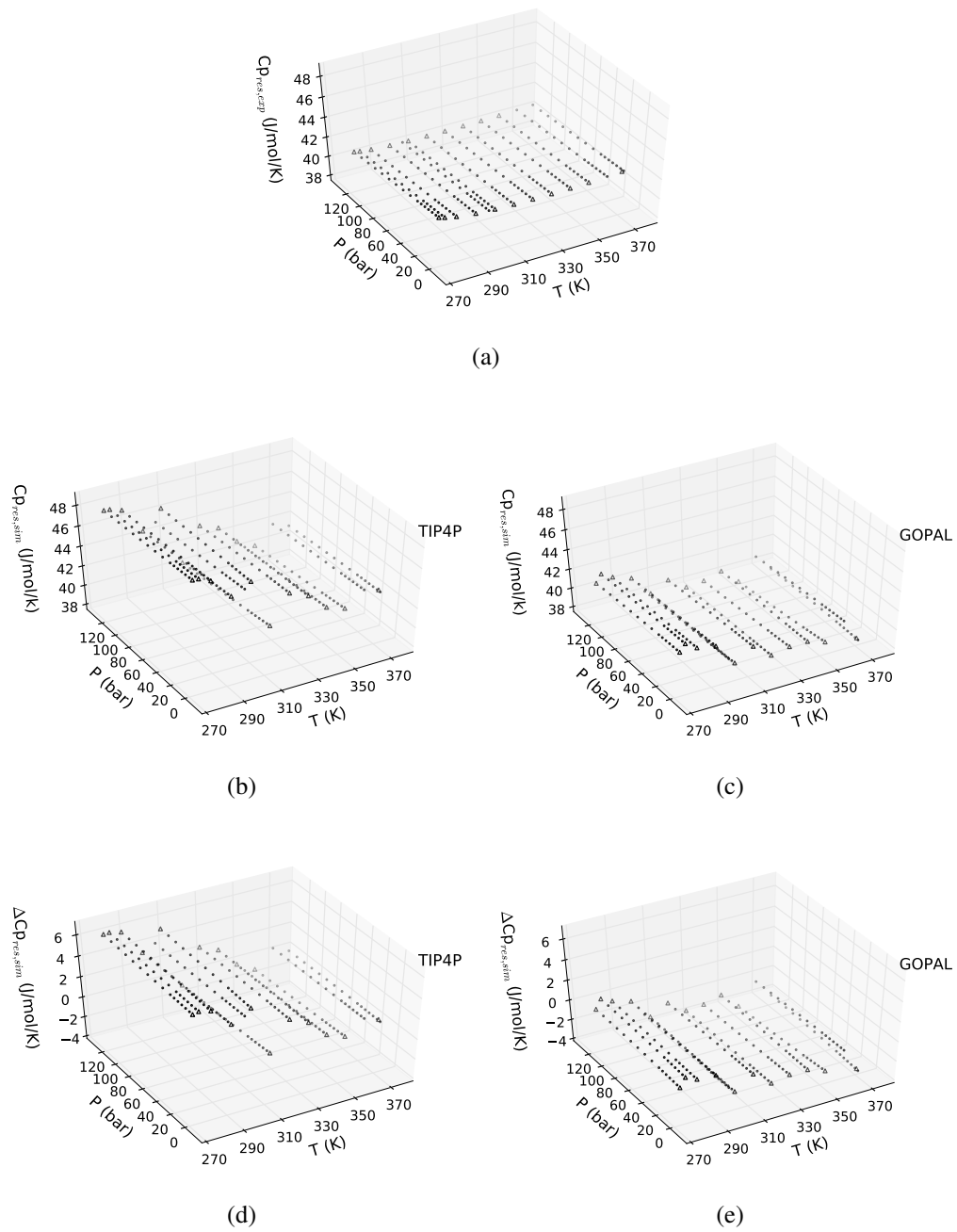


Figure 5.19: MSRE in $C_{p,res}$ reduces by 76% after optimization. (a) Experimental $C_{p,res}$ surface, (b) TIP4P $C_{p,res}$ surface, (c) GOPAL $C_{p,res}$ surface (d) difference between TIP4P and experimental $C_{p,res}$ surfaces, (e) difference between GOPAL and experimental $C_{p,res}$ surfaces

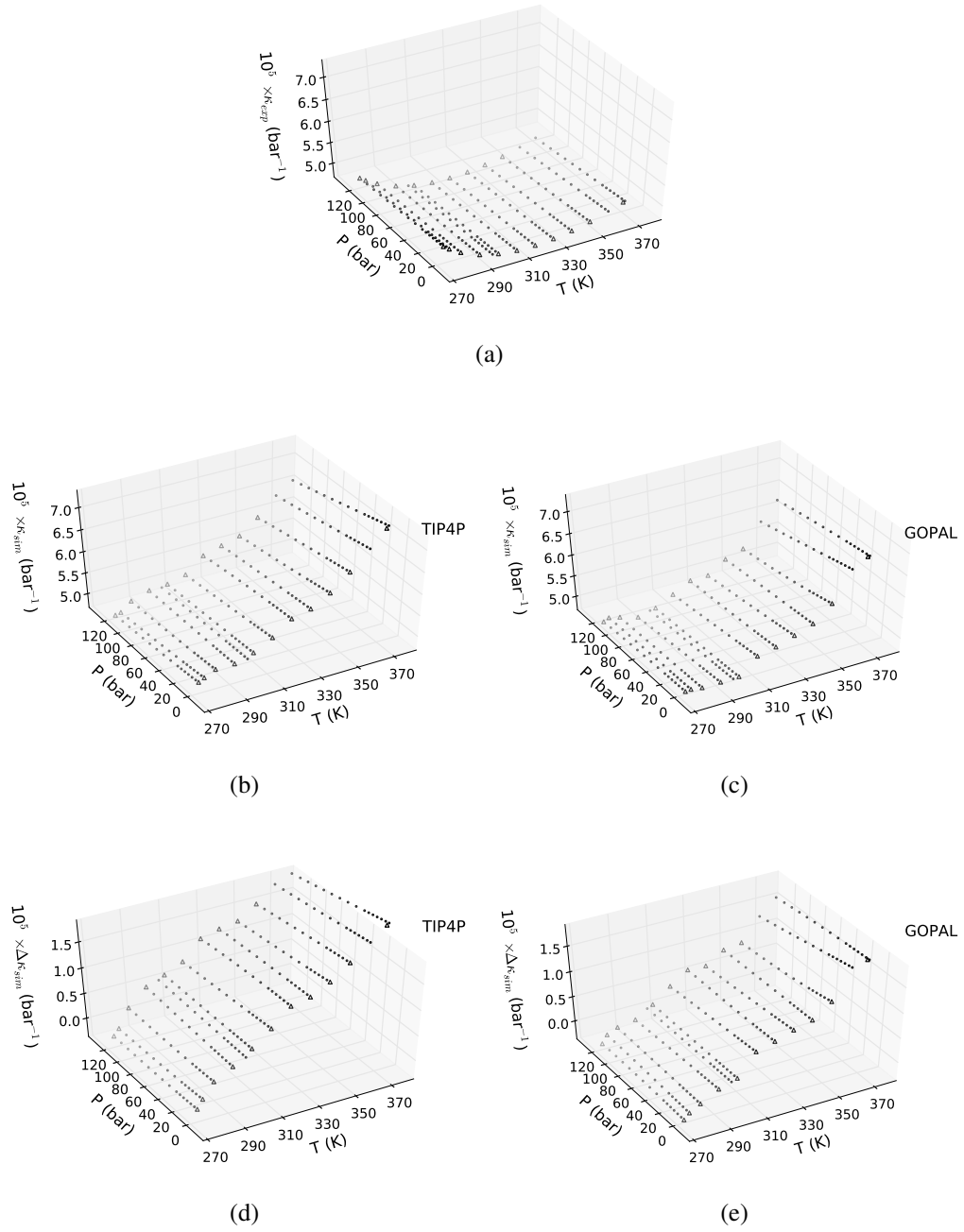


Figure 5.20: MSRE in κ reduces by 54% after optimization. (a) Experimental κ surface, (b) TIP4P κ surface, (c) GOPAL κ surface (d) difference between TIP4P and experimental κ surfaces, (e) difference between GOPAL and experimental κ surfaces

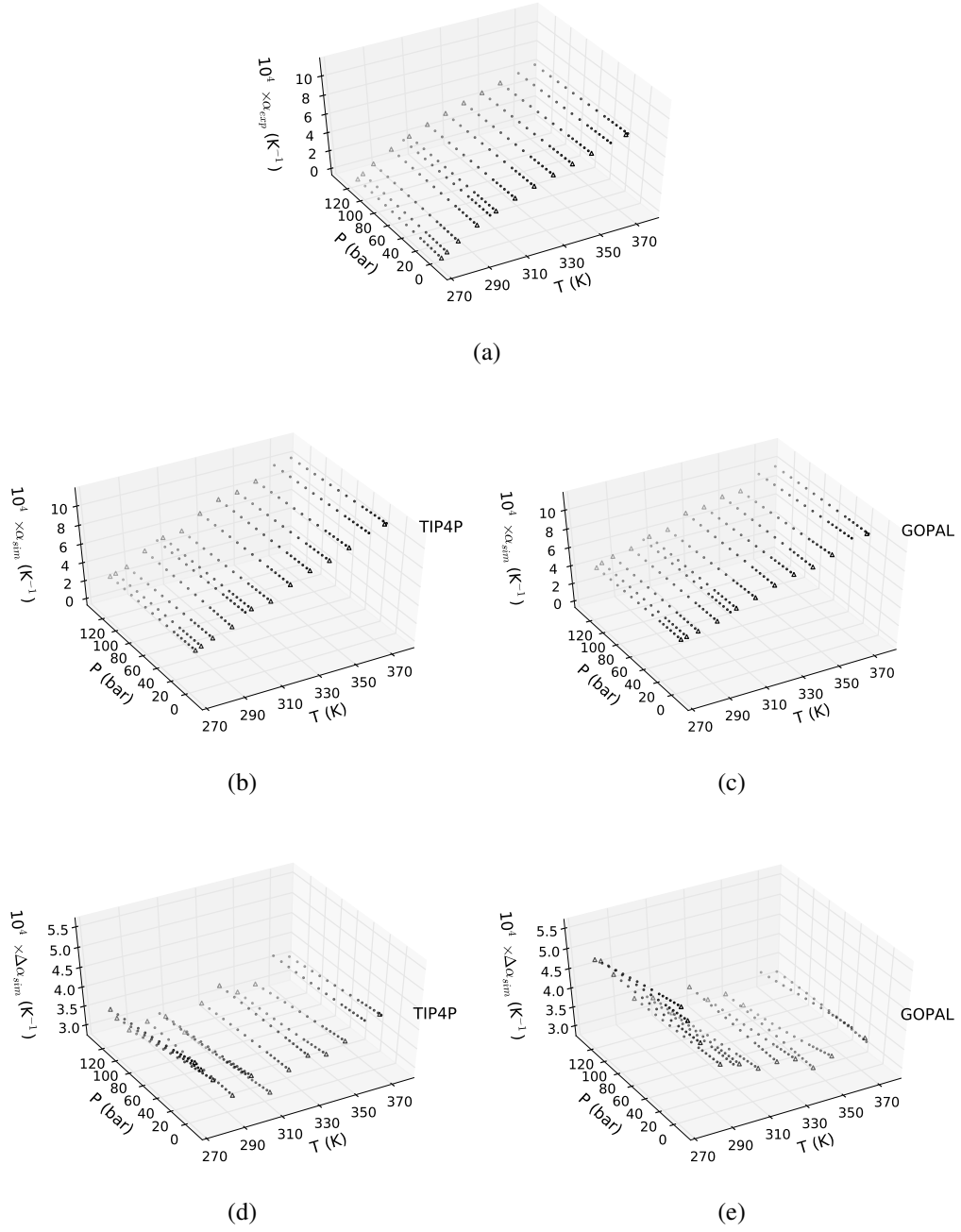


Figure 5.21: MSRE in α seems to increase by 74% after optimization. However, this increase is strongly dominated by the large relative error $\simeq 10^3$ near the melting temperature. (a) Experimental α surface, (b) TIP4P α surface, (c) GOPAL α surface (d) difference between TIP4P and experimental α surfaces, (e) difference between GOPAL and experimental α surfaces

5.4 Conclusions

In this work we have combined the multistate reweighting technique and configuration mapping technique to accelerate the rate limiting property estimation process in the force field parameterization exercise. We have shown the use of this approach by re-parameterizing TIP4P water model. The reparameterized model, GOPAL, shows reduced error in all thermodynamic properties compared to TIP4P model. GOPAL has the lowest error in residual Gibbs free energy surface compared to all other models. GOPAL has a 35% lower MSRE in density and a 99% lower MSRE in G_{res} compared to TIP4P water model. Using an initial trial and error approach and later thermodynamic arguments we have designed an objective function which minimizes the deviation between the experimental and simulated residual Gibbs free energy surface while preserving the first derivatives of the surface. The objective function is tested and further improved in design by parameterizing a SAFT equation of state for water.

The design of the objective function eliminates the need for determining proper weights to be assigned to the properties included in the objective function and seeks a solution of force field parameters which could uniquely and accurately reproduce intermolecular interactions experienced at the atomistic level. The use of explicit constraints on errors in residual internal energy, residual entropy and residual Gibbs free energy while minimizing error in molar volume has been shown to be an effective way to improve error in multiple simulated water properties simultaneously. We also found that in the SAFT as well as atomistic parameterizations, we cannot simultaneously reduce the errors in molar volume, residual internal energy, residual entropy and residual Gibbs free energy. Accuracy in molar volume has to be sacrificed to improve accuracy in residual internal energy, residual entropy and residual Gibbs free energy. The use of mesh adaptive direct search optimization

algorithm facilitates 1) full exploration of the parameter space, 2) tuning the strength of the constraints to efficiently handle even an infeasible starting point. The final optimization for the atomistic model involves 4100 iterations with 1100 free energies estimated at each iteration. Fresh molecular simulations for such exercise would have taken 1544 CPU yrs without reweighting. With reweighting it took less than eight CPU weeks to perform the calculations.

6 Future work: Protocol to determine excess thermodynamic properties for methanol-water mixture using reweighting and mapping techniques and use it to parameterize water and methanol to reproduce both pure fluid properties as well as mixture properties at all compositions

6.1 Introduction

Calculation of excess thermodynamic properties is of great interest to almost all process engineering problems exploring liquid-liquid, vapor-liquid, vapor-liquid-liquid equilibrium. There are a number of activity coefficient models [128, 129, 130, 120] for estimating excess free energy G^E . Using the model for G^E , H^E and V^E can be estimated using the Gibbs Helmholtz equation. S^E can be calculated using the Legendre transform on G^E and H^E . Thus we can essentially get all interesting thermodynamic observables using a excess free energy model for a given mixture.

A model is selected based on the type of mixture we want to model since each model works well for certain mixtures and fail for others. The prime reason for the difference in their applications is the amount of detail each includes about the mixture to model it. The most straight forward models come from Wohl's expansion for G^E , expressed as a power series of effective volume fractions of the two components. For example truncating the Wohl's expression after the first term gives van Laar equation [129]. Similarly Marguels equation is also derived using Whol's formalism [129]. These models are parameterized using experimental observations. Thus the parameters do not explicitly have temperature, pressure or binary interaction strength dependence.

Then there are some models which cannot be derived by Wohl's formulation. Wilson [131] model uses pure component molar volumes and characteristic energy differences to model G^E . NRTL [132] uses the concept of local composition. UNIQUAC [19] uses a combination of a combinatorial part and residual part. The combinatorial is determined based on the composition, molecular shape and size. Using only the pure component properties it describes the entropic contribution to G^E . The residual part depends on the intermolecular forces and determines the enthalpic contribution to G^E . Finally, there are models based on the statistical associated fluid theory [133] (SAFT) in which residual molar Helmholtz energy has contributions from formation of hard spheres (short range repulsions) and chains (chemically bonded aggregation), from dispersion (long range attraction) and from association between different molecules and chains (hydrogen bonding).

UNIQUAC and SAFT come very close to describe contributions to the excess properties in terms of molecular shape, distribution and interaction type. However these still use pure component thermodynamic data, composition and molecular information inexplicitly in the form of certain parameters which represent some combination of the latter three and which are fit to experimental observation. Almost all activity coefficient models assume that G^E is only a function of temperature and composition. The activity coefficient models do not have any term which includes pressure effects. The assumption holds true at low and moderate pressures but not at elevated pressures [129].

We could use molecular simulations to get more accurate estimates of the enthalpic (H^E) and the entropic contributions (S^E) to estimate G^E . Molecular simulations are based on explicit and full atomistic description, use mixing rules to correct interatomic forces at intermediate composition, handle distribution of molecules more accurately and can incorporate temperature and pressure effects.

Activity coefficients derived using molecular simulations theoretically are more accu-

rate than the ones predicted by activity coefficient models. However, using molecular simulations to calculate excess properties of a mixture is a tough problem because interactions as well as geometry change for different number of molecules at different compositions. As a result the configurations sampled while simulating certain composition are never seen in the simulation of other compositions. Thus we cannot do reweighting, which makes free energy analysis and estimation of other observables impossible. There are examples in the literature where people have used data from simulation done at individual compositions to estimate H^E and V^E [134, 135, 136] but G^E using multistate reweighting has never been presented.

Gibbs ensemble Monte Carlo (GEMC) [137, 138] coupled with configurational bias Monte Carlo (CBMC) [139] or Continuous fractional component Monte Carlo (CFC MC) are used to study phase equilibrium and estimate chemical potential, μ_i^E which can be directly used to estimate the activity coefficients γ_i . Chemical potential of a species in a mixture is equal to the corresponding partial molar excess gibbs free energy \bar{G}_i^E .

$$\left(\frac{\partial G^E}{\partial n_i} \right) = \bar{G}_i^E = \mu_i^E = RT \ln \gamma_i \quad (6.1)$$

Although GEMC based methods are more popular, there are a host of other methods that have been proposed to study phase behaviour or pure as well as mixture of fluids. Some of these methods are Gibbs-Duhem integration [140], Transition matrix Monte Carlo [141], hybrid Monte Carlo Wang-Landau method [142]. All these methods are not suitable for large scale parameterization since none of the Monte Carlo methods use reweighting to estimate the chemical potential. Each new parameter set requires a fresh simulation to estimate excess chemical potential which makes high throughput estimation of objective function very slow.

Very few people have looked into methods to evaluate excess free energy using molecular dynamics simulations. Chialvo [143, 144] and Haile [145] proposed a single charging scheme in which simulations are done at the two pure component states and any arbitrary composition to estimate the free energies at all other compositions. Single charging scheme was applied for LJ fluids and later extended to molecules with full molecular detail. Changes in interaction and geometry was done in a way which is difficult to adopt for large scale problems, like parameterization of mixtures, since the implementation requires changes in MD code. We propose the use of MBAR with linear mapping between configurations to push all the effort to the analysis phase.

We demonstrate the use techniques developed in chapter one and two, multistate reweighting with linear mapping, to estimate excess thermodynamic properties for a binary mixture of methanol and water. The simulations will be done at different compositions and MBAR with linear mapping will be used to estimate excess volume, excess enthalpy, excess Gibbs free energy and excess entropy of mixing at various compositions. We will compare the simulated excess thermodynamic properties against the experimentally calculated values. The difference in the experimental and simulated properties could be attributed mostly due to the force field which is not parameterized to reproduce the mixture properties.

Biomolecular force fields like AMBER [146] and CHARMM [95] are parameterized by doing quantum mechanical calculations in condensed phase using continuum solvent models and are biased to get the protein folding characteristics right. OPLS [147] force field is parameterized to reproduce pure liquid density and heat of vaporization. TraPPE [98] force field has been successful to model non-biological molecules and parameterizes by fitting parameters to reproduce correct phase behavior for pure fluids. GROMOS [14] force field is parameterized to fit hydration free energies which is like parameterizing at infinite dilution limit. But most of the chemical engineering problems involve mixtures at finite

concentrations so we need force fields which can accurately model systems with varying amount of chemical heterogeneity in the local environment. However, there are at present no force fields which are parameterized to reproduce correct mixture properties. The prime reason being the absence of a fast and efficient method to estimate excess thermodynamic properties of a mixture.

The protocol to estimate excess thermodynamic properties of mixtures developed in this chapter will be used to parameterize methanol and water force field parameters to simultaneously reproduce pure water properties, pure methanol properties and water-methanol mixture properties at all compositions at normal temperature and pressure (NTP). Estimation of pure fluid properties is already laid out in chapter three. The optimization workflow developed in chapter three can be used as it is.

6.2 Methods

6.2.1 Calculation of excess Gibbs free energy, G^E

Excess free energy, G^E at a given temperature and pressure can be defined as the difference between the non ideal free energy, G , and a standard state G° .

$$G^E = G - G^\circ \quad (6.2)$$

For a binary mixture, if we choose Lewis Randall standard state we can write excess Gibbs free energy for the mixture as:

$$G^E = x_A(G_{mix} - G_{pureA}) + x_B(G_{mix} - G_{pureB}) \quad (6.3)$$

We know partition function for ideal gas instead of ideal solution so we can write G^E

in terms residual properties to shift to ideal gas reference state.

$$G_{x_A}^E = x_A(G_{mix}^{res} - G_{pureA}^{res}) + x_B(G_{mix}^{res} - G_{pureB}^{res}) \quad (6.4)$$

Since $x_A + x_B = 1$

$$G_{x_A}^E = (G_{mix}^{res} - G_{pureB}^{res}) - x_A(G_{pureA}^{res} - G_{pureB}^{res}) \quad (6.5)$$

Here the residual properties are defined with respect to the ideal gas (IG) properties.

$$G_{mix}^{res} = G_{mix} - G_{IG,mix} \quad (6.6)$$

We can re-write Eq. 6.5 using the definition in Eq. 6.6.

$$\begin{aligned} G_{x_A}^E = & ((G_{mix} - G_{pureB}) - (G_{IG,mix} - G_{IG,pureB})) \\ & - x_A((G_{pureA} - G_{pureB}) - (G_{IG,pureA} - G_{IG,pureB})) \end{aligned} \quad (6.7)$$

We can calculate the ideal gas components analytically so there differences are separated from other free energies.

We define the two end states as pure water (A) and pure methanol (B). The intermediate state i will be a binary mixture of $N_{A,i}$ water molecules and $N_{B,i}$ methanol molecules. The total number of molecules will be kept constant at $N_T = N_{A,i} + N_{B,i}$. Thus the mole fraction $x_{A,i} = N_{A,i} / N_T$. We can represent the starting state, pure water as 0 and the end state, pure methanol as 1 and any intermediate state with $0 < i < 1$.

$$G_{x_{A,i}}^E = (\Delta G_{1i} - \Delta G_{IG,1i}) - x_{A,i}(\Delta G_{10} - \Delta G_{IG,10}) \quad (6.8)$$

Using MBAR we cannot calculate the absolute values of $G_{mix,i}$, G_1 , G_0 but we can easily get differences ΔG_{1i} , and ΔG_{10} using MBAR. $\Delta G_{IG,1i}$ and $\Delta G_{IG,10}$ can be calculated analytically by using the ratio of ideal gas partition functions.

The ideal gas partition function for N molecules of single type is:

$$Q_{id} = \frac{1}{N!} \Lambda^{-3N} V^N \quad (6.9)$$

Here Λ is the thermal de Broglie wavelength. Volume V is good for a spherical particle but we have triangular rigid molecules. So we need volume correction to account for the specific shape of the molecule. For a water molecule the correct volume is

$V \cdot 8\pi^2 \cdot r_{O,H1W} \cdot r_{O,H2W} \cdot r_{H1W,H2W}$ where $r_{O,H1W} = r_{O,H2W}$ is the OH bond length and $r_{H1W,H2W}$ is the distance between two hydrogens. Similarly for a methanol molecule the correct volume is $V \cdot 8\pi^2 \cdot r_{O,H1} \cdot r_{O,CH_3} \cdot r_{H1,CH_3}$, where $r_{O,H1}$ is the OH bond length, r_{O,CH_3} is the bond length of united atom methyl sphere and oxygen atom and r_{H1,CH_3} is the distance between hydrogen and the UA methyl sphere. For the sake of simplicity let us call $V \cdot 8\pi^2 \cdot r_{O,H1W} \cdot r_{O,H2W} \cdot r_{H1W,H2W}$ as ϕ_w and $V \cdot 8\pi^2 \cdot r_{O,H1} \cdot r_{O,CH_3} \cdot r_{H1,CH_3}$ as ϕ_m

The ideal gas partition function for a mixture of N_A molecules of water(A) and N_B molecules of methanol(B) can be written as the product of the individual Q_{id} .

$$\begin{aligned}
Q_{id,mix} &= Q_{id,water} \times Q_{id,Methanol} \\
&= \frac{1}{N_A!} \Lambda_A^{-3N_A} (V 8\pi^2 \phi_w)^{N_A} \\
&\quad \times \frac{1}{N_B!} \Lambda_B^{-3N_B} (V 8\pi^2 \phi_m)^{N_B} \\
&= \frac{1}{N_A! N_B!} \Lambda_A^{-3N_A} \Lambda_B^{-3N_B} (V 8\pi^2)^{N_A+N_B} (\phi_w)^{N_A} (\phi_m)^{N_B}
\end{aligned} \tag{6.10}$$

In the ideal gas state the free energy difference between two states i and j having compositions mix_i and mix_j can be estimated by the ratio of Q_{id,mix_i} and Q_{id,mix_j} .

$$\begin{aligned}
\Delta G_{id,ji} &= -kT \ln \left[\frac{Q_{id,mix_i}}{Q_{id,mix_j}} \right] \\
&= -kT \left(\ln \left[\frac{N_{A_j}! N_{B_j}!}{N_{A_i}! N_{B_i}!} \Lambda_A^{-3(N_{A_i}-N_{A_j})} \Lambda_B^{-3(N_{B_i}-N_{B_j})} \right] \right. \\
&\quad \left. + \ln \left[(\phi_w)^{N_{A_i}-N_{A_j}} (\phi_m)^{N_{B_i}-N_{B_j}} \right] \right)
\end{aligned} \tag{6.11}$$

To calculate ΔG_{1i} , and ΔG_{10} we propose to do N_T simulations. The starting state is water and then we will convert 1 water molecule per simulation to a methanol molecule till all molecules are transformed to methanol. We don't know how good the phase space overlap is between the different intermediate states so we take so many steps. The phase space difference can be problematic because methanol and water have different densities so the box volume will change significantly going from pure water to pure methanol. If we get the converged free energy estimates then we can find the minimum number of simulations required to get satisfactorily converged free energy estimates.

We will change the interaction type i.e charges and LJ and the geometry from water to methanol but will keep the masses of atoms same as that of water molecule throughout the

series of transformations. The united atom methyl group will weigh same as the hydrogen atom in all the transformations. This will allow us to by pass the velocity rescaling due to change in mass in all the reevaluation of energies.

We don't have to correct for mass as all the mass containing kinetic energy contributions cancel out. in Eq. 6.8. We will not get the correct transport properties using this procedure but thermodynamic properties will remain unaffected.

The variance in $G_{x_{A,i}}^E$ can be calculated by examining which terms in Eq. 6.8 contribute.

$$\begin{aligned}
 \text{var} \left(G_{x_{A,i}}^E \right) &= \text{var} \left(\Delta G_{1i} - \Delta G_{IG,1i} - x_{A,i}(\Delta G_{10} - \Delta G_{IG,10}) \right) \\
 &= \text{var} \left(\Delta G_{1i} - x_{A,i}\Delta G_{10} - \Delta G_{IG,1i} + x_{A,i}\Delta G_{IG,10} \right) \\
 \text{let } \alpha &= \Delta G_{1i} - x_{A,i}\Delta G_{10} \\
 \text{and } \beta &= -\Delta G_{IG,1i} + x_{A,i}\Delta G_{IG,10} \\
 \text{var} \left(G_{x_{A,i}}^E \right) &= \text{var} (\alpha + \beta) \\
 &= \text{cov} (\alpha, \alpha) + \text{cov} (\beta, \beta) + 2\text{cov} (\alpha, \beta)
 \end{aligned} \tag{6.12}$$

β in Eq. 6.12 is a sum of analytical estimates so $\text{cov}(\beta, \beta) = \text{var}(\beta) = 0$. $\text{cov}(\alpha, \beta)$ is like a covariance between a random variable and a constant which is also zero.

$$\begin{aligned}
\text{var} \left(G_{x_{A,i}}^E \right) &= \text{cov} (\alpha, \alpha) \\
&= \text{var} (\Delta G_{1i} - x_{A,i} \Delta G_{10}) \\
&= \text{cov} (\Delta G_{1i}, \Delta G_{1i}) + \text{cov} (x_{A,i} \Delta G_{10}, x_{A,i} \Delta G_{10}) - 2 \text{cov} (\Delta G_{1i}, x_{A,i} \Delta G_{10}) \\
&= \text{var} (\Delta G_{1i}) + x_{A,i}^2 \text{var} (\Delta G_{10}) - 2 x_{A,i} \text{cov} (\Delta G_{1i}, \Delta G_{10}) \\
&= \text{var} (\Delta G_{1i}) + x_{A,i}^2 \text{var} (\Delta G_{10}) - 2 x_{A,i} \\
&\quad \times (\text{cov} (G_i, G_0) - \text{cov} (G_i, G_1) - \text{cov} (G_1, G_0) + \text{cov} (G_1, G_1))
\end{aligned} \tag{6.13}$$

6.2.2 Calculation of excess enthalpy, H^E

H^E can be calculated with the analog of Gibbs-Helmholtz equation and applying central difference to the temperature derivative.

$$\begin{aligned}
\frac{H^E}{kT^2} &= - \left(\frac{\partial (G^E/kT)}{\partial T} \right)_{P,N} \\
\frac{H_{(T,P,x_i)}^E}{kT^2} &= - \left(\frac{1}{2\delta T} \left(\frac{G_{((T+\delta T),P,x_i)}^E}{k(T+\delta T)} - \frac{G_{((T-\delta T),P,x_i)}^E}{k(T-\delta T)} \right) \right)
\end{aligned} \tag{6.14}$$

The difference in the excess free energies in the numerator of Eq. 6.14 can be evaluated using reweighting. We just need to reevaluate energies at $T+\delta T$ and $T-\delta T$ using samples generated at NTP to estimate the difference.

6.2.3 Calculation of excess volume of mixing V^E

Similar to H^E , V^E can also be calculated with the Gibbs-Helmholtz equation and applying central difference to the pressure derivative.

$$\begin{aligned} \frac{V^E}{kT} &= \left(\frac{\partial(G^E/kT)}{\partial P} \right)_{TN} \\ \frac{V_{(T,P,x_i)}^E}{kT} &= - \left(\frac{1}{2\delta P} \left(\frac{G_{(T,(P+\delta P),x_i)}^E}{kT} - \frac{G_{(T,(P-\delta P),x_i)}^E}{kT} \right) \right) \end{aligned} \quad (6.15)$$

The difference in the excess free energies in the numerator of Eq. 6.15 can be evaluated using reweighting. We just need to reevaluate energies at new pressures $P+\delta P$ and $P-\delta P$ using samples generated at NTP to estimate the difference.

6.2.4 Calculation of excess entropy, S^E

Since we have $G_{x_{A,i}}^E$ and $H_{x_{A,i}}^E$ it is straightforward to calculate the $S_{x_{A,i}}^E$.

$$\begin{aligned} S_{x_{A,i}}^E &= \frac{H_{x_{A,i}}^E - G_{x_{A,i}}^E}{T} \\ \text{var}((S_{x_{A,i}}^E)) &= \frac{\text{var}(H_{x_{A,i}}^E) + \text{var}(G_{x_{A,i}}^E) - 2\text{cov}(H_{x_{A,i}}^E, G_{x_{A,i}}^E)}{T^2} \end{aligned} \quad (6.16)$$

We could also calculate using the temperature derivative of excess free energy.

$$\begin{aligned} S_{=}^E &= \left(\frac{\partial(G^E)}{\partial T} \right)_{P,N} \\ &= - \left(\frac{1}{\delta T} (G_{((T+\delta T),P,x_i)}^E - G_{((T-\delta T),P,x_i)}^E) \right) \end{aligned} \quad (6.17)$$

Both approaches could be used without any additional function calls.

Since we cannot estimate $cov(H_{x_{A,i}}^E, G_{x_{A,i}}^E)$ we will calculate bootstrap error estimate for $S_{x_{A,i}}^E$. Since we will have to bootstrap $H_{x_{A,i}}^E, G_{x_{A,i}}^E$ multiple times to calculate $S_{x_{A,i}}^E$ we can also evaluate bootstrap error estimates for $H_{x_{A,i}}^E, G_{x_{A,i}}^E, V_{x_{A,i}}^E$. This will serve as a sanity check for the error estimates.

We will be using rigid 3 site water model with TIP3P force field parameters and a rigid methanol model with TRAPPE force field parameters. The simulations will be done at 25 °C and 1 atmosphere as we have experimental data at these conditions to compare our simulated results with.

6.2.5 Parameterization of water and methanol

The objective function ξ will include density and heat of vaporization of water and methanol at normal temperature and pressure. ξ will also include excess free energy, excess enthalpy and excess volume for compositions for which the corresponding experimental values are known. We will use the TIP3P parameters and TRAPPE force field parameters as the starting input set for the optimization routine.

Publications

1. H. Paliwal and M. R. Shirts, “A benchmark test set for alchemical free energy transformations and its use to quantify error in common free energy methods,” *Journal of Chemical Theory and Computation*, 7 (12), 4115–4134 (2011)
2. H. Paliwal and M. R. Shirts, “Multistate reweighting and configuration mapping together accelerate the efficiency of thermodynamic calculations as a function of molecular geometry by orders of magnitude,” *Journal of Chemical Physics*, 138 (15), 154108 (2013)
3. H. Paliwal and M. R. Shirts, “Using multistate reweighting to rapidly and efficiently explore molecular simulation parameter space for non bonded interactions,” *Journal of Chemical Theory and Computation*, 9 (11), 4700–4717, (2013)
4. H. Paliwal and M. R. Shirts, “An efficient approach to parameterize energy as well as geometry parameters in atomistic force fields and its use to model liquid water over a range of temperature and pressure,” In preparation.

References

- [1] B. J. Alder and T. E. Wainwright. Studies in Molecular Dynamics. I. General Method. *J. Chem. Phys.*, 31(2):459, 1959.
- [2] Daniel S D Larsson, Lars Liljas, and David van der Spoel. Virus capsid dissolution studied by microsecond molecular dynamics simulations. *PLoS Comput. Biol.*, 8(5):e1002502, January 2012.
- [3] Himanshu Paliwal and M. Shirts. A benchmark test set for alchemical free energy transformations and its use to quantify error in common free energy methods. *J. Chem. Theory Comput.*, 7(12):4115–4134, 2011.
- [4] MR Shirts and J.D. Chodera. Statistically optimal analysis of samples from multiple equilibrium states. *J. Chem. Phys.*, 129(12):124105, 2008.
- [5] Michael R. Shirts. Simple Quantitative Tests to Validate Sampling from Thermodynamic Ensembles. *J. Chem. Theory Comput.*, 9(2):909–926, February 2013.
- [6] Joseph E. Basconi and Michael R. Shirts. Effects of Temperature Control Algorithms on Transport Properties and Kinetics in Molecular Dynamics Simulations. *J. Chem. Theory Comput.*, 9(7):2887–2899, July 2013.
- [7] R. W. Zwanzig. High-temperature equation of state by a perturbation method. i. nonpolar gases. *J. Chem. Phys.*, 22(8):1420–1426, 1954.
- [8] Charles H. Bennett. Efficient estimation of free energy differences from Monte Carlo data. *J. Comput. Phys.*, 22(2):245–268, October 1976.

- [9] William L. Jorgensen, Jayaraman Chandrasekhar, Jeffry D. Madura, Roger W. Impey, and Michael L. Klein. Comparison of simple potential functions for simulating liquid water. *J. Chem. Phys.*, 79(2):926, July 1983.
- [10] H. J. C. Berendsen, J. R. Grigera, and T. P. Straatsma. The missing term in effective pair potentials. *J. Phys. Chem.*, 91(24):6269–6271, November 1987.
- [11] Hans W Horn, William C Swope, Jed W Pitera, Jeffry D Madura, Thomas J Dick, Greg L Hura, and Teresa Head-Gordon. Development of an improved four-site water model for bioMol. Simul.s: TIP4P-Ew. *J. Chem. Phys.*, 120(20):9665–78, May 2004.
- [12] J L F Abascal and C Vega. A general purpose model for the condensed phases of water: TIP4P/2005. *J. Chem. Phys.*, 123(23):234505, December 2005.
- [13] Enrico Matteoli Paul E. Smith, John P. O’Connell. *Fluctuation Theory Of Solutions: Applications In Chemistry, Chemical Engineering And Biophysics*. Crc Pr I Llc, 2013.
- [14] Chris Oostenbrink, Alessandra Villa, Alan E Mark, and Wilfred F van Gunsteren. A biomolecular force field based on the free enthalpy of hydration and solvation: the GROMOS force-field parameter sets 53A5 and 53A6. *J. Comput. Chem.*, 25(13):1656–76, October 2004.
- [15] Ding-Yu Peng and Donald B. Robinson. A New Two-Constant Equation of State. *Ind. Eng. Chem. Fundam.*, 15(1):59–64, February 1976.
- [16] Giorgio Soave. Equilibrium constants from a modified Redlich-Kwong equation of state. *Chem. Eng. Sci.*, 27(6):1197–1203, June 1972.

- [17] Eric Hendriks, Georgios M. Kontogeorgis, Ralf Dohrn, Jean-Charles de Hemptinne, Ioannis G. Economou, Ljudmila Fele Žilnik, and Velisa Vesovic. Industrial Requirements for Thermodynamics and Transport Properties. *Ind. Eng. Chem. Res.*, 49(22):11131–11141, November 2010.
- [18] Aage Fredenslund, Russell L. Jones, and John M. Prausnitz. Group-contribution estimation of activity coefficients in nonideal liquid mixtures. *AIChE J.*, 21(6):1086–1099, November 1975.
- [19] Denis S. Abrams and John M. Prausnitz. Statistical thermodynamics of liquid mixtures: A new expression for the excess Gibbs energy of partly or completely miscible systems. *AIChE J.*, 21(1):116–128, January 1975.
- [20] Ioannis G. Economou. Statistical Associating Fluid Theory: A Successful Model for the Calculation of Thermodynamic and Phase Equilibrium Properties of Complex Fluid Mixtures. *Ind. Eng. Chem. Res.*, 41(5):953–962, March 2002.
- [21] Andreas Grenner, Jürgen Schmelzer, Nicolas von Solms, and Georgios M. Kontogeorgis. Comparison of Two Association Models (Elliott–Suresh–Donohue and Simplified PC-SAFT) for Complex Phase Equilibria of Hydrocarbon–Water and Amine-Containing Mixtures. *Ind. Eng. Chem. Res.*, 45(24):8170–8179, November 2006.
- [22] John D Chodera, William C Swope, Frank Noé, Jan-Hendrik Prinz, Michael R Shirts, and Vijay S Pande. Dynamical reweighting: improved estimates of dynamical properties from simulations at multiple temperatures. *J. Chem. Phys.*, 134(24):244107, June 2011.

- [23] Loup Verlet. Computer "experiments" on classical fluids. i. thermodynamical properties of lennard-jones molecules. *Phys. Rev.*, 159:98–103, Jul 1967.
- [24] Jeff Wereszczynski and J. Andrew McCammon. Statistical mechanics and molecular dynamics in evaluating thermodynamic properties of biomolecular recognition. *Q. Rev. Biophys.*, 45(01):1–25, February 2012.
- [25] Wilfred F van Gunsteren, Dirk Bakowies, Riccardo Baron, Indira Chandrasekhar, Markus Christen, Xavier Daura, Peter Gee, Daan P Geerke, Alice Glättli, Philippe H Hünenberger, Mika A Kastenholz, Chris Oostenbrink, Merijn Schenk, Daniel Trzesniak, Nico F A van der Vegt, and Haibo B Yu. Biomolecular modeling: Goals, problems, perspectives. *Angew. Chem., Int. Ed. Engl.*, 45(25):4064–92, June 2006.
- [26] Albert Y Lau and Benoît Roux. The free energy landscapes governing conformational changes in a glutamate receptor ligand-binding domain. *Structure (London, U. K.)*, 15(10):1203–14, October 2007.
- [27] Berend Smit and Theo L M Maesen. Towards a molecular understanding of shape selectivity. *Nature*, 451(7179):671–8, February 2008.
- [28] Jacob D Durrant and J Andrew McCammon. Molecular dynamics simulations and drug discovery. *BMC Biol.*, 9(1):71, January 2011.
- [29] Michael R. Shirts, Jed W. Pitera, William C. Swope, and Vijay S. Pande. Extremely precise free energy calculations of amino acid side chain analogs: Comparison of common molecular mechanics force fields for proteins. *J. Chem. Phys.*, 119(11):5740–5761, 2003.

- [30] Michael R Shirts and Vijay S Pande. Comparison of efficiency and bias of free energies computed by exponential averaging, the Bennett acceptance ratio, and thermodynamic integration. *J. Chem. Phys.*, 122(14):144107, April 2005.
- [31] David L Mobley, Elise Dumont, John D Chodera, and Ken A Dill. Comparison of charge models for fixed-charge force fields: small-molecule hydration free energies in explicit solvent. *J. Phys. Chem. B*, 111(9):2242–54, March 2007.
- [32] David L Mobley, Christopher I Bayly, Matthew D Cooper, Michael R Shirts, and Ken A Dill. Small molecule hydration free energies in explicit solvent: An extensive test of fixed-charge atomistic simulations. *J. Chem. Theory Comput.*, 5(2):350–358, February 2009.
- [33] Robert W. Zwanzig. High-Temperature Equation of State by a Perturbation Method. II. Polar Gases. *J. Chem. Phys.*, 23(10):1915, 1955.
- [34] Ben Widom. Some topics in the theory of fluids. *J. Chem. Phys.*, 39(11):2808–2812, 1963.
- [35] Chris Oostenbrink and Wilfred F van Gunsteren. Efficient calculation of many stacking and pairing free energies in DNA from a few molecular dynamics simulations. *Chem. Euro. J.*, 11:4340–4348, 2005.
- [36] Chris Oostenbrink and Wilfred F van Gunsteren. Free energies of ligand binding for structurally diverse compounds. *Proc. Nat. Acad. Sci.*, 102(19):6750–6754, 2005.
- [37] Shankar Kumar, John M Rosenberg, Djamal Bouzida, Robert H Swendsen,

and Peter A Kollman. The weighted histogram analysis method for free energy calculations on biomolecules.I. *J. Comput. Chem.*, 13, 13(8, 8), 1992.

- [38] Himanshu Paliwal and Michael R Shirts. Multistate reweighting and configuration mapping together accelerate the efficiency of thermodynamic calculations as a function of molecular geometry by orders of magnitude. *J. Chem. Phys.*, 138(15):154108, April 2013.
- [39] RJ Randall J RJ Randall J Radmer and Peter PA Peter A PA Peter A Kollman. Free energy calculation methods: A theoretical and empirical comparison of numerical errors and a new method qualitative estimates of free energy changes. *J. Comput. Chem.*, 18(7):902–919, May 1997.
- [40] Christophe Chipot. *Free Energy Calculations*. Springer, 1 edition, February 2007.
- [41] Miguel Jorge, Nuno M. Garrido, António J. Queimada, Ioannis G. Economou, and Eugénia A. Macedo. Effect of the Integration Method on the Accuracy and Computational Efficiency of Free Energy Calculations Using Thermodynamic Integration. *J. Chem. Theory Comput.*, 6(4):1018–1027, April 2010.
- [42] Hagai Meirovitch, Srinath Cheluvaraja, and Ronald P White. Methods for calculating the entropy and free energy and their application to problems involving protein flexibility and ligand binding. *Curr. Protein Pept. Sci.*, 10(3):229–243, June 2009.
- [43] A. Pohorille, C. Jarzynski, and C. Chipot. Good Practices in Free-Energy Calculations. *J. Phys. Chem. B*, pages 1420–1426, 2010.

- [44] Tony Lelievre, Gabriel Stoltz, and Mathias Rousset. *Free Energy Computations: A Mathematical Perspective*. Imperial College Press, London, 1 edition, June 2010.
- [45] F. Marty Ytreberg, Robert H. Swendsen, and Daniel M. Zuckerman. Comparison of free energy methods for molecular systems. *J. Chem. Phys.*, 125(18):184114, 2006.
- [46] D Trzesniak, APE Kunz, and WF van Gunsteren. A comparison of methods to compute the potential of mean force. *ChemPhysChem*, 8(1):162–169, January 2007.
- [47] Michael R Shirts, David L Mobley, John D Chodera, and Vijay S Pande. Accurate and efficient corrections for missing dispersion interactions in Mol. Simul.s. *J. Phys. Chem. B*, 111(45):13052–63, November 2007.
- [48] Tom Darden, Darrin York, and Lee Pedersen. Particle mesh Ewald: An N log (N) method for Ewald sums in large systems. *J. Chem. Phys.*, 98(12):10089–10089, 1993.
- [49] Ulrich Essmann, Lalith Perera, Max L. Berkowitz, Tom Darden, Hsing Lee, and Lee G. Pedersen. A smooth particle mesh Ewald method. *J. Chem. Phys.*, 103(19):8577, November 1995.
- [50] Ilario G. Tironi, René Sperb, Paul E. Smith, and Wilfred F. van Gunsteren. A generalized reaction field method for molecular dynamics simulations. *J. Chem. Phys.*, 102(13):5451, April 1995.
- [51] Markus Deserno and Christian Holm. How to mesh up Ewald sums. I. A

- theoretical and numerical comparison of various particle mesh routines. *J. Chem. Phys.*, 109(18):7678, November 1998.
- [52] Paul E. Smith and B. Montgomery Pettitt. Ewald artifacts in liquid state molecular dynamics simulations. *J. Chem. Phys.*, 105(10):4289, September 1996.
- [53] Pekka Mark and Lennart Nilsson. Structure and dynamics of liquid water with different long-range interaction truncation and temperature control methods in molecular dynamics simulations. *J. Comput. Chem.*, 23(13):1211–9, October 2002.
- [54] Henrik G. Petersen. Accuracy and efficiency of the particle mesh Ewald method. *J. Chem. Phys.*, 103(9):3668, 1995.
- [55] Philippe H. Hünenberger and J. Andrew McCammon. Ewald artifacts in computer simulations of ionic solvation and ion–ion interaction: A continuum electrostatics study. *J. Chem. Phys.*, 110(4):1856, 1999.
- [56] M. P. Allen and D. J. Tildesley. *Computer Simulation of Liquids*. Oxford University Press, New York, 1987.
- [57] Patrick Lagüe and Richard W. Pastor. Pressure-based long-range correction for lennard-jones interactions in molecular dynamics simulations: Application to alkanes and interfaces. *J. Phys. Chem. B.*, 108(1):363–368, 2004.
- [58] Pieter J. in’t Veld, Ahmed E. Ismail, and Gary S. Grest. Application of ewald summations to long-range dispersion forces. *J. Chem. Phys.*, 127(14), 2007.

- [59] Mark J Abraham and Jill E Gready. Optimization of parameters for molecular dynamics simulation using smooth particle-mesh Ewald in GROMACS 4.5. *J. Comput. Chem.*, 32(9):2031–40, April 2011.
- [60] Junmei Wang and Tingjun Hou. Application of Molecular Dynamics Simulations in Molecular Property Prediction. 1. Density and Heat of Vaporization. *J. Chem. Theory Comput.*, 7(7):2151–2165, July 2011.
- [61] Berk Hess, Carsten Kutzner, David van der Spoel, and Erik Lindahl. Gromacs 4: Algorithms for highly efficient, load-balanced, and scalable mol. simul. *J. Chem. Theory Comput.*, 4(3):435–447, 2008.
- [62] Sander Pronk, Szilárd Páll, Roland Schulz, Per Larsson, Pär Bjelkmar, Rossen Apostolov, Michael R Shirts, Jeremy C Smith, Peter M Kasson, David van der Spoel, Berk Hess, and Erik Lindahl. GROMACS 4.5: a high-throughput and highly parallel open source molecular simulation toolkit. *Bioinformatics*, 29(7):845–54, April 2013.
- [63] Tamar Schlick. *Molecular Modeling and Simulation*. Springer, 1 edition, August 2002.
- [64] Peter J. Steinbach and Bernhard R. Brooks. New spherical-cutoff methods for long-range forces in macromol. simul. *J. Comput. Chem.*, 15(7):667–683, 1994.
- [65] D. van der Spoel and P. J. van Maaren. The origin of layer structure artifacts in simulations of liquid water. *J. Chem. Theory Comp.*, 2:1–11, 2006.
- [66] Pavel V. Klimovich and David L. Mobley. Predicting hydration free energies

- using all-atom molecular dynamics simulations and multiple starting conformations. *J. Comput.-Aided Mol. Des.*, 24(4):307–316, 2010.
- [67] Shuichi Miyamoto and Peter A. Kollman. Settle: An analytical version of the SHAKE and RATTLE algorithm for rigid water models. *J. Comput. Chem.*, 13(8):952–962, October 1992.
- [68] Hans C Andersen. Rattle: A “velocity” version of the shake algorithm for molecular dynamics calculations. *J. Comput. Phys.*, 52(1):24–34, October 1983.
- [69] Glenn J. Martyna, Mark E. Tuckerman, Douglas J. Tobias, and Michael L. Klein. Explicit reversible integrators for extended systems dynamics. *Mol. Phys.*, 87(5):1117, 1996.
- [70] N. D Lu and D. A Kofke. Accuracy of free-energy perturbation calculations in mol. simul.. i. modeling. *J. Chem. Phys.*, 114(17):7303–7311, May 2001.
- [71] N. D Lu and David A Kofke. Accuracy of free-energy perturbation calculations in mol. simul.. II. heuristics. *J. Chem. Phys.*, 115(15):6866–6875, 2001.
- [72] Di Wu and David A. Kofke. Phase-space overlap measures. i. fail-safe bias detection in free energies calculated by mol. simul. *J. Chem. Phys.*, 123:054103, 2005.
- [73] Di Wu and David A. Kofke. Phase-space overlap measures. II. design and implementation of staging methods for free-energy calculations. *J. Chem. Phys.*, 123:084109, 2005.

- [74] Peter M. Harper, Rafiqul Gani, Petr Kolar, and Takeshi Ishikawa. Computer-aided molecular design with combined molecular modeling and group contribution. *Fluid Phase Equilib.*, 158-160:337–347, June 1999.
- [75] Chris Oostenbrink and Wilfred F van Gunsteren. Free energies of ligand binding for structurally diverse compounds. *Proc. Natl. Acad. Sci. U. S. A.*, 102(19):6750–4, May 2005.
- [76] T.P. Straatsma, M. Zacharias, and J.A. McCammon. Holonomic constraint contributions to free energy differences from thermodynamic integration molecular dynamics simulations. *Chem. Phys. Lett.*, 196(3-4):297–302, August 1992.
- [77] Jean-Paul Ryckaert, Giovanni Ciccotti, and Herman J.C Berendsen. Numerical integration of the cartesian equations of motion of a system with constraints: molecular dynamics of n-alkanes. *J. Comput. Phys.*, 23(3):327–341, March 1977.
- [78] Lu Wang and Jan Hermans. Change of bond length in free-energy simulations: Algorithmic improvements, but when is it necessary? *J. Chem. Phys.*, 100(12):9129, June 1994.
- [79] Stefan Boresch and Martin Karplus. Jacobian factor in free energy simulations. *J. Chem. Phys.*, 105(12):5145–5154, September 1996.
- [80] Stefan Boresch and Martin Karplus. The Role of Bonded Terms in Free Energy Simulations 1. Theoretical Analysis. *J. Phys. Chem. A*, 103(1):103–118, January 1999.

- [81] Stefan Boresch and Martin Karplus. The Role of Bonded Terms in Free Energy Simulations. 2. Calculation of Their Influence on Free Energy Differences of Solvation. *J. Phys. Chem. A*, 103(1):119–136, January 1999.
- [82] Stefan Boresch. The Role of Bonded Energy Terms in Free Energy Simulations - Insights from Analytical Results. *Mol. Simul.*, 28(1-2):13–37, January 2002.
- [83] Markus Christen, Clara D Christ, and Wilfred F van Gunsteren. Free energy calculations using flexible-constrained, hard-constrained and non-constrained molecular dynamics simulations. *ChemPhysChem : a European J. Chem. Phys. and physical chemistry*, 8(10):1557–64, July 2007.
- [84] C. Jarzynski. Targeted free energy perturbation. *Phys. Rev. E: Stat. Phys., Plasmas, Fluids, Relat. Interdiscip. Top.*, 65(4), April 2002.
- [85] Arthur F. Voter. A Monte Carlo method for determining free-energy differences and transition state theory rate constants. *J. Chem. Phys.*, 82(4):1890–1899, February 1985.
- [86] F Marty Ytreberg and Daniel M Zuckerman. Peptide conformational equilibria computed via a single-stage shifting protocol. *J. Phys. Chem. B*, 109(18):9096–103, May 2005.
- [87] Suriyanarayanan Vaikuntanathan and Christopher Jarzynski. Escorted free energy simulations. *J. Chem. Phys.*, 134(5):054107, February 2011.
- [88] Suriyanarayanan Vaikuntanathan and Christopher Jarzynski. Escorted Free

- Energy Simulations: Improving Convergence by Reducing Dissipation. *Phys. Rev. Lett.*, 100(19):190601, May 2008.
- [89] Daniel L. Severance, Jonathan W. Essex, and William L. Jorgensen. Generalized alteration of structure and parameters: A new method for free-energy perturbations in systems containing flexible degrees of freedom. *J. Comput. Chem.*, 16(3):311–327, March 1995.
- [90] Tai Boon Tan, Andrew J Schultz, and David A Kofke. Efficient calculation of temperature dependence of solid-phase free energies by overlap sampling coupled with harmonically targeted perturbation. *J. Chem. Phys.*, 133(13):134104, October 2010.
- [91] Zhiqiang Tan. On a Likelihood Approach for Monte Carlo Integration. *J. Am. Stat. Assoc.*, 99(468):1027–1036, December 2004.
- [92] Xiao-Li Meng and Stephen Schilling. Warp Bridge Sampling. *J. Comput. Graph. Stat.*, 11(3):552–586, 2002.
- [93] D. J. Evans and B. L. Holian. The Nose-Hoover thermostat. *J. Chem. Phys.*, 83(8):4069, 1985.
- [94] Marco Hülsmann, Thorsten Köddermann, Jadran Vrabec, and Dirk Reith. GROW: A gradient-based optimization workflow for the automated development of molecular models. *Comput. Phys. Commun.*, 181(3):499–513, March 2010.
- [95] MacKerell, D. Bashford, Bellott, Dunbrack, J. D. Evanseck, M. J. Field, S. Fischer, J. Gao, H. Guo, S. Ha, D. Joseph-McCarthy, L. Kuchnir, K. Kuczera,

- F. T. K. Lau, C. Mattos, S. Michnick, T. Ngo, D. T. Nguyen, B. Prodhom, W. E. Reiher, B. Roux, M. Schlenkrich, J. C. Smith, R. Stote, J. Straub, M. Watanabe, J. Wiorkiewicz-Kuczera, D. Yin, and M. Karplus. All-Atom Empirical Potential for Molecular Modeling and Dynamics Studies of Proteins[†]. *J. Phys. Chem. B*, 102(18):3586–3616, April 1998.
- [96] Thijs van Westen, Thijs J H Vlugt, and Joachim Gross. Determining force field parameters using a physically based equation of state. *J. Phys. Chem. B*, 115(24):7872–80, July 2011.
- [97] Norman L. Allinger, Young H. Yuh, and Jenn Huei Lii. Molecular mechanics. The MM3 force field for hydrocarbons. 1. *J. Am. Chem. Soc.*, 111(23):8551–8566, November 1989.
- [98] Marcus G. Martin and J. Ilja Siepmann. Transferable Potentials for Phase Equilibria. 1. United-Atom Description of n-Alkanes. *J. Phys. Chem. B*, 102(14):2569–2577, April 1998.
- [99] William L. Jorgensen. Quantum and statistical mechanical studies of liquids. 10. Transferable intermolecular potential functions for water, alcohols, and ethers. Application to liquid water. *J. Am. Chem. Soc.*, 103(2):335–340, January 1981.
- [100] Barbara Kirchner. *Multiscale molecular methods in applied chemistry*. Springer Verlag, Heidelberg ;;New York, 2012.
- [101] Aviel Chaimovich and M Scott Shell. Coarse-graining errors and numerical optimization using a relative entropy framework. *J. Chem. Phys.*, 134(9):094112, March 2011.

- [102] Andrey V Brukhno, Jamshed Anwar, Ruslan Davidchack, and Richard Handel. Challenges in Mol. Simul. of homogeneous ice nucleation. *J. Phys.: Condens. Matter*, 20(49):494243, December 2008.
- [103] William L. Jorgensen. Revised TIPS for simulations of liquid water and aqueous solutions. *J. Chem. Phys.*, 77(8):4156, October 1982.
- [104] Alice Glättli, Xavier Daura, and Wilfred F Van Gunsteren. A novel approach for designing simple point charge models for liquid water with three interaction sites. *J. Comput. Chem.*, 24(9):1087–96, July 2003.
- [105] J. W. Halley, James R. Rustad, and A. Rahman. A polarizable, dissociating molecular dynamics model for liquid water. *J. Chem. Phys.*, 98(5):4110, March 1993.
- [106] Igor M. Svishchev, Peter G. Kusalik, Jian Wang, and Russel J. Boyd. Polarizable point-charge model for water: Results under normal and extreme conditions. *J. Chem. Phys.*, 105(11):4742, September 1996.
- [107] G. Lie and E. Clementi. Molecular-dynamics simulation of liquid water with an ab initio flexible water-water interaction potential. *Phys. Rev. A: At., Mol., Opt. Phys.*, 33(4):2679–2693, April 1986.
- [108] Anders Wallqvist and Olle Teleman. Properties of flexible water models. *Mol. Phys.*, 74(3):515–533, October 1991.
- [109] Roland Faller, Heiko Schmitz, Oliver Biermann, and Florian Müller-Plathe. Automatic parameterization of force fields for liquids by simplex optimization. *J. Comput. Chem.*, 20(10):1009–1017, July 1999.

- [110] Charles Audet and J. E. Dennis. Mesh Adaptive Direct Search Algorithms for Constrained Optimization. *SIAM J. Optim.*, 17(1):188–217, January 2006.
- [111] Charles Audet and J. E. Dennis. A Progressive Barrier for Derivative-Free Nonlinear Programming. *SIAM J. Optim.*, 20(1):445–472, January 2009.
- [112] W. Wagner, J. R. Cooper, A. Dittmann, J. Kijima, H.-J. Kretzschmar, A. Kruse, R. Mareš, K. Oguchi, H. Sato, I. Stöcker, O. Šifner, Y. Takaishi, I. Tanishita, J. Trübenbach, and Th. Willkommen. The IAPWS Industrial Formulation 1997 for the Thermodynamic Properties of Water and Steam. *J. Eng. Gas Turbines Power*, 122(1):150, January 2000.
- [113] W. Wagner. The IAPWS Formulation 1995 for the Thermodynamic Properties of Ordinary Water Substance for General and Scientific Use. *J. Phys. Chem. Ref. Data*, 31(2):387, June 1999.
- [114] Andreas Grenner, Georgios M. Kontogeorgis, Michael L. Michelsen, and Georgios K. Folas. On the estimation of water pure compound parameters in association theories. *Mol. Phys.*, 105(13-14):1797–1801, July 2007.
- [115] Gary N. I. Clark, Andrew J. Haslam, Amparo Galindo, and George Jackson. Developing optimal Wertheim-like models of water for use in Statistical Associating Fluid Theory (SAFT) and related approaches. *Mol. Phys.*, 104(22-24):3561–3581, November 2006.
- [116] Erich A. Mueller and Keith E. Gubbins. An Equation of State for Water from a Simplified Intermolecular Potential. *Ind. Eng. Chem. Res.*, 34(10):3662–3673, October 1995.

- [117] Jiří Kolafa and Ivo Nezbeda. The Lennard-Jones fluid: an accurate analytic and theoretically-based equation of state. *Fluid Phase Equilib.*, 100(null):1–34, September 1994.
- [118] C. G. Gray and K. E. Gubbins. *Theory of Molecular Fluids: Fundamentals, Volume I*. Clarendon Press, 1984.
- [119] Bertrand Guillot. A reappraisal of what we have learnt during three decades of computer simulations on water. *J. Mol. Liq.*, 101(1-3):219–260, November 2002.
- [120] J. P. O’Connell and J. M. Haile. *Thermodynamics: Fundamentals for Applications*. Cambridge University Press, May 2005.
- [121] Manuel M Piñeiro, Claudio A Cerdeiriña, and Milton Medeiros. Thermodynamic response functions of fluids: a microscopic approach based on NpT Monte Carlo. *J. Chem. Phys.*, 129(1):014511, July 2008.
- [122] Steven W Rick. A reoptimization of the five-site water potential (TIP5P) for use with Ewald sums. *J. Chem. Phys.*, 120(13):6085–93, April 2004.
- [123] M.J.D. Powell. A direct search optimization method that models the objective and constraint functions by linear interpolation. In Susana Gomez and Jean-Pierre Hennart, editors, *Advances in Optimization and Numerical Analysis*, volume 275 of *Mathematics and Its Applications*, pages 51–67. Springer Netherlands, 1994.
- [124] W. S. Benedict, N. Gailar, and Earle K. Plyler. Rotation-Vibration Spectra of Deuterated Water Vapor. *J. Chem. Phys.*, 24(6):1139, June 1956.

- [125] M. J. Frisch, G. W. Trucks, H. B. Schlegel, G. E. Scuseria, M. A. Robb, J. R. Cheeseman, J. A. Montgomery, Jr., T. Vreven, K. N. Kudin, J. C. Burant, J. M. Millam, S. S. Iyengar, J. Tomasi, V. Barone, B. Mennucci, M. Cossi, G. Scalmani, N. Rega, G. A. Petersson, H. Nakatsuji, M. Hada, M. Ehara, K. Toyota, R. Fukuda, J. Hasegawa, M. Ishida, T. Nakajima, Y. Honda, O. Kitao, H. Nakai, M. Klene, X. Li, J. E. Knox, H. P. Hratchian, J. B. Cross, V. Bakken, C. Adamo, J. Jaramillo, R. Gomperts, R. E. Stratmann, O. Yazyev, A. J. Austin, R. Cammi, C. Pomelli, J. W. Ochterski, P. Y. Ayala, K. Morokuma, G. A. Voth, P. Salvador, J. J. Dannenberg, V. G. Zakrzewski, S. Dapprich, A. D. Daniels, M. C. Strain, O. Farkas, D. K. Malick, A. D. Rabuck, K. Raghavachari, J. B. Foresman, J. V. Ortiz, Q. Cui, A. G. Baboul, S. Clifford, J. Cioslowski, B. B. Stefanov, G. Liu, A. Liashenko, P. Piskorz, I. Komaromi, R. L. Martin, D. J. Fox, T. Keith, M. A. Al-Laham, C. Y. Peng, A. Nanayakkara, M. Challacombe, P. M. W. Gill, B. Johnson, W. Chen, M. W. Wong, C. Gonzalez, and J. A. Pople. Gaussian 03, Revision C.02. Gaussian, Inc., Wallingford, CT, 2004.
- [126] Pier Silvestrelli and Michele Parrinello. Water Molecule Dipole in the Gas and in the Liquid Phase. *Phys. Rev. Lett.*, 82(16):3308–3311, April 1999.
- [127] Anna V. Gubskaya and Peter G. Kusalik. The total molecular dipole moment for liquid water. *J. Chem. Phys.*, 117(11):5290, September 2002.
- [128] Anthony Goodwin, Jan Sengers, and Cor J Peters, editors. *Applied Thermodynamics of Fluids*. Royal Society of Chemistry, Cambridge, 2010.

- [129] J. M Prausnitz. *Molecular thermodynamics of fluid-phase equilibria*. Prentice-Hall, Englewood Cliffs, N.J., 1969.
- [130] John M. Prausnitz and Frederico W. Tavares. Thermodynamics of fluid-phase equilibria for standard chemical engineering operations. *AIChE J.*, 50(4):739–761, April 2004.
- [131] Grant M. Wilson. Vapor-Liquid Equilibrium. XI. A New Expression for the Excess Free Energy of Mixing. *J. Am. Chem. Soc.*, 86(2):127–130, 1964.
- [132] Henri Renon and J. M. Prausnitz. Local compositions in thermodynamic excess functions for liquid mixtures. *AIChE J.*, 14(1):135–144, January 1968.
- [133] K.E. Gubbins. Theory and computer simulation studies of liquid mixtures. *Fluid Phase Equilib.*, 20:1–25, January 1985.
- [134] Carolyn A. Koh, Hideki Tanaka, John M. Walsh, Keith E. Gubbins, and John A. Zollweg. Thermodynamic and structural properties of methanol-water mixtures: experiment, theory, and Mol. Simul. *Fluid Phase Equilib.*, 83(null):51–58, February 1993.
- [135] L. Vlček and I. Nezbeda. Excess properties of aqueous mixtures of methanol: Simple models versus experiment. *J. Mol. Liq.*, 131-132(null):158–162, March 2007.
- [136] Yang Zhong, G Lee Warren, and Sandeep Patel. Thermodynamic and structural properties of methanol-water solutions using nonadditive interaction models. *J. Comput. Chem.*, 29(7):1142–52, May 2008.

- [137] Athanassios Z. Panagiotopoulos. Direct determination of phase coexistence properties of fluids by Monte Carlo simulation in a new ensemble. *Mol. Phys.*, 61(4):813–826, July 1987.
- [138] A.Z. Panagiotopoulos, N. Quirke, M. Stapleton, and D.J. Tildesley. Phase equilibria by simulation in the Gibbs ensemble. *Mol. Phys.*, 63(4):527–545, March 1988.
- [139] Marcus G. Martin and J. Ilja Siepmann. Novel Configurational-Bias Monte Carlo Method for Branched Molecules. Transferable Potentials for Phase Equilibria. 2. United-Atom Description of Branched Alkanes. *J. Phys. Chem. B*, 103(21):4508–4517, May 1999.
- [140] David A. Kofke. Gibbs-Duhem integration: a new method for direct evaluation of phase coexistence by Mol. Simul. *Mol. Phys.*, 78(6):1331–1336, April 1993.
- [141] Eric C. Cichowski, Todd R. Schmidt, and Jeffrey R. Errington. Determination of Henry’s law constants through transition matrix Monte Carlo simulation. *Fluid Phase Equilib.*, 236(1-2):58–65, September 2005.
- [142] C Desgranges. Phase equilibria of molecular fluids via hybrid Monte Carlo Wang-Landau simulations: applications to benzene and n-alkanes. *J. Chem. Phys.*, 130(24), 2009.
- [143] Ariel Augusto Chialvo. Determination of excess Gibbs free energy from computer simulation by the single charging-integral approach. I. Theory. *J. Chem. Phys.*, 92(1):673, January 1990.

- [144] Ariel A. Chialvo. Accurate calculation of excess thermal, infinite dilution, and related properties of liquid mixtures via molecular-based simulation. *Fluid Phase Equilib.*, 83(null):23–32, February 1993.
- [145] J.M. Haile. On the use of computer simulation to determine the excess free energy in fluid mixtures. *Fluid Phase Equilib.*, 26(2):103–127, January 1986.
- [146] Yong Duan, Chun Wu, Shibasish Chowdhury, Mathew C Lee, Guoming Xiong, Wei Zhang, Rong Yang, Piotr Cieplak, Ray Luo, Taisung Lee, James Caldwell, Junmei Wang, and Peter Kollman. A point-charge force field for molecular mechanics simulations of proteins based on condensed-phase quantum mechanical calculations. *J. Comput. Chem.*, 24(16):1999–2012, December 2003.
- [147] William L. Jorgensen and Julian. Tirado-Rives. The OPLS [optimized potentials for liquid simulations] potential functions for proteins, energy minimizations for crystals of cyclic peptides and crambin. *J. Am. Chem. Soc.*, 110(6):1657–1666, March 1988.

Appendix

	Prediction	Validation using			
		One set	Two sets simultaneously		
sampled at \rightarrow	B	B or E or O	B and E	B and O	E and O
Parameter set \downarrow	(kJ/mol)	(kJ/mol)	(kJ/mol)	(kJ/mol)	(kJ/mol)
ΔH for methane solvation					
Benchmark (B)	1.950 ± 2.111	1.950 ± 2.111	1.879 ± 1.558	-0.983 ± 1.583	N/A
Expensive (E)	-0.316 ± 2.627	-5.935 ± 2.076	-1.553 ± 2.415	N/A	-0.749 ± 1.955
Optimized (O)	0.547 ± 2.809	0.115 ± 2.098	N/A	-6.155 ± 2.451	-0.006 ± 1.684
$\Delta\Delta H$ for methane solvation					
$\Delta H_B - \Delta H_E$	2.266 ± 1.595	7.885 ± 2.961	3.432 ± 2.078	N/A	N/A
$\Delta H_B - \Delta H_O$	1.403 ± 1.883	1.835 ± 2.976	N/A	5.172 ± 2.144	N/A
$\Delta H_E - \Delta H_O$	-0.863 ± 0.881	-6.050 ± 2.952	N/A	N/A	-0.743 ± 0.666

Table S1: Predictions and validation results for enthalpy of methane solvation match for expensive and optimal parameter sets within two standard deviations

	Prediction	Validation using			
		One set	Two sets simultaneously		
sampled at \rightarrow	B	B or E or O	B and E	B and O	E and O
Parameter set \downarrow	(kJ/mol)	(kJ/mol)	(kJ/mol)	(kJ/mol)	(kJ/mol)
Enthalpy ΔH for complete dipole inversion +e/-e to -e/+e					
Benchmark (B)	-2.898 \pm 3.319	-0.564 \pm 2.952	1.714 \pm 2.535	-0.493 \pm 2.578	N/A
Expensive (E)	-5.294 \pm 4.900	4.683 \pm 3.348	0.347 \pm 2.539	N/A	3.830 \pm 2.420
Optimized (O)	-5.301 \pm 5.197	-0.125 \pm 3.381	N/A	0.053 \pm 2.576	3.291 \pm 2.423
$\Delta\Delta H$ for complete dipole inversion +e/-e to -e/+e					
$\Delta H_B - \Delta H_E$	2.396 \pm 3.620	-5.247 \pm 4.464	1.367 \pm 1.926	N/A	N/A
$\Delta H_B - \Delta H_O$	2.403 \pm 4.025	-0.439 \pm 4.488	N/A	-0.546 \pm 2.080	N/A
$\Delta H_E - \Delta H_O$	0.007 \pm 1.946	4.808 \pm 4.758	N/A	N/A	0.538 \pm 0.935

Table S2: Predictions and validation results for enthalpy of dipole inversion match for expensive and optimal parameter sets within two standard deviations

	Prediction	Validation using			
		One set	Two sets simultaneously		
sampled at \rightarrow	B	B or E or O	B and E	B and O	E and O
Parameter set \downarrow	(kJ/mol)	(kJ/mol)	(kJ/mol)	(kJ/mol)	(kJ/mol)
Enthalpy ΔH of anthracene solvation with a vdw cutoff 1.3 nm					
Benchmark (B)	49.220 \pm 2.316	49.220 \pm 2.316	46.783 \pm 1.776	46.471 \pm 1.787	N/A
Expensive (E)	49.816 \pm 3.544	47.324 \pm 2.284	45.784 \pm 1.763	N/A	48.120 \pm 1.647
Optimized (O)	51.136 \pm 3.701	45.898 \pm 2.305	N/A	47.319 \pm 1.785	47.243 \pm 1.655
$\Delta\Delta H$ of anthracene solvation with a vdw cutoff 1.3 nm					
$\Delta H_B - \Delta H_E$	-0.596 \pm 2.699	1.896 \pm 3.253	0.999 \pm 1.406	N/A	N/A
$\Delta H_B - \Delta H_O$	-1.915 \pm 2.912	3.322 \pm 3.268	N/A	-0.848 \pm 1.478	N/A
$\Delta H_E - \Delta H_O$	-1.319 \pm 1.396	1.426 \pm 3.245	N/A	N/A	-0.877 \pm 0.619

Table S3: Predictions and validation results for enthalpy of anthracene solvation match for expensive and optimal parameter sets are within two standard deviations.